Simulation numérique de l'endommagement induit par l'exposition d'un matériau métallique à un plasma

Shihao Bian

UNIVERSITÉ PARIS XIII – SORBONNE PARIS NORD

École doctorale Sciences, Technologies, Santé Galilée

Numerical simulations of hydrogen retention and damage induced by plasma exposure in multi-material components

THÈSE DE DOCTORAT
présentée par

Shihao BIAN

pour l'obtention du grade de
DOCTEUR en Sciences pour l'ingénieur

soutenue le 16 février 2024 devant le jury d'examen constitué de :

GASPÉRINI Monique	Université Sorbonne Paris Nord	Présidente
ESTEVEZ Rafael	Université Grenoble Alpes	Rapporteur
HENAFF Gilbert	ISAE-ENSMA	Rapporteur
RICHOU Marianne	CEA IRFM	Examinatrice
WAUTERS Tom	ITER Organization	Examinateur
BONNIN Xavier	ITER Organization	Co-encadrant
CHARLES Yann	Université Sorbonne Paris Nord	Directeur
MOUGENOT Jonathan	Université Sorbonne Paris Nord	Co-encadrant

Acknowledgements

First, I would like to thank Yann CHARLES, Jonathan MOUGENOT, and Xavier BONNIN, respectively the director and co-supervisors of this thesis, for the quality of their supervision and their availability. I have learned a lot from you, both personally and scientifically.

I would like to thank the entire jury for their participation in the evaluation of this thesis. Thank you to Rafael ESTEVEZ and Gilbert HENAFF for agreeing to review and report on my thesis. Thank you to Marianne RICHOU, Monique GASPERINI, and Tom WAUTERS for agreeing to examine this work.

I would like to thank all the staff at LSPM (researchers, engineers, secretaries) for their support and assistance. I also want to thank everyone who, directly or indirectly, contributed to the completion of this work. Especially my dear college and friend Slim Ben Ayed for his great contribution to vacancy clustering, which consists an very important part of this work.

Finally, I would also like to thank my parents, who unhesitatingly funded my education in France, making my today possible. I also want to thank my classmates and friends in France, who have accompanied me through countless agonizing nights and numerous moments of sorrow. Here, I wish everyone good health and may all your wishes come true.

Contents

Introduction

The necessity for fusion energy arises from its key attributes, such as environmental safety and fuel abundance, distinguishing it from conventional nuclear fission energy. Fusion is regarded as inherently safer, generating no high-level radioactive waste, and poses no risk of global warming or acid rain [1, 2]. The Earth's plentiful supply of fusion fuels like deuterium and lithium promises a sustainable energy future. This backdrop set the stage for the initiation of the ITER (International Thermonuclear Experimental Reactor) project [3], an international collaboration aimed at demonstrating the feasibility and practicality of fusion energy. Focused on developing the tokamak reactor, a device designed for controlled fusion reactions, ITER's core mission is to validate fusion energy as the ultimate energy solution for the 21st century, addressing the pressing energy and environmental challenges facing our world today.

One of the significant challenges in achieving controlled fusion is managing the extreme conditions within the reactor, particularly the interaction between the hot plasma and the containment vessel's lining material. Therefore, selecting appropriate materials is crucial [4]. Performance during abnormal events, such as plasma disruptions and edge-localized modes (ELMs), is vital due to their potential to cause a massive, sudden energy release, endangering the reactor's structural integrity through high transient power loads [5, 6]. These events, along with the stored thermal and magnetic energy in the plasma, can lead to instabilities and confinement loss, posing serious challenges in tokamak devices [7].

In fusion devices like ITER, the management of potential radioactive hazards, especially from tritium, is meticulous. Tritium, a radioactive hydrogen isotope with a 12.3-year half-life, is used in minimal amounts and securely contained within a multi-layer barrier system to prevent environmental release. Fusion reactors naturally avoid generating high activity or long-lived radioactive waste, mainly producing low to medium activity waste, predominantly helium.

Finally, these reactors are designed for inherent safety, with mechanisms ensuring rapid shutdowns to prevent runaway reactions or meltdowns. Neutron activation within the reactor walls is also carefully controlled through specific safety measures, ensuring a safe

and controlled fusion process [8].

This dissertation focuses on the numerical simulation of damage caused to multi-metal materials by plasma irradiation. The core objectives include:

- **Chapter 1: Bibliography**

  Describing the global context of ITER project.

- **Chapter 2: Hydrogen Diffusion and Trapping**

  Investigating the complex dynamics of hydrogen atoms as they diffuse into and are captured by plasma-facing components (PFCs) is crucial in understanding plasma-material interactions. Moreover, the retention of hydrogen within the PFCs, along with its permeation through the cooling pipes, is of particular concern regarding ITER's safety standards.

- **Chapter 3: Vacancy Clustering**

  Assessing how vacancies (empty spaces in the material's lattice) spread and gather within multi-metal materials is crucial in understanding how they can affect the material's structural integrity.

- **Chapter 4: Nanovoid Formation**

  Evaluating the process by which nanovoids form in the material due to the effects of plasma irradiation, leading to further structural changes and possible weaknesses.

Chapter 1

Theoretical Background and Literature Review

In this chapter, it aims to describe the interactions between hydrogen (H) and materials. We will first introduce hydrogen diffusion and trapping processes within materials, revealing their fundamental mechanisms and characteristics. Subsequently, we will explore how impurity atoms influence the retention of hydrogen in materials and the interactions between these impurities and hydrogen. We then investigate the formation and growth mechanisms of hydrogen bubbles and detail the various factors that influence the nucleation of these bubbles. Lastly, we will evaluate existing models pertaining to hydrogen bubbles and introduce some existing studies on bubble formation from hydrogen exposure. The aim of this chapter is to provide readers with a comprehensive understanding of the interactions between hydrogen and materials, laying a theoretical foundation for further research and applications.

1.1 Interactions between Hydrogen and materials

As a licensed nuclear facility, ITER must limit the in-vessel tritium (T) retention to reduce the risks of potential release during accidents, with the inventory limit set at 1 kg. This limit includes 120 g of T trapped on the divertor cryopumps and 180 g of measurement uncertainty, leaving the maximum retention in the in-vessel components at 700 g. Simulations should be conducted to extrapolate the T inventory, particularly in the tungsten (W) divertor, taking into account the impact of H blisters at the surface.

The formation of blisters on tungsten exposed to energetic hydrogen isotopes has been widely reported in the literature [9–13]. They appear as protrusions on the metal surface, often accompanied by cavities forming in the sub-surface region. The exact process behind the formation of these blisters in metals is still under discussion. However, it's generally attributed to the build-up of hydrogen atoms at specific trapping sites. This accumulation

leads to the creation and growth of bubbles that become highly pressurized, with pressure estimates often ranging between 5 to 7 GPa. Filled with molecular hydrogen, these over-pressurized bubbles can then expand through various mechanisms, such as dislocation loop-punching, generalized plastic deformation, or the clustering of vacancies [10]. The bubbles then continue to grow, forming pressurized cavities or cracks in the sub-surface region, which leads to the formation of protrusions on the surface. A clear link between blister formation and hydrogen retention has been observed, as detailed in [14]. The entire process can be summarized as shown in the following Figure 1.1. To gain a comprehensive understanding of blister formation, it is essential to first consider the transport of hydrogen, including both diffusion and trapping. The thermal and mechanical fields, in particular, have significant effects on diffusion. Traps such as vacancies are created by plasma exposure and plastic strain. The reactions between hydrogen and vacancies, as well as the clustering of vacancies, lead to the formation of nanobubbles. These bubbles grow through the absorption of vacancies and plastic deformation, including the effects of pressure, and subsequently influence hydrogen transport. The accumulation of bubbles results in residual strains, while the presence of hydrogen embrittles the material. This combination eventually leads to the formation of a macroscopic crack that inflates into a blister.

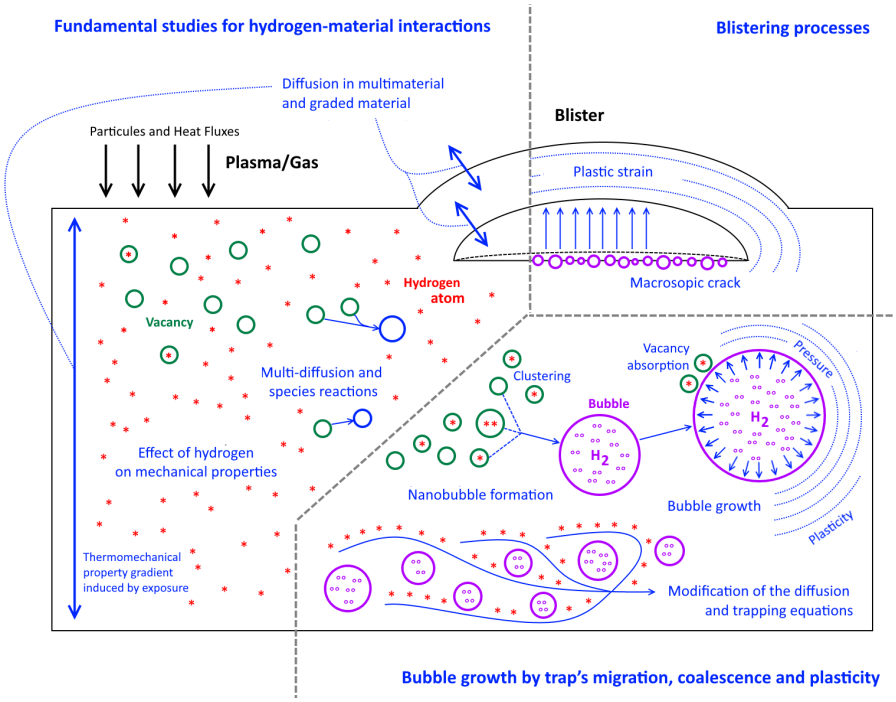

Figure 1.1: Main processes involved in the formation and evolution of bubbles and blisters

1.1.1 Diffusion and Trapping of Hydrogen in the materials

Once inside a material, hydrogen atoms diffuse through interstitial sites and can become trapped at defects. The hydrogen concentration in the material is typically expressed as $C = C_L + C_T$, where C_L represents the concentration of diffusive hydrogen and C_T represents the trapped hydrogen concentration. Additionally, the dimensionless values θ_L and θ_T can be defined. They denote the occupancy of the interstitial and trap sites, respectively, with corresponding densities represented by N_L and N_T:

$$\begin{cases} C_L = N_L \theta_L \\ C_T = N_T \theta_T \end{cases} \tag{1.1}$$

In the case of multi-trapping, the Equation 1.1 is replaced by $C_T = \sum_i C_T^i = \sum_i N_T^i \theta_T^i$, where i represents the number of different types of traps. The diffusive hydrogen flux is then determined by Fick's law, taking into account the effect of hydrostatic pressure $P_H = -\mathrm{tr}(\boldsymbol{\sigma})/3$. Here, $\boldsymbol{\sigma}$ is the stress tensor and $\mathrm{tr}(\boldsymbol{\sigma})$ denotes the trace of the stress tensor [15,16]:

$$\boldsymbol{\varphi} = -D_L \boldsymbol{\nabla} C_L - \frac{D_L V_H}{RT} C_L \boldsymbol{\nabla} P_H \tag{1.2}$$

where R is the perfect gas constant, T the absolute temperature, D_L the hydrogen diffusion coefficient, and V_H the partial molar volume of hydrogen. The mass conservation leads to the following trapping and transport equation, as defined by Sofronis and McMeeking [17]:

$$\frac{\partial C_L}{\partial t} + \frac{\partial C_T}{\partial t} = \boldsymbol{\nabla} \left(D_L \boldsymbol{\nabla} C_L + \frac{D_L V_H}{RT} C_L \boldsymbol{\nabla} P_H \right) \tag{1.3}$$

The trapped hydrogen concentration rate can be computed using the so-called McNabb and Foster equation [18], for $C_L << N_L$ (or $\theta_L << 1$):

$$\frac{\partial C_T}{\partial t} = \frac{p}{N_L} C_L (N_T - C_T) - k C_T \tag{1.4}$$

which corresponds to a kinetic equation for a first-order chemical reaction, with p and k the forward and reverse reaction rate constants [19]. Assuming a constant with time N_T distribution, the Equation 1.4 can be rewritten as:

$$\frac{\partial \theta_T}{\partial t} = p \theta_L (1 - \theta_T) - k \theta_T \tag{1.5}$$

R.A Oriani [20] has proposed an expression for the steady state value of θ_T:

$$K_T \theta_L = \frac{\theta_T}{1 - \theta_T} \tag{1.6}$$

in which $K_T = p/k$ represents the equilibrium constant for the trapping equation 1.5. K_T is also linked to the trap binding energy E_B by $K_T = e^{-E_B/RT}$. Using Oriani relationship, the

Equation 1.3 can be rewritten as in the case of an instantaneous trapping $\frac{d\theta_T}{dt} = 0$ on the one hand, and for a trap density N_T which is only dependent on the equivalent plastic strain ϵ_p (i.e. related to dislocations) [21, 22]:

$$\left(1 + \frac{C_T(1-\theta_T)}{C_L}\right)\frac{\partial C_L}{\partial t} - \boldsymbol{\nabla}\left(D_L \boldsymbol{\nabla} C_L + \frac{D_L V_H}{RT} C_L \boldsymbol{\nabla} P_H\right) + \theta_T \frac{dN_T}{d\epsilon_p}\dot{\epsilon}_p = 0 \tag{1.7}$$

The "strain rate factor $\theta_T \frac{dN_T}{d\epsilon_p}\dot{\epsilon}_p$" [23] has been introduced by Krom et al. in the original equation defined by Sofronis and McMeeking [24] to insure a correct hydrogen balance when trap creation occurs. Last, an effective hydrogen diffusion coefficient D_{eff} can be defined when trapping occurs:

$$\frac{D_L}{D_{eff}} = 1 + \frac{C_T(1-\theta_T)}{C_L} \tag{1.8}$$

In the case of transient trapping [25], the Equation 1.7 becomes:

$$\frac{\partial C_L}{\partial t} + \frac{p}{N_L} C_L(N_T - C_T) - kC_T - \boldsymbol{\nabla}\left(D_L \boldsymbol{\nabla} C_L + \frac{D_L V_H}{RT} C_L \boldsymbol{\nabla} P_H\right) = 0 \tag{1.9}$$

All of the transport and trapping equations of hydrogen have been used in the same Small Scale Yielding (SSY) configuration, as defined in Figure 1.2, in which a parametric study has been conducted. This configuration can be considered a benchmark in the hydrogen transport and trapping studies (see [17, 21, 25–34]).

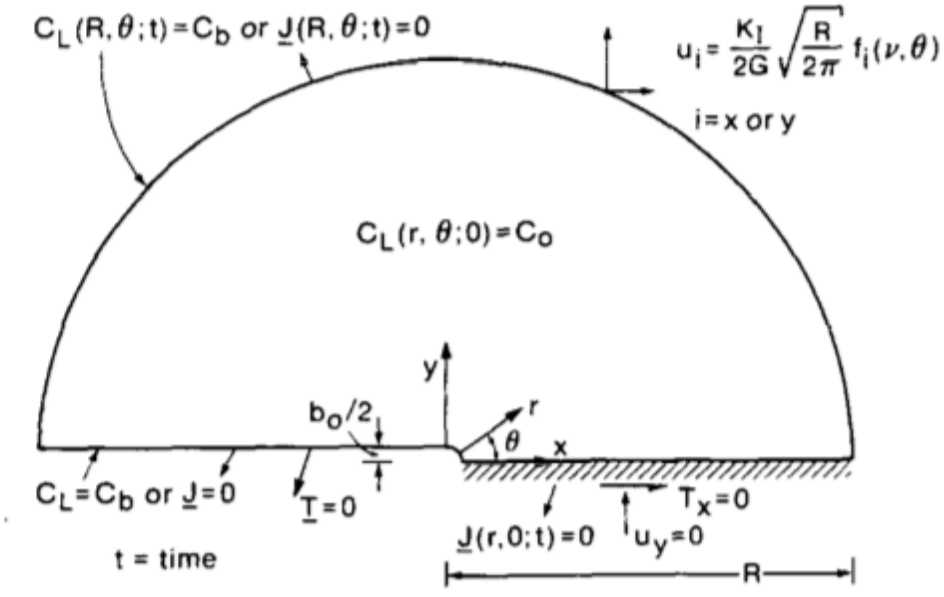

Figure 1.2: SSY configuration [17]

In Figure 1.3 is plotted the diffusive hydrogen distribution at the crack tip, as a function of the forward and reverse reaction rate constants p and k.

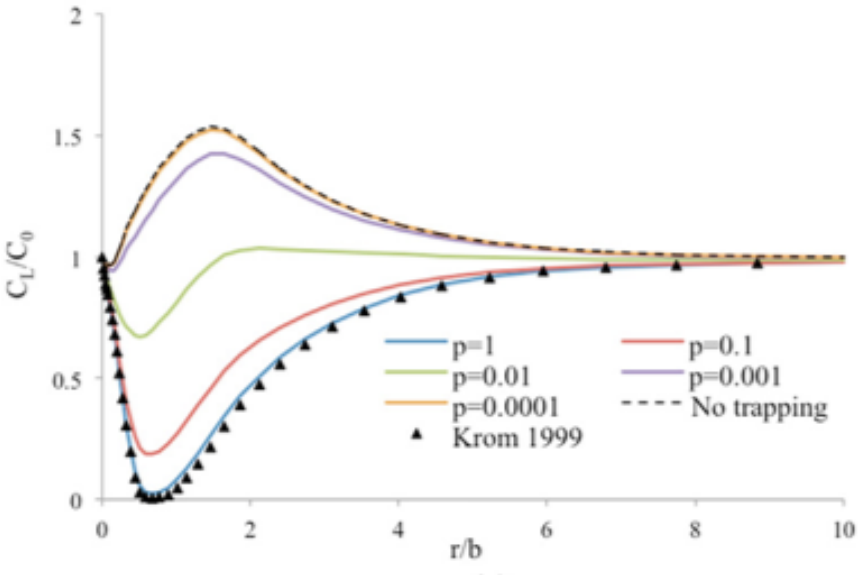

Figure 1.3: C_L distribution at the crack tip in the SSY configuration for several p and k values, and for a loading time of 1.3 s [25].

All these works rely on the N_T function, i.e., the evolution of trap density with plastic strain (no other trap kind is considered).

1.1.2 Influence of Impurity atoms on Hydrogen Retention in Tungsten

The role of impurity atoms in influencing material behavior has been a subject of significant interest in materials science and engineering. In the context of hydrogen retention in tungsten, impurity atoms play a crucial role in shaping the material's ability to absorb and retain hydrogen.

This section explores the mechanisms through which impurity atoms influence the retention of hydrogen, providing insights into the intricate chemistry and physics underlying this phenomenon. By uncovering the complex interactions between impurity elements and hydrogen, this section contributes to our broader comprehension of material performance.

1.1.2.1 Helium

The effect of He on the retention of hydrogen is related to the irradiation ion energy. In the case of low-energy helium-seeded deuterium plasma exposure, the investigations of [35, 36] indicate that He is generally mobile in W with an activation energy of migration around 0.2 eV. Still, it tends to self-trapping, which means that two or more He atoms can form He clusters in solution sites. This self-trapping strongly decreases the He diffusion rate, i.e., it prevents He diffusion over long distances into the bulk of W. The He clusters can eject W atoms creating He-Vacancy complexes (He_xV_y). Furthermore, these complexes can act as trapping sites for hydrogen, enhancing the trapping of hydrogen on the near-surface of W. On the other hand, different grades of W will also influence the trapping of helium and hydrogen [37], as shown in Figure 1.4.

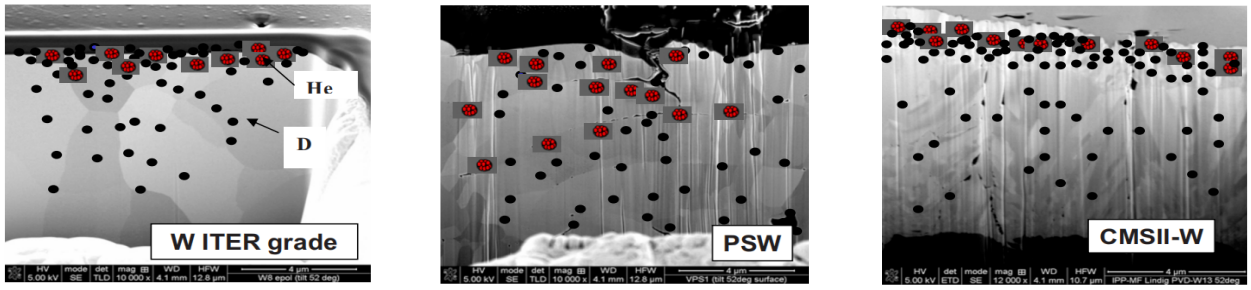

(a) ITER grade W (b) PSW (c) CMSII-W

Figure 1.4: He seeding in D plasma on deuterium retention in different W grades

However, simultaneous irradiation of helium ions and hydrogen ions to tungsten [38,39] were performed in the energy range between 600 eV and 1500 eV, which is higher than the threshold energy for displacement damage for helium $E_{dis} = 500$ eV. In this case, helium ions have the potential to induce displacement damage, leading to significant alterations in the trapping behavior of both helium and deuterium.

In [40], the results obtained for two different near-surface layers He bubbles morphologies revealed that the effects of He irradiation on deuterium retention in tungsten strongly depend on its subsequent thermal cycling. For annealing below 900 K, deuterium retention is similar to the one measured in pristine tungsten. In contrast, for annealing above 1150 K, deuterium retention in the He bubbles-enriched tungsten is increased 3–8 fold compared to non-damaged tungsten. Additionally, the deuterium desorption peak shifts from 540 to 450 K. This increase of deuterium trapping in the He bubbles-enriched tungsten annealed above 1150 K is presumably associated with a modification of the near-surface microstructure concurrent with outgassing of helium.

1.1.2.2 Nitrogen

O.V. Ogorodnikova et al. have investigated the influence of seeding of nitrogen into deuterium plasma on the accumulation of deuterium in tungsten (W ITER grade and W produced by Plansee, respectively) by experiments (Experimental conditions: T = 370 K, -100 V bias and a fluence of about 5×10^{24} (D/m^2)) [41]. It is shown that the seeding of nitrogen into deuterium plasma does not prevent blister formation and even results in an increase in the size of blisters in some cases. A comparison of blisters on W Plansee and W ITER reveals that more blisters with larger sizes were observed on W Plansee compared to W ITER (see Figures 1.5 to 1.8).

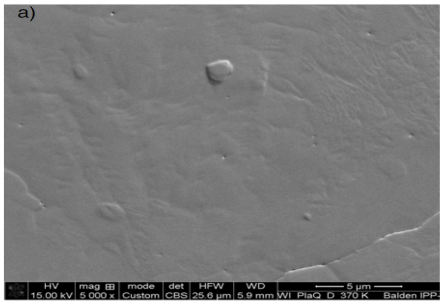

Figure 1.5: W ITER: After pure D plasma exposure [41].

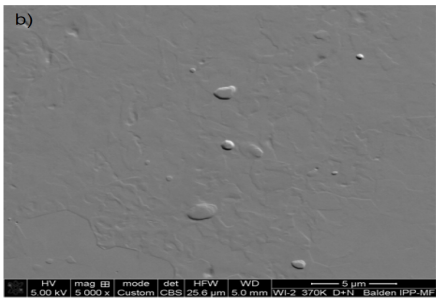

Figure 1.6: W ITER: After 1% N seeding into D plasma exposure [41].

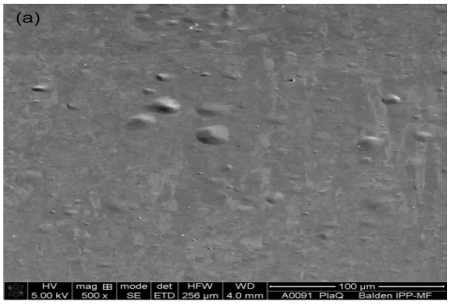

Figure 1.7: W Plansee: After pure D plasma exposure [41].

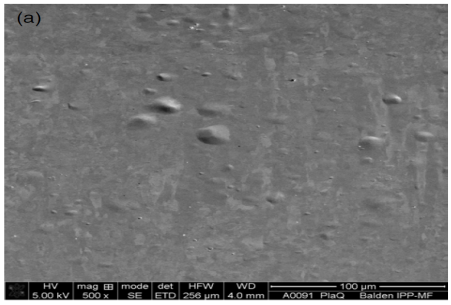

Figure 1.8: W Plansee: After 1% N seeding into D plasma exposure [41].

In addition, the presence of nitrogen in surface layers increases deuterium diffusion into the bulk. The deuterium density at a depth of 6 micrometers is $3 \sim 4$ times higher for N-seeded D plasma compared to pure deuterium plasma.

L. Gao et al. have also investigated the bulk tungsten samples exposed to deuterium plasma with a fluence of 10^{24} (D/m^2) with or without nitrogen pre-implantation at 300 and 500

K, respectively [42]. NRA (Nuclear Reaction Analysis) was applied for the determination of nitrogen and deuterium retention on the near-surface. Optical microscopy was used to investigate the surface modification by blistering after implantation (see Figures 1.9 to 1.12). At a temperature of 500 K, the W/N layer appears to augment the diffusion of deuterium into the bulk material, while also inhibiting deuterium loss from the surface. This leads to a significantly higher concentration of deuterium within the bulk and the formation of larger blisters compared to the scenario without prior nitrogen pre-implantation.

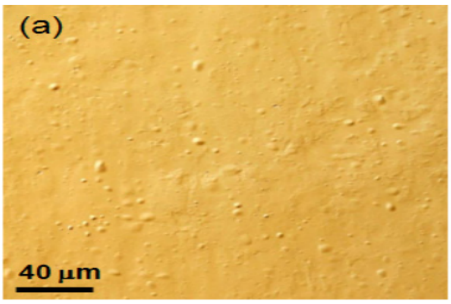

Figure 1.9: Pure D plasma at 300 K [42].

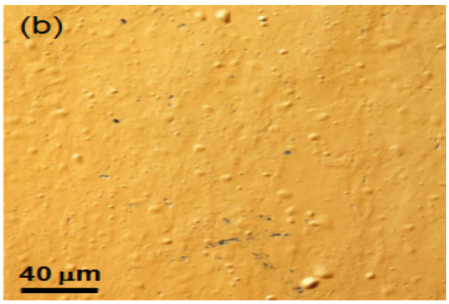

Figure 1.10: N-seeded D plasma at 300 K [42].

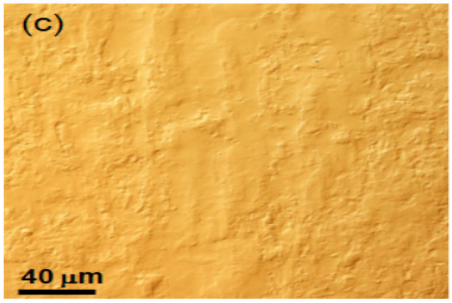

Figure 1.11: Pure D plasma at 500 K [42].

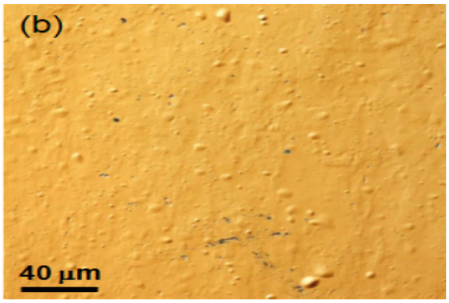

Figure 1.12: N-seeded D plasma at 500 K [42].

In [43], the research suggests that while nitrogen has little effect on hydrogen dissolution in interstitial sites, it does significantly degrade the material's capacity to trap hydrogen atoms within vacancies. Additionally, nitrogen impedes the accumulation of hydrogen in these vacancies. Consequently, it can be expected a lower hydrogen retention concentration in the nitrogen-enriched layer near the surface than in the pure tungsten surface (see Figure 1.13). On the other hand, the high concentration of nitrogen increases the time to desorb a hydrogen atom from its lattice site, acts to increase the apparent activation energy for hydrogen diffusion, and thus significantly decreases the effective diffusivity of hydrogen. Hence, it is assumed that the nitrogen-enriched layer on the tungsten surface can act as

a diffusion barrier for the re-emission of implanted hydrogen, leading to the enhancement of hydrogen diffusion into the bulk, and consequently, an increase of hydrogen retention in tungsten bulk (see Figure 1.14).

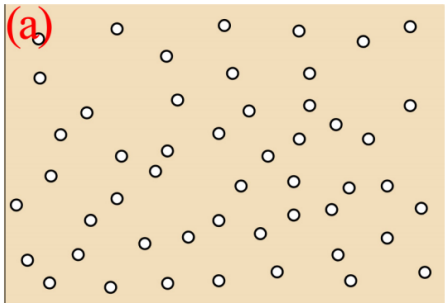

Figure 1.13: W exposed to pure H plasma [43].

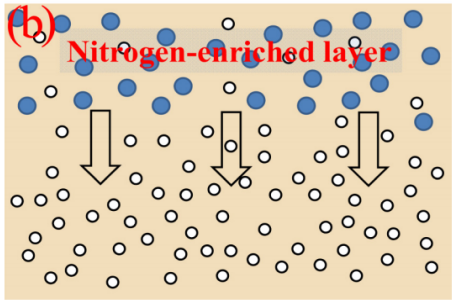

Figure 1.14: W exposed to nitrogen-seeded H plasma [43].

1.1.2.3 Argon & Neon

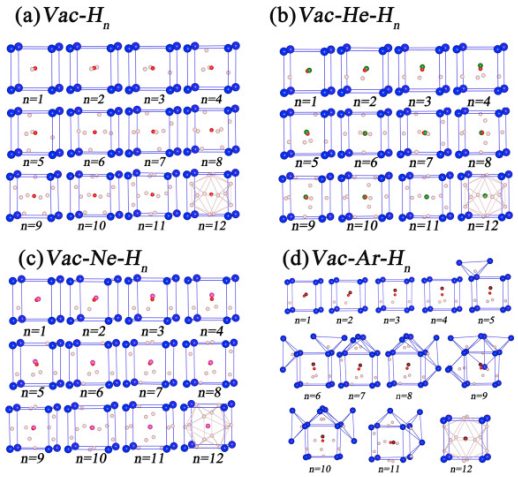

Figure 1.15: Stable configurations for vacancy-inert gas-hydrogen complexes [44].

Kong et al. have systematically investigated the interaction between the inert gas element Argon with hydrogen in tungsten using first-principles calculations [44]. They evaluated the binding energies of hydrogen with inert gas interstitial defects and vacancy-inert gas complexes and showed their stable configurations (see Figure 1.15). Generally, the concentration of inert gas defects in tungsten is quite low and even negligible because the inert gas atoms are insoluble in tungsten. However, the concentration would be significantly

increased when the tungsten was exposed to the inert gas ions, where an inert gas-enriched layer would be formed below the tungsten surface. On the whole, the inert gas defect can reduce the hydrogen diffusivity causing the formation of the inert gas-enriched layer below the tungsten surface greatly reducing the effective diffusion of hydrogen isotopes and this is a cause of the effects of the inert gas on the hydrogen retention.

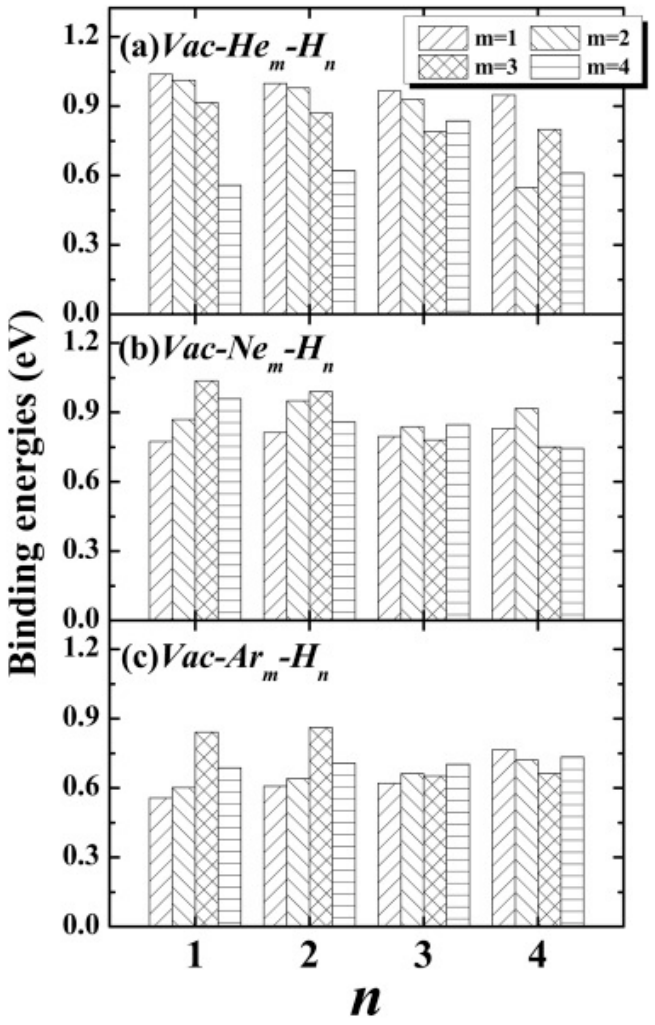

Figure 1.16: The binding energy of the n_{th} interstitial hydrogen atom with the stable $Vac - IGA_m - H_n$ complexes [44].

A.Kreter et al. have investigated the influence of helium, argon, neon, and nitrogen as plasma impurities on the deuterium retention in tungsten in the linear plasma devices PSI-2 and PISCES-A [45]. The experiments were performed at tungsten sample temperatures of 500 K and 770 K. Thermal desorption spectra of deuterium atoms for the cases of pure D,

D + Ar, and D + Ne plasmas at $T = 500$ K, are shown in Figure 1.17. The effects of argon and neon appear to be similar, both leading to an increase of the deuterium retention (see Figure 1.18). However, at $T = 770$ K (thermal desorption spectra are not shown here), the effects of both argon and neon invert: the D retention drops (see Figure 1.19).

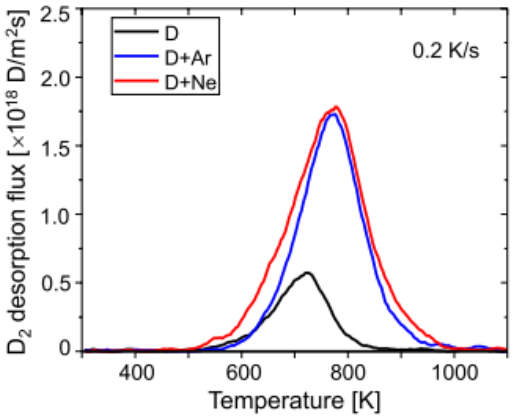

Figure 1.17: TDS of tungsten samples exposed to pure D, D + Ar, and D + Ne plasmas [45].

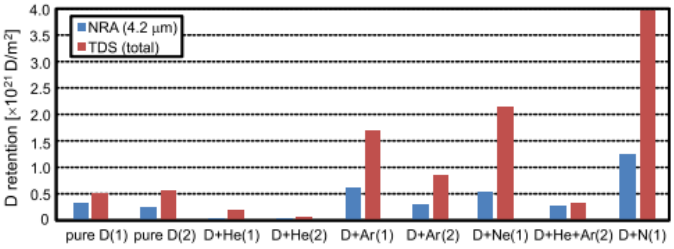

Figure 1.18: Deuterium retention measured by NRA and TDS for different plasma compositions at $T = 500$ K. Indexes (1) and (2) indicate the respective experimental series [45].

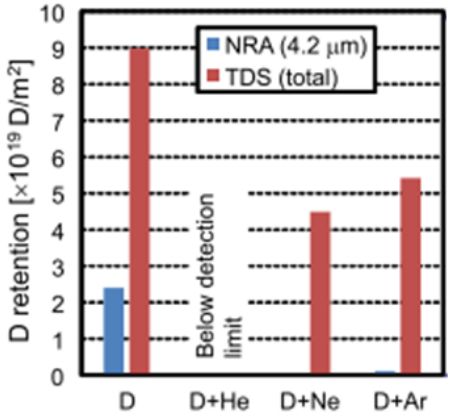

Figure 1.19: Deuterium retention measured by NRA and TDS for different plasma compositions at $T = 770$ K [45].

1.1.3 Formation of bubbles

The present study centers around hydrogen-induced cracking (HIC), a process primarily characterized by the formation of gas bubbles within the sample, eventually leading to blistering on its surface. On a macroscopic level, HIC is manifested by the formation of blisters on sample surfaces, which can occur as a result of processes such as cathodic loading [46] or plasma exposure [47]. This blistering phenomenon is not limited to specific materials, as it has been observed in a wide range of substances including titanium [48], aluminium [47], molybdenum [49], tungsten [50], and iron [51].
It has been assumed that blisters are caused by the creation and the growth of dihydrogen bubble formations [52], as illustrated in Figure 1.21.

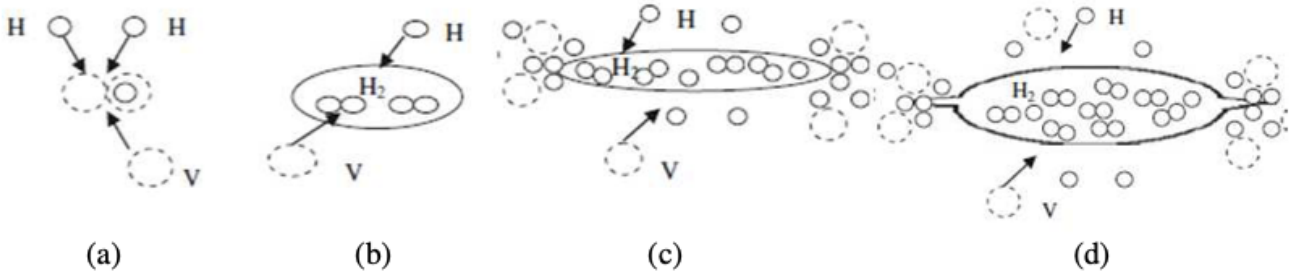

Figure 1.21: Blistering process, as proposed by Ren et al. [52]: (a) Hydrogen trapping on vacancies, (b) Vacancies clustering and creation of H_2 bubbles, (c) Bubble growth by vacancy diffusion and plastic deformation (due to the internal gas pressure), (d) Microcracking and blistering.

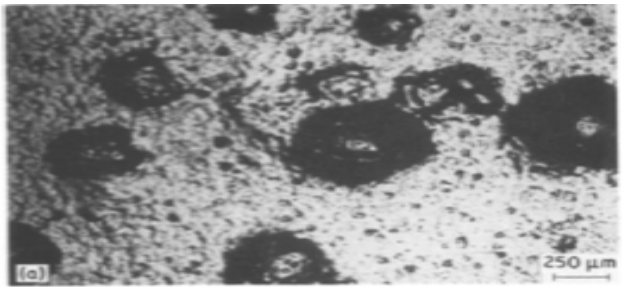

(a) Iron [46]

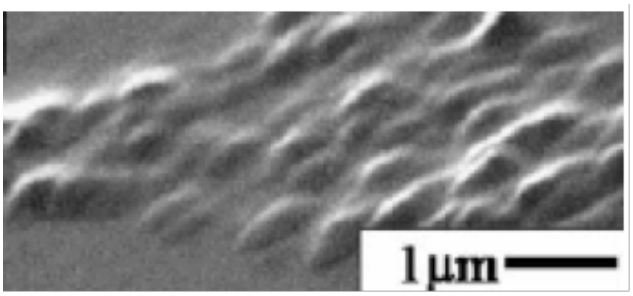

(b) Molybdenum [49]

Figure 1.20: Blisters observed for Iron and Molybdenum.

Several studies have explored the origin of these bubbles. For instance, Condon and Schober [53] proposed that these bubbles emerge when the concentration of hydrogen or vacancies significantly exceeds their solubility values. Ren et al. [52] pointed out that the presence of trapped hydrogen within vacancies leads to the formation of bubbles through clustering. Moreover, recent observations have revealed that bubbles can also form following local debonding due to embrittlement, as noted by Tiegel et al. [54].

Griesche et al. [55] conducted a 3D tomography scan of blisters (see Figure 1.22), revealing the presence of hydrogen within the crack. This observation supports earlier findings reported by Hoshihira et al. in their studies on aluminum and molybdenum samples [49]. Such findings have been interpreted as confirming the assumptions made by Ren et al.

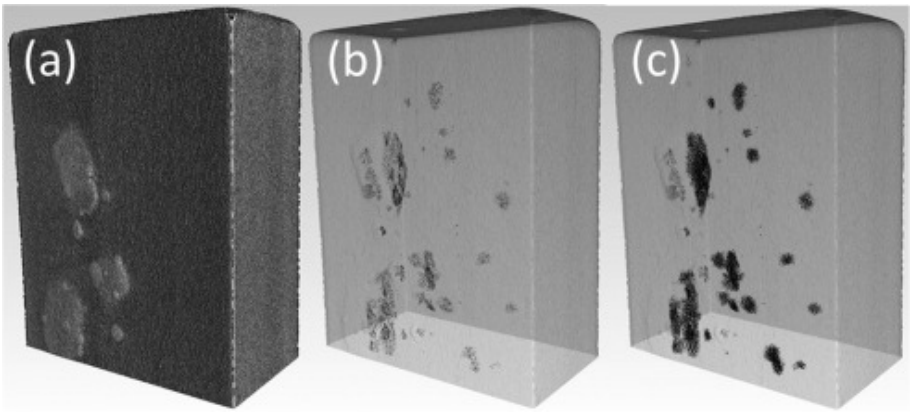

Figure 1.22: Blisters in iron, observed by neutron tomography [55]: (a) Surface with blisters, (b) Crack distribution, (c) Hydrogen distribution.

They hypothesized that the formation of blistering cracks is attributed to the micro-voids they observed on the crack face. These voids were formed as a result of hydrogen-vacancy clusters reaching a critical threshold.

1.1.3.1 Nuleation and growth of bubbles

This section is dedicated to the finite element modeling of various aspects of the blistering process, including void nucleation, growth, and ultimately, crack initiation and propagation. Since, to the best of our knowledge, there is no existing comprehensive model for this scheme, we begin by focusing on void nucleation and growth, followed by an examination of blistering.

For the initiation stage, the vacancy clustering model is employed, focusing on the transport (including trapping) of hydrogen by mobile vacancies. This model has been extensively investigated using methods such as Object Kinetic Monte Carlo (OKMC) [56] and cluster dynamics simulations [57–59], which require tracking a significant number of clusters (up to 1000 clusters, including mobile ones). Thermodynamic approaches have also been developed, following the pioneering work of Wampler [60]. A similar approach was taken in the context of reacting nanoparticles [61]. Clustering energy can be calculated using Density Functional Theory (DFT) [62, 63]. Critical cluster features necessary for bubble formation have also been explored [64].

For growth, two processes have been pointed out: growth by plasticity and vacancy clustering. Based on dislocation loop emission, a first model linking internal pressure, surface energy, and void growth has been proposed by Greenwood et al. [65], and confirmed by molecular dynamics calculations [66]. This model has been extended later by Wolfer to include several dislocation emissions and their interactions [67, 68]. Global fracture initiation between two

growing bubbles has been investigated by Evans [69] as a function of their internal pressure. Thermodynamic formulations of the void growth due to vacancy diffusion, coupled with internal pressure, have been proposed for several configurations and materials [70–72]. No studies focused on the coupled effect of vacancy diffusion and dislocation emission on void growth have been found.

The Greenwood approach has been used in the work of Sang et al. [73] to model a predefined bubble population growth in a Rate Equation model or to get the bubble's size evolution in aluminium sample exposed to plasma [74]. These approaches, however, are limited for they assume an initial bubble radius and position and most importantly lead to an unstable bubble growth. Last, such numerical models focus only on one growth mechanism, with neither bubble formation nor interactions with mechanical fields and vacancies. Little work might be found accounting for such interactions: based on a given bubble population, Ayadi et al. [51] include in a finite element model the trapping of hydrogen in bubbles, the induced pressure increase, leading to a phenomenological bubble increase (coupled with plasticity) and material swelling. This rustic modeling work, generalizing the approach proposed by Martinsson and Sandström [75], does not include bubble initiation, nor their influence on plasticity development or blistering. Several works aimed to propose a thermodynamical framework for bubble creation and growth by defect diffusion, including mechanical field coupling in the specific case of perfectly plastic materials, as Fischer and Svoboda [76] or Chandler et al. [77]. The most advanced approach has been proposed by Millet et al. [78, 79] through a 2D phase field modeling of bubble creation and expansion due to vacancy diffusion, but with no mechanical fields.

Finite element computations were used to capture the phenomenon of void growth due to internal pressure, in the context of elastoplasticity. These works used a unit cell, made of a spherical porosity filled with pressurized hydrogen gas. The condition of this porosity creation can also be accounted for, as in the work of Barrera and Cocks [80], in which inclusion debonding is modeled using cohesive elements. Ayadi et al. [51] computed the pore increase as a function of its internal pressure and the surrounding plasticity; Ogosi et al. [81] did the same at the single crystal level, considering, furthermore, a modification of the matrix yield stress due to hydrogen. Liang et al. [82] (and later Diaz et al. [83]) investigated the effect of hydrogen on the plasticity-induced pore growth, generalizing the ductile damage development in metallic materials.

Although this phenomenon is not directly related to the creation and growth of hydrogen-induced bubbles, it is of interest because it pertains to the formation and expansion of plasticity-induced voids, as depicted in Figure 1.23.
To model this damage, Gurson [85,86] proposed a modification of the yield criterion to include the porosity, later modified by Tvergaard [87] and Needleman to become the GTN model:

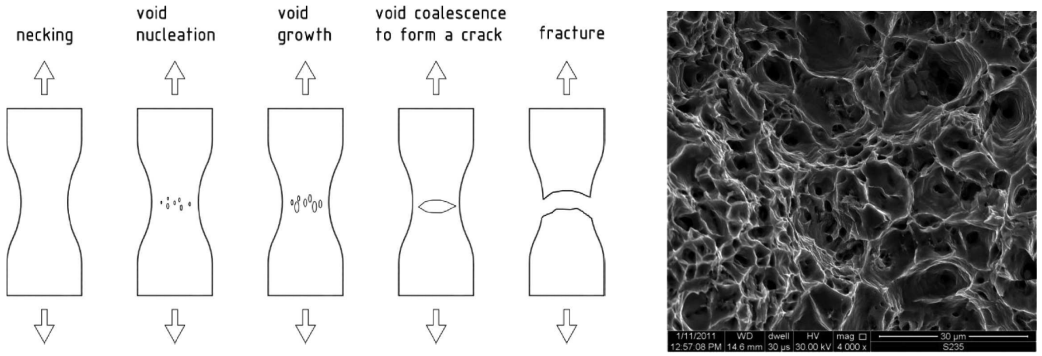

(a) (b)

Figure 1.23: (a) Ductile fracture process by void creation and growth. (b) Ductile crack on an S235JR steel sample, on which voids can be seen [84].

$$\phi(\sigma, \sigma_0, f) = \frac{\sigma_{eq}^2}{\sigma_0^2} + 2q_1 f cosh\left(\frac{3}{2}\frac{q_2\sigma_m}{\sigma_0}\right) - (1 + q_1^2 f^2) = 0 \tag{1.10}$$

in which f represents the void volume fraction [88]. q_1, q_2 and q_3 are material parameters, σ_{eq} the von Mises stress and σ_0 the yield stress. σ_m represents the hydrostatic stress (equal to $-\text{tr}(\boldsymbol{\sigma})/3$). f evolves with the equivalent plastic strain ϵ_p by [89].

$$\dot{f} = \dot{f}_{growth} + \dot{f}_{nucleation} \tag{1.11}$$

where $\dot{f}_{growth}$ denotes the void growth by plasticity, so that

$$\dot{f}_{growth} = (1 - f)\text{tr}\,\dot{\epsilon}_p \tag{1.12}$$

and $\dot{f}_{nucleation}$ represents the creation of new voids by [90]

$$\dot{f}_{nucleation} = A\dot{\sigma_0} \tag{1.13}$$

A represents the probability of the formation of new voids between ϵ_p and $\epsilon_p + d\epsilon_p$ in the form of Gaussian distribution, and $\dot{\sigma_0}$ represents the increment of equivalent tensile flow stress. It is worth noting that $\text{tr}\,\dot{\epsilon}_p$ represents the volume increase linked to void expansion.

Several extensions have been proposed to this model: among others void coalescence [89, 91, 92], internal pressure [93, 94], secondary void nucleation [95], or size effects [96, 97].

1.1.3.2 Factors related to the formation of blisters

Several studies have investigated the necessary conditions for blisters to occur [14, 98, 99]. The ion fluence, ion energy and surface temperatures (see Figure 1.24) are critical parameters influencing the build-up of tritium inventory in the material.

In general, for fluxes below 10^{22} $m^{-2}\mathrm{s}^{-1}$, blister formation is suppressed for a surface temperature higher than 700 K because the increased diffusivity reduces the transient H concentration in the near-surface region to values below that needed for blistering [9].

At particle flux densities similar to those expected at the ITER divertor strike-points (around 10^{24} $\mathrm{m}^{-2}.\mathrm{s}^{-1}$) not only blisters but also nanobubbles (diameter 10–20 nm) are observed in the near-surface region. Second, blistering persisted until much higher a surface temperature (up to 1273 K) than reported for lower flux density experiments [100]. Indeed, temperature variations during plasma exposure have a pronounced effect on D-induced blistering and retention in tungsten [101].

The basic explanation lies in the balance between the particle source at the surface and the diffusion. As the flux is increased, a higher diffusion rate (and hence temperature) is required to prevent H accumulation in the sub-surface region and the associated blister formation.

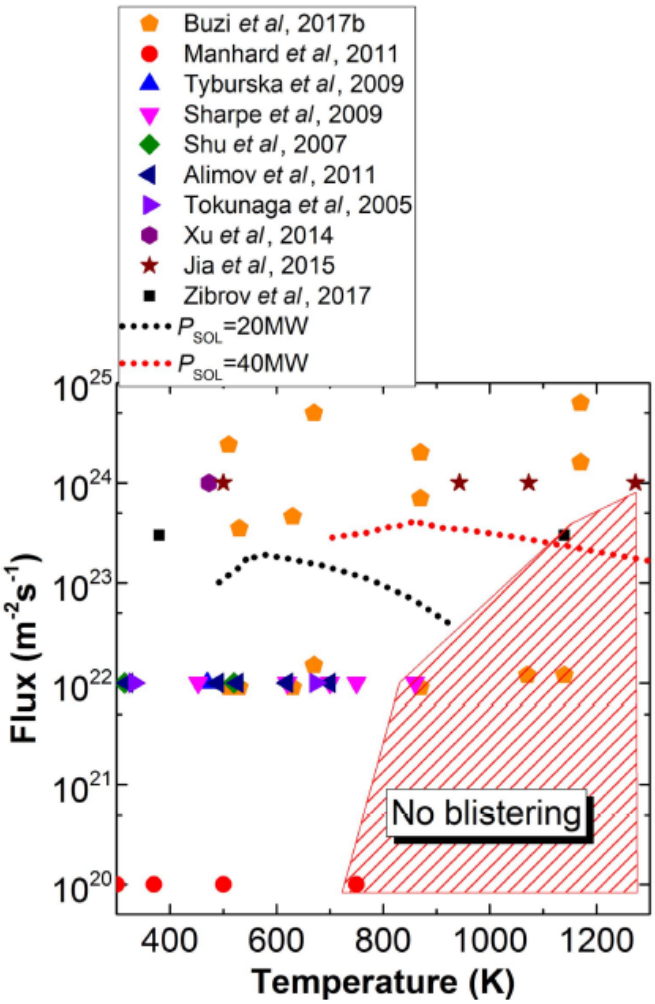

Figure 1.24: Overview of blister formation conditions as a function of incident H flux and surface temperature

The dashed area indicates where blisters are not observed. Black and red dashed lines indicate the peak ion flux and surface temperature derived from SOLPS simulations for pure H operations during the non-active phases of ITER. Different symbols illustrate the experimental conditions reported in [9, 102–108].

There are a large number of factors that affect the formation of blisters, however, they can be divided into three major categories as illustrated in Figure 1.25. In addition to this, each category contains different subcategories.

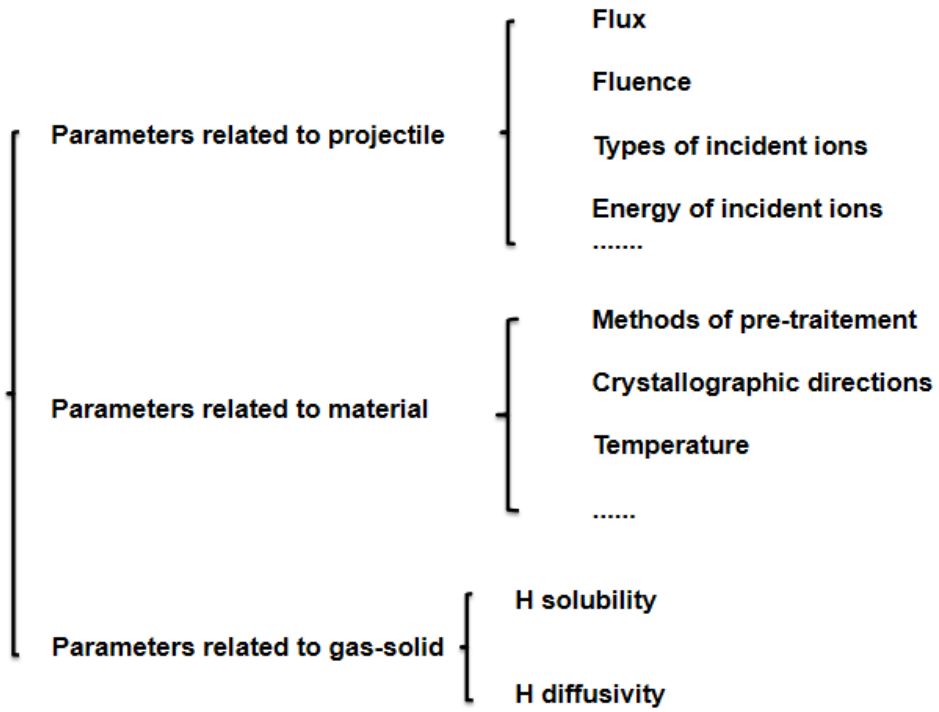

Figure 1.25: Factors related to the formation of blisters.

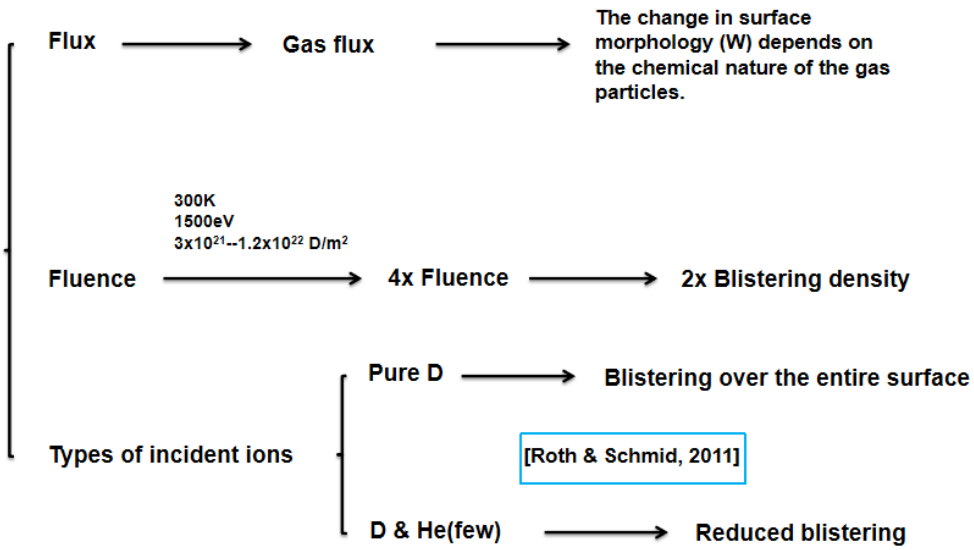

Figure 1.26: Factors related to the exposure.

Figure 1.26 gives examples for the first category related to exposure. The change in tungsten

surface morphology when exposed to gas flux depends on the chemical nature of the gas particles. Studies performed by implanting Be foils with 1500 eV deuterium ions at fluences ranging between $3 \times 10^{21} \sim 1.2 \times 10^{22}$ (D/m^2) at 300 K showed that when the fluence is increased by a factor four, blistering density increases by a factor two [109]. When exposed to pure D plasma, it developed blisters all over the surface whereas when exposed to deuterium plasma with a low content of He, the formation of blisters is suppressed in tungsten surface [14].

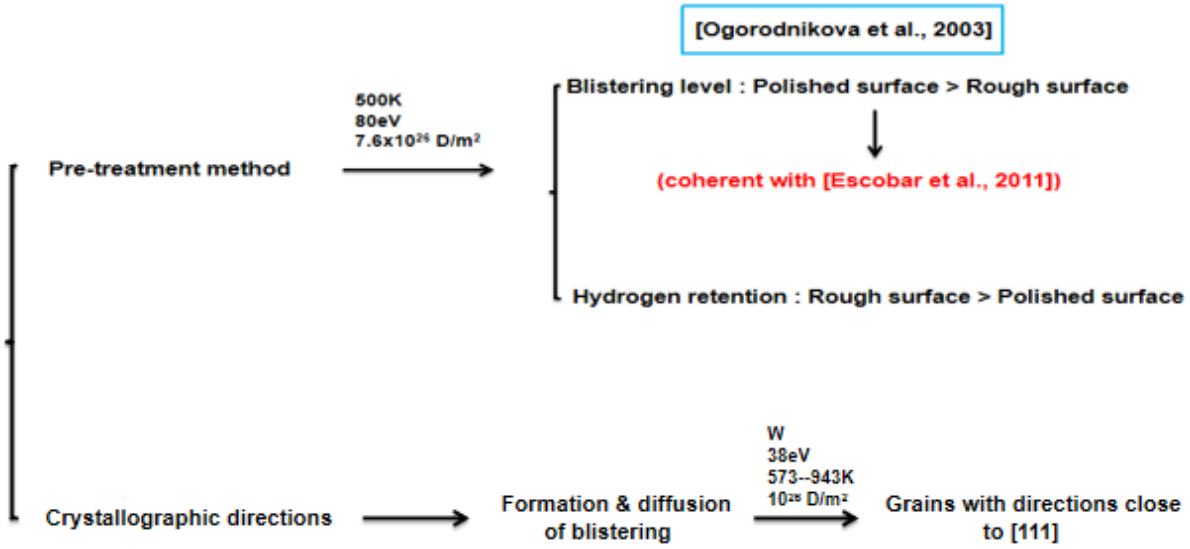

Figure 1.27: Factors related to material. W behaviour [110] is coherent with behaviour found in Fe [111].

Figure 1.27 shows us some examples for the second category related to the material. Nishijima et al. exposed samples with different levels of roughness to deuterium plasma with 80 eV ions at a fluence of $7.6 \cdot 10^{26}(D/m^2)$ at 500 K, the sample with the lowest roughness showed enhanced blister formation [112] and other studies reached a similar conclusion: blisters were not detected on rough surfaces. Nonetheless, hydrogen retention in these samples is higher than in polished tungsten samples. Through these experimental phenomena, we suggest that: compared with rough surfaces, smooth surfaces are more prone to blister formation. On the other hand, in [113], experiments performed with tungsten samples exposed to deuterium plasma with a flux ranging from 10^{22} to 10^{25} $(ions/m^2/s)$, a fluence of $10^{26}(ions/m^2)$, an ion energy of 38 eV and a sample temperature ranging from 573 to 943 K showed that blisters form more quickly on grains with directions close to [111]. Moreover, some studies are focused on the damages created at the atomic scale: vacancy creation due to ion exposure [114] or the neutron damage [115].

1.1.3.3 Blistering modeling

Finite element modeling of blistering is usually made without any consideration of the underlying processes that have led to the creation of a pressurized crack. Few works, especially, include the creation and propagation of cracks in the context of hydrogen-induced blisters, but focus on the ability of pre-existing cracks to propagate, depending on the gas pressure enclosed. These works are very similar to disk pressure test simulations [116, 117], which are dedicated to the selection of materials for hydrogen storage purposes[1].

First, investigations were conducted to get the stress map around blisters, depending on their configurations. Kang et al. [119] made a parametric study on pre-existing cracks under a transient thermal load to investigate the von Mises stress distribution, as a function of blister's shape, in the case of a plasma-facing component in fusion reactors. Toda et al. [120] analyzed the von Mises stress map around an aluminium cast defect, as a function of its internal pressure. The shape of this defect was designed using tomography (see Figure 1.28).

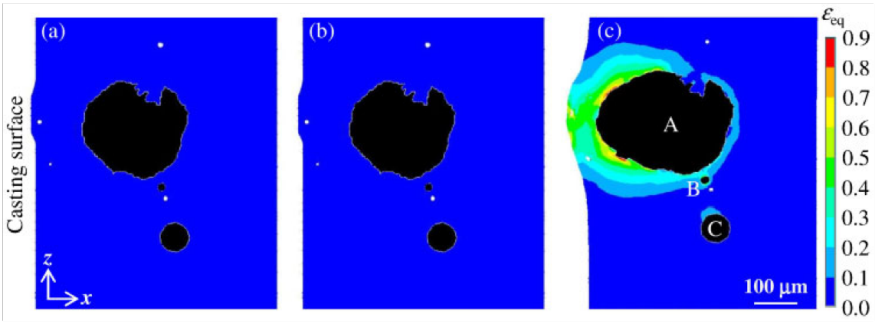

Figure 1.28: Von Mises stress distribution around a pressurized defect, for an internal pressure equal to (a) 0.4 MPa, (b) 4.7 MPa and (c) 8.2 MPa [120].

You [121] re-used the configurations proposed by [122], by assuming a pre-existing non-propagating crack, and performed a parametric study on the blister height as a function of the internal pressure, the cap thickness, the cap internal stress, and the material yield stress (see the configuration in Figure 1.29).

[1] "Blistering, another source of H damage is often considered as less noxious than [Hydrogen Embrittlement]. Yet a blister rupture is that of an embedded disk strained by increasing gas pressure and can be a case of localized [Hydrogen Gas Embrittlement]" [118].

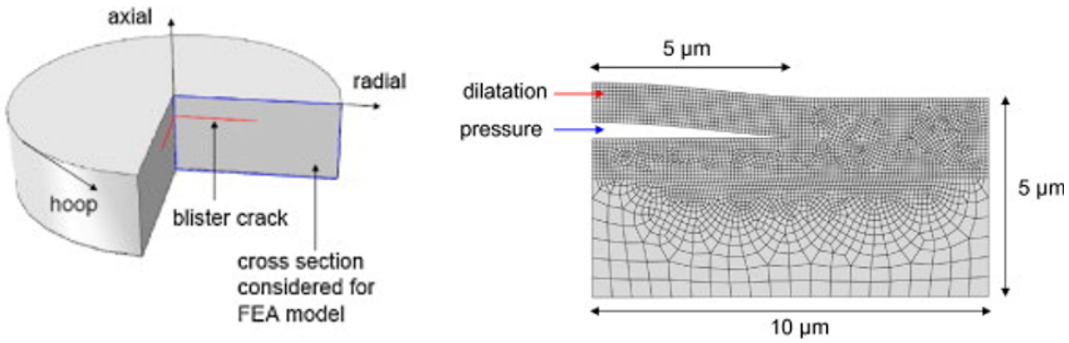

(a) (b)

Figure 1.29: (a) Studied configuration and (b) its axisymmetric finite element model [121].

Some results of this study are presented in Figure 1.30. Especially, in 1.30a can be observed the increase of the radial stress with the decrease of the blister height, induced by the augmentation of the yield stress. Such a result can be linked to the ability of blister bursting, depending on the mechanical behavior of materials.

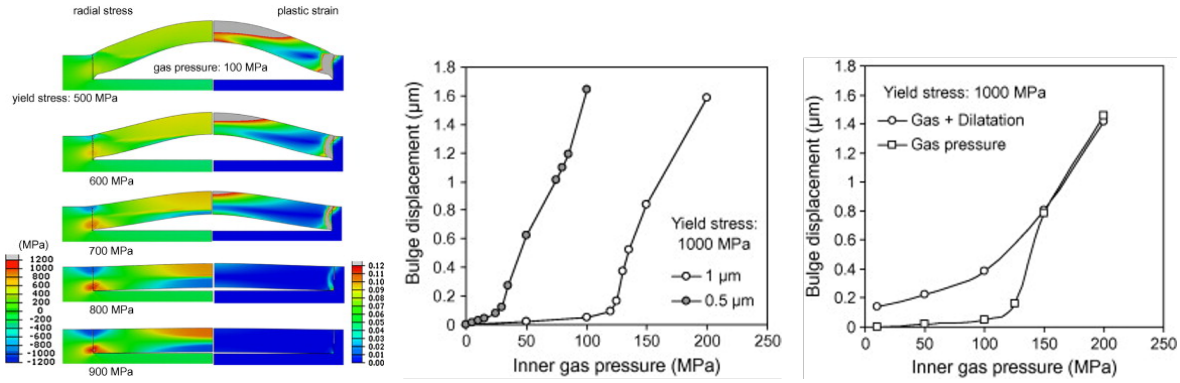

(a) (b) (c)

Figure 1.30: (a) σ_{rr} and ϵ_p maps for several yield stress values (σ_Y =900 down to 500 MPa), for an internal pressure equal to 100 MPa. (b) Blister height for a cap thickness equal to 0.5 and 1 μm, and σ_Y=1 GPa. (c) Effect of residual strains on the blister height for a cap thickness equal to 1 μm, and σ_Y=1 GPa [121].

This study has been completed by a numerical analysis of the crack ability to propagate, by Li and You [123], based on a computation of the J-integral at the crack tip for several configurations and internal pressure values[2].

[2]The J-integral is linked to energy release rate G and is, therefore, used as a propagation criterion when

This kind of analysis was also used in the computational works dedicated to blisters in the context of hydrogen storage: a crack is introduced in the tank thickness, with no possibility to propagate, and parametric studies are conducted, based on internal crack pressure value, tank inner pressure, crack configuration, etc..., on the J-integral value at the crack tip. Several examples are presented thereafter.

Hu et al. [125] considered a main blister crack and a secondary one on the cap surface to investigate bursting (figure 1.31). Depending on the toughness value (linked here to the critical J-integral value, J_c), the ability of the crack to propagate can be investigated (figure 1.31b).

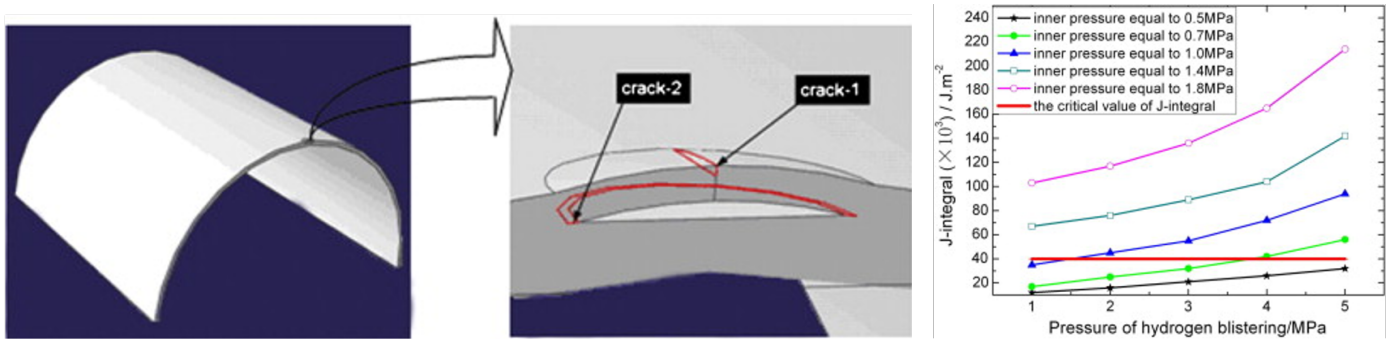

(a) (b)

Figure 1.31: (a) Configuration of the blister studied by FE method and (b) evolution of the J-integral for several tanks and crack inner pressures, with a comparison of its critical value J_c [125].

Ji et al [126] investigated the effect of several blisters on the J-integral value, as a function of both tank and crack internal pressure and the distance between blisters (Figure 1.32).

compared to the material toughness [124]. It is classically computed by FE software, by post-processing a computation result.

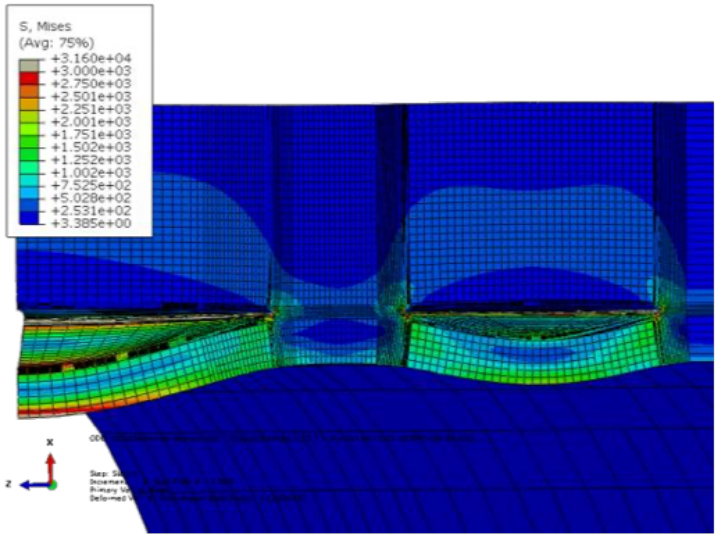

Figure 1.32: Von Mises stress repartition in neighboring blisters, for an internal pressure of 500 MPa, a tank pressure of 0.35 MPa, and a blister distance equal to 5 mm [126].

González et Morales [127] (and latter Razak et al. [128]) focused too on the interactions between internally loaded cracks, though non-aligned, as a function of the internal pressure (see Figure 1.33).

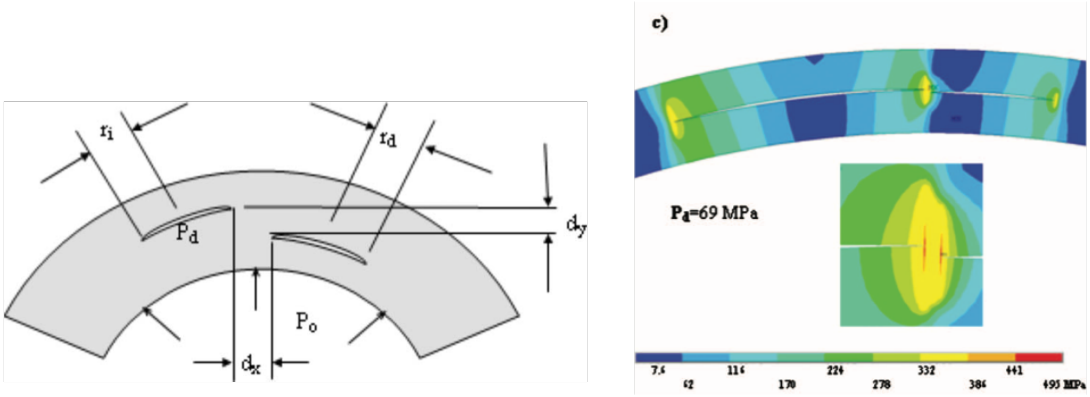

(a) (b)

Figure 1.33: (a) Configuration for the crack in the tank thickness. (b) Von Mises repartition for a crack internal pressure equal to 69 MPa [127].

The work proposed by Traida et al. [129], in the very same context of hydrogen storage, differs from the previous one due to the use of cohesive elements. The global geometry is simplified,

and a pre-existing crack is set, loaded by internal pressure. The crack propagation is here possible, thanks to a cohesive element's TSL modified by the local hydrogen concentration.

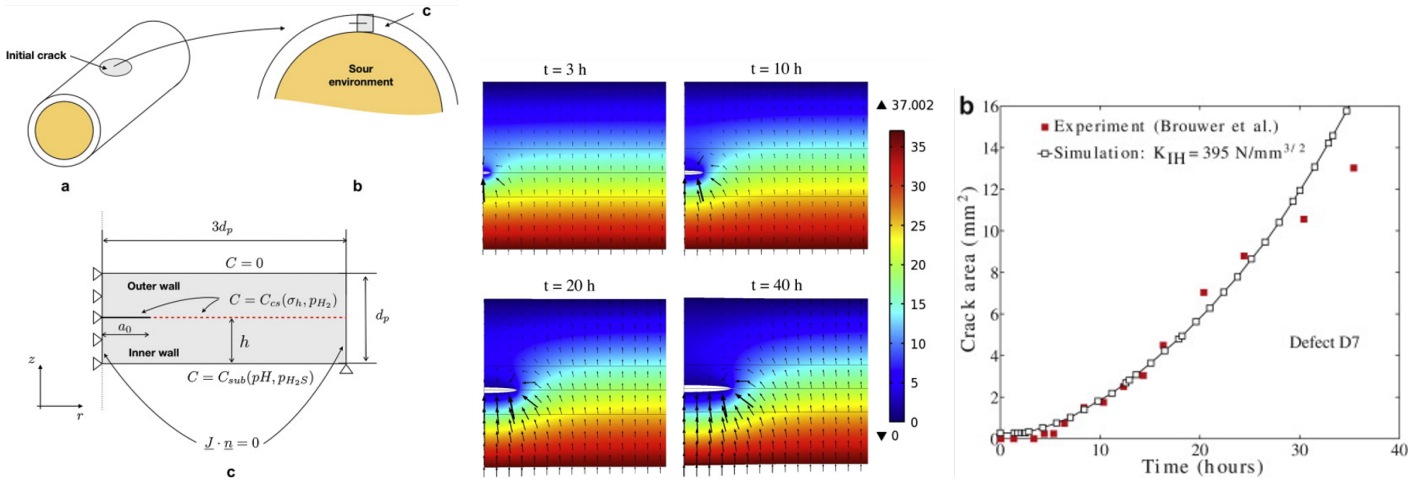

(a) (b) (c)

Figure 1.34: (a) Crack configuration and boundary conditions. (b) Evolution of the hydrogen concentration due to to the slow crack propagation and (c) comparison between the experimental and numerical crack velocity [129].

Last, it is worth noting that blistering, in the context of film debonding, is widely investigated using the finite element approach. Assumptions, however, do not differ from the hydrogen-related works: a pre-existing crack is defined, and its ability to propagate is investigated based on fracture mechanics criteria, on using cohesive elements. Main differences rely on the boundary conditions (see, among otters, the work of Kattamis et al. [130], for thin films blistering, induced by ink diffusion and thermo-mechanical loading, or Hong and Cheong's [131], which is focused on thin film blistering due to local heating. A specific test called the blister test dedicated to the characterization of thin film adhesion has also been designed and modelled [132–134]).

1.1.4 Existing models: from H exposure to blister formation

Huge efforts have been done to create models and to develop codes for HI transport. Tables 1.1 and 1.2 regroup some of the work done by different teams. These works illustrate a brief overview of the capability of models to describe the early stages of blister creation (from H exposure to first cluster formation). In this section we will focus on several points from these models to determine which capabilities must be included in an integrated model of blister formation.

Table 1.1: Comparison of existing models of hydrogen migration (diffusion/trapping)

Model	Ref.	steady or transient trapping	diffusion related to mechanical field (∇P)	temperature resolution T($\underline{x}$,t)	V_1H_x	V_xH_y
McNabb-Foster	[18]	Transient				
Oriani	[20]	Steady				
Sofronis et al.	[17, 24, 135]	Steady	✓			
Krom et al.	[21, 23]	Steady	✓			
Benannoune, Charles et al. (Abaqus)	[136, 137]	Transient	✓	✓		
Sang, Bonnin, Quiros et al. (HIIPC)	[73, 138] [47, 139]	Transient		✓		
Longhurst (TMAP)	[140]	Transient		✓		
Delaporte-Mathurin et al. (FESTIM)	[141, 142] [143]	Transient		✓		
Hodille et al. (MHIMS)	[144, 145]	Transient	✓		✓	
Ebihara et al.	[146]	Transient		✓	✓	✓
Abderrazak et al. (COMSOL Multiphysics)	[147]	Steady	✓			
D. Matveev et al. (TDS)	[148]	transient		✓	✓	

Table 1.2: Comparison of existing models of hydrogen migration (vacancy mobility)

Model	Resolved variable	Mobility of traps	Trap reaction
McNabb-Foster	C		
Oriani	θ		
Sofronis et al.	θ	✓	
Krom et al.	θ	✓	
Benannoune, Charles et al. (Abaqus)	C or μ	✓	✓
Sang, Bonnin, Quiros et al. (HIIPC)	C		
Longhurst (TMAP)	C or μ		
Delaporte-Mathurin et al. (FESTIM)	C or μ		
Hodille et al. (MHIMS)	C		
Ebihara et al.	C		✓
Abderrazak et al. (COMSOL Multiphysics)	C		
D. Matveev et al. (TDS)	θ		

In Table 1.1, V_1H_x denotes the capture of x hydrogen atoms in one vacancy, and V_xH_y the capture of y hydrogen atoms in x vacancies.

1.1.4.1 Temperature and pressure assisted diffusion

The majority of models of the mechanical community [21,135] include the effect of hydrostatic pressure in the diffusion equation as presented in section 1 (and listed in Table 1.1 at the ∇P column). Mainly in these works the temperature is constant and the diffusion coefficient is also assumed constant.
However, the temperature is a significant factor in the diffusion and trapping of hydrogen, which is through the Arrhenius equation, directly linked with hydrogen diffusivity.

$$D_L = D_0 \exp^{-\frac{E_d}{k_B T}} \tag{1.14}$$

where D_0 is the preexponential factors, independent of temperature, of hydrogen diffusivity, k_B the Boltzmann constant, E_d the diffusive energy. The diffusion coefficients in all the

models developed by the plasma community are temperature dependent. The importance of the 2D thermal field to have a good estimation of the H transport at the component scale is underlined in [137, 141].

Two ways are proposed to include the variation of the diffusivity with the temperature: (i) it is simply to impose a stationary profile; or (ii) solving the heat equation (as listed on the temperature resolution column of the Table 1.1). The first way is enough if the model is applied for small geometry or without periodic heat loads; however for larger geometries or when heat flux varies with time, heat equation must be solved.
In addition, the thermal influence also refers to thermophoresis, which is also known as the Soret effect. This phenomenon indicates the effect of the gradient of temperature $\boldsymbol{\nabla} T$ on the diffusion of matter. In our case, this description can be written as follows

$$\boldsymbol{J} = -D_L \boldsymbol{\nabla} C_L - C_L D_T \boldsymbol{\nabla} T \tag{1.15}$$

where D_T is the thermodiffusion coefficient. The thermophoresis effect is integrated in TMAP [149] and MHIMS [145]. As shown in Figure 1.35, for high fluence up to 10% difference is found on tritium retention when the Soret effect is considered in tungsten (but with the heat of transport of the iron). Due to lack of data for the tungsten, this effect is usually not included in the simulations.

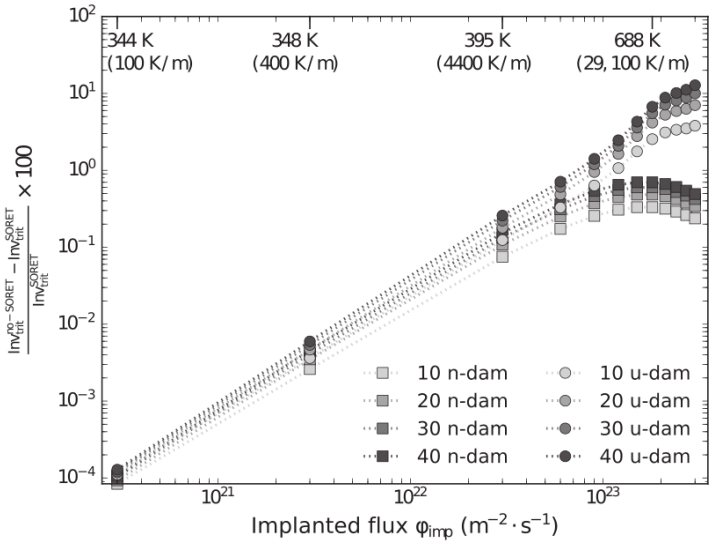

Figure 1.35: Difference in percent between the tritium retention when the Soret effect is taken into account and when it is not for undamaged W (u-dam, circle) and neutron-damaged W (n-dam, square). The maximal temperature as well as the temperature gradient in the material is displayed as a top x-axis. [145]

1.1.4.2 Chemical potential

When there are multiple materials, there will be a discontinuity of concentration of hydrogen at the interfaces induced by the variation of the hydrogen solubility. In this case, the chemical potential μ must be continuous (instead of the concentration):

$$\mu = \mu^0 + RT \ln \left(\frac{C_L}{N_L} \right) \tag{1.16}$$

where μ^0 is the chemical potential in a reference. Delaporte-Mathurin et al. [142] assumed a continuity of chemical potential at the equilibrium, through equivalent conservation of $\frac{C_L}{S}$, where S is the solubility of hydrogen in the material considered.

As listed in Table 1.2, some codes can solve either the concentration (C) or the chemical potential (μ) as a main resolved variable. Some models solve the occupancy ratio θ (e.g. $\theta_L = C_L/N_L$), however, this approach is not the most appropriate to take into account the transient trapping (as explained in [150]).

1.1.4.3 Trapping

As shown in section 1.1.1, two major models were proposed to take into account the trapping of HI: the transient trapping proposed by McNabb and Foster [18] (Equation 1.4) and the equilibrium one proposed by Oriani [20] (Equation 1.6). The transient modeling must be used to simulate cycles of exposure but the implementation could be difficult in the finite element approach. Benannoune et al. [136] propose an analytical solution to implement transient trapping without directly solving the partial differential equation in Abaqus code. This method was used by [83] in Abaqus. This approach allows us to reduce computational time. However, most codes solve directly the McNabb and Foster PDE including ones based on FEM [141].

Most models consider that trap energy is independent of the occupancy (i.e. only one energy per trap) e.g. [18, 20, 73, 136, 140, 141]. The work of Schmid et al. presents a modified diffusion-trapping model with a fill level dependent on detrapping energies that can also explain isotope exchange experiments. Density functional theory (DFT) calculations predict that even mono-vacancies can store between 6 and 12 H atoms with detrapping energies that depend on the fill level of the mono-vacancy. The new fill level dependent diffusion trapping model allows to test these DFT results by bridging the gap in length and time scale between DFT calculations and experiment. As pointed out in [151], trapping at single occupancy traps with fixed detrapping energy fails to explain isotope exchange experiments, instead a trapping model with multi-occupancy traps and fill-level-dependent detrapping energies is required. This approach is also included in MHIMS code [152] and used to model thermal desorption spectrometry (TDS) experiments performed on single crystal tungsten

after deuterium ions implantation. Detrapping energies obtained from the model to adjust the temperature of TDS spectrum observed experimentally are in good agreement with DFT values within a deviation below 10%. The desorption spectrum as well as the diffusion of deuterium in the bulk are rationalized in light of the model results. The disadvantage of this model is that you need as many equations to solve trap levels as you have. Ebihara et al. [146] used a unique equation to represent the occupancy-dependent trap energies for iron, in their model the trap energy varies linearly between two H trapping energies given by molecular simulation. This model allows to reduce the number of equations to solve, so the computational time; however, isotope exchange can not be taken into account.

1.1.4.4 Hydrogen dragging by mobile dislocations

Conversely, dislocation motion affects the hydrogen concentration by dragging their Cottrell atmosphere [153]. Anomalous hydrogen transport (i.e., faster than expected while based only on a Fick equation) has been extensively explained in the 70's by this phenomenon in several materials (nickel [154–156], copper [157], pure aluminium [158] and aluminium alloys [156, 159], steel [159–163], Inconel [156, 159], iron [156, 159, 164]). It is worth noting that other explanations have been pointed out to explain this transport acceleration [165,166].

Hwang et al. [164] have performed experiments on iron single crystals submitted to both permeation and tensile tests, in a direction for which only one slip system is activated. While measuring the hydrogen permeation flux, they observed reproducible peaks, attributed to the emergence of a dislocation at the outer surface, releasing its Cottrell atmosphere (Figure 1.36).

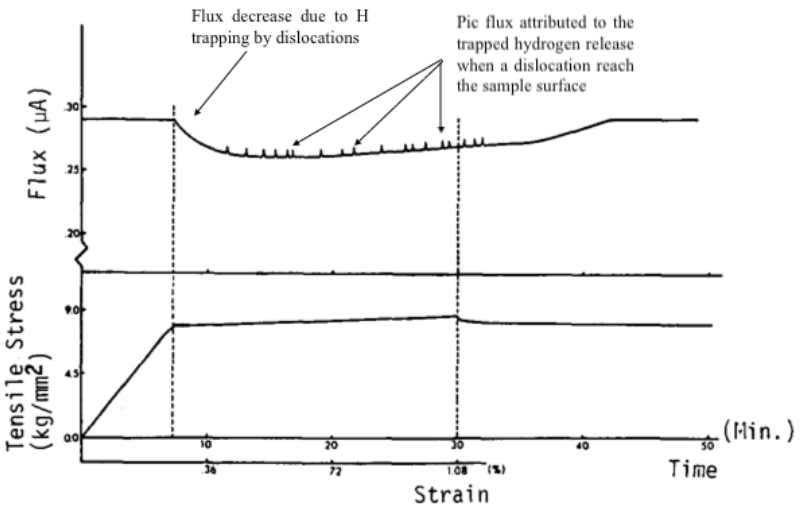

Figure 1.36: Permeation flux through an iron single crystal submitted to a tensile test; peaks denote the release of trapped hydrogen when a dislocation reaches the outer sample surface [164].

Very few models exist to account for this phenomenon. Tian et al. [167] were the first to propose a relationship between trapped hydrogen velocity $\bar{v}$ and the dislocation driving force F. They also pointed out the maximal velocity $\bar{v}_v$ at which the Cottrell atmosphere is no longer attached to a dislocation (releasing the trapped hydrogen atoms)

$$\bar{v}_c = \frac{D_H}{kT}\frac{E_B}{30b} \tag{1.17}$$

in which D_H is the hydrogen diffusion coefficient, k the Boltzmann constant, T the temperature, E_B the dislocation binding energy and b the Burgers vector norm.
In 2015, Dadfarnia et al. [31] proposed a modification of the Krom's transport and trapping equation 1.7 by including an extra term they assumed to be representative of the hydrogen dragging by mobile dislocation

$$\left(1+\frac{C_T(1-\theta_T)}{C_L}\right)\frac{\partial C_L}{\partial t} - \boldsymbol{\nabla}.\left(D_L\boldsymbol{\nabla}C_L + \frac{D_L\bar{V}_H}{RT}C_L\boldsymbol{\nabla}P_H\right) + \theta_T\frac{dN_T}{d\epsilon_p}\dot{\epsilon}_p + \boldsymbol{\nabla}.(\theta_T N_T^m \boldsymbol{v}^d) = 0 \tag{1.18}$$

$\boldsymbol{v}^d$ represents the dislocation velocity and N_T^m the part of the trap density N_T which is mobile. v^d is linked to the strain rate $\dot{\epsilon}_p$ by

$$\dot{\epsilon}_p = \rho_m \boldsymbol{b}.\boldsymbol{v}^d \tag{1.19}$$

ρ_m is the mobile dislocation density so that

$$N_T^m = \lambda \frac{\rho_m}{a} \tag{1.20}$$

where $\lambda = \sqrt{2}$ or $\sqrt{3}$ for bcc and fcc lattices, and a is the lattice parameter.

They applied this approach on the SSY configuration used by Sofronis and McMeeking [17], and Krom et al. [23] to point out the effect of such a modification on the hydrogen distribution ahead a crack tip.

This approach has been extended at the crystal scale by Charles et al. [168], by linking $\boldsymbol{v}^d$ to slip systems. They conducted a parametric study on the crystallographic texture of a polycrystalline bar, to show how grain orientations can affect trapped hydrogen dragging by dislocation (Figure 1.37).

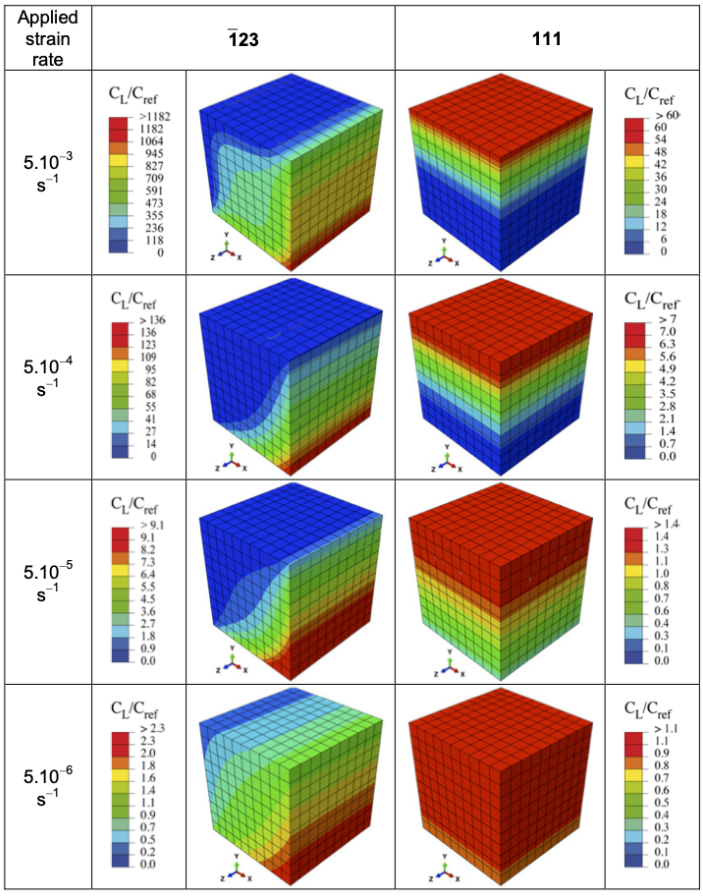

Figure 1.37: Influence of the applied strain rate and crystal orientation on the hydrogen distribution when the Dadfarnia's flux is accounted for [168].

1.1.4.5 Traps creation

As mentioned in section 1.1.1, the effect of plastic deformation ϵ_p on the density of dislocation N_T has been concluded by A.J. Kumnick and H.H. Johnson (in iron) [169], and by D. Terentyev et al. (in tungsten) [170]. Trap sites are also produced by ions exposure [114] and can be modeled by a trap production source term in the equations [110, 151]. Neutrons can also induce material modification [115] but it seems that there's no proposed model, which includes these damages at the mesoscopic scale. Last, vacancies can be created by an excess of solute concentration at the surface and induce a super-saturated layer (SSL) [171].

1.1.4.6 Trap mobility and clustering

D. Matveev et al. [148] used a CRDS (Coupled Reaction Diffusion Systems) model to simulate deuterium (D) retention, migration and release in single-crystalline beryllium, in the case of transient trapping. In their investigations, the multiple trapping was taken into account. It refers to the capture of several deuterium atoms (5 max) in a single trap, e.g. vacancy

$$H + VH_n \Longrightarrow VH_{n+1} \quad \text{for n=0...4} \tag{1.21}$$

K. Ebihara et al. [146] investigated a numerical analysis of hydrogen thermal desorption spectra for iron with Hydrogen-Enhanced Strain-Induced vacancies. The model they used is based on McNabb and Foster's theory, considering the diffusion of vacancies. It refers to a multiple trapping process, which involves one or several hydrogen atoms (29 max) trapped in one or several vacancies (9 max).

$$V_x + H_y \Longrightarrow V_xH_y \quad \text{for x=1...9 and y=1...29} \tag{1.22}$$

They propose an equation for the vacancy density C_{V_i} evolution (Eq. 1.23) including vacancy diffusion, creation or destruction of vacancy (thermodynamic equilibrium), aggregation of monovacancy (+ terms) or dissociation of monovacancy (- terms)

$$\frac{\partial C_{V_i}}{\partial t} = D_{V_i}\frac{\partial^2 C_{V_i}}{\partial x^2} - S_{V_i}D_{V_i}(C_{V_i} - C_{V_i}^{eq}) + b^+_{V_1+V_{i-1}}C_{V_1}C_{V_{i-1}} - b^+_{V_1+V_1}C_{V_1}C_{V_i} + b^-_{V_{i+1}}C_{V_{i+1}} - b^-_{V_i}C_{V_i} \tag{1.23}$$

The data of trap mobility and reaction for tungsten are proposed by [172,173]. The fill-level-dependent energy for tungsten (V_xH_y) can be found in [63, 174–176].

Clustering models and codes are also being developed for He bubble formation [173, 177, 178] but only He clusters are simulated and so the nanobubble can not grow by vacancy absorption. This assumption is surely correct for He bubbles which stay small but not for H ones.

1.1.5 Hydrogen Embrittlement

The main hydrogen influence on metals, or the most famous one, is the modification of their failure properties: hydrogen presence induces an untimely failure, as well as the failure process by itself. This phenomenon is associated to numerous scientific works and reviews (among others: Del-Pozo et al. [179], Li et al. [180], Sergeev et al. [181, 182], Dwivedi et al. [183], Shirband et al. [184], Hirth [185]).

It is usually considered that a classical ductile failure, in the presence of hydrogen, evolves toward a brittle one, along planes of cleavage or grains boundaries when the sample is exposed to hydrogen [186, 187], as illustrated in Figure 1.38 for martensitic steel.

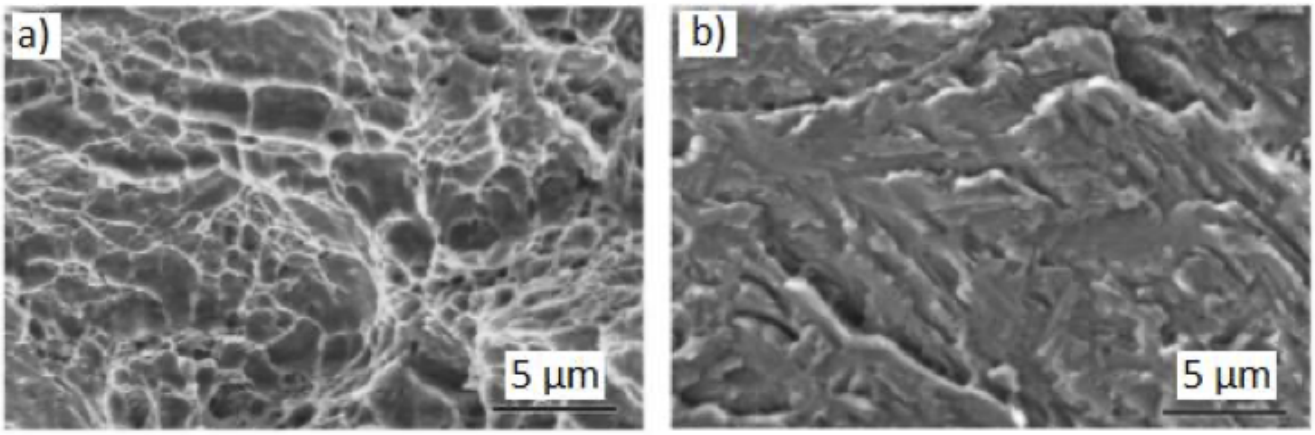

Figure 1.38: Failure process in martensitic steel (b) with or (a) without hydrogen exposition [187].

Macroscopically, this modification in the failure process alters the tensile curves of materials (see Figure 1.39 for an AISI 4135 steel).
The underlying processes to the macroscopic embrittlement are still unclear, depending on the material and the hydrogen loading conditions, and a lot of processes have been proposed in the literature. Among them, a few phenomena are classically used to explain hydrogen embrittlement (see [189] or [190] for a more complete list):

- HELP (Hydrogen-Enhanced Localized Plasticity): plastic strain is highly localised (due to the interactions between hydrogen and dislocations), leading to localized damage, and, then, failure [189, 191];
- HEDE (Hydrogen-Enhanced Decohesion): hydrogen tends to decrease the material toughness, leading a ductile-brittle transition for the material failure [192, 193];

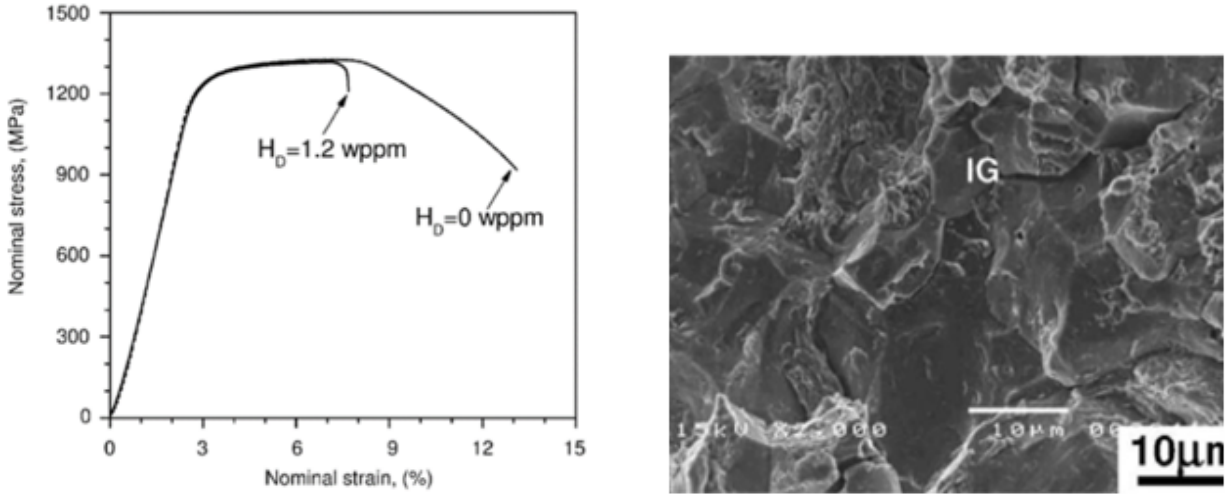

(a) (b)

Figure 1.39: (a) Stress-strain curves for an AISI 4135 steel with/without hydrogen, pointing out the untimely failure due to the embrittlement process, (b) crack surfaces, denoting the brittle intergranular failure process [188].

- HIC (Hydrogen-Induced Cracking): hydrogen interacts with vacancies, and, eventually, creates bubbles that can evolve toward cracks or blisters [194, 195]

The prevalence of one of these phenomena is a matter of debate, as illustrated, e.g., by the recent critical analysis made by Lynch on the scientific works dealing with hydrogen embrittlement [196], or the analysis proposed by Djukic et al. [197] and Liang et al. [198] on the interplay of HELP and HEDE phenomena in the hydrogen-assisted failure of iron or steels. Last, the main vector of embrittlement has also been reinvestigated recently, with some authors pointing out that hydrogen flux rather than hydrogen concentration can be responsible for embrittlement [199].

Finite element modeling, however, mainly relies on HEDE mechanism, and especially on cohesive modeling approach (see Jemblie et al. [200] for a review): an interfacial finite element is introduced in the mesh to mimic crack initiation and propagation, with a mechanical behavior based on the interface $\boldsymbol{\Delta}$ opening and the cohesive stress $\boldsymbol{T}$. A classical Traction Separation Law (TSL) between $\boldsymbol{\Delta}$ and $\boldsymbol{T}$ is plotted in Figure 1.40, where the TSL is plotted as a function of a normalized hydrogen concentration Θ. For $\Theta = 0$, the initial failure properties are found, and especially, the Griffith energy Γ [201], which corresponds to the needed energy to create a crack, so that

$$2\Gamma = \int_0^{+\infty} \boldsymbol{T}\, d\boldsymbol{\Delta} \tag{1.24}$$

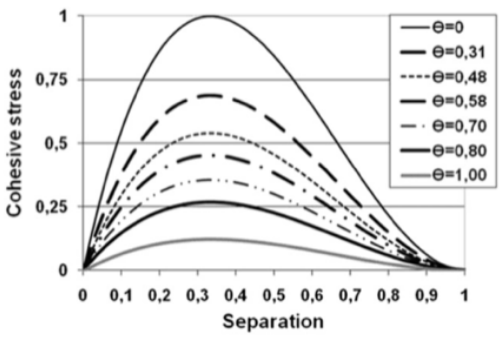

Figure 1.40: TSL as a function of normalized hydrogen concentration Θ [202]

.

The relationship between the TSL and the hydrogen concentration is usually phenomenological, based on thermodynamical considerations [203, 204], based on small-scale computations [202, 205, 206], or even identified from experimental results [207]. Few works account for a ductile-brittle transition. For a few years, a novel approach, based on phase field, to model crack propagation, is used in finite element simulations [208–210].

1.2 Material Structural Properties

In this section, we delve into the intricacies of a material's structural characteristics, aiming to uncover the close interplay between plasticity, hardening, and dilatational strain. Through an analysis of these pivotal subtopics, we gain a comprehensive understanding of the material's behavior under various strain and deformation conditions.

1.2.1 The correlation between plasticity and dislocation density

Kumnick and Johnson [169] carried out permeation tests on pre-strained pure iron samples. Based on the time lag method, they identified the trap density N_T from the evolution of the hydrogen permeation flux. On the basis of their results, Sofronis and McMeeking [17] proposed the following relationship for $N_T(\epsilon_{pl}^{eq})$ (see Figure 1.41).

$$\log N_T = 23.26 - 2.33e^{-5.5\epsilon_{pl}^{eq}} \tag{1.25}$$

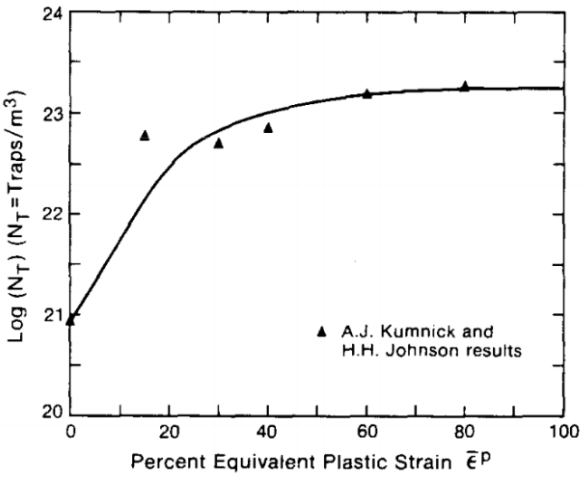

Figure 1.41: Evolution of the trap density as a function of the equivalent plastic strain in iron [17].

Equation 1.25 has been widely used in computational works dealing with hydrogen trapping by dislocations, even for materials that are not pure iron, as, e.g., [211], in which this relationship is used for an AISI 4340 steel, or the work of Olden et al. [212], in which the following simplified form of Equation 1.25 is used for a 25% Cr duplex stainless steel:

$$N_T = (49\epsilon_{pl}^{eq} + 0.1)\frac{N_L}{K_T} \tag{1.26}$$

Equation 1.25, however, is not the only one available in the literature for iron or steel, as pointed out by the survey made by Colombo et al. [213], and summarized on Equation 1.27.

$$\begin{cases} \log N_T = 27.14 - 2.33e^{-5.5\epsilon_{pl}^{eq}} \text{ for AISI 1020 [214]} \\ \log N_T = 23.94 + 24.68(\epsilon_{pl}^{eq})^{0.7} \text{ for FeE 690T steel [215]} \\ \log N_T = 34.66 - 2.33e^{-5.5\epsilon_{pl}^{eq}} \text{ for PSB1080 steel [216]} \\ \log N_T = 27.33 - 2.33e^{-5.5\epsilon_{pl}^{eq}} \text{ for AISI 4140 steel [213]} \end{cases} \tag{1.27}$$

All these expressions are plotted below:

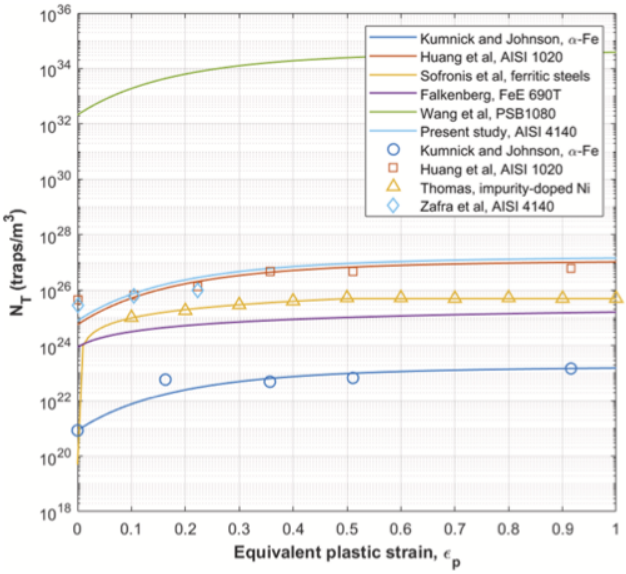

Figure 1.42: Evolution of the trap density as a function of the equivalent plastic strain in iron [213].

For tungsten, Terentyev et al. [170] estimated the dislocation density ρ_{dis} from the equivalent plastic deformation by a Kocks-Mescking type hardening model [217] (see Figure 1.43), leading to the following relationship

$$\rho_{dis} = \left(10^{12} - \frac{M}{bL}\right) e^{-kM\epsilon_{pl}^{eq}} + \frac{M}{bL} \tag{1.28}$$

in which M is the Taylor coefficient, b is the Burgers vector norm, L is a characteristic length corresponding to the dislocation mean free path (equal to 0.2 micrometers), and k is a recovery parameter (equal to 1.1).

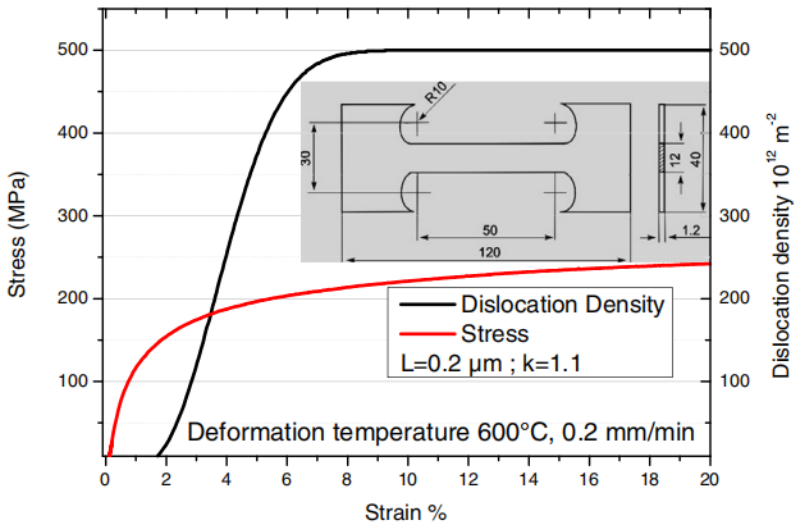

Figure 1.43: Evolution of the dislocation density by fitting the strain-hardening curve of Kocks-Mescking hardening model [170].

By using the relationship between ρ_{dis} and N_T [24] (see Equation 1.27), the N_T evolution with the equivalent plastic strain to be used in Equation 7, can thus be derived.

1.2.2 Modification of the material hardening

In the presence of hydrogen, the plastic response of the material can be modified. It has been observed, e.g., in [218] that the presence of hydrogen can decrease the hardening of aluminum samples (see Figure 1.44a), while this hardening is increased in steel ones (see Figure 1.44b). This has also been observed on Nickel single crystal [219].

This effect is linked to the interactions between hydrogen and dislocations, which trap hydrogen atoms in a so-called Cottrell atmosphere [221]. First, hydrogen atoms tend to increase dislocation mobility on the one hand by reducing the Peierls friction [222], and to decrease their interactions, especially for pile-up on the other hand, leading to plastic localisation, as observed by Brass and Chêne for Nickel single crystals [223], or in a 310S stainless steel [224] (see Figure 1.45).

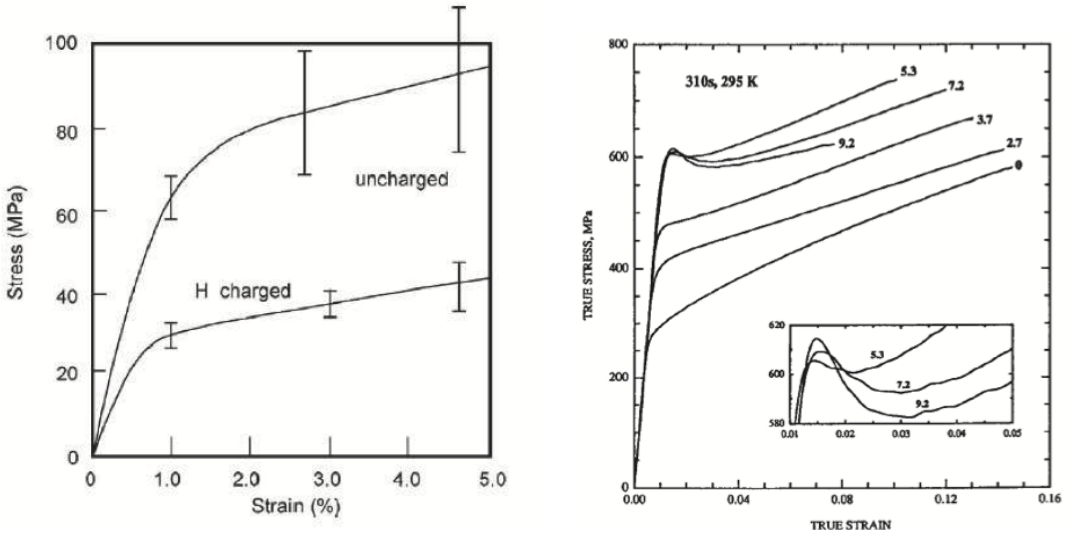

(a) (b)

Figure 1.44: Stress-strain curves from (a) 99.9% pure aluminium samples [218] and (b)S310 steel samples [220].

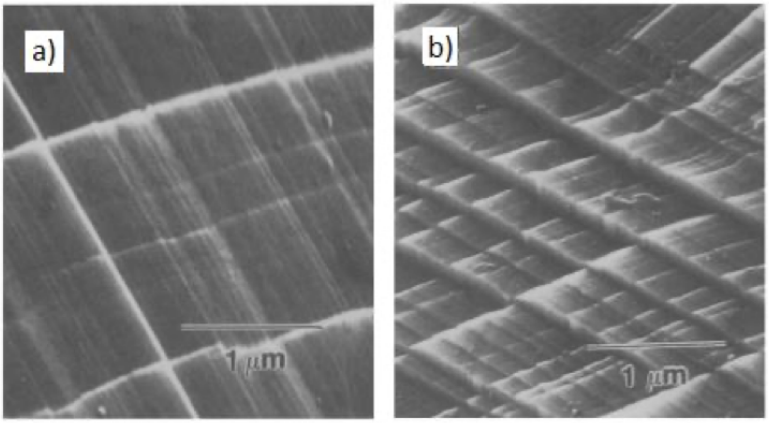

Figure 1.45: Slip localization observed on the surface of a 310S stainless steel (b) with and without (a) hydrogen loading [224].

This is illustrated, especially, in the experiments performed by [225], in which a dislocation pile-up is observed using a Transmission microscope, while hydrogen is introduced (see Figure 2.50c): the distance between dislocations is reduced, demonstrating the screening of dislocations by hydrogen.

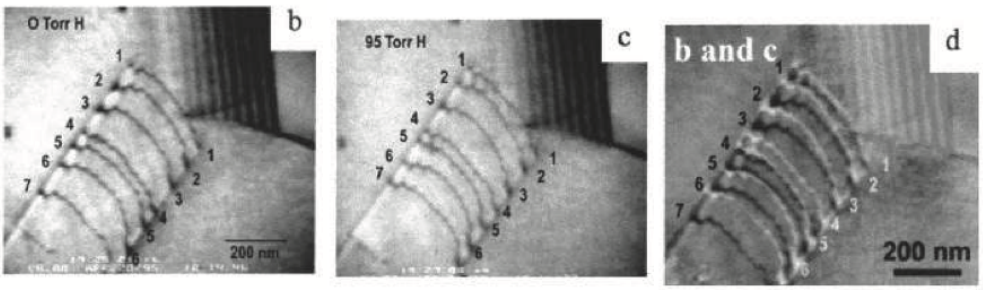

Figure 1.46: Evolution of the trap density as a function of the equivalent plastic deformation in iron. [225]

The reason for these contradictory effects of hydrogen on plasticity remains debated, and are strongly material-dependent [226], and is basically related to the effect of hydrogen on dislocations [227].

Only a few models account for hydrogen effect on plasticity. All of them are phenomenological, used for parametric studies, and little motivated by experimental data or observations. In these models, the yield stress σ_0 is related to the local hydrogen concentration C [24] so that

$$\sigma_Y(\epsilon_{pl}^{eq}, C) = \sigma_0(C)\left(1 + \frac{\epsilon_{pl}^{eq}}{\epsilon_0}\right)^N \tag{1.29}$$

where ϵ_{pl}^{eq} represents the equivalent plastic strain, and ϵ_0 and N are material parameters, and with $\sigma_0(C)$ is expressed as

$$\sigma_0(C) = [(\xi - 1)C + 1]\sigma_0 \tag{1.30}$$

σ_0 is the hydrogen-free yield stress and ξ a material parameter. C is the total hydrogen concentration. This model has been used to investigate plasticity-related void growth in cells precharged with hydrogen by Liang et al. [82] (see Figure 1.47), or by Miresmaeili et al. [228] to investigate the plastic localisation in samples under a tensile test.

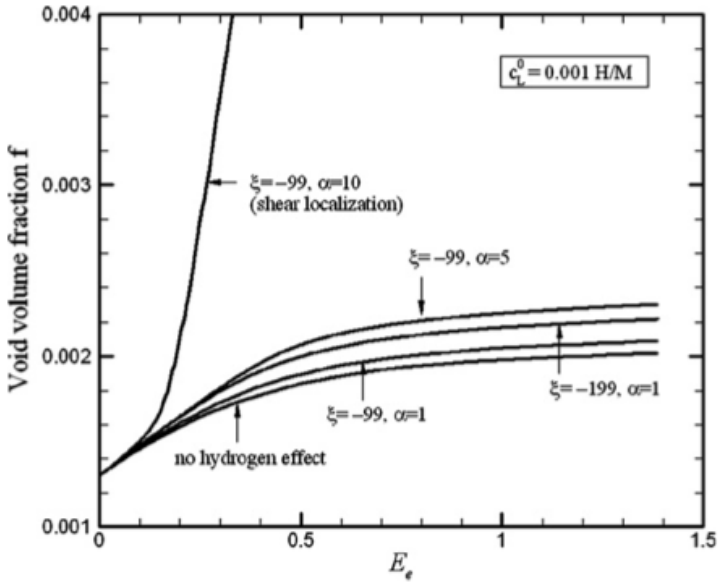

Figure 1.47: Effect of hydrogen on void growth as a function of the applied loading (α denotes the number of hydrogen atoms per trap site) [82].

An adaptation at the crystal scale has been proposed by Ogosi et al. [81, 229], following the work of Vasios [230], in which the critical resolved shear stress on the slip system α, denoted τ_c^α, is set dependent of the hydrogen trapped concentration C_T

$$\dot{\tau}_c^\alpha(C_T) = \dot{\tau}_{c,0}^\alpha(1 + H_f C_T) \tag{1.31}$$

in which $\dot{\tau}_{c,0}$ is the hydrogen-free critical resolved shear stress rate and H_f a phenomenological parameter. A much more complex approach to crystal plasticity modified by hydrogen has been recently proposed by Yuan et al. [231].

Sasaki et al. [32] proposed an alternative relationship for Equation 1.29, by modifying the yield stress as follows for ferritic steels

$$\sigma_Y(\epsilon^p, c) = \sigma_0 \left(1 + \frac{\epsilon_p}{\epsilon_0}\right)^{0.5n \log_\xi \frac{C_T}{N_L}} \tag{1.32}$$

where n is the work-hardening coefficient, and ξ a material parameter.

1.2.3 Dilatational strain

While diffusing, hydrogen atoms induce a dilatational strain (see Figure 1.48), as observed for several materials (see the review of Peisl for more details [232]).

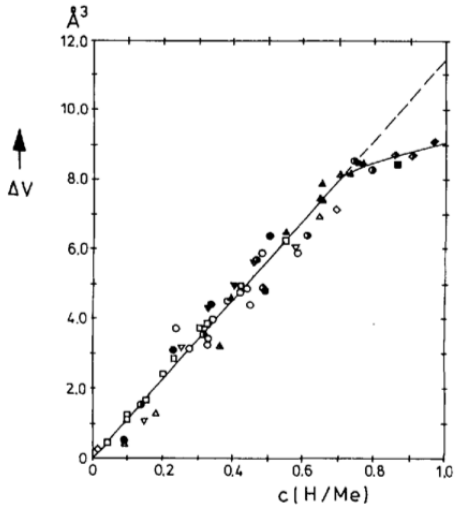

Fig. 3.12. Volume change ΔV vs hydrogen concentration c for a series of fcc metals and alloys in single-phase regions (25 °C) (*Baranowski* et al. [3.64]). ◇ ◑ palladium, ■ nickel, ▽ irridium-palladium, □ gold-palladium, ○ ◑ silver-palladium, △▲ platinum-palladium, ▼ copper-palladium, ● copper-nickel

Figure 1.48: Dilatation strain versus hydrogen concentration for several materials [232].

Such a phenomenon has been linked with a so-called 'skin-effect' in the steady-state hydrogen distribution in metallic specimens with no mechanical fields [233].

Such an expansion strain has been introduced by Sofronis et al. [24] as

$$\epsilon_{ij}^H = \frac{1}{3}\frac{\lambda}{1+\frac{\lambda(C-C_0)}{3}}\dot{C}\delta_{ij} \tag{1.33}$$

where $\lambda = \Delta v/\Omega$, Δv being the volume change per atom of hydrogen, related to the partial molar volume of hydrogen by $\bar{V}_H = \Delta N_A$ (N_A is the Avogradro number). Ω is the mean atomic volume of the metal atom. C_0 is a reference concentration, and C the total hydrogen concentration. Last, δ_{ij} is the Kronecker symbol so that $\delta_{ij} = 1$ if $i = j$, and 0 if not. For small $\dot{C}$ values, Equation 1.33 becomes [135]

$$\epsilon_{ij}^H \approx \frac{\dot{C}\Delta v}{3\Omega}\delta_{ij} \tag{1.34}$$

Such dilatation stress has scarcely been used in finite element models [234], though some observed anisotropic diffusion in Nickel single crystals has been explained this kind of expansion in a mechanically anisotropic medium [235].

Chapter 2

Thermomechanically assisted diffusion and trapping of Hydrogen

In this chapter, we focus on components pivotal to controlled nuclear fusion research: the DFW (Diagnostic First Wall), TBMs (Test Blanket Modules), and divertor monoblock. The DFW plays an instrumental role in supporting vital plasma diagnostics. The TBMs, on the other hand, explore tritium breeding, a crucial step for ensuring fuel sustainability. Meanwhile, the divertor is dedicated to maintaining plasma purity by effectively eliminating impurities. Together, these components handle the paramount challenges of plasma stability, consistent fuel supply, and efficient heat management, underscoring their importance in utilizing nuclear fusion as a promising energy alternative.

The two kinds of stainless steel components of interest are detailed in [236]:

- Support pieces of Test Blanket Modules (TBMs) with a total plasma-exposed surface of around 20 m^2, well protected from plasma flux but exposed to photon and charge-exchange fluxes. Surface temperature can be considered to be at equilibrium with the coolant temperature of 100 °C.
- Diagnostic First Wall (DFW) pieces with a total plasma-facing surface of around 30 m^2 exposed to an average thermal flux of 0.2 MW/m^2 [237].

Initially, it's about the modeling assumptions for the DFW. We established a reference case grounded in the research by Benannoune et al. [238], complete with pertinent boundary conditions. Subsequently, we present various parametric studies specifically pertaining to the DFW:

- influence of the surface temperature.
- influence of the thermal expansion.

- influence of the hydrogen diffusion coefficient.

For each parametric study, we discuss pertinent physical fields, placing particular emphasis on hydrogen permeation within a specific section of the DFW. Finally, we scale up our findings on inventory and permeation to the broader context of the ITER tokamak, encompassing both the TBMs and DFW.

2.1 Physics & Models

The computations involve several coupled physics:

- heat transfer.
- hydrogen transport and trapping.
- elastoplasticity.

2.1.1 Heat transfer

At each material point, the temporal evolution of the temperature T follows the following equation

$$\rho C_p \frac{\partial T}{\partial t} = \boldsymbol{\nabla}.(\lambda \boldsymbol{\nabla} T) \tag{2.1}$$

where ρ is the density, C_p the specific heat, and λ the thermal conductivity. The temporal variation of the temperature induces, furthermore, a thermal expansion strain tensor $\boldsymbol{\epsilon}_{th}$ so that

$$\boldsymbol{\epsilon}_{th} = \alpha(T - T_{init})\boldsymbol{I} \tag{2.2}$$

T_{init} is the initial temperature, α the thermal expansion coefficient, and $\boldsymbol{I}$ the unit tensor. For a 316 stainless steel, the different parameters are summarized in Table 2.1.

2.1.2 Transient trapping of H

The evolution of the trapped hydrogen concentration can be deduced from the so-called McNabb and Foster equation, for $C_L \ll N_L$ (or $\theta_L \ll 1$), which corresponds to a first-order reaction chemical equation [239, 240]

$$\frac{\partial C_{T,i}}{\partial t} = \frac{k_i}{N_L} C_L (N_{T,i} - C_{T,i}) - p_i C_{T,i} \tag{2.3}$$

where k_i and p_i are the trapping and detrapping reaction rates so that

$$p_i = \nu_0 e^{-\frac{E_{d,i}}{k_b T}} \tag{2.4}$$

and

$$k_i = \frac{D_L}{l^2} \tag{2.5}$$

$E_{d,i}$ is the trapping energy for the i-th trap, l represents the distance between two interstitial sites, and ν_0 the hydrogen atom jump attempt frequency (set to 8.53×10^{13} s^{-1}). k_b is the Boltzmann constant. Only one kind of trap is considered and the values of diffusion and trapping parameters are given in Table 2.4. N_T is here considered as dependent on the equivalent plastic strain ϵ_{pl}^{eq}, to account for the effect of an evolving dislocation density during the cycles experienced by the DFW.

2.1.3 Material hardening

The material thermo-elasto-plastic behavior is assumed to be isotropic, with an isotropic hardening.

The Young's modulus E is set temperature-dependent, following the data given in [241] (see Table 2.2), while the Poisson's ratio ν is assumed to be constant and equal to 0.3. This material dimensionless parameter, between 0 and 0.5, characterized the relative variation of the radius of a cylinder submitted to a tensile test: if ν=0, the section radius is constant while the length of the cylinder increases. If ν=0.5, the volume of the cylinder remains constant during the tensile test.

The yield stress is modeled by using the following Johnson-Cook relationship [242]

$$\sigma = (A + B\epsilon_p^n)(1 + C \ln \dot{\epsilon}^*)(1 - T^{*m}) \tag{2.6}$$

where A and B are material parameters, $\dot{\epsilon}^*$ is a reference strain rate (here assumed to be equal to 1/s), and T^* a dimensionless temperature so that

$$T^* = \frac{T - T_{amb}}{T_{melting} - T_{amb}} \tag{2.7}$$

T_{amb} and $T_{melting}$ represent respectively the initial temperature (set to 293 K) and the melting temperature (considered to be equal to 1672 K for 316L stainless steel). The other parameters can be found in Table 2.3.

2.2 Properties of the material

Table 2.1: Thermo-mechanical parameters

Parameter	Value	Ref.
$\rho(kg/m^3)$	7921-0.614T+0.0002T^2	[241]
C$_p(J/kg/K)$	440.79+0.5807T-0.001T$^2 + 7 \times 10^{-7}T^3$	[241]
$\lambda(W/m/K)$	14.307+0.0181T-6$\times 10^{-6}T^2$	[241]
α	1.12×10^{-5}	[238, 243]

Table 2.2: Evolution of the Young's modulus E with the temperature T [241]

T (°C)	20	150	260	350	425	480	540	650	1200
E (GPa)	210.3	191.7	180.0	191.0	188.2	186.2	156.5	113.7	68.0

Table 2.3: Johnson-Cook parameters [241, 244]

A (MPa)	B (MPa)	C	n	m
305	1161	0.01	0.61	0.517

Table 2.4: Diffusion & Trapping parameters

Parameter	Value	Ref.
D_L (m^2/s)	$1.45 \times 10^{-6} \times \exp\left(-\frac{0.59}{k_b T}\right)$	[245]
N_L (m^{-3})	8.42×10^{28}	[245]
N_T (m^{-3})	$10^{25.26-2.33\times\exp(-5.5\epsilon_{pl}^{eq})}$	[246, 247]
E_d (eV)	0.7	–

2.3 Implementation & Validation

The chemo-thermo-mechanical equation set described above is solved in Abaqus in a fully coupled way (strong coupling), based on the 'coupled temp-displacement' procedure and the development of specific User Subroutines (see [248] for details on the implementation):

1: a User MATerial (UMAT) subroutine: to solve the mechanical problem and to calculate the hydrostatic pressure gradient and the equivalent plastic strain.

2: a User MATerial Heat Transfert (UMATHT) subroutine: to solve the hydrogen transport and transient multi-trapping differential equation, assisted by thermal and mechanical fields. The resolution of the McNabb and Foster equation is made using an approximation of the solution [249, 250].

3: a User ELement (UEL) subroutine: to add a degree of freedom at each node of the Finite Element model, and to link this degree of freedom to a transient heat transfer problem.

4: a User EXPANsion (UEXPAN) subroutine: to compute the thermal expansion at each point. The deformation considered in UMAT is the purely mechanical one ($\boldsymbol{\epsilon} - \boldsymbol{\epsilon}_{th}$).

The flowchart of this implementation is presented in Figure 2.1.

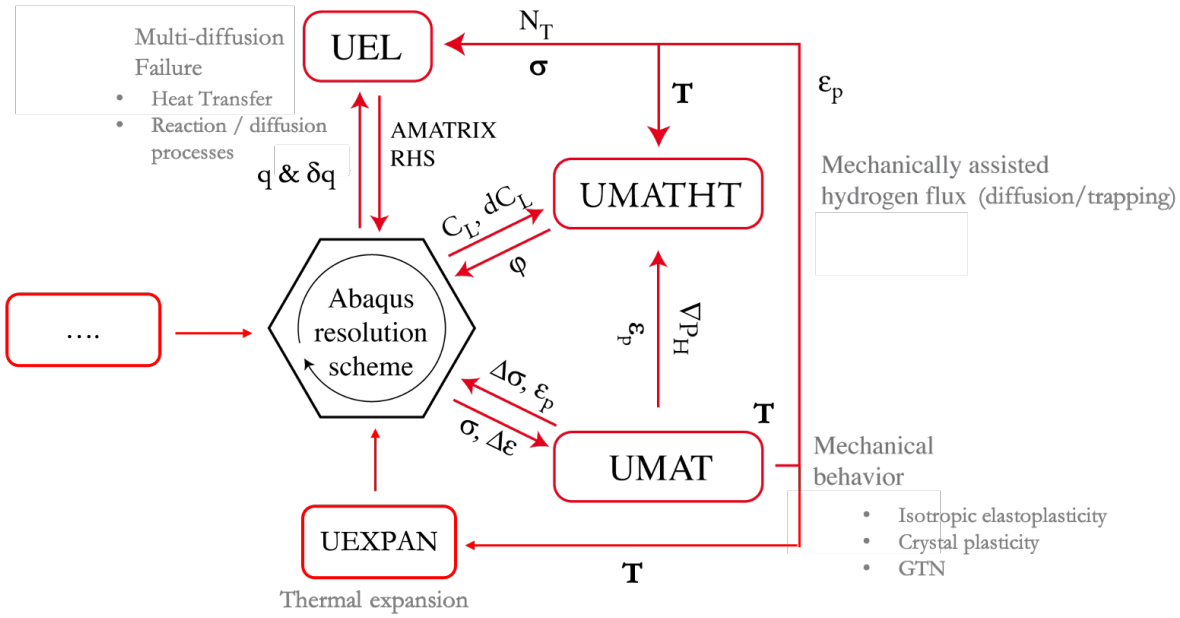

Figure 2.1: User Subroutines developed to add chemo-thermo-mechanical features to Abaqus software.

2.4 Diagnostic First Wall (DFW)

2.4.1 Geometry & Mesh

Here presents the reference configuration. The global geometry of the DFW has been provided by ITER (in the form of a CAD file) and is presented in Figure 2.50a. For the sake of simplicity, only a small section of this geometry is considered (indicated by a red rectangle). This section (Figure 2.50b) is modeled in Abaqus in 2D and is meshed with around 4000 fully integrated linear elements. The mesh has been optimized based on the results from mechanical and hydrogen diffusion fields.

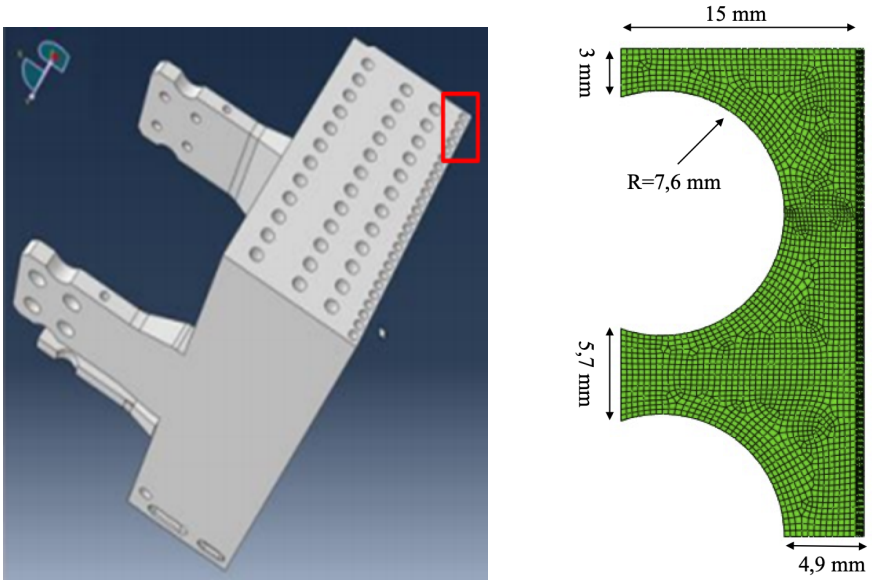

(a) (b)

Figure 2.50: (a) DFW and part modeled in this study (in red rectangle), (b) Mesh & dimensions

2.4.2 Reference scenario and boundary conditions

The boundary conditions are presented in Figure 2.51. Symmetry boundary conditions are imposed on the lower and left edges, while plane strain is assumed (i.e. no normal deformation to the 2D surface). The water circulation in the cooling pipes induces a constant pressure on the DFW equal to 4 MPa.

On the right edge, exposed to plasma, a temperature, and a diffusing tritium concentration are imposed. The upper surface is considered a free surface for hydrogen ($C_L = 0$) and a symmetry one for temperature (normal thermal flux equal to zero). On cooling pipes, $C_L = 0$ and T are imposed.

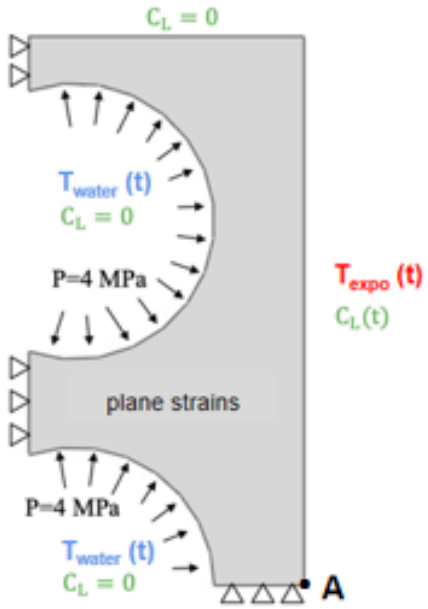

Figure 2.51: Boundary conditions applied on the DFW section. The exposed free surface is on the right.

The reference loading scenario (as proposed in [251]) is presented in Figure 2.52: it is composed of 160 3-day loading cycles (Phase 1) for hydrogen and temperature, followed by an 8-month baking cycle (Phase 2) at a constant temperature without hydrogen. One cycle corresponds to the temporal concatenation over 3 days of plasma operations consisting of 13 daily plasma pulses for 16 months. Hydrogen implantation is modeled by a hydrogen concentration $C_{L,0}$ at the exposure surface, such as [252, 253] (assuming instantaneous recombination)

$$C_{L,0} = \frac{R_p \Gamma}{D_L(503K)} = 1.46 \times 10^{14} (atm/mm^3) \tag{2.8}$$

where Γ represents the charge exchange flux of tritium ($2 \times 10^{19}\, atm/m^2/s$) which corresponds to a medium load flux at the upper plug port [251]), R_p represents the average implantation depth (set equal to 13 nm) [238]. We have considered pure tritium in our simulation. Indeed it is a 50% - 50% D-T plasma, however, we don't know if this percentage will be respected

in the material because the transport (diffusion & trapping) is not equivalent for the two isotopes. So we can't just halve the inventory. It is better to keep the worst-case scenario: D comes out of the material, and T stays there. Moreover, surface recombination is typically included and it is often a rate-determining factor:

$$C_{L,0} = \sqrt{\frac{\Gamma}{K_r(T = 503K)}} = 3.2 \times 10^{15}(atm/mm^3) \tag{2.9}$$

where K_r is the recombination coefficient [251]. In our present work, we haven't taken this second term into account, but it's better to verify its value and compare it to the first term. As we can see that the second item is 22 times larger than the first item, we are planning to consider this second term in future computations, for example, on the ITER monoblock.

Three calculations are carried out to exhibit the influence of mechanical fields on hydrogen diffusion in the DFW section:

- no mechanical fields (hydrogen transport and trapping, coupled with heat transfer).
- pressure from the cooling pipes.
- pressure from the cooling pipes and thermal expansion.

2.4.3 Results for Phase 1

The diffusion fields at the end of Phase 1 are given in Figure 2.53 for the three cases. It can be observed that, while the cooling pipes-induced pressure increases the level of C_L, at least near the exposed surface. The penetration depth of C_L seems not affected by mechanical fields.
This impact of stress field on C_L levels is linked to the hydrostatic pressure effect on hydrogen flux (see Equation 2.12) which affects the maximal C_L level [254]. To detail that effect, in Figure 2.54 are plotted the P_H distributions when only the cooling pipes pressures are considered (Figure 2.54a) and with all the mechanical fields, at the higher and lower exposition temperatures (Figures 2.54b and 2.54c respectively).

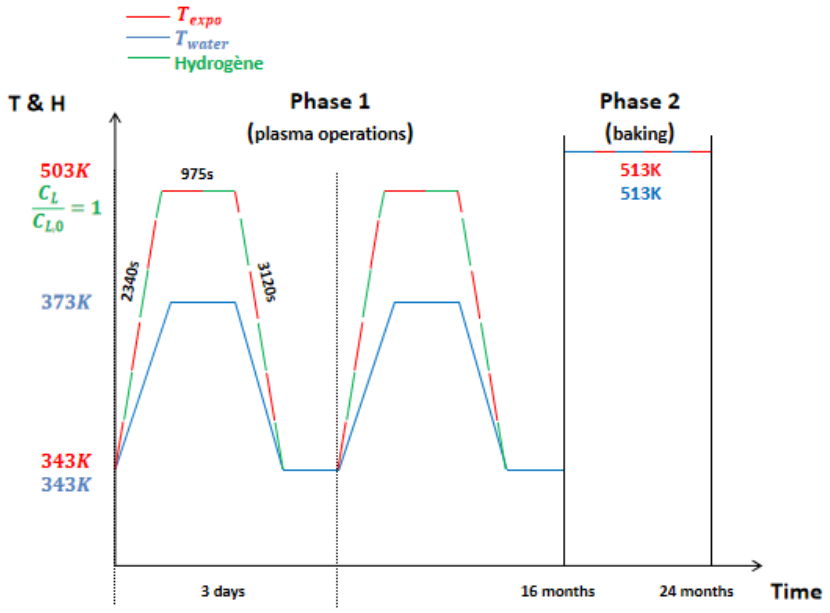

Figure 2.52: Reference loading scenario for the exposed surface (T_{expo} and C_L) and the cooling pipes (T_{water})

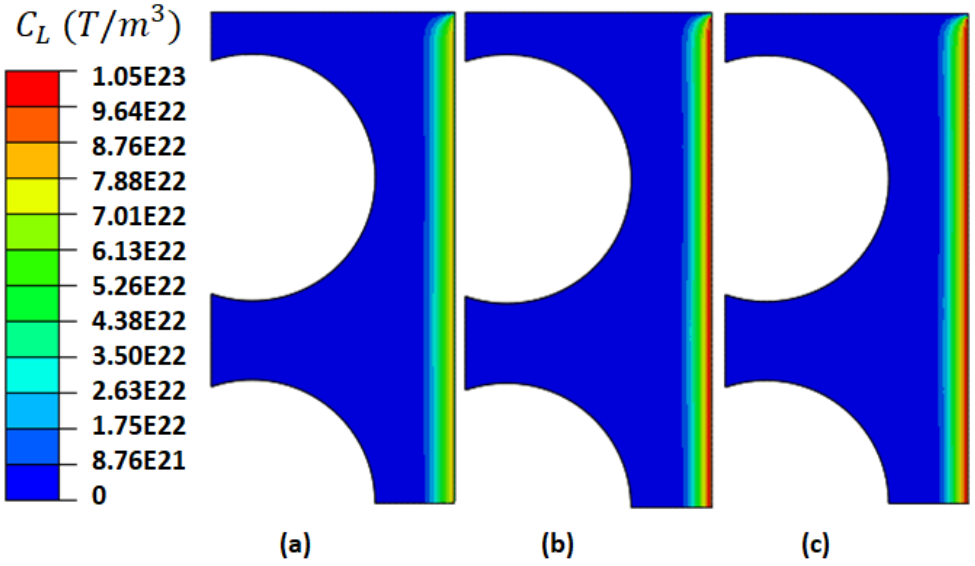

Figure 2.53: Distribution of C_L at the end of Phase 1: (a) without any mechanical fields, (b) water pressure only, (c) water pressure & thermal expansion.

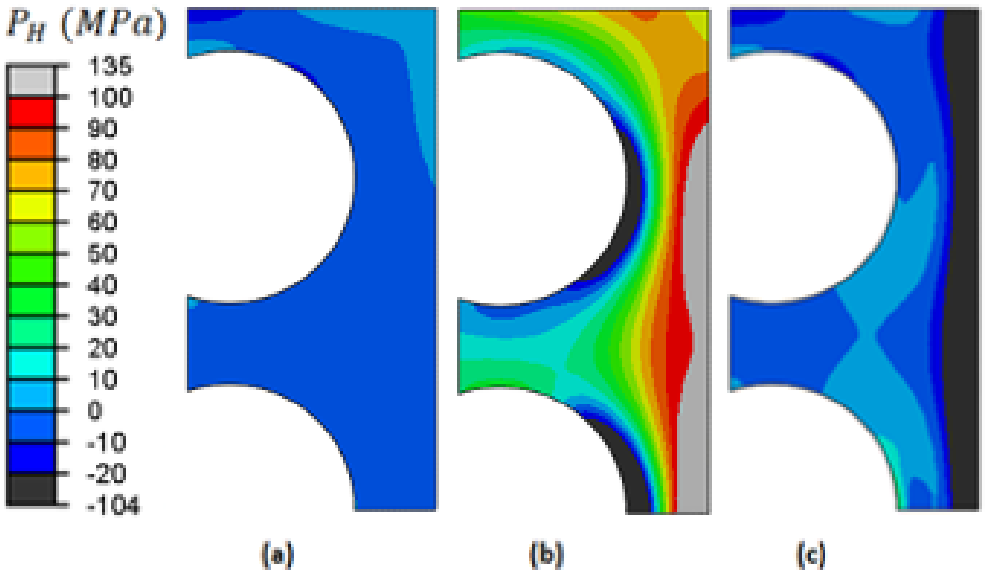

Figure 2.54: Hydrostatic pressure field at the end of Phase 1: (a) only the cooling pipes pressures are considered; with all the mechanical fields, at the higher (b) and lower exposition temperatures (c).

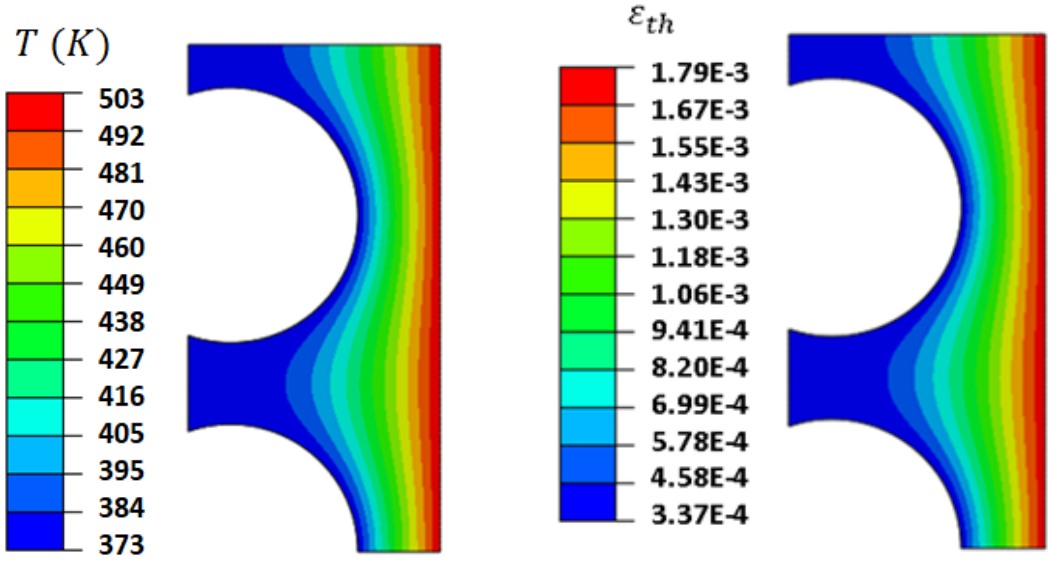

Figure 2.55: (a) Temperature field at T_{max} and (b) Thermal strain fields at the end of Phase 1.

When only the cooling pipe pressure is accounted for, it can be seen that the DFW section is slightly under dilatation (negative pressure), leading to an increase of the C_L maximal value. The extra effect of thermal strains on the C_L field is small, however. During the hot phase of each cycle (higher T_{expo}), two opposite effects are involved: while the important temperature field leads to an increase of the tritium diffusion coefficient (see the temperature field in Figure 2.55a), thermal strains (Figure 2.55b) induced compression stresses (positive P_H, see Figures 2.54b) which tends to slow the tritium diffusion. During the cool phase of each cycle, these two contradictory effects are also present; from the C_L fields, it can be concluded that they neutralize each other, leading to a small effect of the thermal strain fields.

The impact of mechanical fields on tritium retention can be investigated by introducing the total amount Q_{tot} of tritium in the DFW section, which is such that

$$Q_{tot} = \int_V (C_L + C_T)\, dV = \sum_{Gauss\, Point} (C_L^i + C_T^i) V_i = Q_L + Q_T \tag{2.10}$$

where V_i represents the volume associated the each Gauss n°i point in the mesh. As the problem is here 2D, V_i is reduced to a surface and Q_{tot} is in atomes/m.

The evolution of Q_{tot} is represented in Figure 2.56a. The impact of the pressure of the cooling pipe is here very clear: at each cycle, Q_{tot} increases continuously, exhibiting cycles corresponding to the loading ones. When the DFW section is exposed to both hydrogen and temperature, Q_{tot} increases. Q_{tot} decreases as soon as these boundary conditions are modified (no more hydrogen concentration and T_{expo}=513 K). This behavior denotes an important hydrogen desorption process, and thus, important hydrogen mobility. It can last be conjectured that, when the number of cycles increases, so does the maximal Q_{tot} value.

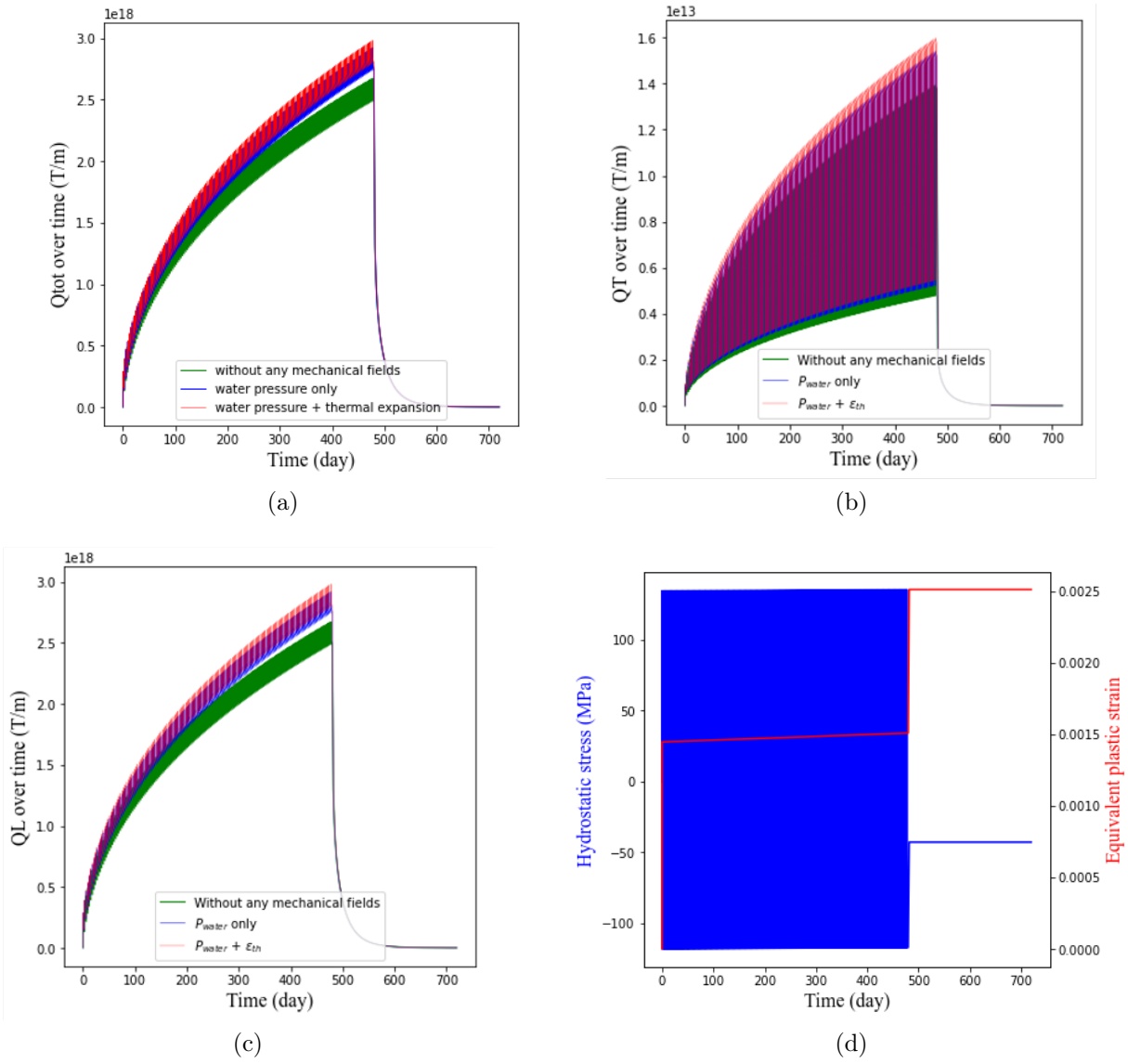

Figure 2.56: Evolution (a) of the total amount of tritium per unit thickness Q_{tot}, (b) of the total diffusing tritium Q_L and (c) of the total trapped tritium Q_T as a function of time for the three configurations, (d) hydrostatic stress (blue) & equivalent plastic strain (red) at point A (see Figure 2.51) over time if all the mechanical fields are resolved.

When considering thermal strain fields, the additional impact on Q_{tot} appears to be relatively small, as previously observed. Thermal strains have minimal effects on the C_L fields, while plasticity development results in a slight increase in the C_T field (after Phase 1, N_T has

evolved from 8.5×10^{22} to 8.9×10^{22}, in (m^{-3}), as shown in Figure 2.56 (d)). The trapped tritium inventory is significantly smaller compared to the diffusing one, as illustrated in Figure 2.56 (b) and (c), with $Q_T/Q_L \approx 0.0000053$. The impact of cooling pipe pressure on Q_L is approximately 10%, while thermal strains induce an additional 2%.

Thermal strains, last, lead to the generation, at each exposure cycle, of plastic strain, localized near the exposed surface (see Figure 2.57). A plastic strain localization can be observed near the symmetry boundary condition (lower surface) corresponding to a possible overestimated value linked to the modeling assumptions. As a consequence, the trap density is modified and increases slightly at each cycle (Figure 2.58), leading to an increase in the trapped hydrogen concentration. The dramatic increase in dislocations is because of the 'instantaneous increase of temperature' between the end of Phase 1 and the start of Phase 2 (slope tends to infinity). Last, a viscous effect can appear at high temperatures, inducing an impact of the strain rates (or thermal strain rates) on plasticity. But so far, this is not accounted for in our modeling.

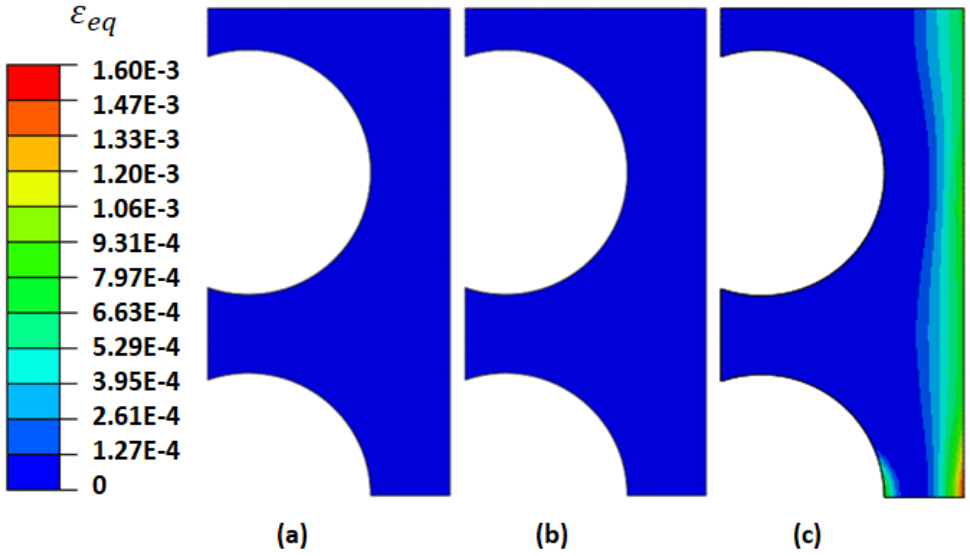

Figure 2.57: Equivalent plastic strain field at the end of Phase 1: (a) without any mechanical fields, (b) water pressure only, (c) water pressure & thermal expansion.

As it can be seen, accounting for the mechanical field leads to an increase in hydrogen inventory in the DFW section. However, thermal strain, though being quite important, unexpectedly does have not a strong influence on tritium inventory, compared to the cooling pipe pressure.

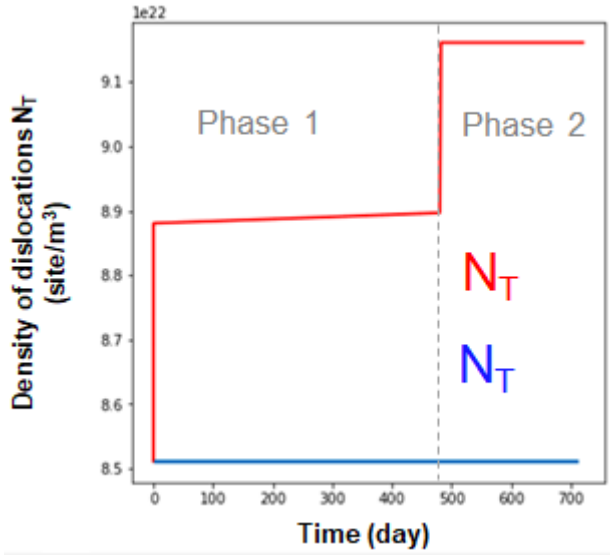

Figure 2.58: Evolution of trap density at point A: without thermal expansion (blue), with thermal expansion (red).

2.4.4 Results for Phase 2

After Phase 1, Phase 2 (baking phase) consists of a constant temperature equal to 513 K applied on the DFW section outer boundaries. During baking, the heat is provided by the cooling pipes. The temperature of 513K (240 °C) is imposed as a boundary condition on the cooling pipes. However, since thermal equilibrium occurs very quickly and there is no heat flow applied to the exposure surface during baking, we also have chosen to impose a temperature of 513K on the exposure surface (vacuum side). This facilitates hydrogen diffusion and detrapping. In a stress-free configuration, H transport is only driven by traps and C_L gradients, while mechanical fields (and especially compression) can affect the global desorption process. This is illustrated in Figure 2.59, on which the hydrogen flux $\|\boldsymbol{\varphi}\|$ for the three studied configurations (at the time when the flux is maximum) is shown, while in Figures 2.60a and **??** are plotted the evolution of the permeation rate R with time through the cooling pipe so that

$$R = \iint_{S_{cooling\ pipes}} \boldsymbol{\varphi}.\boldsymbol{n} dS \tag{2.11}$$

where $\boldsymbol{n}$ represents a unit vector normal to the surface dS.

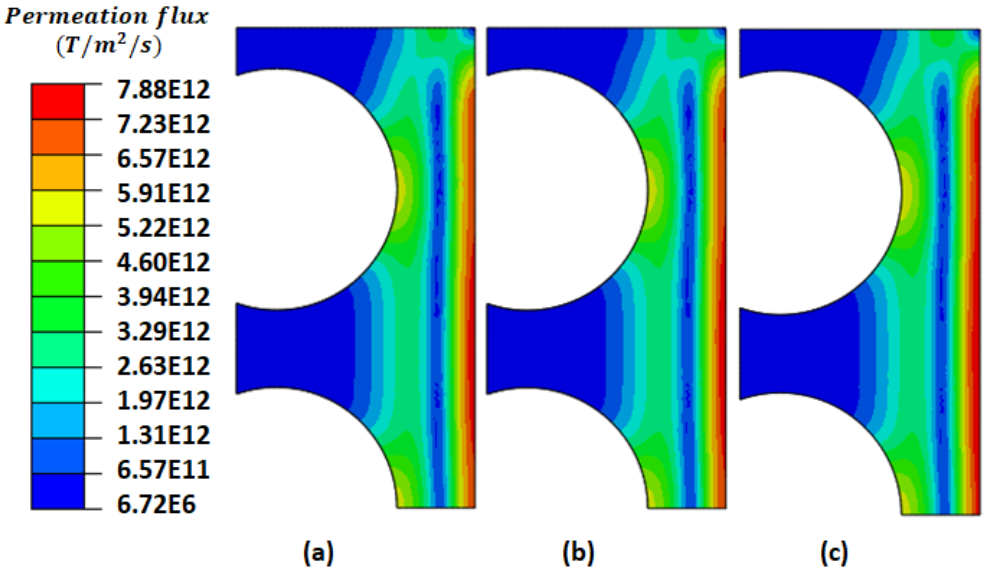

Figure 2.59: tritium flux $\|\boldsymbol{\varphi}\|$ in the DFW section during Phase 2 when the desorption rate through the cooling pipes is maximum (14th day): (a) without any mechanical fields, (b) water pressure only and (c) water pressure & thermal expansion. (the flux is only of C_L. More specifically it is not the permeation flux, but the diffusing hydrogen flux.)

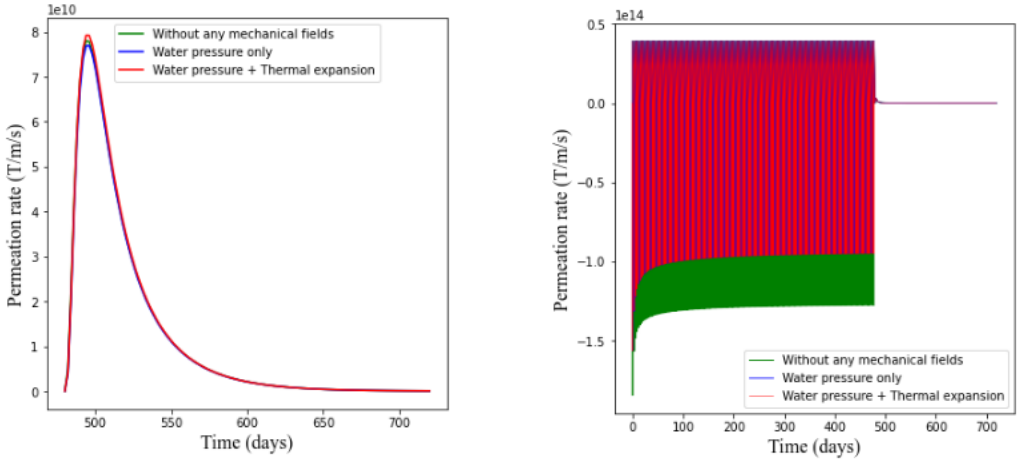

(a) (b)

Figure 2.60: Evolution of the tritium permeation rate during Phase 2 through the cooling pipe and the exposure edge.

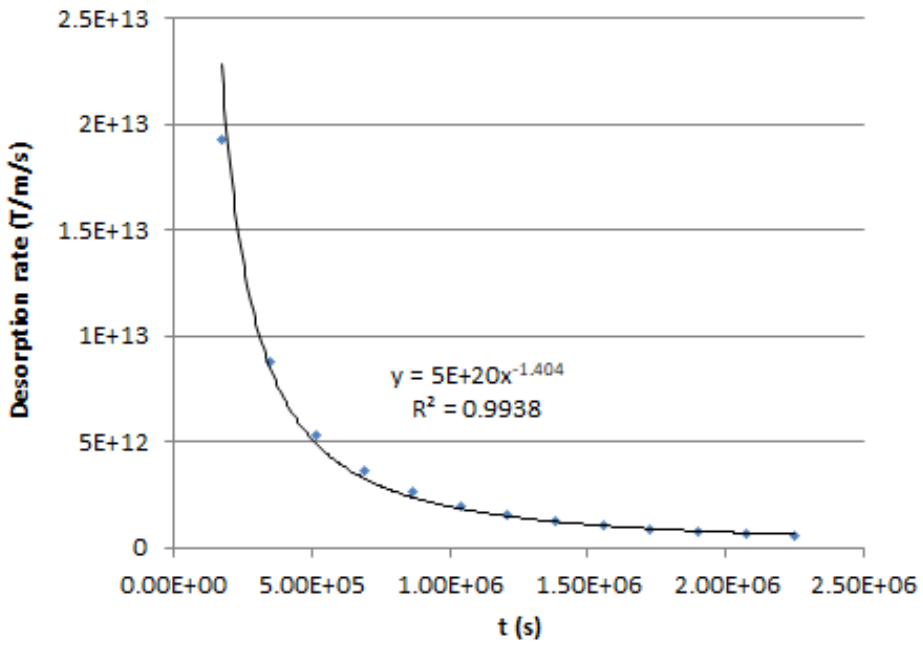

Figure 2.61: Power law dependency for the desorption rate during the first 28 days of Phase 2.

In Figure 2.59, it can be observed that the impact of mechanical fields on the hydrogen flux $\|\boldsymbol{\varphi}\|$ is negligible. The main tritium flux is localized at the exposure surface, meaning that during Phase 2, desorption occurs mainly on that surface and not at the cooling pipes. However, this latter is not zero and few tritium is released in the cooling channels.

This is illustrated in 2.60, on which the permeation rate R evolution with time (during phase 2) is plotted at the cooling pipes and at the exposure edge. No influence of the mechanical fields can be noticed, while R is much more important at the exposure edge than the one at the cooling channels.

2.4.5 Conclusion

For the reference configuration, it has been shown that the mechanical fields, induced by both plane strain, symmetry assumptions, and thermal expansion, have a slight effect on hydrogen fields during the different phases of the DFW section. It has also been seen that boundary conditions induce plastic strain localization in their vicinity, leading to a needed interrogation on their relevance; this localization, however, has no influence on the tritium retention or the desorption flux in the DFW section. The outgassing of the earlier stage in

vacuum shows a power law dependency as $R = 5 \cdot 10^{20} t^{-1.404}$ (see Figure 2.61).

2.4.6 Parametric studies

In this section, the effect of the following parameters on field partition is investigated:

- the thermal strains:
  1. the maximal value of the exposition surface temperature T_{expo}^{max}.
  2. the thermal expansion coefficient α.
- the diffusion parameter;
- the DFW modeling assumptions:
  1. the geometry of the DFW section;
  2. the concatenation assumptions.

For each case, the reference value is the one set in the reference configuration. All mechanical fields are in the following account.

2.4.6.1 Influence of the maximal value of T_{expo}

The maximal exposition temperature T_{expo}^{max} in this section is set to the reference case's one $+/-100$ K (i.e., 403 K and 603 K). It is worth noting that a modification on T_{expo}^{max} induces a modification of the tritium boundary condition $C_{L,0}$ (see equation 2.8), as the diffusion coefficient depends on the temperature. The higher the temperature, the lower the hydrogen concentration, from $4.29 \times 10^{15}\, atm/mm^3$ at 403 K down to $1.53 \times 10^{13}\, atm/mm^3$ at 603 K (see Table 2.5).
The consequences on the C_L field due to a T_{expo}^{max} modification can be observed in Figure 2.62.

As it can be observed, the impact of T_{expo}^{max} is important: an increase of 100 K induces a deeper penetration of tritium in the DFW section. This can be linked on the one hand to a lower trapping effect, and on the other hand, to an enhanced hydrogen transport. The C_L field for a decrease of 100 K on T_{expo}^{max}, for which detrapping is less easy and transport slower, supports the previous analysis: as it can be seen in Figure 2.62b, the tritium penetration in the DFW section is negligible at the end of Phase 1.

As the thermal field is affected, so is the thermal expansion, and thus, both plastic strain and hydrostatic pressure (respectively plotted in Figure 2.63 and Figure 2.64). When T_{expo}^{max} decreases (respectively increases), then the thermal strain decreases (respectively increases), and so does the pressure field (in conjunction with the plane strain assumption). As a

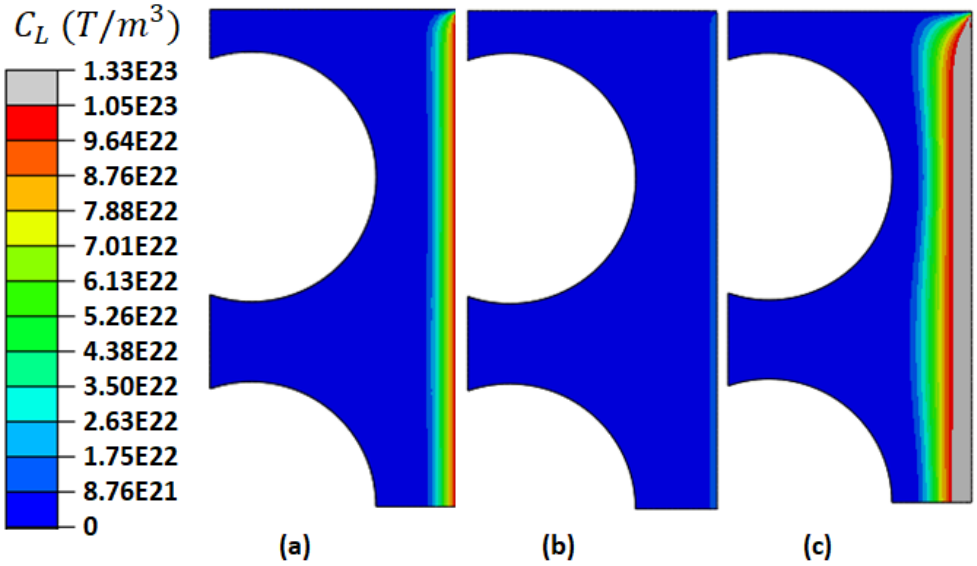

Figure 2.62: C_L field at the end of Phase 1 for T_{expo}^{max} equal to (a) 503 K (reference configuration), (b) 403 K and (c) 603 K.

consequence, the induced plastic strain decreases (respectively increases) as well. This relationship between P_H and ϵ_p fields can be seen by comparing Figures 2.63 and 2.64, at the end of Phase 1: the lower the P_H value, the bigger the plastic strain.

Table 2.5: D_L & $C_{L,0}$ values at different temperatures.

	$D_L\,(mm^2/s)$	$C_{L,0}(atom/mm^3)$
403 K	6.064×10^{-8}	$4.29{\times}10^{15}$
503 K (reference configuration)	1.777×10^{-6}	$1.46{\times}10^{14}$
603 K	1.698×10^{-5}	$1.53{\times}10^{13}$

For the sake of illustration of this process, the temporal evolution of these two fields at point A is plotted in Figure 2.65 (see the location of point A in Figure 2.51). For T_{expo}^{max}=403 K, there is no plastic strain development during phase 1; for 603 K, at each cycle, the plastic strain increases up to 4%.

The impact of the T_{expo}^{max} modification on the C_L and C_T fields, last, can also be seen by plotting the evolution of Q_{tot} with time during the whole loading process (Phase 1 and 2, see Figure 2.66). First, it can be observed that at least in Phase 1, Q_{tot} is greater when the exposure temperature is lower. This is because the boundary condition $C_{L,0}$ decreases

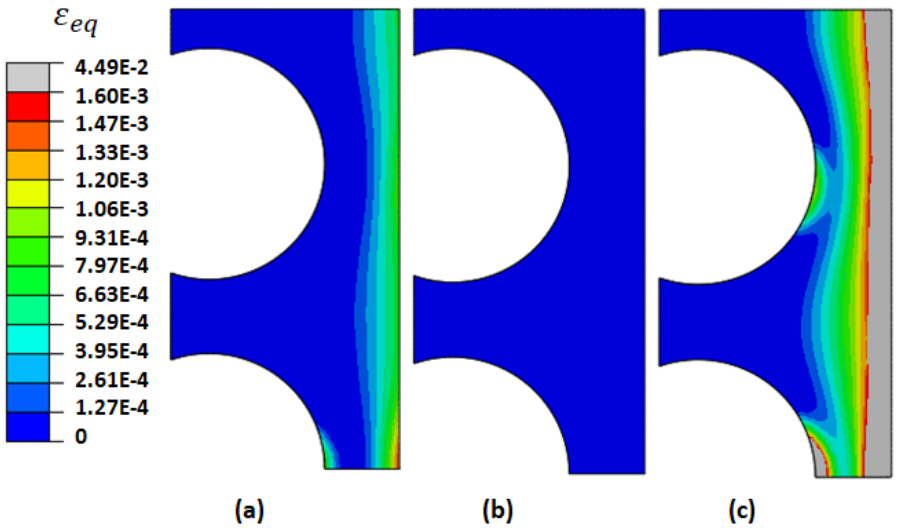

Figure 2.63: Equivalent plastic strain field at the end of Phase 1 for T_{expo}^{max} equal to (a) 503 K (reference configuration), (b) 403 K and (c) 603 K.

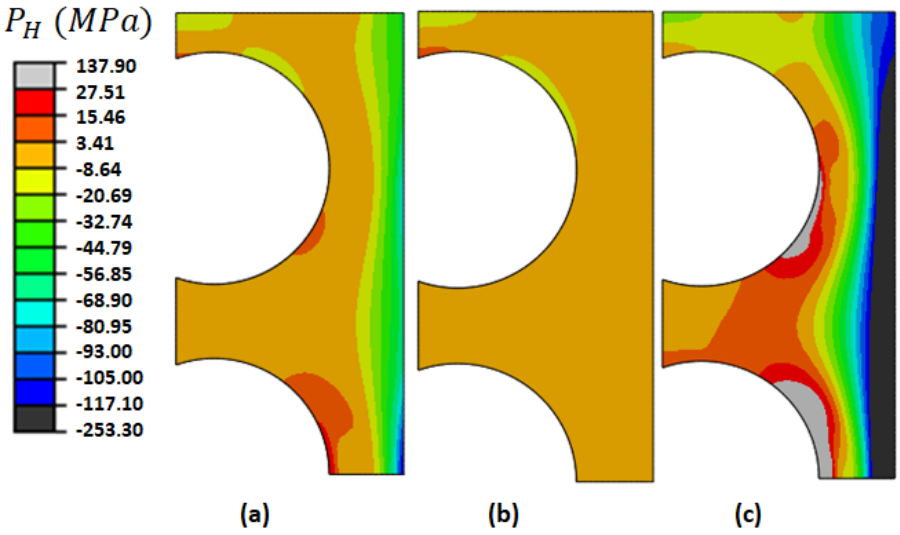

Figure 2.64: Hydrostatic pressure field at the end of Phase 1 for T_{expo}^{max} equal to (a) 503 K (reference configuration), (b) 403 K and (c) 603 K.

with temperature (see equation 2.8 and Table 2.5). Secondly, it can be seen that the cycle amplitude decreases when T_{expo}^{max} increases: when the temperature increases, hydrogen diffusion becomes faster and thus, during the hot part of a cycle, hydrogen goes farther

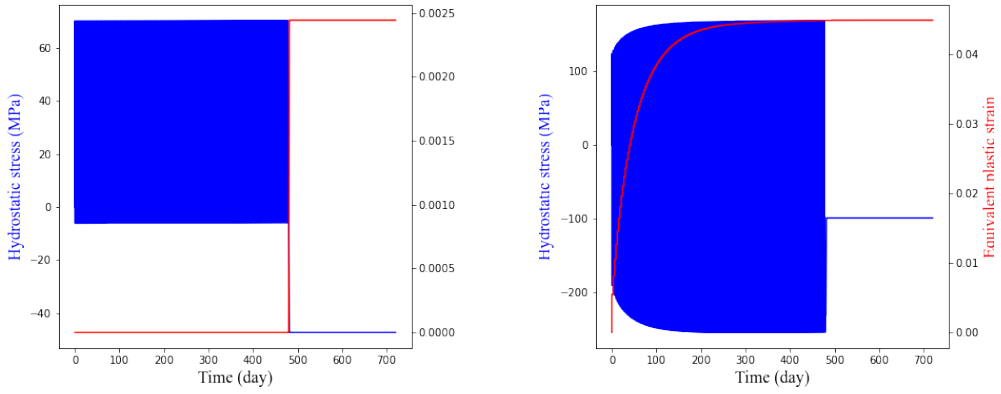

(a) (b)

Figure 2.65: Evolution with time of P_H (blue) & ϵ_{eq} (red) on point A (see Figure 2.51) for T_{expo}^{max} equal to (a) 403 K and (b) 603 K.

from the exposure surface. During the cold part, desorption occurs while hydrogen diffusion is slower, but hydrogen has been too far from the exposed surface and the desorption is negligible.

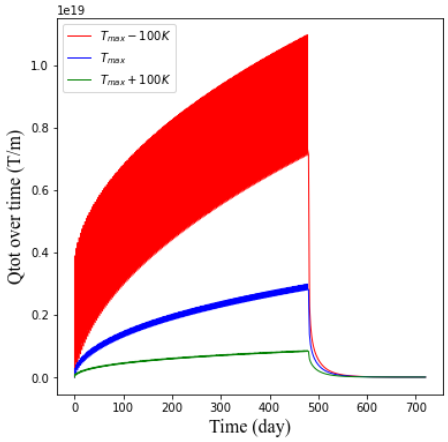

Figure 2.66: Evolution of Q_{tot} with time for the three different exposure temperatures.

2.4.6.2 Influence of the thermal expansion α

In this section, the effect of the variation of the thermal expansion coefficient is focused on (i.e., $\alpha = 1.677 \cdot 10^{-5}\, K^{-1}$, $1.7 \cdot 10^{-5}\, K^{-1}$, which is the reference value, and $1.817 \cdot 10^{-5} K^{-1}$) [243].

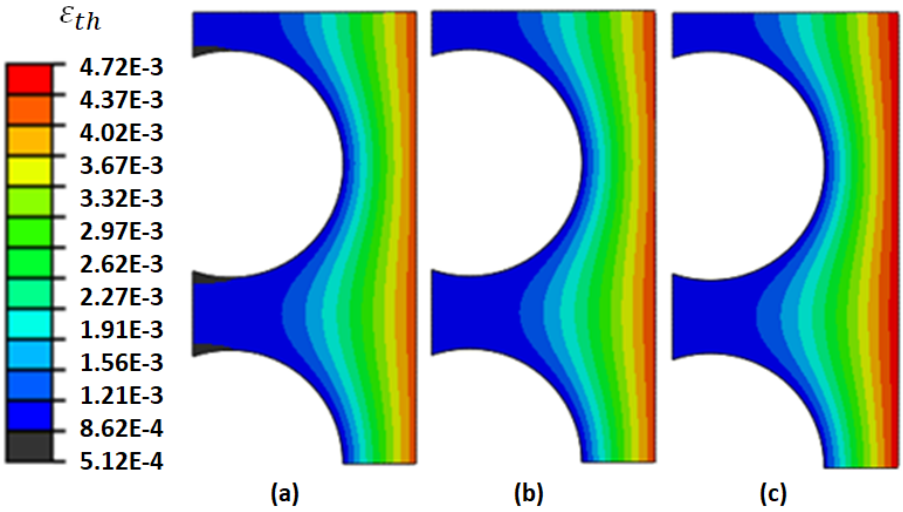

Figure 2.67: thermal strain fields at the last cycle of Phase 1(T_{max}) for (a) $\alpha = 1.677 \cdot 10^{-5}$, (b) $\alpha = 1.7 \cdot 10^{-5}$, (c) $\alpha = 1.817 \cdot 10^{-5}$.

The effect of this variation can be seen in Figure 2.67, which represents the thermal strain at the end of Phase 1: when α increases, the thermal strain increases, as expected. As a consequence, because of the plane strain assumption, $|P_H|$ increases, and so does the plastic strain (and thus, so does the trap density), as illustrated in Figure 2.70 and Figure 2.71.

The increase of trap density with α should have mitigated hydrogen penetration in the DFW section. However, as it can be seen in Figure 2.68, the modification of α has no influence on C_L fields. This result is confirmed by the Q_{tot} evolution with time, plotted in Figure 2.69 (a).

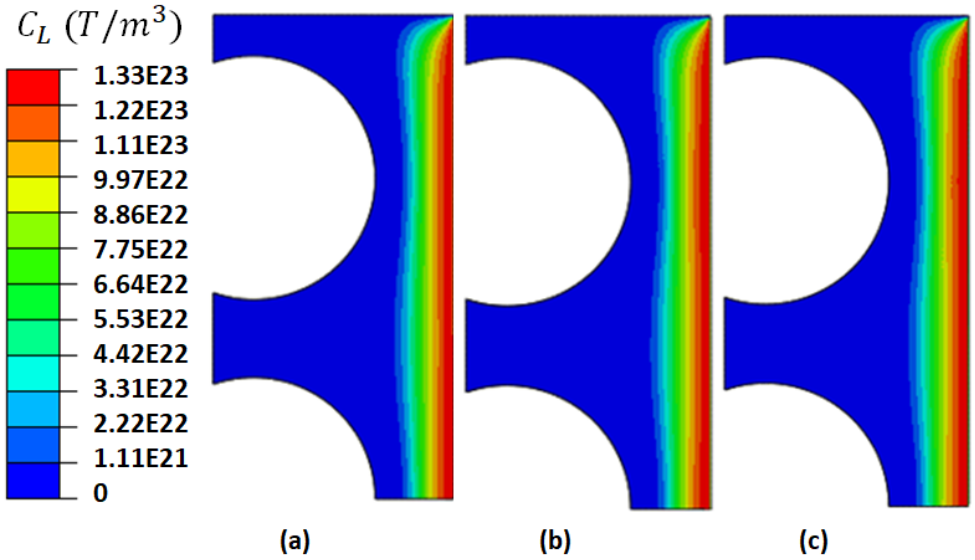

Figure 2.68: C_L fields at the end of Phase 1 for (a) $\alpha = 1.677 \cdot 10^{-5}$, (b) $\alpha = 1.7 \cdot 10^{-5}$, (c) $\alpha = 1.817 \cdot 10^{-5}$.

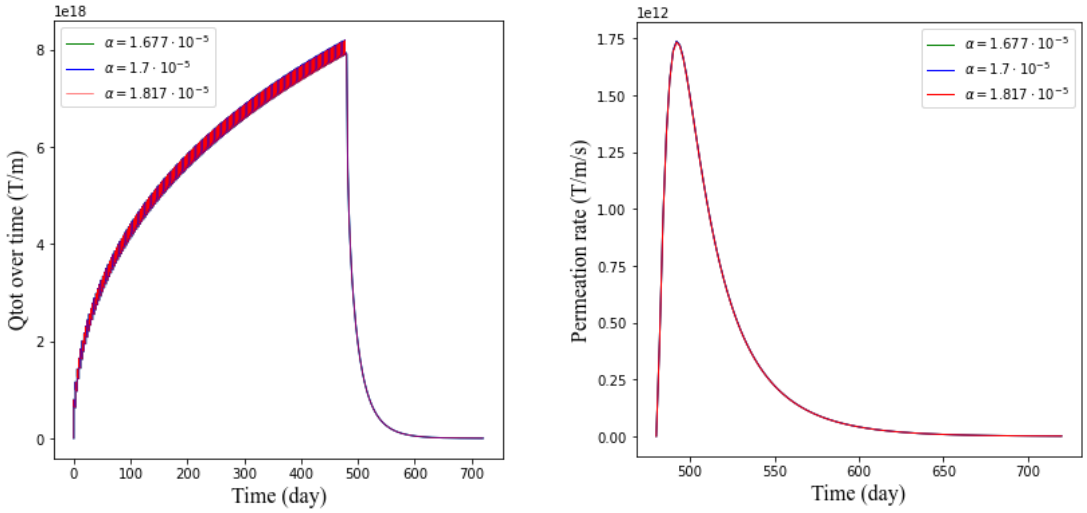

Figure 2.69: (a) Q_{tot} temporal evolution for all different thermal expansion coefficients. (b) Desorption rate R evolution with time for all different thermal expansion coefficients.

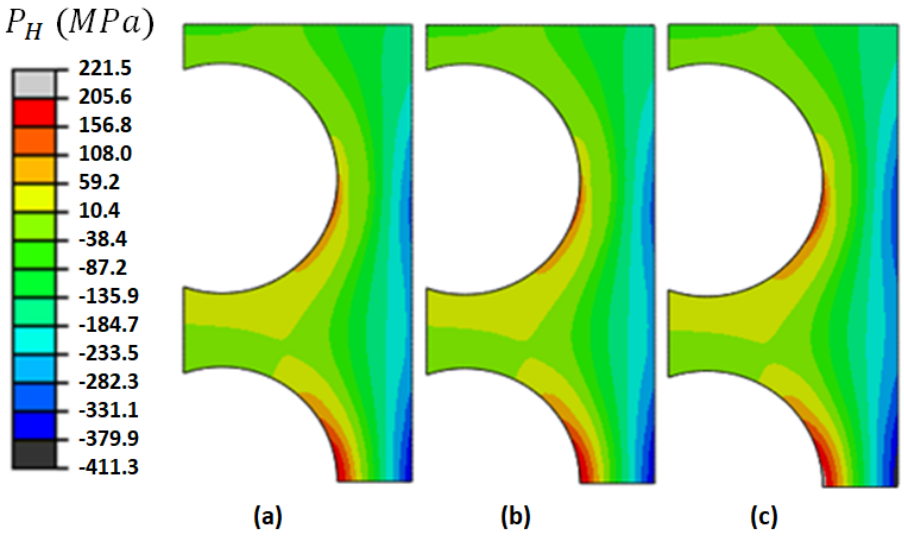

Figure 2.70: P_H fields at the end of Phase 1: (a) $\alpha = 1.677 \times 10^{-5}$, (b) $\alpha = 1.7 \times 10^{-5}$, (c) $\alpha = 1.817 \times 10^{-5}$.

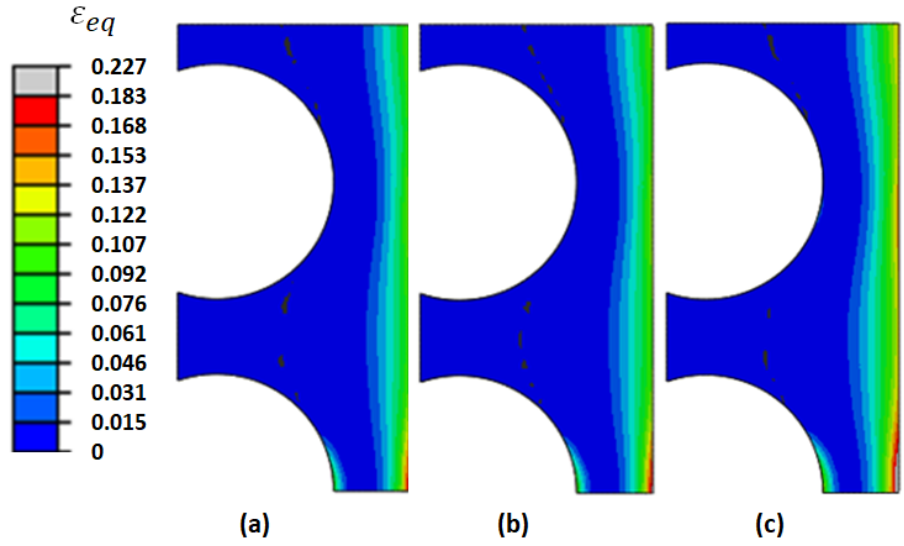

Figure 2.71: ϵ_p fields at the end of Phase 1: (a) $\alpha = 1.677 \times 10^{-5}$, (b) $\alpha = 1.7 \times 10^{-5}$, (c) $\alpha = 1.817 \times 10^{-5}$.

This non-influence of α on C_L fields can be understood by reconsidering the influence of the thermal strains in the reference configuration. As observed, temperature variations induce opposing effects on diffusion, with an increase in D_L accompanied by a compressive stress

field, or vice versa, which effectively cancel each other out. Consequently, thermal strains have a limited impact on the C_L field, and the same holds true for α. The desorption rate R during Phase 2 can also be seen in Figure 2.69 (b): R evolution with time appears to be non-sensitive to α.

2.4.6.3 Influence of the diffusion coefficient

The effect of the diffusion coefficient $D_L = D_0 e^{-\frac{E_m}{k_B T}}$ on the fields in the DFW section is investigated in the present section. Three different D_0 values are used, corresponding to Hydrogen, Deuterium, and tritium (see Table 2.6) and so the concentration during exposure $C_{L,0}$ is modified (see Equation 2.8). For the three diffusion coefficients, the C_L fields are shown in Figure 2.68, and in Figure 2.72 (a) is plotted the evolution of Q_{tot} with time. It can be observed that a increase of D_0 induces an increase of the particle penetration in the DFW section at the end of phase 1, and a decrease of the maximal C_L value (equal to $C_{L,0}$). The Q_{tot} evolution with time enhances the effect of $C_{L,0}$ on the global particle inventory: even if the diffusion is faster for higher D_0 (and if the particles penetrate deeper in the DFW section), the decrease of $C_{L,0}$ leads to a decrease in Q_{tot}. In Figure 2.69 (b) is plotted the desorption rate R for the three difference D_0 values: in such a process, the impact of the diffusion coefficient seems to be preponderant, and consequently, the higher D_0, the higher R.

Table 2.6: Variation of diffusion coefficient

Element	D_0 (m^2/s)	$C_{L,0}$ ($atoms/mm^3$)
Hydrogen	2.51×10^{-6}	8.45×10^{13}
Deuterium	1.78×10^{-6}	1.19×10^{14}
Tritium	1.45×10^{-6}	1.46×10^{14}

2.4.6.4 Influence of the the DFW section geometry

In this following section, the effect of two modeling assumptions is investigated: first, the DFW section geometry and then the cycle concatenation.

As it has been pointed out several times, the chosen geometry to model the hydrogen diffusion and trapping in the DFW can induce very important artifacts in the results. In this section, the 2D assumption is not questioned, but the size of the DFW section is focused on. Especially, in the reference configuration, partial cooling pipes have been chosen, following the work of S. Benannoune [238]. Two other geometries are considered here:

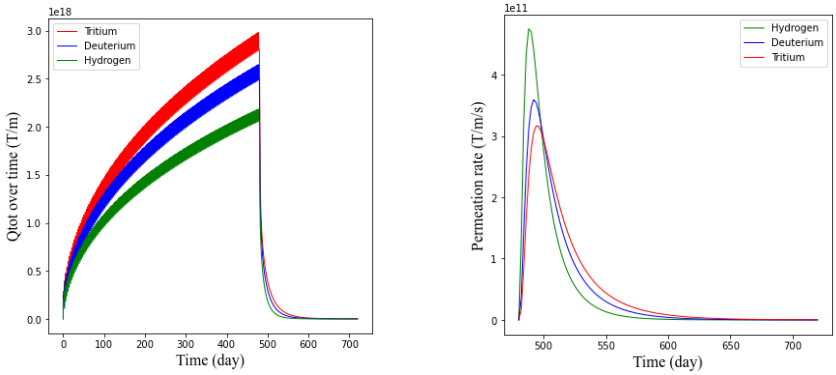

(a) (b)

Figure 2.72: (a) Q_{tot} evolution with time for the H isotopes. (b) Desorption rate R evolution with time

- Two complete cooling pipes.
- Three complete cooling pipes.

All boundary conditions and material properties used in the cases above are same as the reference case. In Figures 2.73 to 2.75 are presented the comparisons between the new configurations and the reference one.

2.4.6.5 Influence of cycle concatenation

For the reference case, we have assumed that several loading cycles were concatenated in one single 3-day cycle. Due to the plastic strain development in each cycle, and the consequences for the mechanical and hydrogen fields, a comparison is made in the following between two scenarios: the reference one (160 cycles), and a set of 1-day cycles (480 cycles). For the sake of efficiency, only the effect on mechanical fields is investigated. Especially, the equivalent plastic strain, the Figures of which at the end of Phase 1 are presented in Figure 2.76.

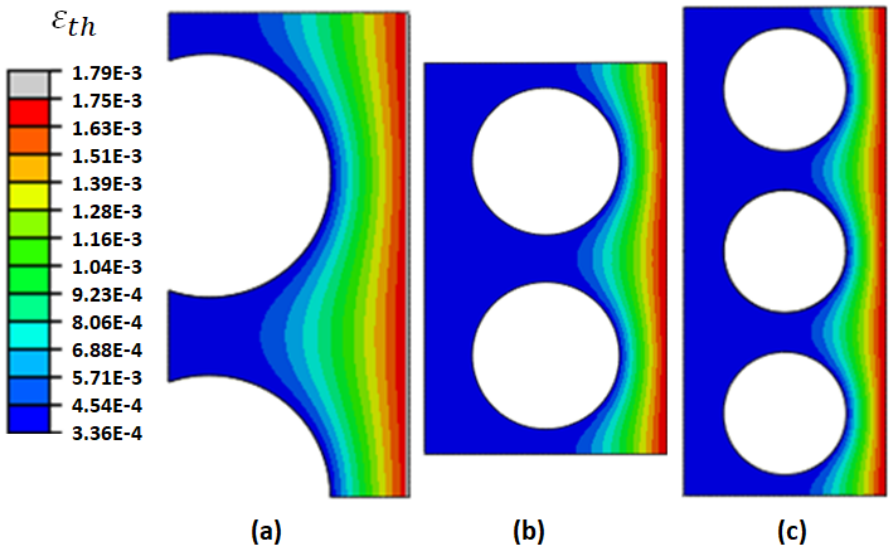

Figure 2.73: Thermal expansion fields at the last cycle of Phase 1(T_{max}): (a) Reference case, (b) 2 cooling pipes, (c) 3 cooling pipes.

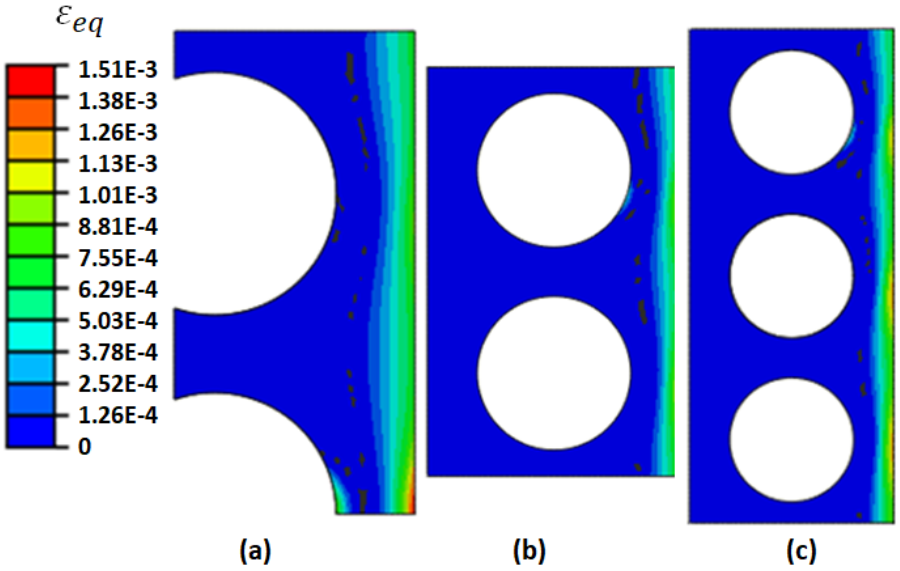

Figure 2.74: Equivalent plastic strain field at the end of Phase 1: (a) Reference case, (b) 2 cooling pipes, (c) 3 cooling pipes.

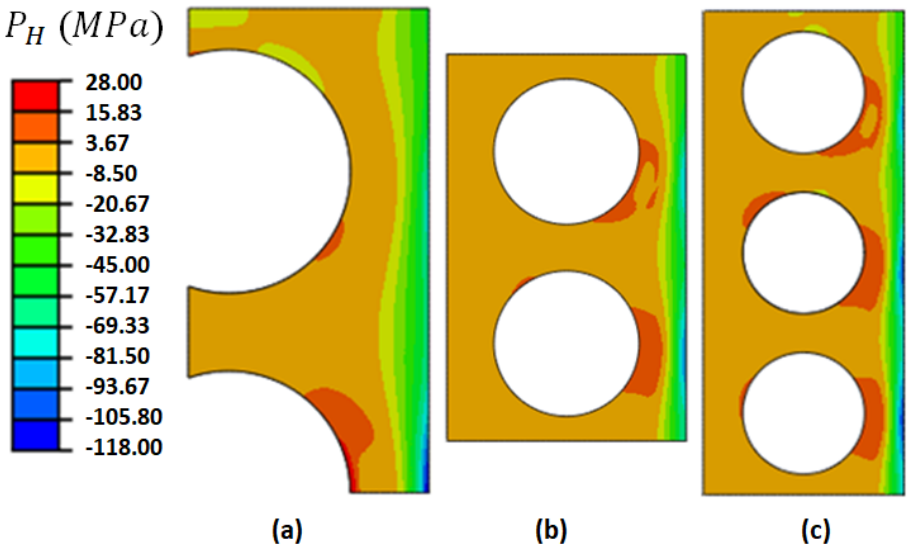

Figure 2.75: Hydrostatic stress fields at the end of Phase 1: (a) Reference case, (b) 2 cooling pipes, (c) 3 cooling pipes.

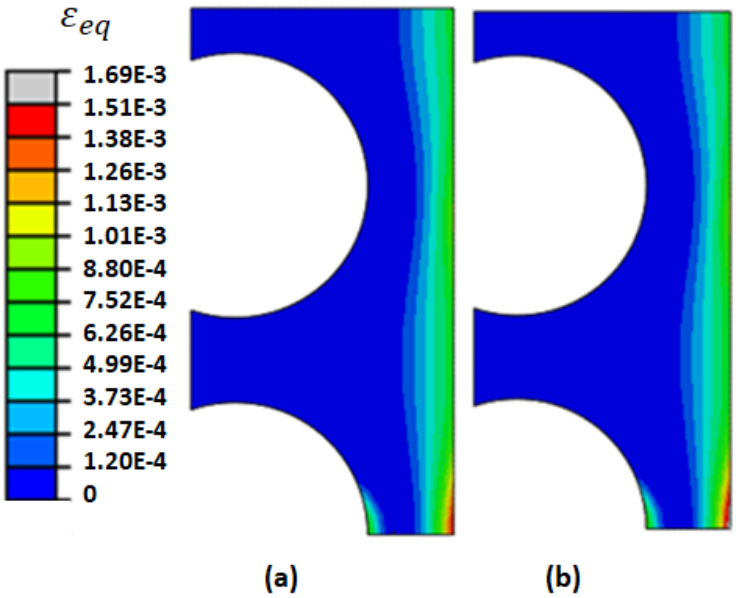

Figure 2.76: Equivalent plastic strain field at the end of Phase 1 for (a) 160 cycles, (b) 480 cycles.

As it can be observed, there are no clear differences between these two figures. If we focus on some specific points, which are located on the plasma-exposed surface (points A, T, and M, see Figure 2.77a), it can be observed that the main impact of the number of cycles is localized at the lower surface (point A), where a symmetry boundary condition is imposed.

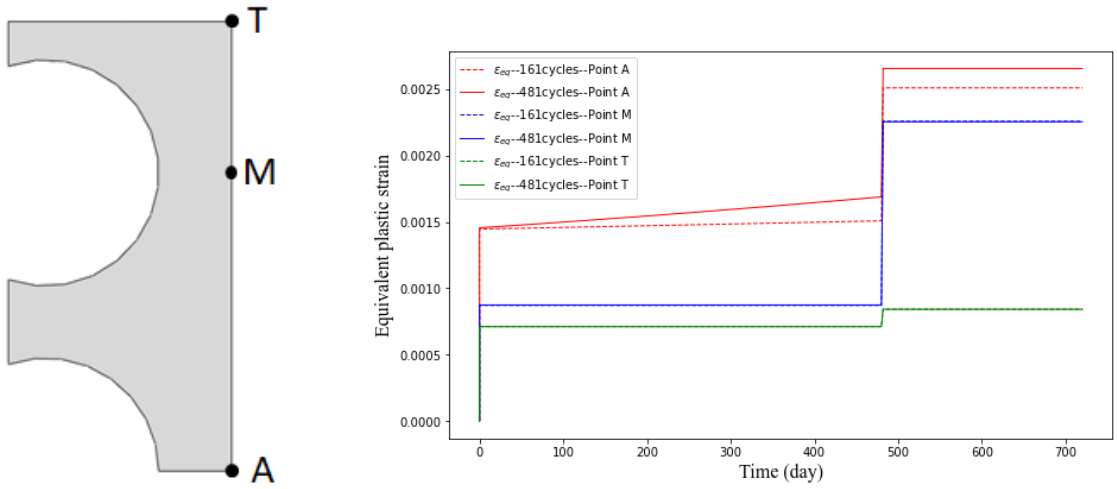

(a) (b)

Figure 2.77: (a) Points chosen. (b) Equivalent plastic strain.

For 480 1-day cycles, the equivalent plastic strain is 12% greater than the one computed for 160 3-day cycles. The differences everywhere is lower than 1%. It can thus be concluded that the concatenation assumption does not have an important impact on the mechanical fields, but near the lower surface, where the impact of the imposed boundary conditions has been already questioned.

2.4.6.6 Towards a 3D model

As it has been seen in the previous section, the boundary conditions and the DFW section geometry have a strong impact on the hydrogen field. When aiming to get a realistic estimation of hydrogen retention in DFW components, this problem has to be addressed.

A complete 3D thermo-mechanical modeling of the DFW has been conducted, using the same equations, parameters, and boundary conditions as for the reference case, for 1 cycle only. 3754973 linear pyramidal elements have been used, with a smaller size near the exposed face. T_{water} boundary condition has been applied to the first cooling pipe only, and no water-related pressure is here considered. The results at the end of the hot phase of the 1st cycle (3315 s) are plotted in Figures 2.78 to 2.81.

It can first be seen that the temperature variation affects a depth far greater than the size of the studied DFW sections (as it has been seen in the previous section). This can be due to the absence of any extra thermal boundary condition on cooling pipes which are not in the first row. The temperature gradient and the thermal strain induce stress concentration at the exposed surface, and eventually, plasticity.

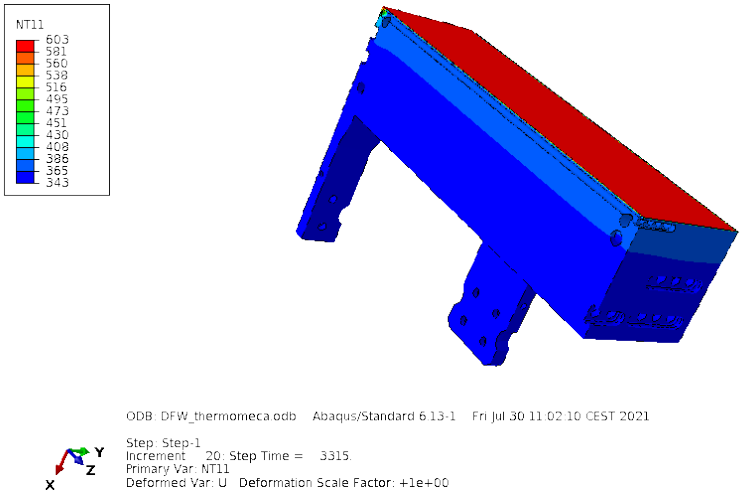

Figure 2.78: T (K) at the end of the thermal loading (3315 s).

In Figure 2.82 is plotted the strain along two paths, along the DFW length (ϵ_{33}), located just above the 1st cooling pipe row (oscillations are due to the badly shaped elements or not adapted ones). The first path is defined in the DFW symmetry plane, at its center, and the second in the lateral free surface. For the 2D configuration, this strain corresponds to the

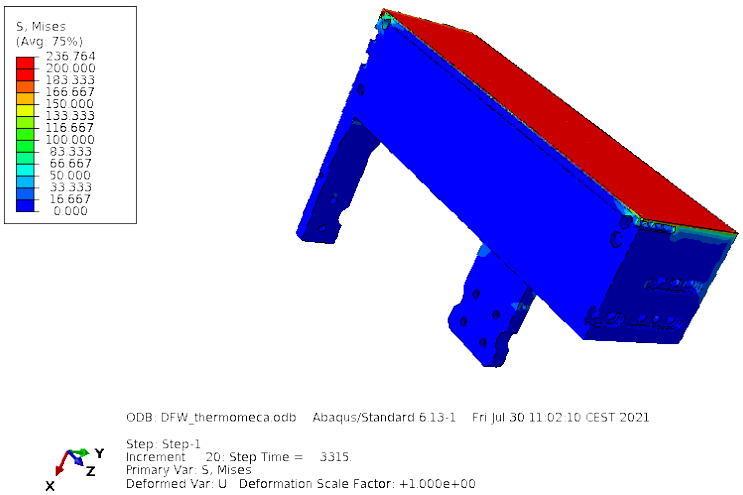

Figure 2.79: σ_{vM} (MPa) at the end of the thermal loading (3315 s).

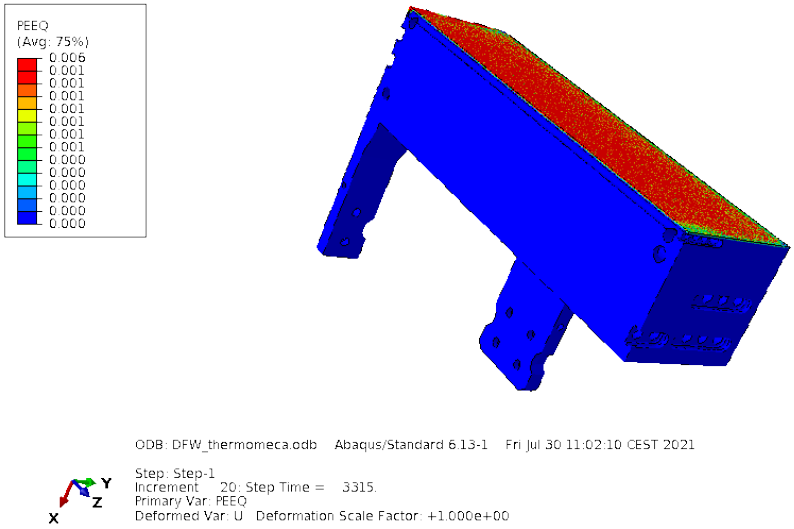

Figure 2.80: ϵ_p at the end of the thermal loading (3315 s).

normal one, and is set equal to 0 when a plane strain assumption is used. Results plotted in Figure 2.82 allows to question this assumption for one cycle. At the end of the plasma exposure, for 3315 s, it can be seen that ϵ_{33}=0 along the path on the DFW's lateral free surface (i.e. the plane strain assumption is relevant), while in the center, ϵ_{33}=0.05%: plane strain assumption is here a little bit restrictive, and further investigations are required to get the evolution of ϵ_{33} with cycles.

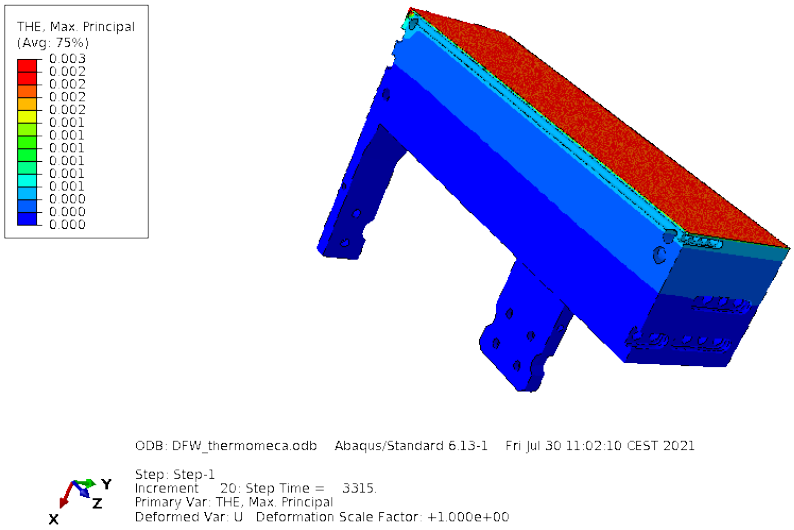

Figure 2.81: ϵ_{th} at the end of the thermal loading (3315 s).

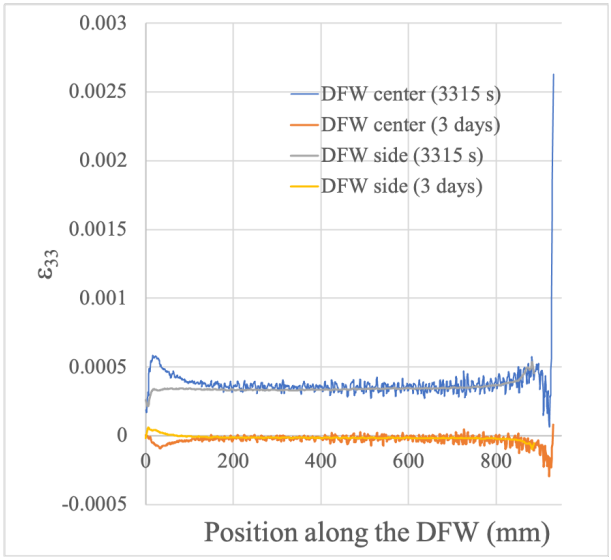

Figure 2.82: ϵ_{33} evolution along the DFW length, just above the first cooling pipe range at the center and the free face of the DFW, at the end of the thermal loading (3315 s) and of the 1st cycle.

2.4.6.7 Results at the tokamak scale

We extrapolate the results to estimate the total inventory and permeation flux for the stainless steel parts exposed to the plasma. The goal is to estimate the worst and the best cases (as we showed, the mechanical behavior increases the inventory and permeation flux) in terms of tritium safety.

Our extrapolation is based on the results obtained for four cases based on the DFW reference case with T_{expo}^{max} presented in Table 2.7. For the DFW case T_{expo}^{max} is based on the average surface temperature for a heat flux of 0.2 MW/m^2.

The total inventory (tritium/mm) for the 4 cases are presented in Figure 2.83. The maximum retention in Table 2.7 corresponds to the value at the end of the Phase 1 divided by the length of the exposure surface (30.2 mm), multiplied by the surface of the component (20 $\times 10^6$ mm^2 for the TBMs and 30 $\times 10^6$ mm^2 for the DFW surface) and next multiplied by M_T (3 g/mol) / N_A (6.022$\times 10^{23}$ mol^{-1}) to have the results in g. For these conditions, the results with and without mechanical fields are very close, the maximum retention in all stainless steel components is estimated to 102 mg.

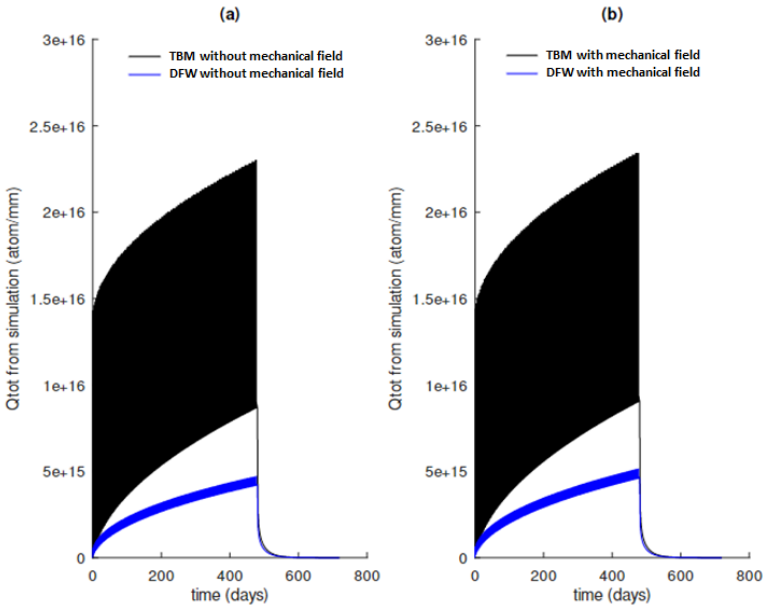

Figure 2.83: Total inventory for the 4 cases used to extrapolate the inventory in all the stainless steel components. (a) cases without mechanical fields resolution (b) cases with mechanical fields resolution.

The permeation fluxes (tritium/mm/s) for the 4 cases are presented in Fig 2.84. After the baking (end of Phase 2), almost nothing remains in the DFW section. There likely is no hydrogen permeation during Phase 1 (in the proposed modeling) because the hydrogen does not diffuse until then and is limited to the vicinity of the exposure surface. The mass in Table 2.7 is equal to the time-integrated value over Phase 2 divided by the length of the exposure surface, next multiplied by the surface of the component and next multiplied by M_T (3 g/mol) / N_A (6.022×10^{23} mol^{-1}) to make the results in gram. For these conditions, the results with and without mechanical field are similar, the total permeation across all stainless steel components is estimated to be 10.1 mg.

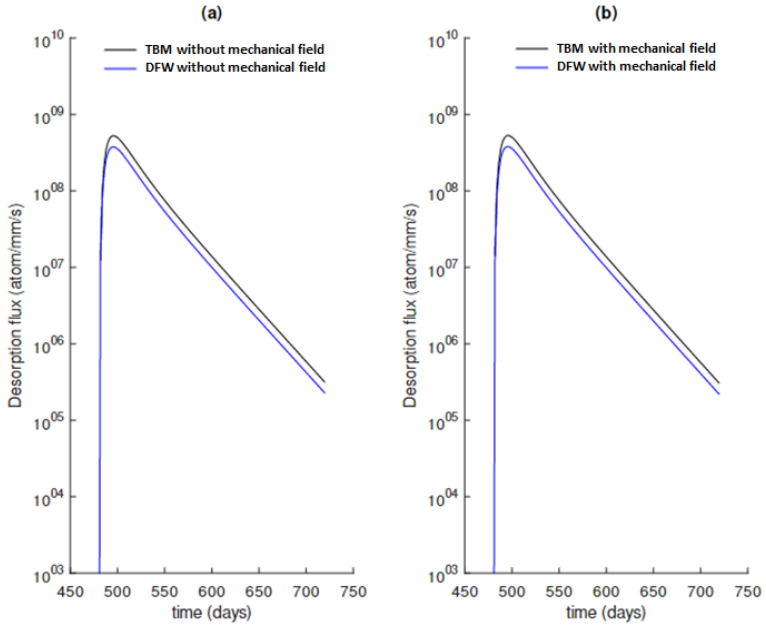

Figure 2.84: Flux in cooling pipe for the 4 cases used to extrapolate the inventory in all the stainless steel components for (a) cases without mechanical field resolution, (b) cases with mechanical field resolution.

Table 2.7: Specific conditions and results of the extrapolation at the tokamak scale

Case name	T_{expo}^{max} (K)	Max retention	Mass permeation
DFW with mechanical fields	462	25 mg	4.2 mg
DFW without mechanical fields	462	23 mg	4.2 mg
TBM with mechanical fields	373	77 mg	5.9 mg
TBM without mechanical fields	373	76 mg	5.8 mg

Of course, these results are first and general estimations due to the geometry approximations. It is dangerous to extrapolate calculations on part of the geometry to its whole knowing that the mechanical stresses are not the same everywhere. That is why, as a perspective, we started simulations on the whole DFW component as shown in Figure 2.78 to 2.81.

2.5 Divertor monoblock

In ITER, the divertor plasma-facing components are actively cooled monoblocks (Figure 2.85). They consist of tungsten armor and CuZrCr cooling pipes in which pressurised water evacuates the heat deposited by the plasma power loads. A significant part of the plasma load is carried by energetic tritium ions that impact on the components, of which a fraction permeates in the monoblock to remain trapped or even enter the coolant flow. The related tritium retention and permeation must be understood.

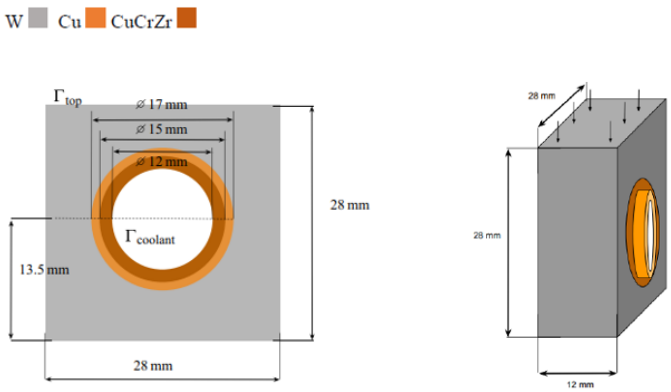

Figure 2.85: ITER monoblock: (a) front view (b) lateral view.

The multi-material characteristics of monoblocks have led to specific developments, to be able

to model concentration discontinuities at bi-material interfaces [255]. These developments are first presented, and then, all relevant material properties are summarized, and a comparison with the FESTIM code [141] is conducted without any mechanical fields. A reference case is next defined and a parametric study on the monoblock is made to evaluate the impact on hydrogen retention and permeation. The last part is devoted to cycling modeling.

2.5.1 Modeling of diffusion at a bi-material interface

Because the monoblock is a multi-material component, understanding the tritium transport by simulation needs a model of diffusion across materials. Compared to previous works made on DFW, a multimaterial diffusion feature must be added to our general model. Several studies have focused on the problematic of diffusion across a bi-material interface, as summarized in the introduction of [256]: if no experimental evidence is available, solute accumulation at an interface (and an averaged concentration discontinuity) can occur [255, 257]. Such an explanation has been widely used in studies focused on the failure processes of multi-layered electronic components, controlled by moisture absorption: to model concentration discontinuity, several approaches have been proposed, being either phenomenological [258] or based on thermodynamics [259]. One of these consists in the introduction of a virtual gas layer between the two materials [260], assuming chemical equilibrium between the solute and the gas at both interfaces, hereafter described.

In the context of hydrogen in metals, H transport, represented by H flux, is usually modelled using a generalized Fick law, modified to include the effect of the hydrostatic pressure P_H [21] (and if the Soret effect is neglected [261])

$$\boldsymbol{\varphi} = -D_L \boldsymbol{\nabla} C_L - \frac{D_L V_H}{RT} C_L \boldsymbol{\nabla} P_H. \tag{2.12}$$

where D_L is the hydrogen diffusion coefficient , C_L the diffusing hydrogen concentration of hydrogen, V_H the hydrogen partial molar volume, R the ideal gas constant and T the absolute temperature. This flux can also be written as a function of the hydrogen chemical potential μ_L, so that [17, 262]

$$\mu_L = \mu_L^0 + RT \ln\left(\frac{\theta_L}{1-\theta_L}\right) + V_H P_H \approx \mu_L^0 + RT \ln\left(\theta_L\right) + V_H P_H \tag{2.13}$$

where μ_L^0 represents the chemical potential of diffusing hydrogen in a reference state, and with $\theta_L N_L = C_L$, considering $\theta_L \ll 1$. N_L represents the material's interstitial site density. In such a case, hydrogen flux can be written as [263]

$$\boldsymbol{\varphi} = -\frac{D_L C_L}{RT} \boldsymbol{\nabla} \mu_L, \tag{2.14}$$

which is equivalent to Equation 2.12. The equilibrium with hydrogen gas at the interface leads to

$$\mu_L = \frac{1}{2}\mu_g \tag{2.15}$$

where μ_g represents the di-hydrogen chemical potential, so that

$$\mu_g = \mu_g^0 + RT \ln\left(\frac{P}{P_0}\right) \tag{2.16}$$

P being the partial pressure of the di-hydrogen gas, leading to

$$\mu_L^0 + RT \ln(\theta_L) + V_H P_H = \frac{1}{2}\mu_g^0 + \frac{1}{2}RT \ln\left(\frac{P}{P_0}\right) \tag{2.17}$$

i.e.,

$$C_L \exp\left(\frac{V_H P_H}{RT}\right) = N_L \exp\left(\frac{\mu_g^0 - 2\mu_L^0}{2RT}\right)\sqrt{\frac{P}{P_0}} \tag{2.18}$$

After introducing the solubility S, at the gas-material interface, Sieverts' law can be derived [264]:

$$C_L \exp\left(\frac{V_H P_H}{RT}\right) = S\sqrt{P} \tag{2.19}$$

At the bi-material interface, considering a thin gas layer with a pressure P, thus

$$\frac{C_L^1}{S^1} \exp\left(\frac{V_H^1 P_H}{RT}\right) = \sqrt{P} = \frac{C_L^2}{S^2} \exp\left(\frac{V_H^2 P_H}{RT}\right) \tag{2.20}$$

i.e.,

$$\frac{C_L^1}{S^1} \exp\left(\frac{(V_H^1 - V_H^2)\, P_H}{RT}\right) = \frac{C_L^2}{S^2} \tag{2.21}$$

leading to the continuity of the quantity $\Phi = C_L/S$ if $V_H^1 = V_H^2$ or if $P_H = 0$.

Furthermore, to ensure mass conservation, hydrogen flux continuity must also be ensured, so that

$$D_L^1 \boldsymbol{\nabla} C_L^1 - \frac{D_L^1 V_H^1}{RT} C_L^1 \boldsymbol{\nabla} P_H = D_L^2 \boldsymbol{\nabla} C_L^2 - \frac{D_L^2 V_H^2}{RT} C_L^2 \boldsymbol{\nabla} P_H \tag{2.22}$$

P_H field being continuous at any bi-material interface.

In this work, we have assumed that V_H is a constant for any material[1], equal to the tungsten's one, for the sake of simplicity. Equation 2.21 becomes consequently

$$\frac{C_L^1}{S^1} = \frac{C_L^2}{S^2} \tag{2.23}$$

Ensuring the continuity of C_L/S instead of C_L in Finite Element computations is possible if C_L/S becomes a degree of freedom of the problem.

[1]The implementation in Abaqus of processes needing a full μ continuity remains challenging.

2.5.2 Hydrogen transport equation

This approach, based on both continuities of Φ and $\boldsymbol{\varphi}$ is widely used in mass transport simulations, including the "mass diffusion" simulation procedure proposed in Abaqus Software [265].

To ensure these two continuities in the current modeling framework, the computations are performed using Φ instead of C_L as degree of freedom. The consequences on the global transport equations, and the related implementation in the UMATHT subroutine are thereafter described.

The total hydrogen concentration is (in the case of i different traps)

$$C = C_L + \sum_i C_{t,i} \tag{2.24}$$

The transport and trapping equation, which is

$$\frac{\partial C}{\partial t} = \boldsymbol{\nabla}.\left(D_L \boldsymbol{\nabla} C_L + \frac{D_L V_H}{RT} C_L \boldsymbol{\nabla} P_H.\right) \tag{2.25}$$

is thus rewritten as

$$S\frac{\partial \Phi}{\partial t} + \Phi\frac{dS}{dT}\frac{\partial T}{\partial t} + \sum_i \frac{\partial C_{t,i}}{\partial t} = \boldsymbol{\nabla}.\left(D_L S \boldsymbol{\nabla}\Phi + D_L \Phi \frac{dS}{dT}\boldsymbol{\nabla} T + \frac{D_L S V_H}{RT}\Phi \boldsymbol{\nabla} P_H\right) \tag{2.26}$$

The hydrogen flux is thus

$$\boldsymbol{\varphi} = -D_L S \boldsymbol{\nabla}\Phi - D_L \Phi \frac{dS}{dT}\boldsymbol{\nabla} T - \frac{D_L S V_H}{RT}\Phi \boldsymbol{\nabla} P_H \tag{2.27}$$

Last, the trapping kinetic equation is so that [266]

$$\frac{\partial C_{t,i}}{\partial t} = \frac{k}{N_L} C_L \left(N_{t,i} - C_{t,i}\right) - p C_{t,i}. \tag{2.28}$$

2.5.3 UMATHT implementation

The reader should refer to [267] for a global presentation of the UMATHT development, its internal variables, and its application to hydrogen transport and trapping.

The *temp* variable is set to $\Phi = C_L/S$, and *dtemp* to $d\Phi = d\left(C_L/S\right) = dC_L/S - C_L dS/S^2$.

The hydrogen flux has been defined in the previous section, and thus $\boldsymbol{dfdt}$ and $\boldsymbol{dfdg}$ variables are so that

$$\boldsymbol{dfdt} = \frac{\partial \boldsymbol{\varphi}}{\partial \Phi} = -D\frac{dS}{dT}\nabla \mathbf{T} \tag{2.29}$$

and

$$\boldsymbol{dfdg} = \frac{\partial \boldsymbol{\varphi}}{\partial \boldsymbol{\nabla}\Phi} = -\left(DS\right)\mathbf{I} \tag{2.30}$$

u is so that $u = C$, leading to the following incremental relationship

$$u(t+\delta t) = u(t) + (dudt)\delta\Phi + \Phi\frac{dS}{dT}\delta T \tag{2.31}$$

where $dudt$ is so that

$$dudt = \frac{\partial C}{\partial \Phi} = S\left(1 + \sum_i \frac{\partial C_{t,i}}{\partial C_L}\right) \tag{2.32}$$

Last, in the context of transient trapping, $\partial C_{t,i}/\partial C_L$ is computed using the Generalized Oriani's Approximation (GOA), as defined in [268].

2.5.4 Material properties

In this section, all relevant parameters to conduct the chemo-thermo-mechanical simulation in monoblock are summarized. All thermal and elastic properties have been provided by ITER [269], except the CuCrZr's Poisson ratio, which comes from literature.

2.5.4.1 Heat transfer properties

The heat transfer equation is

$$\rho C_p \frac{\partial T}{\partial t} = \boldsymbol{\nabla}.(\lambda \boldsymbol{\nabla} T) \tag{2.33}$$

where ρ is the material density, C_p its specific heat, and λ its thermal conductivity. A temperature variation ΔT induces a thermal expansion strain tensor $\boldsymbol{\epsilon}_{th}$ so that

$$\boldsymbol{\epsilon}_{th} = \alpha \Delta T \boldsymbol{I} \tag{2.34}$$

ΔT is the difference between the initial and current temperatures, α the thermal expansion coefficient, and $\boldsymbol{I}$ the unit tensor. All relevant parameters are listed in Tables 2.8 to 2.11.

Table 2.8: Densities.

Material	$\rho\ (kg/m^3)$	Temperature range
W	$(19.3027 - 2.3786 \times 10^{-4}T - 2.2448 \times 10^{-8}T^2) \times 10^3$	$20 \sim 1500°C$
Cu	$(8.872 - 4.5628 \times 10^{-4}T - 8.7038 \times 10^{-8}T^2) \times 10^3$	$20 \sim 500°C$
CuCrZr	$[1 - 3 \times 10^{-6}$ $\times(16.6 + 6.24 \times 10^{-3}T - 9.05 \times 10^{-6}T^2 + 7.2 \times 10^{-9}T^3)$ $\times(T - 20)] \times 8900$	$20 \sim 700°C$

Table 2.9: Specific heats.

Material	$C_p\ (J/kg/K)$	Temperature range
W	$128.308 + 3.2797 \times 10^{-2}T - 3.4097 \times 10^{-6}T^2$	$20 \sim 3000°C$
Cu	$383.3915 + 0.1413T - 2.9794 \times 10^{-5}T^2$	$20 \sim 1000°C$
CuCrZr	$388 + 9.49 \times 10^{-2}T + 6.32 \times 10^{-6}T^2$	$20 \sim 700°C$

Table 2.10: Conductivities.

Material	$\lambda\ (W/m/K)$	Temperature range
W	$174.9274 - 0.1067T + 5.0067 \times 10^{-5}T^2 - 7.8349 \times 10^{-9}T^3$	$20 \sim 3500°C$
Cu	$368.2324 - 0.2612T + 3.07 \times 10^{-4}T^2$	$20 \sim 500°C$
CuCrZr	$323 + 0.138T - 2.83 \times 10^{-4}T^2 + 2.11 \times 10^{-7}T^3$	$20 \sim 700°C$

Table 2.11: Expansion coefficients.

Material	$\alpha\ (10^{-6}/°C)$	Temperature range
W	$4.43 + 5.5 \times 10^{-4}T - 1.47 \times 10^{-7}T^2 + 6.07 \times 10^{-11}T^3$	$20 \sim 3200°C$
Cu	$16.0734 + 8.371 \times 10^{-3}T - 3.4349 \times 10^{-6}T^2$	$100 \sim 950°C$
CuCrZr	$16.6 + 6.24 \times 10^{-3}T - 9.05 \times 10^{-6}T^2 + 7.2 \times 10^{-9}T^3$	$20 \sim 700°C$

2.5.4.2 Thermo-Mechanical properties

Elastic properties are first summarized in Table 2.12, and then, hardening is identified.

Table 2.12: Elastic properties

Material	E (GPa)	ν
W	$397.903 - 2.3066 \times 10^{-3}T - 2.7162 \times 10^{-5}T^2$ $(20 \sim 2400°C)$	$0.279 + 1.0893 \times 10^{-5}T$ $(20 \sim 2000°C)$
Cu	$126.4176 - 3.7884 \times 10^{-2}T - 1.8237 \times 10^{-5}T^2$ $(20 \sim 400°C)$	0.34 $(20 \sim 400°C)$
CuCrZr	$128 - 2.59.10^{-2}T - 4.87.10^{-5}T^2$ $(20 \sim 700°C)$	$-4.2\text{x}10^{-7}T^2 + 7\text{x}10^{-4}T + 0.16$ (293K $\sim$ 1073K) [270]

The true/engineering stress-strain curves for the three materials at different temperatures were provided by the **I**ter **M**aterial **P**roperties **H**andbook (**IMPH**) [269], and reproduced in Figure 2.86. These data have been fitted, based on a least square method, assuming an isotropic hardening defined by the following saturating law:

$$\sigma_Y = \sigma_0 + K\left(1 - \exp^{-C\epsilon_p}\right) \tag{2.35}$$

σ_Y denotes the yield stress, σ_0 the elastic limit, ϵ_{pl}^{eq} the equivalent plastic strain. K and C are two material parameters that need to be identified.

IMPH's stress-strain curves have been converted into true stress-true plastic strain ones, and the relevant parameters were identified using a least square approach. The comparison between the experimental and numerical curves is presented in Figure 2.87, and the related parameters are summarized in Table 2.13.

Table 2.13: Hardening parameters identified from experimental data

Material	T (°C)	σ_0 (MPa)	K (MPa)	C
W	316	157.6	353.5	17.1
	426	140	386.3	9.3
	530	128.4	330.3	9
Cu	23.8	239.2	106.2	1259.9
	100	224.9	90.5	1097.3
	200	221.2	60.7	971.82
	300	170.5	45.2	1131.7
	350	132.9	52.4	1313.8
CuCrZr	20	388.7	69.3	169.3
	100	364.4	69.2	129.6
	200	329.34	56	215
	300	300	50.2	138.17

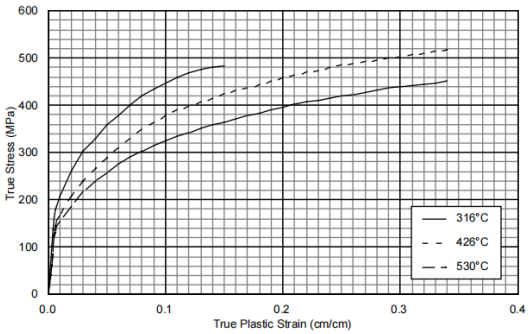

(a)

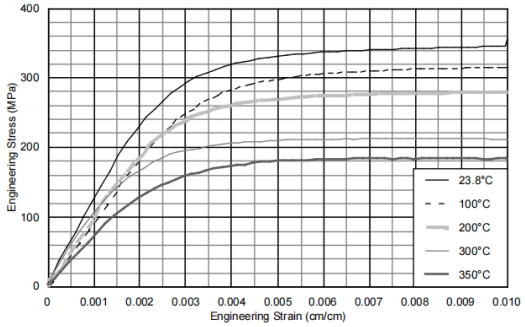

(b)

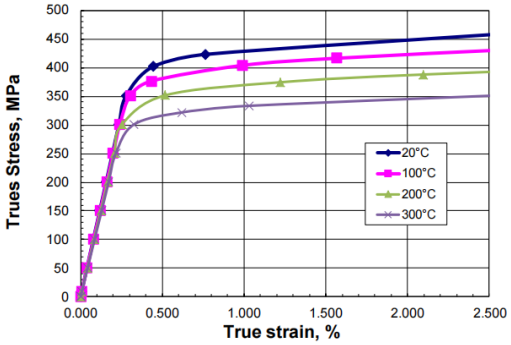

(c)

Figure 2.86: Experimental stress-strain curves at various T for (a) W, (b) Cu, (c) CuCrZr.

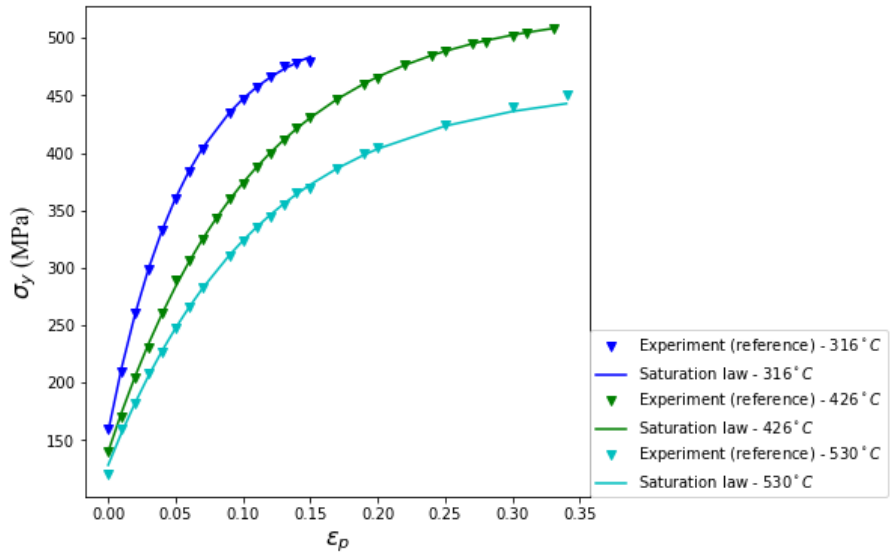
σ_y (MPa)
ε_p
Experiment (reference) - 316°C
Saturation law - 316°C
Experiment (reference) - 426°C
Saturation law - 426°C
Experiment (reference) - 530°C
Saturation law - 530°C

(a)

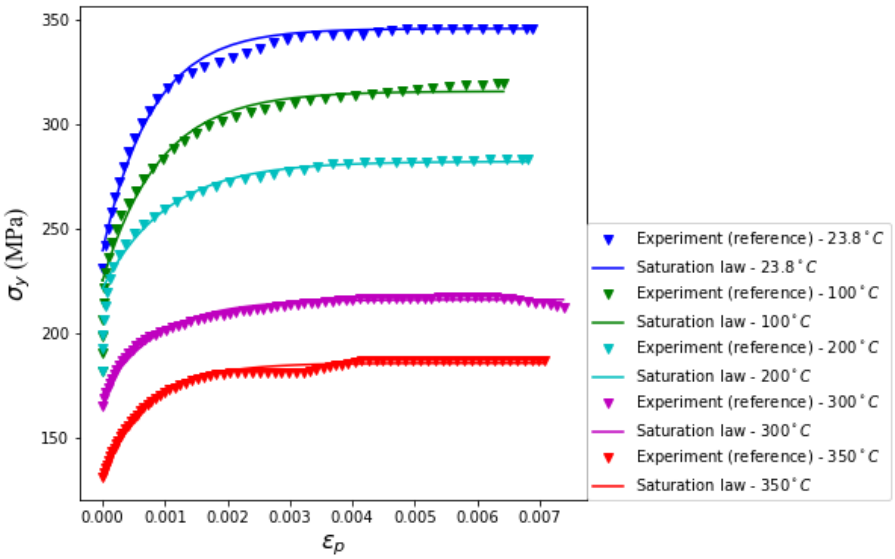
σ_y (MPa)
ε_p
Experiment (reference) - 23.8°C
Saturation law - 23.8°C
Experiment (reference) - 100°C
Saturation law - 100°C
Experiment (reference) - 200°C
Saturation law - 200°C
Experiment (reference) - 300°C
Saturation law - 300°C
Experiment (reference) - 350°C
Saturation law - 350°C

(b)

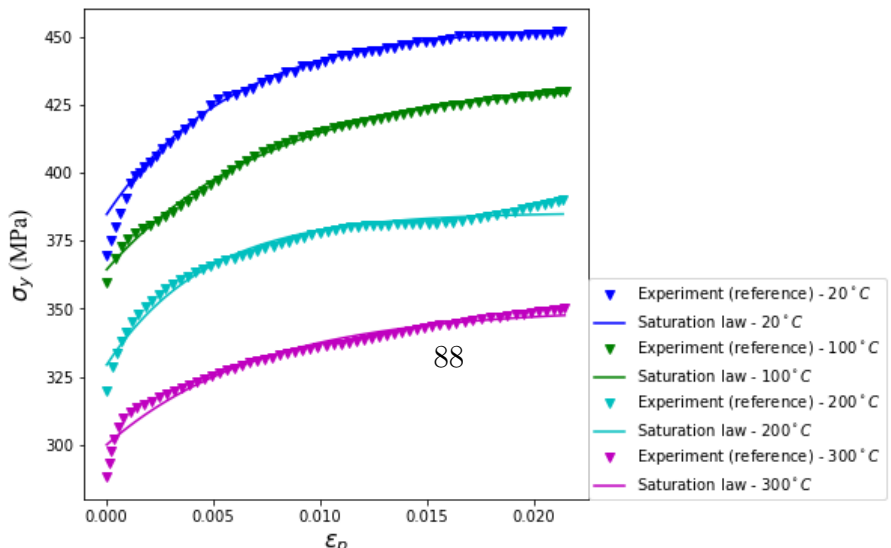
σ_y (MPa)
ε_p
Experiment (reference) - 20°C
Saturation law - 20°C
Experiment (reference) - 100°C
Saturation law - 100°C
Experiment (reference) - 200°C
Saturation law - 200°C
Experiment (reference) - 300°C
Saturation law - 300°C

2.5.4.3 Diffusion and trapping properties

The relevant hydrogen transport parameters for the three materials are described in this section and summarized in Tables 2.14 and 2.15. For the sake of clarity, their expressions are recalled below. The diffusion coefficient is

$$D_L = D_0 \exp\left(-\frac{E_m}{k_B T}\right) \tag{2.36}$$

where T is the temperature (in Kelvin), E_m the diffusion energy (in eV) and k_B the Boltzmann constant. The solubility S (see equation 2.19) is

$$S = S_0 \exp\left(-\frac{E_s}{k_B T}\right). \tag{2.37}$$

where E_s is the solution energy (in eV). The trapping and detrapping parameters are

$$\begin{cases} k = \frac{D_L}{l^2} \\ \\ p = \nu_0 \exp\left(-\frac{E_p}{k_B T}\right) \end{cases} \tag{2.38}$$

where l is the lattice constant, ν_0 the Debye frequency and E_p the detrapping energy.

Table 2.14: Diffusion parameters [144, 271–279]

Material	$D_0\,(m^2/s)$	$E_m\,(eV)$	S_0 $\left(\frac{atm}{mm^3\sqrt{MPa}}\right)$	$E_s\,(eV)$	N_L (atm/m^3)	V_H (mm^3/mol)
W	4.1×10^{-7}	0.2 (19.3 kJ/mol)	1.87×10^{18}	1.03	6.32×10^{28}	1700
Cu	6.6×10^{-7}	0.39 (37.4 kJ/mol)	3.14×10^{18}	0.572	8.49×10^{28}	1460
CuCrZr	3.9×10^{-7}	0.42 (40.37 kJ/mol)	4.28×10^{17}	0.4	2.61×10^{28}	1460

Table 2.15: Trapping parameters [141, 142, 144, 272, 275, 279, 280]

Material	$E_p\,(eV)$	$l\,(m)$	$\nu_0\,(s^{-1})$	$N_{T1}\,(traps/m^3)$ (intrinsic)	$N_{T2}\,(traps/m^3)$ (intrinsic)
W	0.87 | 1	$316.52\text{x}10^{-12}$	10^{13} | 10^{13}	$6.95\text{x}10^{25}$	$3.16\text{x}10^{25}$
Cu	0.5	$361.49\text{x}10^{-12}$	$8\text{x}10^{13}$	$4.25\text{x}10^{24}$	-
CuCrZr	0.85	$362.10\text{x}10^{-12}$	$8\text{x}10^{13}$	$1.30\text{x}10^{24}$	-

As the dislocations will evolve with loading time in monoblocks, and as they act as traps for hydrogen, it is mandatory to be able to get the evolution of their density with the macroscopic plastic strain ϵ_p. In [281], the effect of plastic strain on deuterium retention in tungsten by thermal desorption spectroscopy (TDS) has been investigated, from which a trap density evolution with plastic strain in tungsten have been proposed by [282], based to an inverse identification (see Figure 2.88):

$$N_{T2}^{created}(\epsilon_p) = 1.85 \times 10^{15}\left(1 - e^{-57.6\epsilon_p}\right) \qquad (traps/mm^3) \tag{2.39}$$

$$N_{T2} = N_{T2}^{intrinsic} + N_{T2}^{created} = 3.16 \times 10^{16} + 1.85 \times 10^{15}(1 - e^{-57.6\epsilon_p}) \qquad (traps/mm^3) \tag{2.40}$$

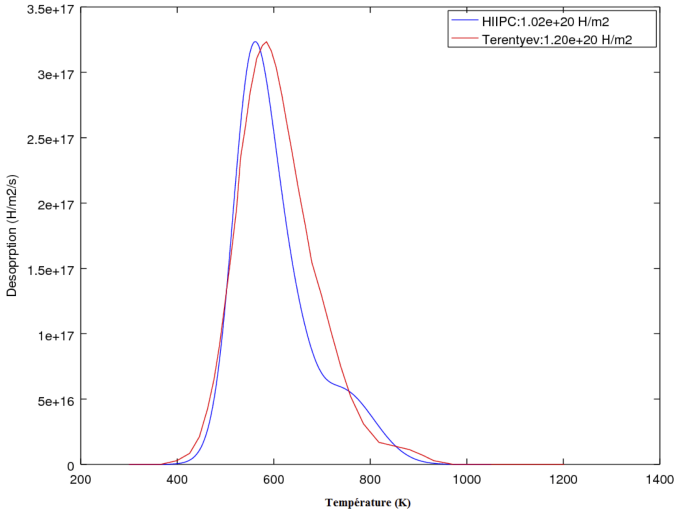

Figure 2.88: Comparison between the experimental TDS [282] and the numerical one based on equation 2.39

The evolution of $N_{T2}^{created}$ with plastic strain is plotted in Figure 2.89.

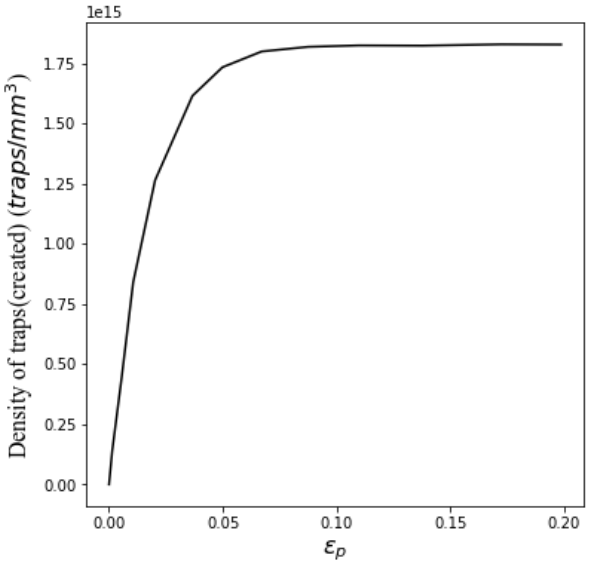

Figure 2.89: Evolution of density of dislocations created by plastic deformation in W (based on equation 2.39).

2.5.5 Comparison between Abaqus and FESTIM results

The aim of this part is to compare the results provided by FESTIM and Abaqus codes, on a monoblock configuration with the diffusion and trapping of H, but without any mechanical fields, for the sake of implementation validation. The concentration discontinuity, especially, will be focused on. First of all, the considered geometry, meshes, and boundary conditions are presented and then the results will be compared.

2.5.5.1 Geometry & Boundary conditions

The model is presented in Figure 2.90, thanks to the geometry symmetry, only 1/4 of the geometry is constructed. On symmetry planes, normal fluxes[2] $\boldsymbol{\varphi}.\boldsymbol{n}$ and normal displacement are set to zero. To mimic the presence of the other monoblocks (periodicity), the same kind of boundary conditions have been imposed on the cooling pipe section (i.e., the surface S_{pipe} in Figure 2.90).

[2]heat or diffusing hydrogen flux

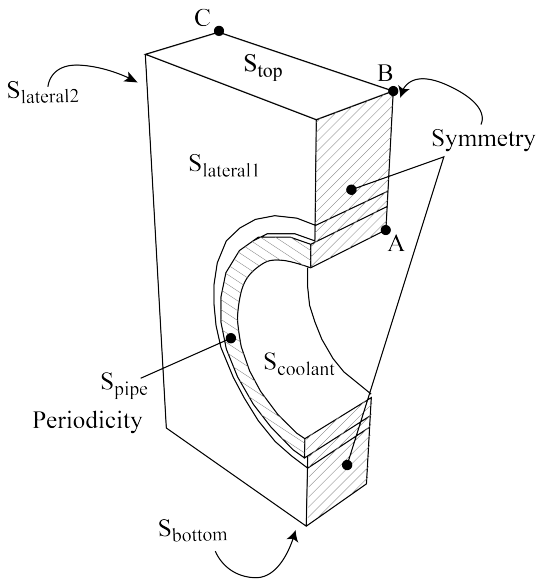

Figure 2.90: Geometry & Boundary conditions of monoblock.

All boundary conditions are summarized in Table 2.16. The top surface, being directly subjected to a plasma flow, experiences substantial heat and hydrogen fluxes. An equivalence between the hydrogen concentration $C_{L,surface}$, and the implantation particle flux φ_{imp}, has been utilized as follows [280, 283]:

$$C_{L,surface} = \frac{\varphi_{imp} R_p}{D_L(T)} \tag{2.41}$$

where R_p is the average implantation depth (set to $9.52\text{x}10^{-10}\, m$). φ_{imp} depends on the incident particles flux φ_{inc}, and on the reflection coefficient r [284]

$$\varphi_{imp} = (1 - r)\varphi_{inc} \tag{2.42}$$

φ_{inc} is set to $10^{24}\,\mathrm{m^{-2}s^{-1}}$, and r to 0.799 [285]. It is assumed that the temperature at the surface $\mathrm{S_{coolant}}$ matches the coolant temperature, which is T=323 K (refer to Table 2.16), thereby any effects of heat convection have not been taken into account at the cooling pipe.

Table 2.16: Boundary conditions applied to ITER monoblock

Surface	Heat	Hydrogen	Simulation time	Effects of mechanical fields
S_{top}	$T = 1000\,K$	$C_L = 3.8 \times 10^{20}$ atoms/m^3 (Equation 2.41)	$1.56 \times 10^5\,s$	No
$S_{coolant}$	$T = 323\,K$	$C_L = 0$		
$S_{lateral1}$	$(-\lambda \boldsymbol{\nabla} T) \cdot \boldsymbol{n} = 0$			
$S_{lateral2}$				
S_{bottom}				
S_{pipe}				

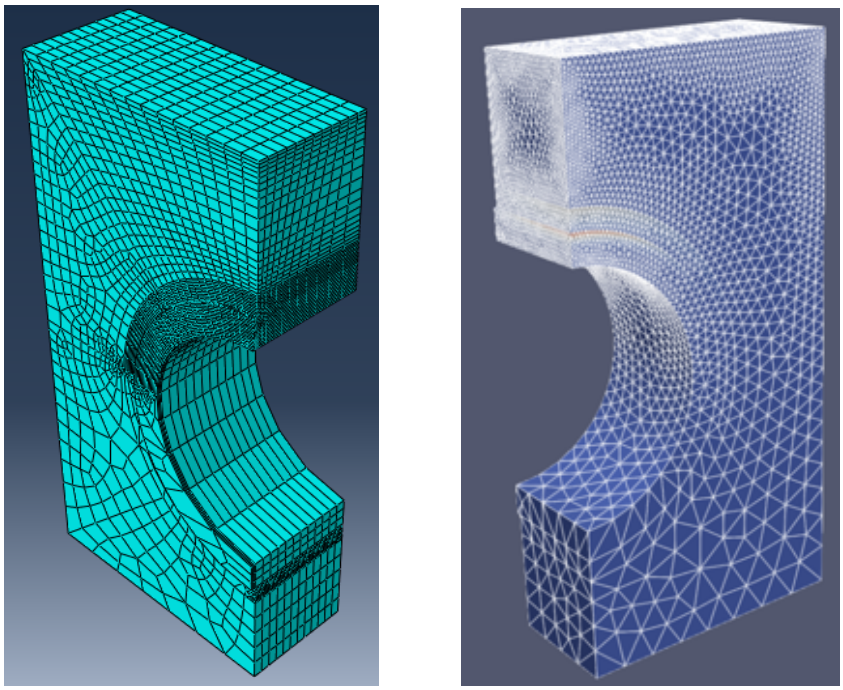

(a) (b)

Figure 2.91: (a) Abaqus and (b) FESTIM meshes.

Meshes are presented in Figure 2.91. The Abaqus model consists of 19266 full integration linear elements (C3D8T in Abaqus, Figure 2.91 (a)), while the FESTIM model contains

143790 linear triangular elements (Figure 2.91 (b)). The half-upper part of Cu layer and CuCrZr cooling pipe has been refined to get a compromise between computation time and the relevance of the computing results.

2.5.5.2 Results

To compare the results obtained by the two softwares, the evolution of different fields on the AB line (see Figure 2.90) has been plotted.

- **Heat transfer**:

  The temperature evolution has been compared on AB at the end of the computation (Figure 2.92).

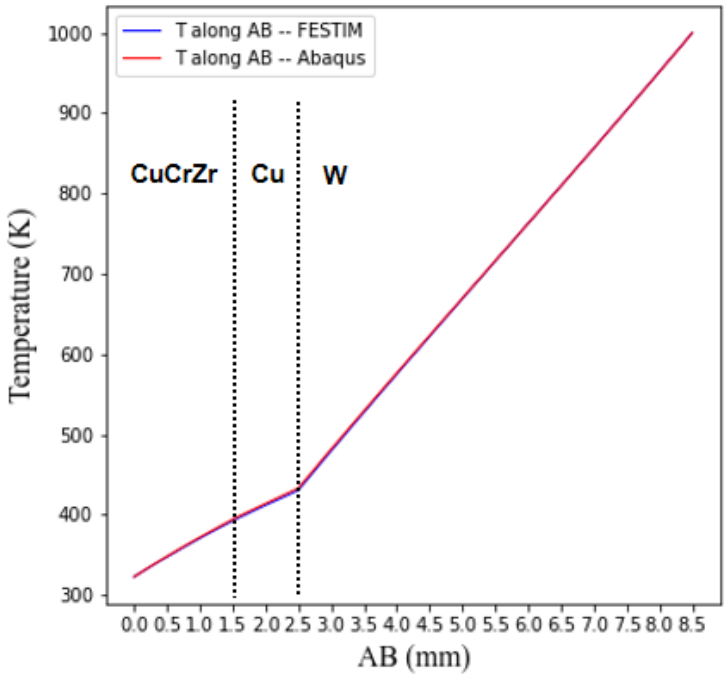

Figure 2.92: Temperature evolution along AB at the end of the computation (10^5 s).

It can be observed that both software provide the same solution. In each material, the temperature evolution is linear (due to steady state), but its slope depends on the material properties, to ensure the continuity of the normal heat flux.

- **Hydrogen transport and trapping**:

  The C_L/S evolution has been compared along AB, at the end of the computation (Figure 2.93).

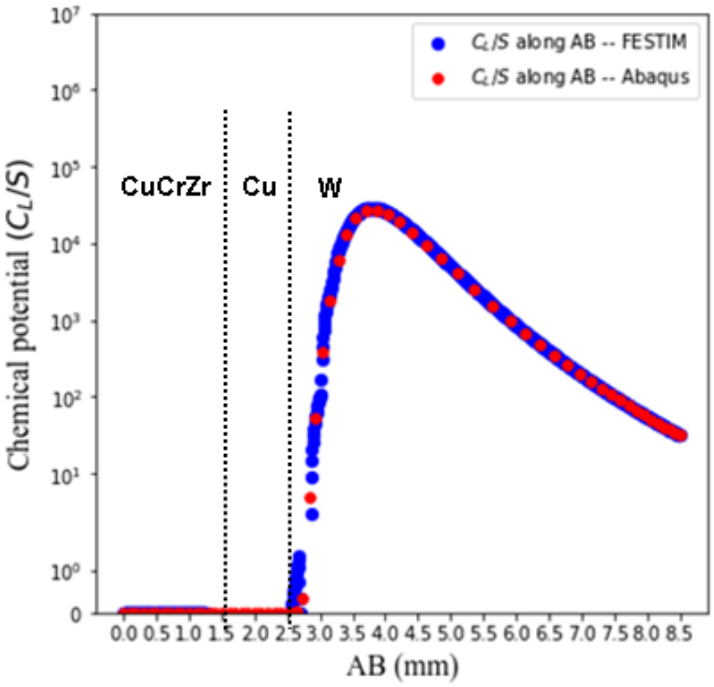

Figure 2.93: Chemical potential along AB at the end of the computation (10^5 s).

As expected, C_L/S is continuous along AB: this result is directly linked to the assumption that has been made during the implementation stage, i.e., C_L/S is a degree of freedom. Both codes provide the same result. The solubility evolution is presented in Figure 2.94: because of the temperature evolution, S evolves as well in each material, and is discontinuous at each material interface (a slight difference between Abaqus and FESTIM can be observed in the tungsten part).

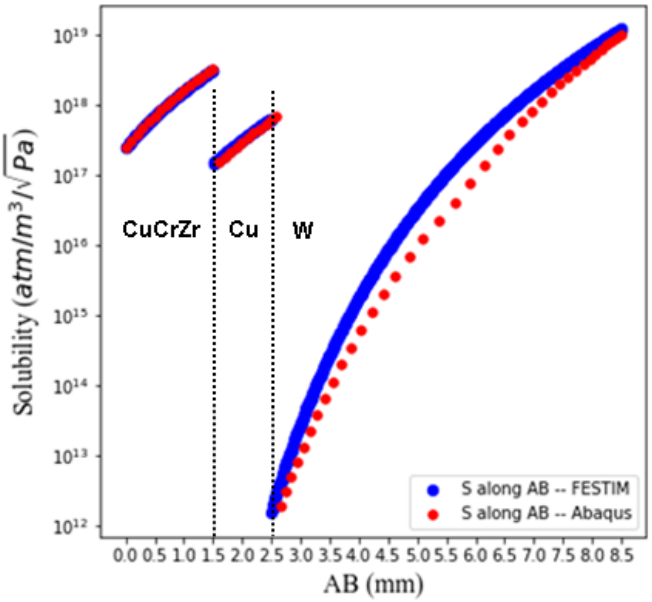

Figure 2.94: Solubility along AB at the end of the computation (10^5 s).

The C_L evolution is presented in Figure 2.95 for two cases:

* case one: only diffusion is included (no trapping), plotted in orange and green.

* case two: both diffusion and trapping are solved (plotted in blue and red).

From the curves of case 1, it can be observed the C_L discontinuity at each material interface (due to solubility variations), as expected. In case two, the diffusion process is too slow (because of trapping), and hydrogen can't reach the interface. In both cases, no differences between Abaqus and FESTIM can be observed.

This conclusion is also true while observing the C_T evolution along AB (Figure 2.96); H gets trapped only in the tungsten part. Finally, it can be concluded that the Abaqus implementation of C_L/S continuity is verified as it provides the same results as FESTIM.

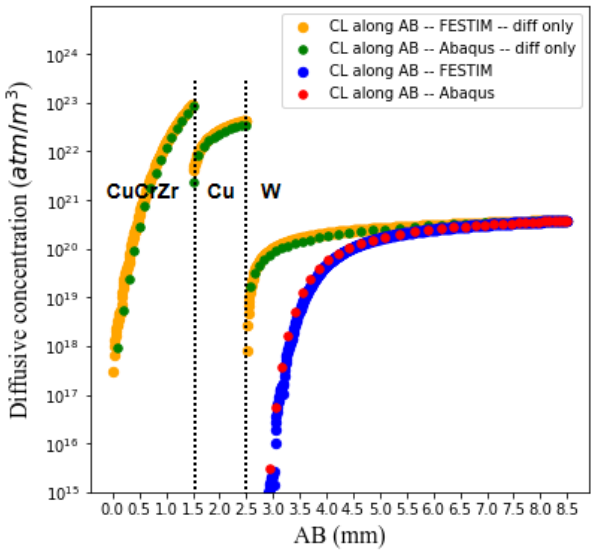

Figure 2.95: C_L evolution along AB at the end of the computation (10^5 s).

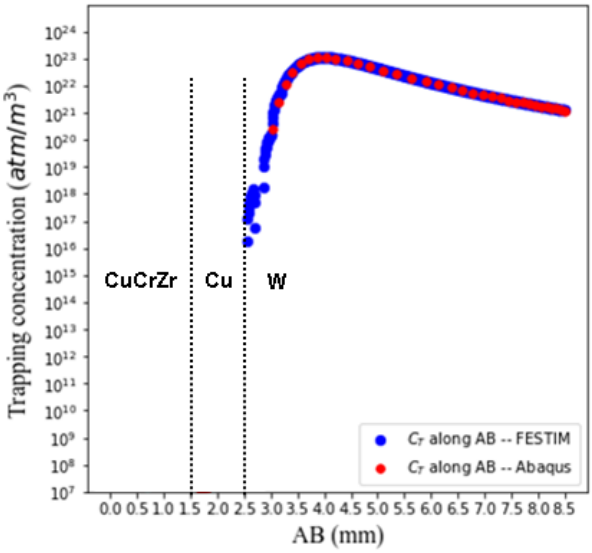

Figure 2.96: C_T evolution along AB at the end of the computation (10^5 s).

2.5.5.3 Mesh influence

In this part, the impacts of mesh size on H retention and on the required computation time are investigated. For the sake of simplicity, no trapping is considered and the total diffusing hydrogen quantity (Q_L) is checked. Results can be seen in Figure 2.97 for FESTIM and Figure 2.98 for Abaqus, and the computation time is presented in Table 2.17.

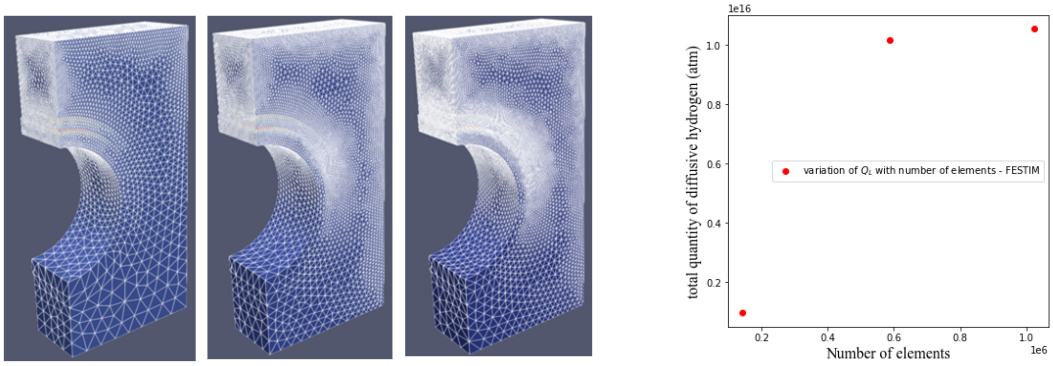

(a) (b)

Figure 2.97: FESTIM: (a) Model discretization with three different meshes: 143790 / 586047 / 1022600 elements, (b) Q_L evolution with the number of elements.

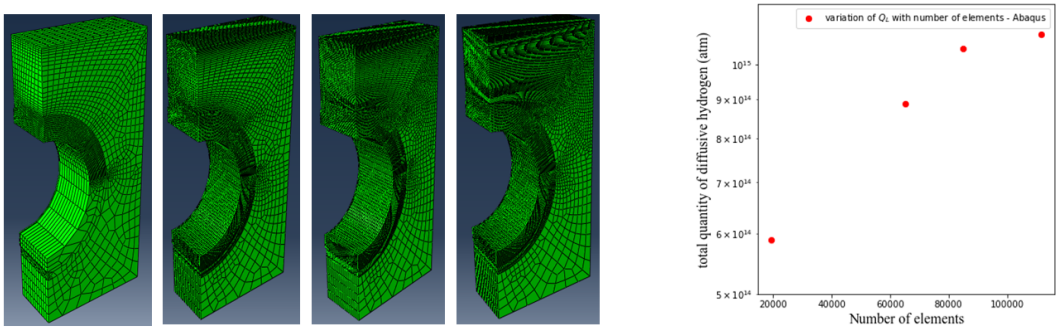

(a) (b)

Figure 2.98: Abaqus: (a) Model discretization with four different meshes: 19266 / 65202 / 84786 / 111714 elements, (b) Q_L evolution with the number of elements.

For both softwares, it can be observed that Q_L converges towards a saturating value (1.1×10^{16} for FESTTIM and 6.8×10^{15} for Abaqus) when the number of element increases, and this

value can be estimated by 1022600 elements for FESTIM and 111714 elements for Abaqus. This differences in term of element number for convergence can be sourced from the element used: linear pyramids in FESTIM (1 Gauss integration point) and linear full integration brick elements in Abaqus (8 Newton-Cotes integration points, adapted for diffusion problems in the 'coupled temp-displacement analysis').

The increase of the number of elements leads to a non negligible increase of the computation time, as listed in Table 2.17 for Abaqus, in conjunction with the Q_L value evolution: between 19266 and 65202 elements (i.e., $\times 3.4$), the computation time increased by a factor of 7.5 and the Q_L value increased by 34%. Between 65202 and 84786 elements, computing time increased by 60% and 15% for Q_L.

Table 2.17: Comparison of computation time and relevant error of amount of diffusing H based on different numbers of elements.

Abaqus - diffusion only		
Number of elements	t	Relevant error of Q_L
19266	0.8h	34% (19266 $\longrightarrow$ 65202)
65202	6h	15% (65202 $\longrightarrow$ 84786)
84786	9.5h	4% (84786 $\longrightarrow$ 111714)
111714	15h	-

For the sake of efficiency, the sparsest mesh (19266 elements) is chosen as the reference mesh for all following simulations.

2.5.6 ITER plasma operations: reference case

In this part, a loading reference case is defined for the monoblock. This reference case contains the scenario of thermal and H-related loading (plasma exposure). The material properties used are the ones provided by **IMPH** [269] (detailed in previous sections).

2.5.6.1 Scenario

The simulation scenario consists of three phases, which are continuous plasma loading phase (Phase 1), baking phase (Phase 2) and maintenance phase (Phase 3), respectively (see Figures

2.99 and 2.100). A temperature of 373K is imposed on $S_{coolant}$, a heat flux as well as a concentration, corresponding to $\varphi_{imp} = 0.201 \times 10^{24}\, H.m^{-2}s^{-1}$ (equation 2.41) on the surface S_{top}. The duration of Phase 1 is 156000 s, a time that has been estimated by assuming a scenario of thirteen 25s-pulses per day during 16 months (160 cycles, i.e. 3 days as a cycle). This scenario of plasma loading doesn't necessarily reflect the operational ITER plasma loadings. For more precise details, refer to [286]. Phase 2 and Phase 3 are described in detail thereafter.

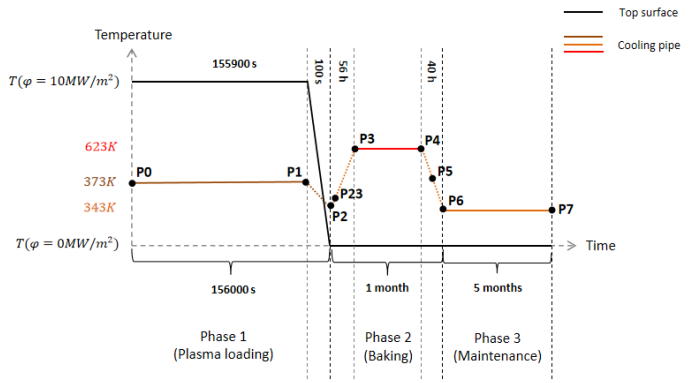

Figure 2.99: Thermal flux φ_{heat} on S_{top} due to the plasma exposure & temperature variation of cooling pipe.

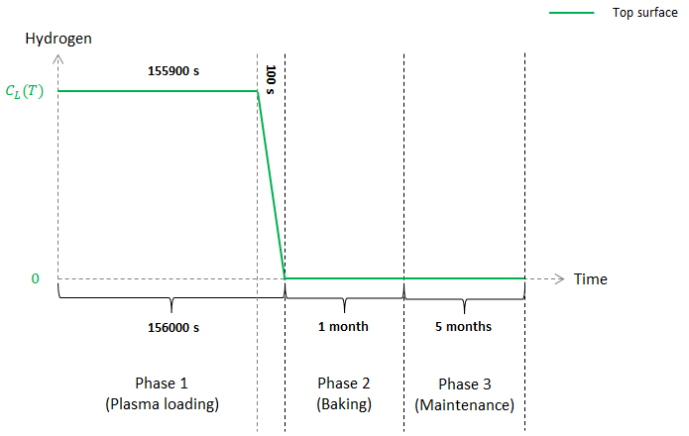

Figure 2.100: C_L value at the S_{top} due to the plasma exposure.

The evolution of the temperature on $S_{coolant}$ is as follows:

- **P0 to P1**: constant temperature, equal to 373 K;
- **P1 to P2**: linear decrease within 100 s for the temperature from 373 K to 343 K. During this stage, the heat flux on the S_{top} decreases linearly as well (that can be useful for convergence issues);
- **P2 to P3**: linear increase of the temperature of the cooling pipe, up to 623 K with an imposed ramp of 5°C/h (achieved within 56 h);
- **P3 to P4**: the rest of 1 month-baking Phase for a constant baking temperature of the cooling pipe, equal to 623 K;
- **P4 tp P6**: linear decrease of the temperature of the cooling pipe, down to 343 K with an imposed ramp of 7°C/h (achieved within 40 h);
- **P6 to P7**: constant temperature (343 K) throughout 5 months.

2.5.6.2 Thermomecanical fields

In Figure 2.101 are presented the hydrostatic stress fields P_H at points P1, P2, P3, and P6. During Phases 1 and 2, the monoblock appears to be globally in compression (i.e., $P_H = -1/3\,\mathrm{tr}\,\boldsymbol{\sigma} > 0$), due to the competition between the boundary conditions (symmetry and periodicity) and the thermal expansion (see Figure 2.102a for the temperature fields at P1).

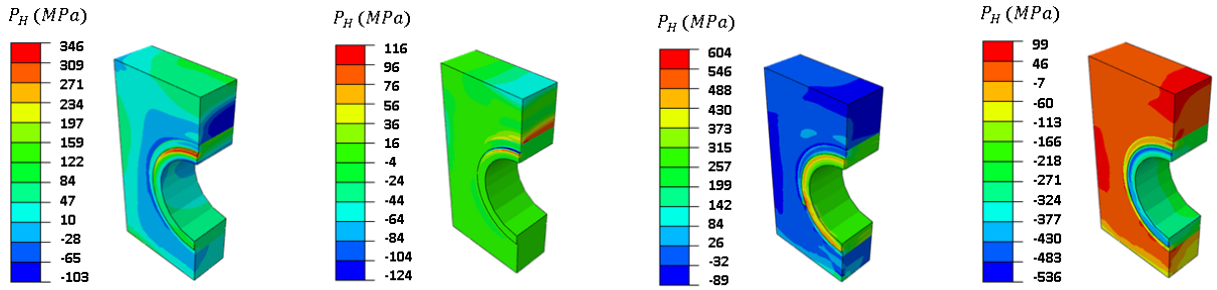

(a) (b) (c) (d)

Figure 2.101: P_H fields at points (a) P1, (b) P2, (c) P3, (d) P6.

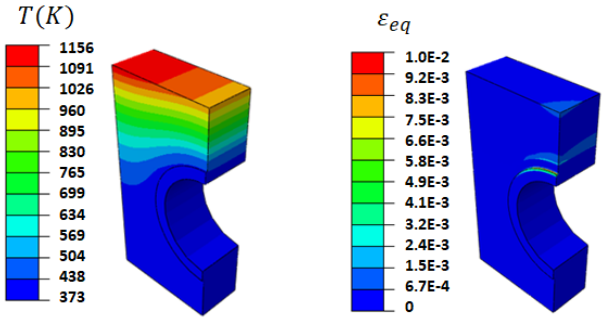

Figure 2.102: (a) Temperature, (b) equivalent plastic strain field at P1.

This compression has a direct effect on hydrogen diffusion, which is slowed in compressed areas, and accelerated in tensile ones. It is worth to point out that at each time point of the scenario, there is an important variation in P_H field at bi-material interfaces, inducing tensile areas at P1, and compressed ones at P2.

The other impact of P_H is the creation of plasticity (see Figure 2.102b), which is localized to S_{top}, where the thermal expansion is maximum, and to the bi-material interfaces. This last point is an important issue of elastoplastic materials assembly under thermal loadings [287]. It has been shown that, depending on the interface geometry and on the thermal loadings, singular mechanical fields can appear (known as "spine singularity"), inducing very high stresses, and thus, plasticity.

During Phase 3, the monoblock is roughly in tension, accelerating the hydrogen transport. Last, the increase of plastic strain leads to an increase of the dislocation-related trap density, as illustrated in Figure 2.104 at point B (see Figure 2.90 for its location), i.e. both on the symmetry planes and on the exposed surface. As it can be observed, the impact of plasticity on the evolution trap density is very limited.

2.5.6.3 H retention and permeation

In Figure 2.103 presents the evolution of hydrogen retention during all phases: we observe that between P1 and P2, the H retention increased by a factor of over ten in just 100 s, indicating a computational instability. Furthermore, the mesh quality is also one of the important factors influencing the numerical results.

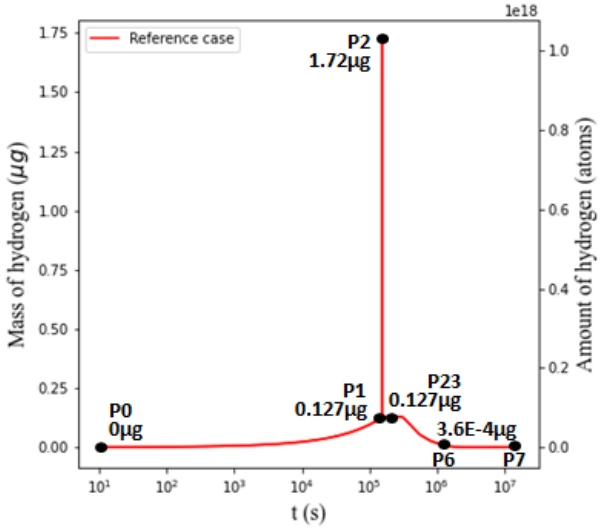

(a)

Figure 2.103: H retention evolution in 1/4 monoblock with time.

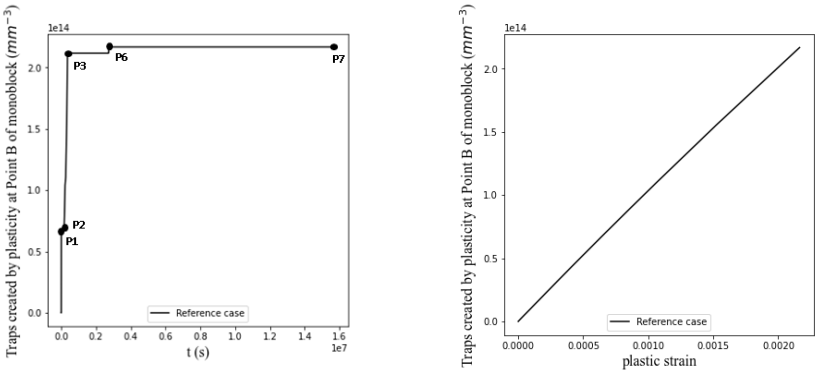

(a) (b)

Figure 2.104: (a) Temporal evolution of plasticity-induced trap density at point B (see Figure 2.90), (b) Relationship between trap density and equivalent plastic strain

During Phase 1, spanning from P0 to P2, hydrogen enters the monoblock via S_{top} and diffuses towards the hydrogen-free zone, which is oriented towards the cooling pipe. As a result, the cumulative hydrogen content within the monoblock grows over time, as illustrated in Figures 2.105 (a) and 2.105 (b). However, the movement of hydrogen is impeded at the W/Cu bi-material interface, as depicted in Figure 2.106a. The assumption of C_L/S continuity results in a pronounced elevation of C_L transitioning from W to Cu. This is because, at 400 K, Cu has a significantly higher solubility for hydrogen compared to W. This temperature is approximately the interface temperature at the conclusion of Phase 1, as shown in Figure 2.106b.

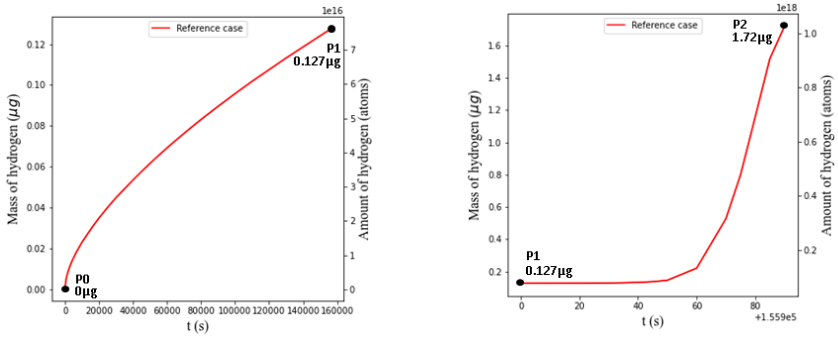

(a) (b)

Figure 2.105: Evolution of (a) H retention evolution between P0 $\sim$ P1, (b) H retention evolution between P1 $\sim$ P2.

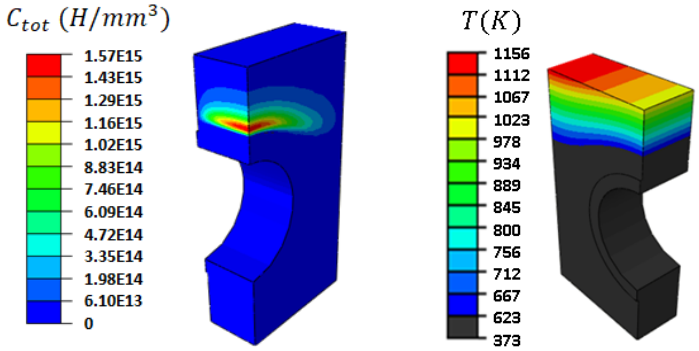

(a) (b)

Figure 2.106: (a) C_{tot} and (b) T distribution at P1.

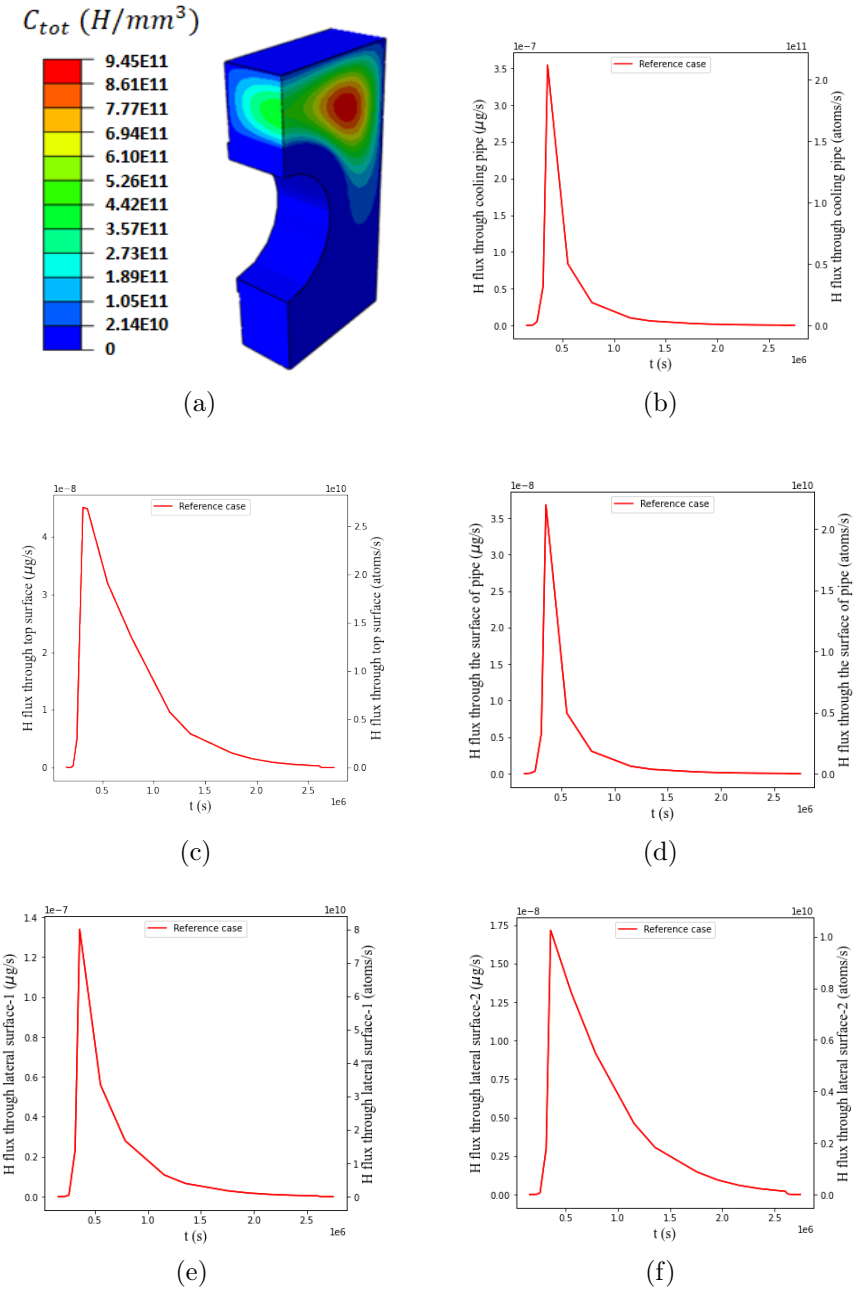

Figure 2.107: (a) C_{tot} distribution at the end of Phase 2 (P6). Evolution with time during Phase 2 of the H flux through the surfaces (1/4 of the monoblock) : (b) $S_{coolant}$, (c) S_{top}, (d) S_{pipe}, (e) $S_{lateral1}$, (f) $S_{lateral2}$.

During Phase 2 (P2 $\sim$ P6), the monoblock's temperature is homogeneous (and equal to 623 K); as hydrogen particle flux is no longer imposed, desorption occurs, leading to detrapping. This desorption takes place through all outer monoblock surfaces. When focusing on the cooling pipe (Figure 2.107b), a desorption peak can be observed at the beginning of Phase 2, then a steep decrease. The desorption through the other surfaces are also presented in Figures 2.107c, 2.107d, 2.107e and 2.107f. At the end of Phase 2, hydrogen is mainly located in the center of the tungsten part (Figure 2.107a), with a level much lower than the one at the end of Phase 1 ($9.45.10^{11}\ H/mm^3$ versus $1.57.10^{15}\ H/mm^3$).

During Phase 3 (P6 $\sim$ P7), no modification of hydrogen retention or distribution in the sample is observed (see Figures 2.108a and 2.108c). As a consequence, the permeation towards the cooling pipe remains very low (near zero), as can be seen in Figure 2.108b).

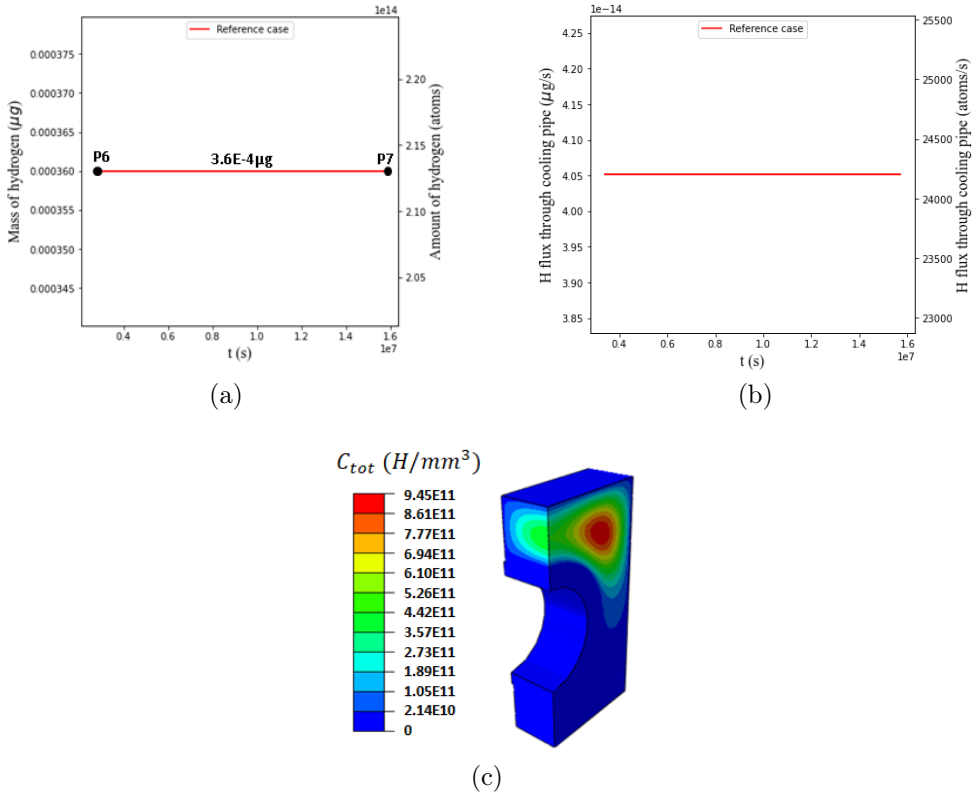

Figure 2.108: Evolution of time during Phase 3 of (a) H retention, (b) H flux through the cooling pipe, and (c) C_{tot} distribution at P7 (1/4 monoblock).

2.5.6.4 Discussion

All the results regarding the H retention in the quarter of monoblock are summarized in Table 2.18.

Table 2.18: Total H retention in the quarter of monoblock

Unit: μg	Phase 1 (P1)	Phase 2 (1 week)	Phase 2 (2 weeks)	Phase 2 (P6)	Phase 3 (P7)
H retention	0.127	0.029	0.0069	3.6×10^{-4}	3.6×10^{-4}
Δm from end of Phase 1		0.098 (77%)	0.1201 (95%)	0.12664 (99.7%)	0.12664 (99.7%)
H permeation through $S_{coolant}$		0.05 (51.2%)	0.057 (47.5%)	0.05851 (46.2%)	0.05851 (46.2%)
H permeation through S_{top}		0.014 (14%)	0.0192 (16%)	0.02102 (16.6%)	0.02102 (16.6%)
H permeation through S_{pipe}		0.005 (5.2%)	0.0058 (4.8%)	0.00595 (4.7%)	0.00595 (4.7%)
H permeation through $S_{lateral1}$ and $S_{lateral2}$		0.029 (29.6%)	0.029 (31.7%)	0.04166 (32.5%)	0.04166 (32.5%)

It can be assumed that only for H transport, continuous exposure is more or less equivalent to cyclic exposure, because the H transport will be frozen when the plasma pulse is off [288]. The retention at the end of Phase 1 must be close to the retention at the end of plasma operations.

At the end of Phase 1, the retention in the quarter of a monoblock is 0.127 µg. The total number of MBs is actually 292,000: Each divertor cassette has 16 PFUs on the inboard (with 138 MBs/PFU) and 22 PFUs on the outboard (with 143-146 MBs/PFU). By generalizing to the entirety of MBs (which is a very strong assumption, as the plasma exposure is not the same everywhere), we found a total inventory of 148 mg ($0.127 \times 4 \times 292000$). However, we assume that only a few MBs per PFU receive the full loads, so 19008 is plausible (352 MBs per CA, CA=54), and we found a total inventory of 9.7 mg ($0.127 \times 4 \times 54 \times 352$). Differences are due to the plasma exposure difference. This point is discussed later, in the parametric study section dedicated to the plasma flux values impact.

Because the hydrogen is restrained mainly in a zone where the temperature is lower than the baking temperature, it is easy to desorb it. That is why nearly all the hydrogen is desorbed during the baking Phase: only 0.3% of the retention is still in the monoblock after baking. Around 46.2% of the mass passes through the cooling tube. Last, it can be observed that the fraction of H flowing out through the cooling pipe during the Phase 2 is not linear: after 1 week, there is still 51.2% and 47.5% after 2 weeks. Because the temperature of the Phase

2 is lower than the baking temperature (343 K versus 623 K), no H transport happens. A small amount of hydrogen always remains in the monoblock during the maintenance stage, the main part being located in the middle top of the monoblock.

2.5.6.5 Parametric study

In this part, the impact of boundary conditions used in the reference scenario on the H retention and permeation is investigated. The following boundary conditions are considered:

1. the baking temperature T_{baking} (Phase 2).
2. the temperature of cooling pipe $T_{cooling\,pipe}$ during Phase 1.
3. the heat and particle fluxes on S_{top}.
4. the mechanical fields (water pressure on $S_{coolant}$, thermal expansion).
5. H desorption on S_{top}.

- Impact of the baking temperature:

  Two temperatures are considered in this part: 573 K and 513 K, instead of 623 K. In Figure 2.109a is plotted the evolution of the total hydrogen content in the sample with time, as a function of T_{baking}, considering the same Phase 1. Different H retention is reported in Table 2.19 as well, for the sake of comparison.

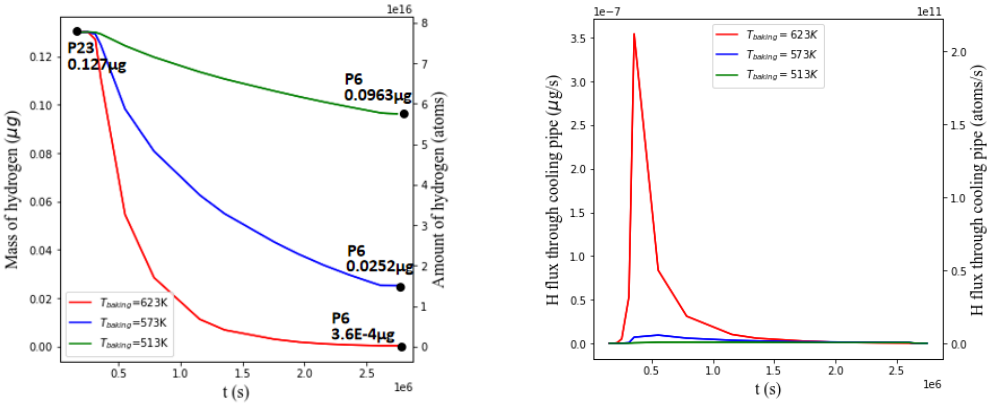

(a) (b)

Figure 2.109: Evolution with time during Phase 2 (P2 $\sim$ P6) of (a) H retention and (b) H permeation through the cooling pipe for T_{baking}=623, 573 and 513 K (1/4 monoblock).

It can be observed that a decrease of T_{baking} leads to an increase in hydrogen retention. This can be explained by the decrease of hydrogen diffusivity with T, plus an increase of detrapping. This diffusivity modification with T induces a decrease of the permeation towards the cooling pipe when T_{baking} decreases (Figure 2.109b), as diffusion in the Cu and CuCrZr parts becomes slower and slower.

Table 2.19: Total H retention in the quarter of monoblock

Unit: μg	Phase 1 (P1)	Phase 2 (1 week)	Phase 2 (2 weeks)	Phase 2 (P6)	Phase 3 (P7)	T_{baking}
H retention	0.127	0.029	0.0069	$3.6 \cdot 10^{-4}$	$3.6 \cdot 10^{-4}$	623K (Reference case)
Δm from end of Phase 1		77%	95%	99.7%	99.7%	
H retention	0.127	0.081	0.055	0.0252	0.0252	573K
Δm from end of Phase 1		36%	57%	80%	80%	
H retention	0.127	0.12	0.11	0.0963	0.0963	513K
Δm from end of Phase 1		6%	13%	24%	24%	

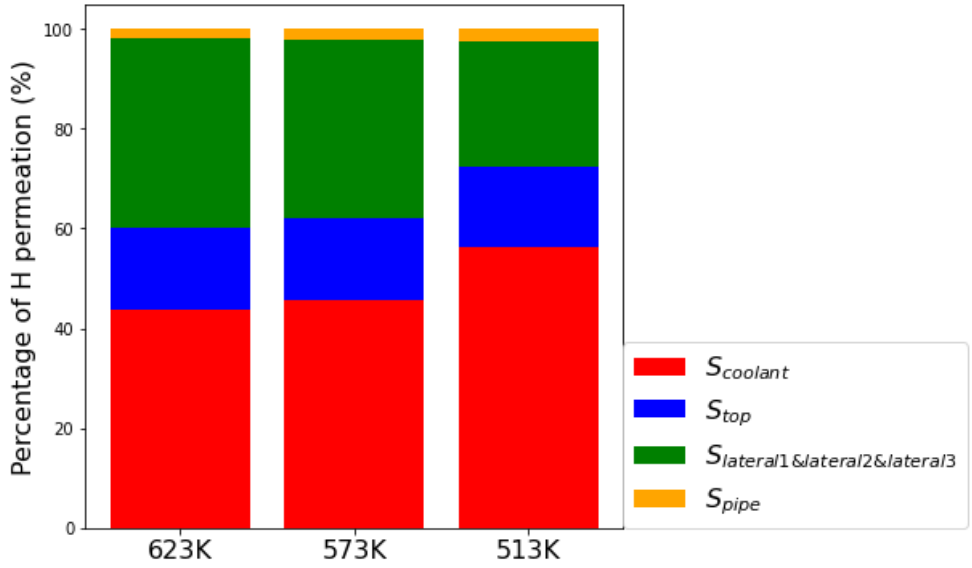

(a)

Figure 2.110: Percentage of H permeation towards different surfaces.

In Figure 2.110, the distribution of H permeation towards different surfaces (see Figure 2.90) is depicted. We can see that at $T_{baking} = 623\,K$, the H permeation towards the cooling pipe is minimized in comparison to the situations at $T_{baking} = 573\,K$ and $T_{baking} = 513\,K$.

- Impact of the cooling pipe temperature during Phase 1:

  In this part, $T_{cooling\,pipe}$ =343 K is considered instead of 373 K for the reference scenario. For the two $T_{cooling\,pipe}$ values, the evolution with time of the H retention during Phase 1 and 2 are plotted in Figures 2.111a and 2.111c, respectively, while in Figure 2.111e is presented the H permeation through the cooling pipe during Phase 2. Table 2.20 summarized the evolution of the H retention during the whole scenario, for the two cooling pipe temperatures.

Table 2.20: Total H retention in the quarter of monoblock

Unit: μg	Phase 1 (P1)	Phase 2 (1 week)	Phase 2 (2 weeks)	Phase 2 (P6)	Phase 3 (P7)	$T_{coolingpipe}$
H retention	0.127	0.029	0.0069	$3.6 \cdot 10^{-4}$	$3.6 \cdot 10^{-4}$	373K (Reference case)
Δm from end of Phase 1		77%	95%	99.7%	99.7%	
H retention	0.127	0.0381	0.0092	$4.8 \cdot 10^{-4}$	$4.8 \cdot 10^{-4}$	343K
Δm from end of Phase 1		70%	93%	99.6%	99.6%	

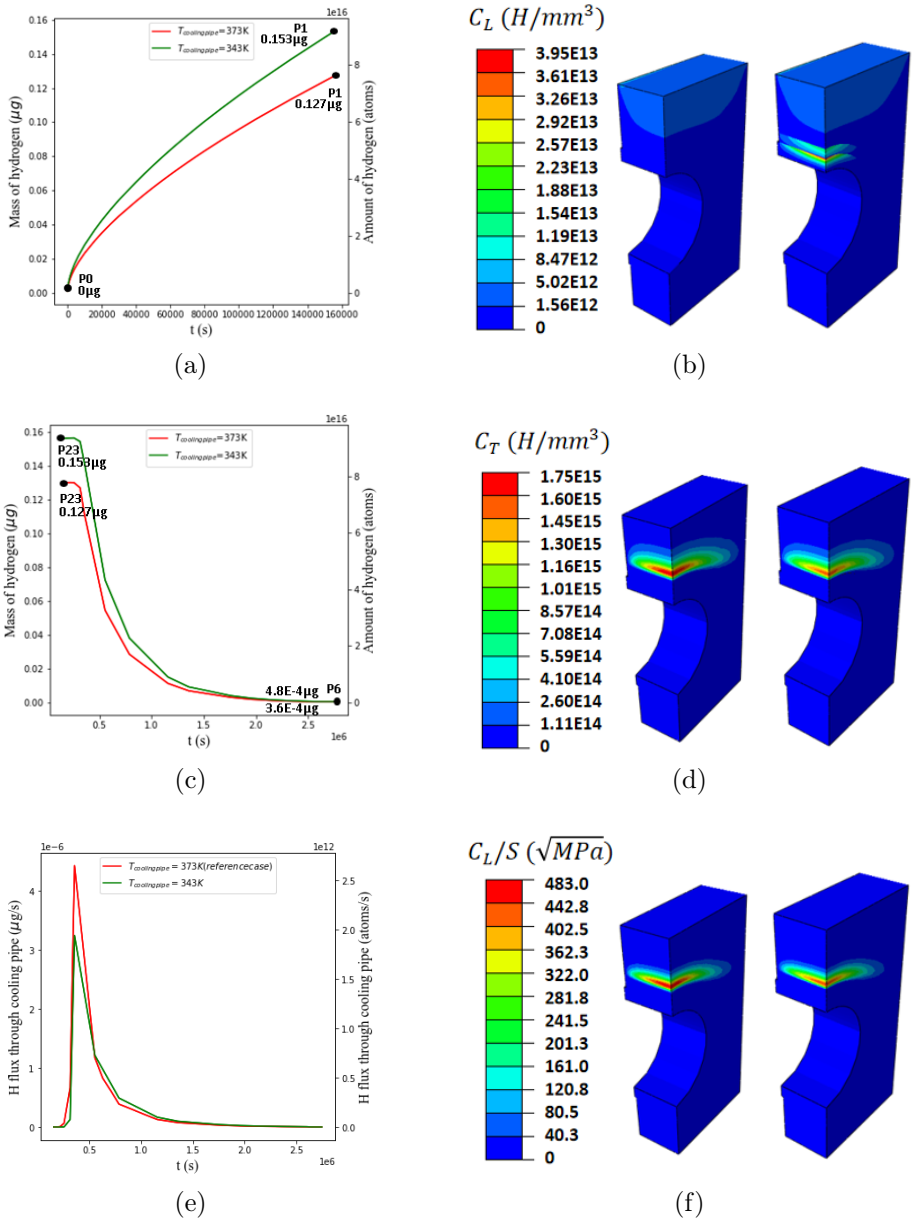

Figure 2.111: For the two $T_{cooling\,pipe}$ values, evolution with time of the H retention during (a) Phase 1, (c) Phase 2, (e) Evolution with time of H permeation through the cooling pipe during Phase 2, (b) C_L, (d) C_T, and (f) C_L/S distributions at P1: $T_{cooling\,pipe}$ =343 K (left), and 373 K (right) (1/4 monoblock).

A decrease of $T_{cooling\,pipe}$ induces an increase of H retention during Phase 1, which is not intuitive as a decrease of T induces a decrease of hydrogen transport parameters: it could have been expected, consequently, a decrease of H retention (and it is observed for C_L - see Figure 2.111b). However, a decrease of T induces as well a decrease of the detrapping process: in Figure 2.111d, it can be observed that C_T is greater for the lower $T_{cooling\,pipe}$ value, and that $C_T >> C_L$.

- Impact of the heat and particle fluxes during Phase 1:

  During Phase 1, φ_{inc} is set to 10^{23}, 10^{22} and 10^{20} ($m^{-2}s^{-1}$), and compared to the reference configuration ($\varphi_{inc} = 10^{24}\ m^{-2}s^{-1}$). As heat flux is related to particle flux [285], a modification of the former is also imposed:

  * $\varphi_{inc} = 10^{24}\,H/m^2/s \longrightarrow \varphi_{th} = 10\,MW/m^2$ (reference case)
  * $\varphi_{inc} = 10^{23}\,H/m^2/s \longrightarrow \varphi_{th} = 0.5\,MW/m^2$
  * $\varphi_{inc} = 10^{22}\,H/m^2/s \longrightarrow \varphi_{th} = 0.3\,MW/m^2$
  * $\varphi_{inc} = 10^{20}\,H/m^2/s \longrightarrow \varphi_{th} = 0.1\,MW/m^2$

  For all the various φ_{inc} are plotted in Figure 2.112a and 2.112b the evolution with time of the H retention during Phase 1 and 2 respectively, and in Figure 2.112c is presented, during Phase 2, the H flux toward the cooling pipes. In Table 2.21 are summarized the evolution of the H retention during the whole scenario, for the φ_{inc} values. Table 2.22 gives the retention values at the end of Phase 1 by generalizing to the entirety of divertor (which is a very strong assumption, as the plasma exposure is not the same everywhere).

Table 2.21: Total H retention in the quarter of monoblock

Unit: μg	Phase 1 (P1)	Phase 2 (1 week)	Phase 2 (2 weeks)	Phase 2 (P6)	Phase 3 (P7)	Particle flux
H retention	0.127	0.029	0.0069	$3.6 \cdot 10^{-4}$	$3.6 \cdot 10^{-4}$	$10^{24} m^{-2} s^{-1}$ (Reference case)
Δm from end of Phase 1		77%	95%	99.7%	99.7%	
H retention	3.4	0.0386	0.0088	$4.6.10^{-4}$	$4.6.10^{-4}$	$10^{23} m^{-2} s^{-1}$
Δm from end of Phase 1		98.9%	99.7%	99.9%	99.9%	
H retention	1.66	0.00383	0.00088	$4.6.10^{-5}$	$4.6.10^{-5}$	$10^{22} m^{-2} s^{-1}$
Δm from end of Phase 1		99.8%	99.9%	99.99%	99.99%	
H retention	0.57	$2.79.10^{-5}$	$3.46.10^{-6}$	0	0	$10^{20} m^{-2} s^{-1}$
Δm from end of Phase 1		99.99%	99.99%	100%	100%	

For the smallest φ_{inc} value ($10^{20}\, H/m^2/s$), the surface temperature does not allow an important hydrogen penetration in the monoblock (Figure 2.114); H inventory remains time-independent (Figure 2.112a), and (quite) no desorption to the cooling pipe is observed during Phase 2 (Figure 2.112c). An increase of φ_{inc} ($10^{22}\, H/m^2/s$ and $10^{23}\, H/m^2/s$) is concomitant with a surface temperature increase and thus, a D_L increases: H concentration near S_{top} increases (Equation 2.41) and H goes deeper in the monoblock. As a consequence, H inventory at the end of Phase 1 increases (Figure 2.112a). For $\varphi_{inc} = 10^{23}\, H/m^2/s$, H inventory evolution with time increases as H goes deeper and deeper in the component. However, further increase of φ_{inc} is linked to an important variation of temperature (Figure 2.113): the C_L value at the surface S_{top} thus decreases (Equation 2.41, see Table 2.23), as does the H inventory. Trapping is limited and located near the cooling pipe.

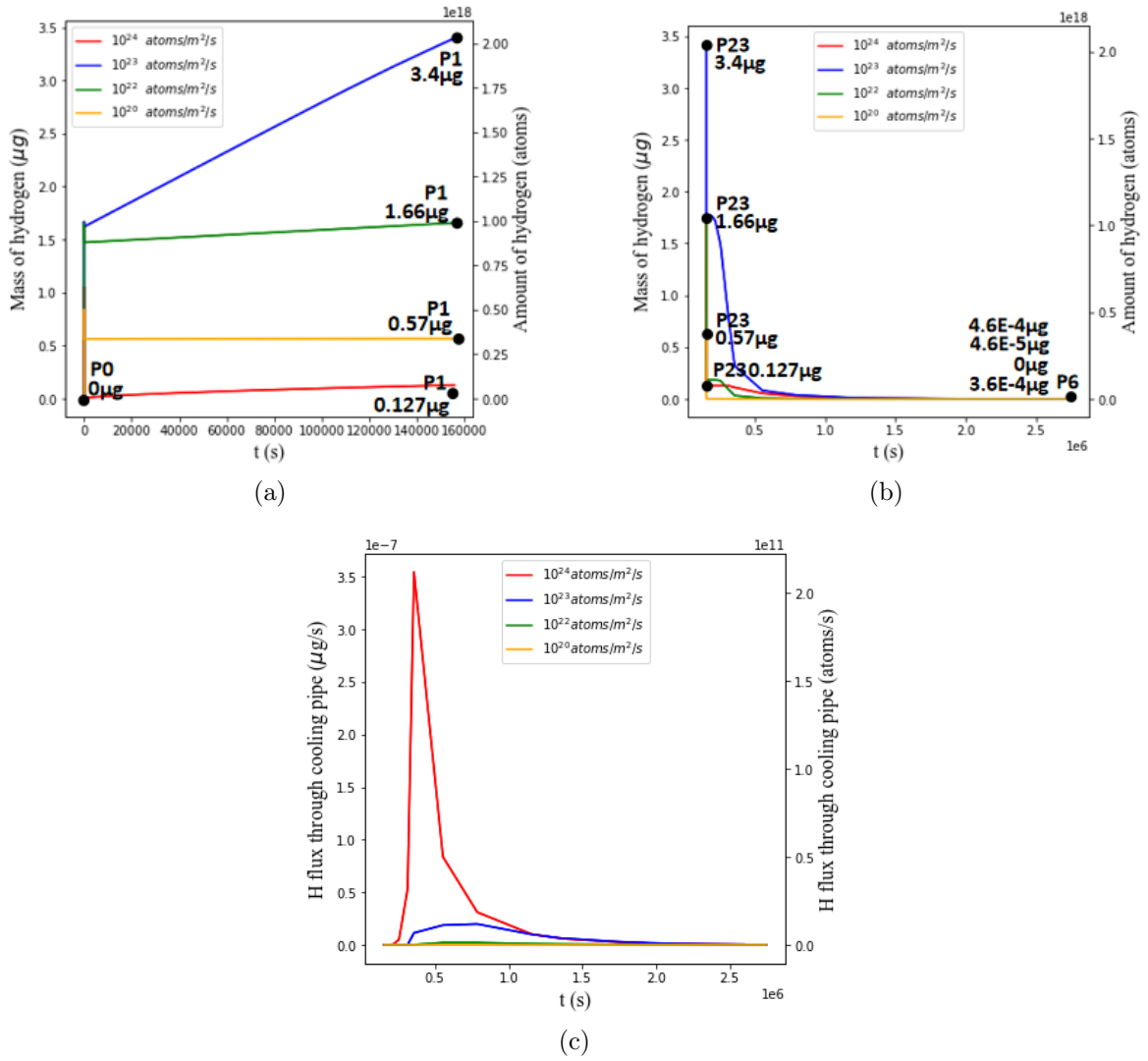

Figure 2.112: H retention evolution with time during (a) Phase 1, (b) Phase 2, (c) evolution of H flux through cooling pipe with time during Phase 2 (1/4 monoblock).

Table 2.22: Total H inventory in all the divertor (at the end of Phase 1) under different particle fluxes.

particle flux $(m^{-2}s^{-1})$	Q_{tot} (mg) (local MBs exposure)	Q_{tot} (mg) (full MBs exposure)
10^{24} (Reference case)	9.7	148
10^{23}	259	3971
10^{22}	126	1939
10^{20}	43	666

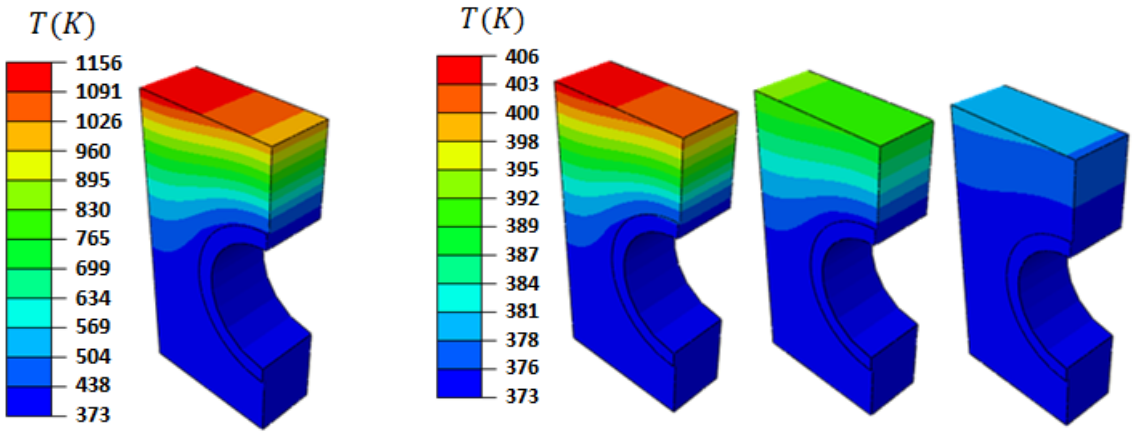

(a) (b)

Figure 2.113: Temperature field at P1 for φ_{inc} equal to (a) 10^{24}, (b) 10^{23} & 10^{22} & 10^{20} $H/m^2/s$ (1/4 monoblock).

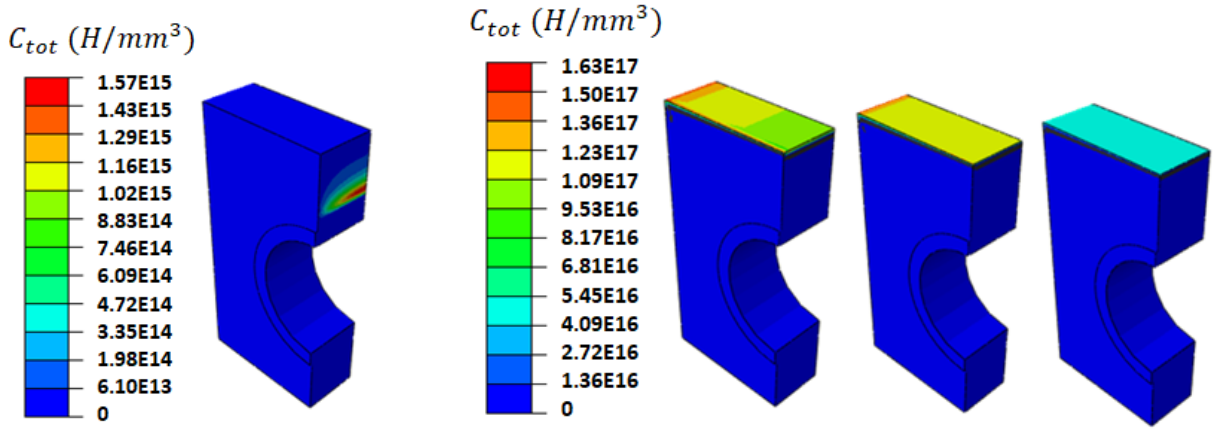

(a) (b)

Figure 2.114: C_{tot} field at P1 for φ_{inc} equal to (a) 10^{24}, (b) 10^{23} & 10^{22} & 10^{20} $H/m^2/s$ (1/4 monoblock).

Table 2.23: Value of the boundary condition on C_L (Equation 2.41) as a function of φ_{inc}.

φ_{inc} $(m^{-2}s^{-1})$	C_L $(atoms/mm^3)$
10^{20}	2.06×10^{10}
10^{22}	1.79×10^{12}
10^{23}	1.42×10^{13}
10^{24}	3.48×10^{12}

In Table 2.22, 'local MBs exposure' represents the number of MBs is 19008 (54 CA with 352 MBs per CA), which corresponds to 352 MBs per CA. 'full MBs exposure' represents the number of MBs is 292000, assuming all MBs on inboard and outboard receive the full loads of H.

- Impact of mechanical fields:

  In this part, all mechanical fields are removed to capture their impact on H retention and permeation. Results are summarized in Table 2.24.

Table 2.24: Total H retention in the quarter of monoblock

Unit: μg	Phase 1 (P23)	Phase 2 (1 week)	Phase 2 (2 weeks)	Phase 2 (P6)	Phase 3 (P7)	Mechanical fields
H retention	0.127	0.029	0.0069	3.6×10^{-4}	3.6×10^{-4}	Yes (Reference case)
Δm from end of Phase 1		77%	95%	99.7%	99.7%	
H retention	0.123	0.027	0.0065	8.2×10^{-6}	8.2×10^{-6}	No
Δm from end of Phase 1		78%	98%	99.9%	99.9%	

  In Figure 2.115a is plotted the total H inventory evolution with time during Phase 1: it can be observed that the mechanical fields impact for the reference scenario is very limited. Furthermore, desorption to the cooling pipe appears to be not affected by the mechanical fields (Figure 2.115c). The impact of mechanical fields is here limited because the reference case is a continuous exposure case. Considering the plasma pulses, the temporal temperature variations will induce plastic deformation at each pulse. Therefore, the plastic strain values obtained will be greater than for the continuous exposure case, and therefore, the mechanical fields will no longer be negligible.

- Impact of H desorption on S_{top}:

  Last, the boundary condition during Phase 2 has been modified on S_{top} to mimic the presence of a thin oxide layer that forbids any H desorption (at this surface, during Phase 2, the normal hydrogen flux is set to 0, instead of $C_L = 0$). The results are summarized in Table 2.25.

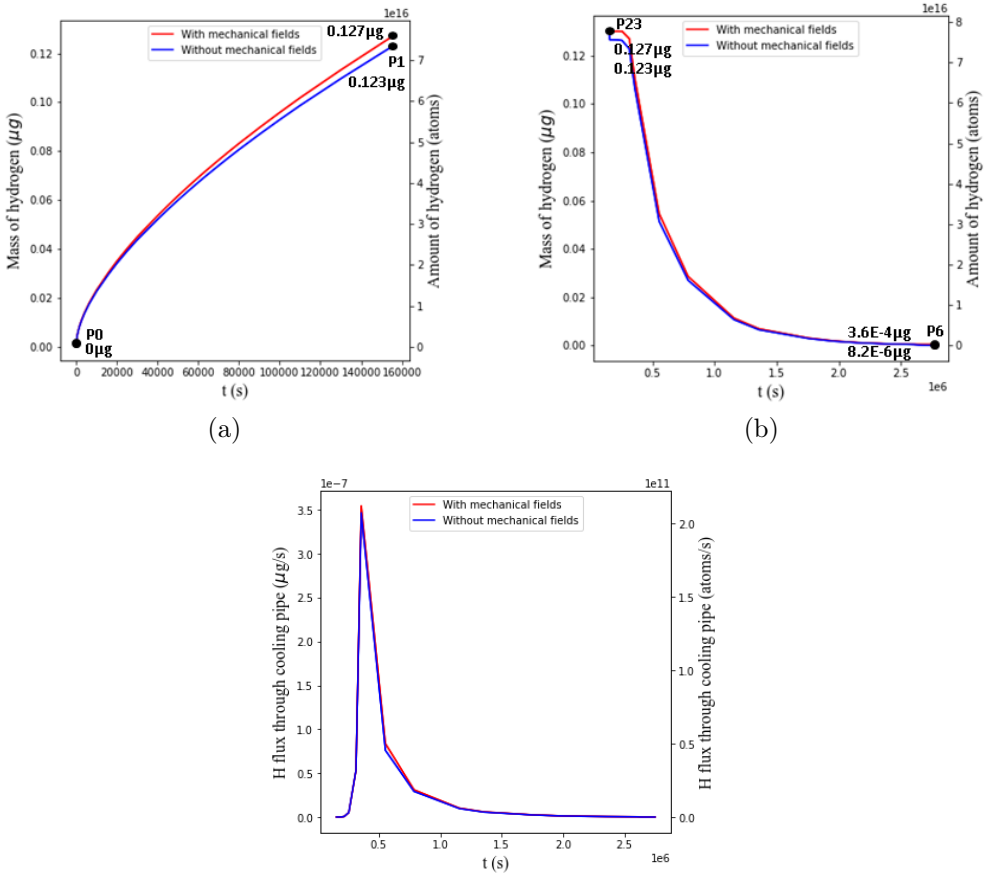

Figure 2.115: H retention evolution with time during (a) Phase 1, (b) Phase 2, and (c) H permeation through the cooling pipe during Phase 2 (1/4 monoblock).

Table 2.25: Total H retention in the quarter of monoblock

Unit: μg	Phase 1 (P23)	Phase 2 (1 week)	Phase 2 (2 weeks)	Phase 2 (P6)	Phase 3 (P7)	H desorption through top surface
H retention	0.127	0.029	0.0069	$3.6 \cdot 10^{-4}$	$3.6 \cdot 10^{-4}$	Yes (Reference case)
Δm from end of Phase 1		77%	95%	99.7%	99.7%	
H retention	0.127	0.043	0.017	0.0027	0.0027	No
Δm from end of Phase 1		66%	87%	98%	98%	

The evolution with time of H retention in the monoblock during Phase 2 can be seen in Figure 2.116a: as the desorption surfaces are smaller than in the reference case, the diminution of stored H amount is slower. This does not affect, however, the permeation flux to the cooling pipe (Figure 2.116b).

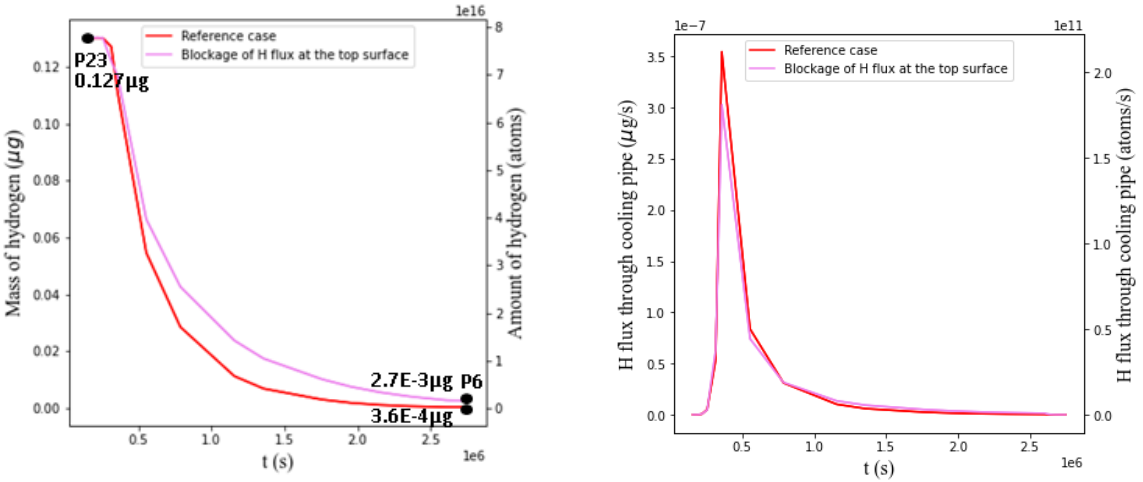

(a) (b)

Figure 2.116: Evolution with time during Phase 2 of (a) H retention and (b) H permeation through cooling pipe (1/4 monoblock).

- :

In this section, we have included additional calculations for further elucidation. The relationship of incident particle flux and the heat flux, and the corresponding T_{max} obtained from our calculations, are presented below according to [285]:

$$1.0 \times 10^{20}\,\mathrm{atoms/m^2/s} \rightarrow 1 \times 10^{5}\,\mathrm{W/m^2} \rightarrow \mathrm{T_{max}} = 380\,\mathrm{K}$$
$$1.0 \times 10^{22}\,\mathrm{atoms/m^2/s} \rightarrow 3 \times 10^{5}\,\mathrm{W/m^2} \rightarrow \mathrm{T_{max}} = 393\,\mathrm{K}$$
$$1.0 \times 10^{23}\,\mathrm{atoms/m^2/s} \rightarrow 5 \times 10^{5}\,\mathrm{W/m^2} \rightarrow \mathrm{T_{max}} = 406\,\mathrm{K}$$
$$6.6 \times 10^{23}\,\mathrm{atoms/m^2/s} \rightarrow 1 \times 10^{6}\,\mathrm{W/m^2} \rightarrow \mathrm{T_{max}} = 439\,\mathrm{K}$$
$$8.4 \times 10^{23}\,\mathrm{atoms/m^2/s} \rightarrow 6 \times 10^{6}\,\mathrm{W/m^2} \rightarrow \mathrm{T_{max}} = 808\,\mathrm{K}$$
$$8.9 \times 10^{23}\,\mathrm{atoms/m^2/s} \rightarrow 7 \times 10^{6}\,\mathrm{W/m^2} \rightarrow \mathrm{T_{max}} = 891\,\mathrm{K}$$
$$9.4 \times 10^{23}\,\mathrm{atoms/m^2/s} \rightarrow 8 \times 10^{6}\,\mathrm{W/m^2} \rightarrow \mathrm{T_{max}} = 976\,\mathrm{K}$$
$$9.9 \times 10^{23}\,\mathrm{atoms/m^2/s} \rightarrow 9 \times 10^{6}\,\mathrm{W/m^2} \rightarrow \mathrm{T_{max}} = 1064\,\mathrm{K}$$
$$1.0 \times 10^{24}\,\mathrm{atoms/m^2/s} \rightarrow 1 \times 10^{7}\,\mathrm{W/m^2} \rightarrow \mathrm{T_{max}} = 1156\,\mathrm{K}$$

Incident particle flux ($H/m^2/s$)	10^{20}	10^{22}	10^{23}	10^{24}
$T_{baking} = 350°C$ (623 K)	0.35%	0.56%	0.58%	43.7%
$T_{baking} = 300°C$ (573 K)				45.6%
$T_{baking} = 240°C$ (513 K)	0%	0%	0%	56.2%
$T_{baking} = 200°C$ (473 K)	0%	0%	0%	52.4%

Table 2.26: Percentage of H desorbed towards the $S_{coolant}$ at various baking temperatures.

Incident particle flux ($H/m^2/s$)	10^{20}	10^{22}	10^{23}	10^{24}
$T_{baking} = 350°C$ (623 K)	90.2%	89.5%	88.2%	16.3%
$T_{baking} = 300°C$ (573 K)				16.6%
$T_{baking} = 240°C$ (513 K)	93.65%	93.7%	93.3%	16.3%
$T_{baking} = 200°C$ (473 K)	93.2%	95.3%	95.2%	26.2%

Table 2.27: Percentage of H desorbed towards the S_{top} at various baking temperatures.

Incident particle flux ($H/m^2/s$)	10^{20}	10^{22}	10^{23}	10^{24}
$T_{baking} = 350°C$ (623 K)	0.02%	0%	0.02%	2%
$T_{baking} = 300°C$ (573 K)				2.1%
$T_{baking} = 240°C$ (513 K)	0%	0%	0%	2.5%
$T_{baking} = 200°C$ (473 K)	0%	0%	0%	2.3%

Table 2.28: Percentage of H desorbed towards the S_{pipe} at various baking temperatures.

Incident particle flux ($H/m^2/s$)	10^{20}	10^{22}	10^{23}	10^{24}
$T_{baking} = 350°C$ (623 K)	9.43%	9.94%	11.2%	38%
$T_{baking} = 300°C$ (573 K)				35.7%
$T_{baking} = 240°C$ (513 K)	6.35%	6.3%	6.7%	25%
$T_{baking} = 200°C$ (473 K)	6.8%	4.7%	4.8%	19.1%

Table 2.29: Percentage of H desorbed towards the $S_{laterals}$ at various baking temperatures.

From a detailed analysis of the four Tables (Table 2.26 to Table 2.29), the behavior of hydrogen desorption across various surfaces under different conditions paints a comprehensive picture of its dynamics. For the particle flux of 10^{24}, as the baking temperature increases, although the H desorbed from S_{top} and $S_{coolant}$ decreases, correspondingly, the H desorbed from $S_{laterals}$ increases. For the other three particle fluxes 10^{23}, 10^{22} and 10^{20}, S_{top}, being the heat-bearing surface, has the highest proportion of H desorption compared to the other surfaces.

he system ensures a constant overall hydrogen desorption, but the distribution of this desorption across different surfaces varies with temperature and particle flux. Such insights into the shifts in desorption balance across the surfaces can provide a deeper understanding of hydrogen's distribution and behavior under varying conditions.

Heat flux (MW/m^2)	Incident particle flux ($H/m^2/s$)	H retention (Phase 1) (mg)	H retention (Phase 2) (mg)	Mass difference (mg)	Percentage of H desorption towards $S_{coolant}$	H desorption towards $S_{coolant}$ (mg)
0.5	1×10^{23}	3.400	0.237	3.163	0%	0
1	6.6×10^{23}	8.270	1.310	6.960	0%	0
5	8.0×10^{23}	0.995	0.697	0.298	0.2%	0.0006
6	8.4×10^{23}	0.541	0.442	0.099	2.1%	0.002
7	8.9×10^{23}	0.337	0.291	0.046	10.9%	0.005
8	9.4×10^{23}	0.231	0.198	0.033	28.5%	0.009
9	9.9×10^{23}	0.170	0.139	0.031	45.9%	0.014
10	1×10^{24}	0.127	0.096	0.031	56.2%	0.017

Table 2.30: Impact of heat flux and incident particle flux on H retention and desorption at $T_{baking} = 240°C$ (513 K).

In Table 2.30, a more detailed investigation of H retention and desorption has been performed. We can see that, at lower heat fluxes (0.5 & 1 (MW/m^2)), there's a higher retention of hydrogen within the monoblock. However, a baking process can effectively remove a significant portion of this retained hydrogen. As the heat flux increases, not only does the retention of hydrogen decrease but there's also a noticeable rise in the desorption of hydrogen towards the $S_{coolant}$ direction. It's evident across all scenarios that baking plays a crucial role in reducing the overall retained amount of hydrogen.

2.5.7 Cyclic plasma exposure

In this part, the impact of the kind of plasma exposure on H retention is investigated. Two different cyclic scenarios are presented, based on respectively a 3-day and a 702 s cycle (Figures 2.117a and 2.117b). The 3-day cycle, as in the DFW scenario, corresponds to the concatenation of 39 plasma impulsions. for the sake of comparison, these two cyclic scenarios and the reference case are compared for the same fluence value, equal to $1.56 \times 10^{29}\, H/m^2$. As a consequence, 42 3-days and 283 702 s cycles will be considered (see Table 2.31). Boundary conditions are the same in the reference case (considering an incident particle flux equal to $\varphi_{inc} = 10^{24}\, m^{-2}.s^{-1}$). Simulation parameters are given in Table 2.31[3]

[3]As computation time is very long for the 702 s cycle scenario, only 39 cycles have been completed.

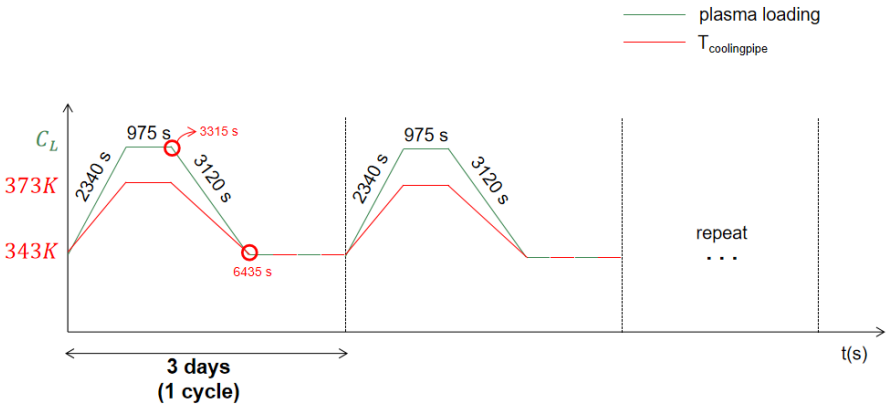

(a)

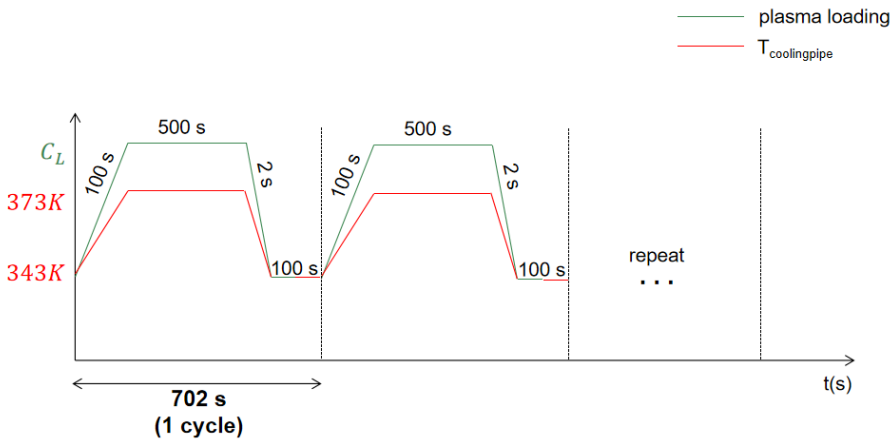

(b)

Figure 2.117: Scenario of cyclic plasma exposure (Phase 1): (a) 39 plasma pulses for one cycle (similar to the DFW one), (b) 1 plasma pulse for one cycle.

Table 2.31: Loading parameters for the 3 scenarios.

Scenario	Fluence per cycle (H/m^2)	Cycle duration (s)	φ_{inc} $(H/m^2/s)$	Nb of cycles for equivalent fluence
Continuous case (Reference case)	1.56×10^{29}	1.56×10^5	10^{24}	1
Cyclic case - 3days	3.71×10^{27}	259200	10^{24}	42
Cyclic case - 702s	5.51×10^{26}	702	10^{24}	283

2.5.8 Impact on plasticity

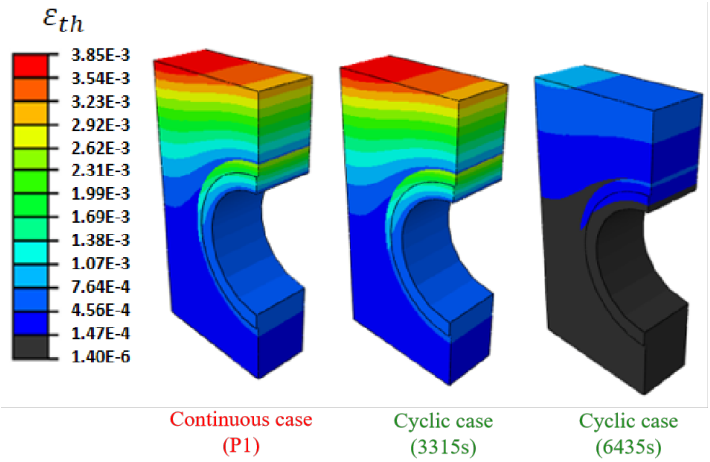

Figure 2.118: Thermal strain field: 3315 s and 6435 s correspond to the end of the plateau of the 1st cycle, and the end of the cooling process, respectively (see Figure 2.117 (a)).

Figure 2.118 represents the thermal strain field for the continuous case and cyclic 3-day case. There's no variation of ϵ_{th} for continuous case, on the contrary, a remarkable variation of ϵ_{th} for cyclic case occurs periodically due to the variable temperature of cooling pipe and thus induces a variable hydrostatic stress field illustrated in Figure 2.119.

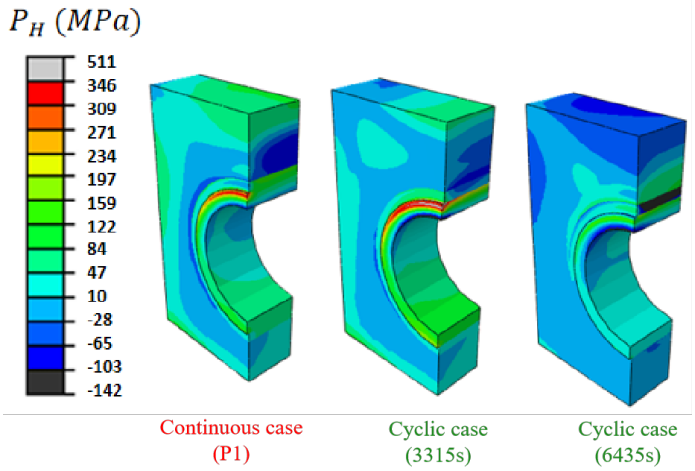

Figure 2.119: Hydrostatic stress field: 3315 s and 6435 s correspond to the end of the plateau of the 1st cycle, and the end of the cooling process, respectively (see Figure 2.117 (a)).

In Figure 2.120 are compared the plastic strain field at the end of the continuous (reference case) and 3-day cyclic (160 cycles of 2.117a) scenarios. It can be observed that there is no modification of the plastic strain location, but the levels reached are much more important in the cyclic case: as plastic strain is driven by thermal expansion incompatibilities (bi-material interfaces) and the temperature gradient. Consequently, plastic strains are mostly at bi-material interfaces.

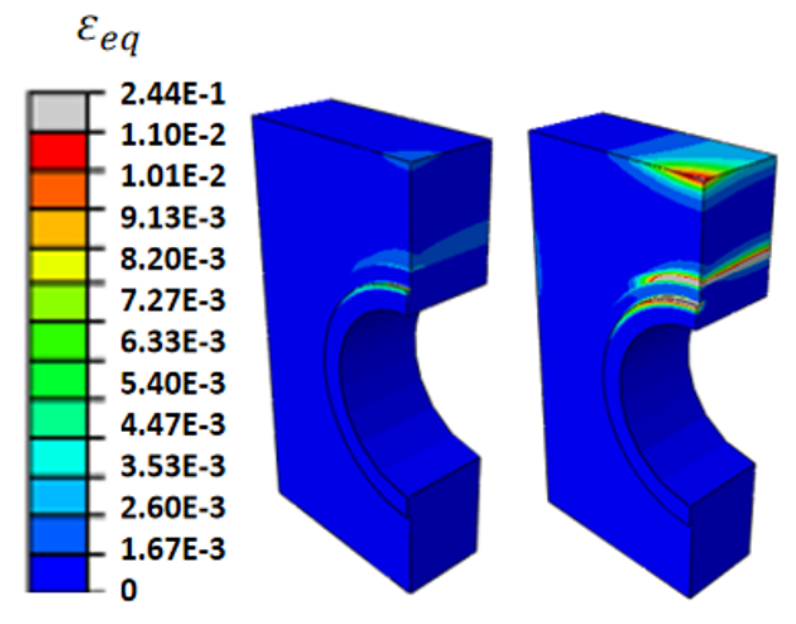

Figure 2.120: Plastic strain distribution at the end of the reference case (left) and cyclic case 2.117a (right).

2.5.9 Impact on H retention

For the 3 scenarios, H retention evolution with H fluence is plotted in Figure 2.121 (a). It can be observed that plasticity affects H retention: both continuous and 702-s cycle scenarios induce a higher plasticity level, associated with lower H retention.

In Figure 2.121b are compared the evolution, per cycle, of H retention for the two cyclic scenarios. As exposure time is shorter for the 702-s one, H goes less deep in the monoblock than for the 3-day one. Furthermore, because plastic strain fields are more important, H trapping is more important as well, with consequences on hydrostatic pressure fields.

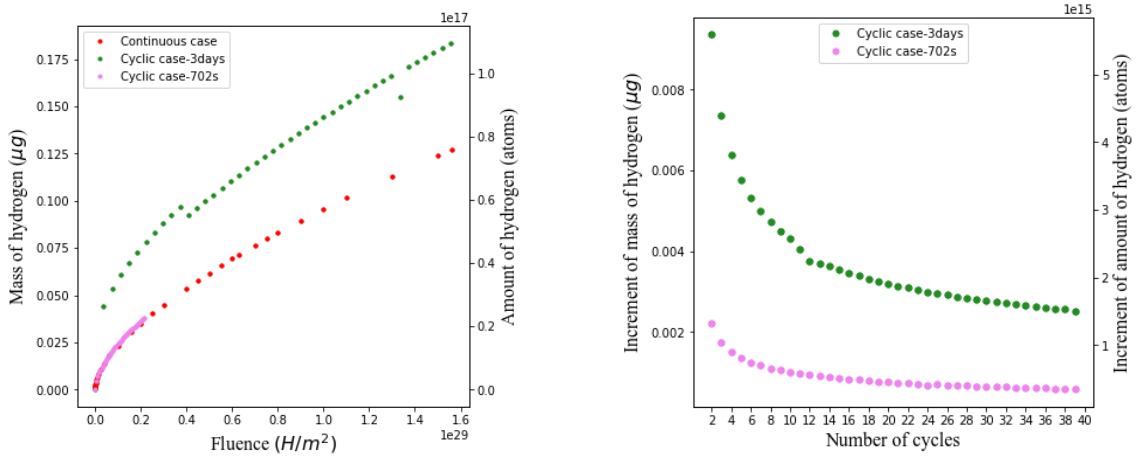

(a) (b)

Figure 2.121: (a) Evolution of H retention in the monoblock for the three different scenarios, (b) evolution of increment of H retention with the number of cycles for the two cyclic scenarios.

2.6 Conclusion

The impact of different parameters on the monoblock response has been analyzed in this chapter. During plasma operations, depending on the particle flux, the hydrogen is retained close to the surface (low flux) or deeper in the monoblock (higher flux). In all the cases, no permeation to the cooling pipe is detected. The retention does not linearly depend on the flux while the thermal effect is important. The retention extrapolation of the entire divertor is much lower than the safety limit. Of course, the retention depends on the fluence and also depends on the duration of the pulses chosen during the plasma operations.

H permeation to the cooling pipe is not negligible during the baking Phase. It has been investigated as a function of several parameters: it has been shown that baking temperature allows to remove quite all the H stored in the sample and that some parts of this H are evacuated in the cooling system.

It has especially been pointed out that the monoblock plastic strain state is highly dependent on the number of cycles experienced by the sample: due to thermal expansion mismatch, the plastic strain is localized at the bi-material interfaces and increases at each cycle. This points out the possible creation of cracks by (cycling) fatigue effects, in correlation with H embrittlement, a topic that is out of the scope of the current study.

Chapter 3

Clustering of Vacancies

After delving into the diffusion and trapping of hydrogen, key initial steps in surface blistering, we now shift our focus to vacancy clustering. This chapter is dedicated to modeling vacancy clustering within the monoblock, as these clusters often serve as a precursor to the formation of nanovoids in the material. This part is based on the Internship of Slim Ben Ayed [289].

3.1 Introduction

During plasma exposure of a sample, defects such as vacancies could be created or annihilated, and also they could be traps for hydrogen atoms, either already existing in the sample or due to plasma [290, 291]. Depending on their nature, they can also move and interact with each other: mono-vacancies, e.g., tend to gather to form bigger defects (vacancy clusters). At some point, hydrogen atoms trapped in such clusters can recombine into di-hydrogen, thereby creating a gaseous atmosphere: this process induces bubbles, which can grow, depending on various parameters (internal pressure, further vacancy clustering...). Last, residual stresses are induced, leading to material swelling and, eventually, failure (blistering) [292].

The vacancy mobility and clustering model is first presented (Section 3.2), as well as the implementation in Abaqus. Computations for a reference case of the monoblock are performed, and the temperature field, as well as the concentration of vacancies/vacancy clusters (up to C_{V_9}), are presented (Section 3.4). In [293], the thermal evolution of vacancies and vacancy clusters in tungsten has been studied. The tungsten was irradiated with H ions at 290 K and then annealed at temperatures in the range of 500–1800 K. Annealing at 700 K resulted in the formation of clusters containing 10–15 vacancies (V_{10} - V_{15}), while at 800 K and higher temperatures, clusters containing about 20 vacancies (V_{20}) or more were formed. This is the case in which the presence of hydrogen is taken into account and the hydrogen will block the annihilation of vacancy clusters. In this present work, we didn't account for this interaction between H and V_i, and the larger vacancy cluster $V_i > V_9$ will be modified

and included in the Gurson model, which is a material model describing the fracture induced by porosity (vacancy clusters, nanovoids, cavities...).

Finally, some parametric studies and a discussion of vacancy creation due to plasma irradiation, are also performed (Section 3.4.4 & 3.4.5).

3.2 Mathematical model

The clustering process is mainly based on the model proposed in [146] for iron (and for applications without thermal gradient), which is based on a reaction-diffusion approach. Furthermore, we are, in addition, considering that the diffusion coefficient is not a constant, but depends upon the coordinate:

$$\begin{cases} \frac{\partial C_{V_i}}{\partial t} = \nabla(D_{V_i}\nabla C_{V_i}) - S_{V_i}D_{V_i}(C_{V_i} - C_{V_i}^{eq}) - \sum_{j=1}^{n-1} b_{V_1+V_j}^{+} C_{V_1}C_{V_j} + \sum_{j=2}^{n} b_{V_j}^{-} C_{V_j} \quad \text{for i=1} \\ \\ \frac{\partial C_{V_i}}{\partial t} = \nabla(D_{V_i}\nabla C_{V_i}) - S_{V_i}D_{V_i}C_{V_i} + b_{V_1+V_{i-1}}^{+} C_{V_1}C_{V_{i-1}} - b_{V_1+V_i}^{+} C_{V_1}C_{V_i} \\ +b_{V_{i+1}}^{-} C_{V_{i+1}} - b_{V_i}^{-} C_{V_i} \quad \text{for } 2 \leq \text{i} \leq \text{n} \end{cases} \tag{3.1}$$

C_{V_i} represents the concentration of a cluster composed of i vacancies. Different terms of equation 3.1 are clarified below.

3.2.1 Diffusion

The diffusion term is described by Fick's law:

$$\frac{\partial C_{V_i}}{\partial t} = \nabla(D_{V_i}\nabla C_{V_i}) \tag{3.2}$$

with $D_{V_i} = D_{0V_i}\exp\left(-\frac{Q_{V_i}}{RT}\right)$ the diffusion coefficient for the cluster made of i vacancies. D_{0V_i} is the pre-factor, which is independent on temperature and Q_{V_i} the activation energy of the diffusion.

3.2.2 Creation/Annihilation

To account for the existence of vacancy or vacancy clusters concentration at thermodynamic equilibrium, the creation/annihilation term has been introduced in the form of a sink or a source:

$$-S_{V_i}D_{V_i}(C_{V_i} - C_{V_i}^{eq}) \tag{3.3}$$

where S_{V_i} denotes the sink strength, in m^{-2}. $S_{V_i}D_{V_i}$ the creation or annihilation rate for vacancies or vacancy clusters, in s^{-1}. $C_{V_i}^{eq}$ is the thermodynamic equilibrium concentration of C_{V_i} (assumed to be zero for i>1 [146]).

3.2.3 Clustering reaction

Last, the process of agglomeration or dissociation of a cluster is modeled by a chemical reaction, assuming that any cluster size modification is related to a single vacancy (added or removed):

$$V_1 + V_i \rightleftharpoons V_{1+i} \tag{3.4}$$

The reaction rate is assumed to be:

$$\text{for i=1} \begin{cases} \dot{C}_{V_i}^{agglomeration} = -\sum_i^{n-1} b_{V_i+V_1}^{+} C_{V_i} C_{V_1} \\ \dot{C}_{V_i}^{dissociation} = \sum_{i+1}^{n} b_{V_{i+1}}^{-} C_{V_{i+1}} \end{cases} \tag{3.5}$$

$$\text{for } 2 \leq \text{i} \leq \text{n} \begin{cases} \dot{C}_{V_i}^{agglomeration} = b_{V_1+V_{i-1}}^{+} C_{V_1} C_{V_{i-1}} + b_{V_{i+1}}^{-} C_{V_{i+1}} \\ \dot{C}_{V_i}^{dissociation} = -b_{V_i+V_1}^{+} C_{V_i} C_{V_1} - b_{V_i}^{-} C_{V_i} \end{cases} \tag{3.6}$$

The equations 3.5 & 3.6 describe respectively the processes of agglomeration and dissociation of vacancies, with the kinetic constants $b_{V_i+V_1}^{+}$ and $b_{V_{i+1}}^{-}$ such that [146]

$$b_{V_i+V_1}^{+} = 4\pi(r_{V_i} + r_{V_1})(D_{V_i} + D_{V_1}) \tag{3.7}$$

and

$$b_{V_{i+1}}^{-} = 4\pi(r_{V_i} + r_{V_1})(D_{V_i} + D_{V_1})\, N_S \exp\left(-\frac{E_{V_i}^{b}}{RT}\right) \tag{3.8}$$

$E_{V_i}^{b}$ is the trapping energy for a vacancy on an i-sized cluster, $r_{V_i} = (3iV_{atomic}/4\pi)^{1/3} + r_0$ being the trapping radius of a vacancy, with $r_0 = 1.37$ Å representing the vacancy interaction radius. V_{atomic} is the atomic volume ($V_{atomic} = \frac{V_m}{N_A}$, the ratio of molar volume of tungsten at room temperature $V_m = 9.55\ cm^3$ [294] and Avogadro constant $N_A = 6.02 \times 10^{23}\ mol^{-1}$), and $N_S = N_L(i-1)/i$ the number of available sites in which a vacancy can be created, N_L the density of lattice sites of tungsten ($N_L = \frac{\rho_W N_A}{M}$, with the mass density of tungsten $\rho_W = 19.3\ g/cm^3$ [295] and the molar mass of tungsten $M = 183.8\ g/mol$ [295]).

3.2.4 Weak formulation

For the sake of simplicity, the weak formulations written in this section are related to C_{V_1}, C_{V_2} and C_{V_3}, and to the following two reactions:

$$\begin{cases} V_1 + V_1 \rightleftharpoons V_2 \\ \\ V_1 + V_2 \rightleftharpoons V_3 \end{cases} \tag{3.9}$$

The associated reaction rates are:

$$\begin{cases} \dot{C}^r_{V_1 \to V_2} = -\dot{C}^r_{V_2 \to V_1} = b^+_{V_1+V_1} C_{V_1} C_{V_1} - b^-_{V_2} C_{V_2} \\ \\ \dot{C}^r_{V_1 \to V_3} = \dot{C}^r_{V_2 \to V_3} = -\dot{C}^r_{V_3 \to V_1} = -\dot{C}^r_{V_3 \to V_2} = b^+_{V_1+V_2} C_{V_1} C_{V_2} - b^-_{V_3} C_{V_3} \end{cases} \tag{3.10}$$

which can be rewriten as

$$\begin{cases} \frac{\partial C_{V_1}}{\partial t} = D_{V_1} \Delta C_{V_1} - S_{V_1} D_{V_1} (C_{V_1} - C^{eq}_{V_1}) + \dot{C}^r_{V_2 \to V_1} + \dot{C}^r_{V_3 \to V_1} \\ \\ \frac{\partial C_{V_2}}{\partial t} = D_{V_2} \Delta C_{V_2} - S_{V_2} D_{V_2} C_{V_2} + \dot{C}^r_{V_1 \to V_2} + \dot{C}^r_{V_3 \to V_2} \\ \\ \frac{\partial C_{V_3}}{\partial t} = D_{V_3} \Delta C_{V_3} - S_{V_3} D_{V_3} C_{V_3} + \dot{C}^r_{V_1 \to V_3} \end{cases} \tag{3.11}$$

so we have:

$$\begin{cases} \frac{\partial C_{V_1}}{\partial t} = D_{V_1} \Delta C_{V_1} - S_{V_1} D_{V_1} (C_{V_1} - C^{eq}_{V_1}) - b^+_{V_1+V_1} C_{V_1} C_{V_1} + b^-_{V_2} C_{V_2} - b^+_{V_1+V_2} C_{V_1} C_{V_2} + b^-_{V_3} C_{V_3} \\ \\ \frac{\partial C_{V_2}}{\partial t} = D_{V_2} \Delta C_{V_2} - S_{V_2} D_{V_2} C_{V_2} + b^+_{V_1+V_1} C_{V_1} C_{V_1} - b^-_{V_2} C_{V_2} - b^+_{V_1+V_2} C_{V_1} C_{V_2} + b^-_{V_3} C_{V_3} \\ \\ \frac{\partial C_{V_3}}{\partial t} = D_{V_3} \Delta C_{V_3} - S_{V_3} D_{V_3} C_{V_3} + b^+_{V_1+V_2} C_{V_1} C_{V_2} - b^-_{V_3} C_{V_3} \end{cases} \tag{3.12}$$

Let's consider a domain Ω (different from the atomic volume Ω presented in section 3.2.3), whose boundary is $\partial\Omega$. This boundary can be partitioned in $\partial\Omega_{C_{V_i}}$, on which the value of C_{V_i} is imposed, and $\partial\Omega_{\varphi_{V_i}}$, on which the normal C_{V_i} flux ($\overline{\varphi}_{V_{iN}}$) is imposed. The weak formulation of the equation system 3.12 is consequently:

for C_{V_1}: $\forall\ \delta C$ virtual field continuous enough, such that $\delta C = 0$ on $\partial\Omega_{C_{V_1}}$

$$\begin{aligned}\int_\Omega \frac{\partial C_{V_1}}{\partial t}\delta C dV =& D_{V_1}\int_\Omega \Delta C_{V_1}\delta C dV - S_{V_1}D_{V_1}\int_\Omega (C_{V_1}-C_{V_1}^{eq})\delta C dV - b^+_{V_1+V_1}\int_\Omega C_{V_1}^2\delta C dV \\ & - b^+_{V_1+V_2}\int_\Omega C_{V_1V_2}\delta C dV + b^-_{V_3}\int_\Omega C_{V_3}\delta C dV + b^-_{V_2}\int_\Omega C_{V_2}\delta C dV\end{aligned} \tag{3.13}$$

for C_{V_2}: $\forall\ \delta C$ virtual field continuous enough, such that $\delta C = 0$ on $\partial\Omega_{C_{V_2}}$

$$\begin{aligned}\int_\Omega \frac{\partial C_{V_2}}{\partial t}\delta C dV =& D_{V_2}\int_\Omega \Delta C_{V_2}\delta C dV - S_{V_2}D_{V_2}\int_\Omega C_{V_2}\delta C dV - b^+_{V_1+V_1}\int_\Omega C_{V_1}^2\delta C dV \\ & - b^-_{V_2}\int_\Omega C_{V_2}\delta C dV + b^-_{V_3}\int_\Omega C_{V_3}\delta C dV - b^+_{V_1+V_2}\int_\Omega C_{V_1}C_{V_2}\delta C dV\end{aligned} \tag{3.14}$$

for C_{V_3}: $\forall\ \delta C$ virtual field continuous enough, such that $\delta C = 0$ on $\partial\Omega_{C_{V_3}}$

$$\begin{aligned}\int_\Omega \frac{\partial C_{V_3}}{\partial t}\delta C dV =& D_{V_3}\int_\Omega \Delta C_{V_3}\delta C dV - S_{V_3}D_{V_3}\int_\Omega C_{V_3}\delta C dV - b^+_{V_1+V_1}\int_\Omega C_{V_1}^2\delta C dV \\ & - b^-_{V_3}\int_\Omega C_{V_3}\delta C dV + b^+_{V_1+V_2}\int_\Omega C_{V_1}C_{V_2}\delta C dV\end{aligned} \tag{3.15}$$

By performing the following integration by parts

$$\int_\Omega \Delta C_{V_i}\delta C dV = \int_\Omega \boldsymbol{\nabla}.(\boldsymbol{\nabla} C_{V_i}\delta C dV) - \int_\Omega \boldsymbol{\nabla} C_{V_i}\boldsymbol{\nabla}\delta C dV \tag{3.16}$$

with

$$\int_\Omega \boldsymbol{\nabla}(\boldsymbol{\nabla} C_{V_i}\delta C)dV = \int_{\partial\Omega}(\boldsymbol{\nabla} C_{V_i}\cdot\boldsymbol{n})\delta C dS \tag{3.17}$$

and $-D_{V_i}\boldsymbol{\nabla} C_{V_i}\cdot\boldsymbol{n} = \varphi_{V_{iN}}$ ($\boldsymbol{n}$ being its outgoing normal vector), equations 3.13 to 3.15 become:

for C_{V_1}: $\forall \delta C$, virtual field continuous enough, such that $\delta C = 0$ on $\partial\Omega_{C_{V_1}}$

$$\int_{\partial\Omega_{\varphi_{C_1}}} \overline{\varphi}_{C_{1N}} \delta C dS = \int_\Omega \frac{\partial C_{V_1}}{\partial t} \delta C dV + D_{V_1} \int_\Omega \boldsymbol{\nabla} C_{V_1} \boldsymbol{\nabla} \delta C dV + S_{V_1} D_{V_1} \int_\Omega (C_{V_1} - C_{V_1}^{eq}) \delta C dV$$
$$+ b^+_{V_1+V_1} \int_\Omega C_{V_1}^2 \delta C dV + b^+_{V_1+V_2} \int_\Omega C_{V_1} C_{V_2} \delta C dV - b^-_{V_3} \int_\Omega C_{V_3} \delta C dV$$
$$- b^-_{V_2} \int_\Omega C_{V_2} \delta C dV \tag{3.18}$$

for C_{V_2}: $\forall\ \delta C$ virtual field continuous enough, such that $\delta C = 0$ on $\partial\Omega_{C_{V_2}}$

$$\int_{\partial\Omega_{\varphi_{C_2}}} \overline{\varphi}_{C_{2N}} \delta C dS = \int_\Omega \frac{\partial C_{V_2}}{\partial t} \delta C dV + D_{V_2} \int_\Omega \boldsymbol{\nabla} C_{V_2} \boldsymbol{\nabla} \delta C dV + S_{V_2} D_{V_2} \int_\Omega C_{V_2} \delta C dV$$
$$- b^+_{V_1+V_1} \int_\Omega C_{V_1}^2 \delta C dV + b^+_{V_1+V_2} \int_\Omega C_{V_1} C_{V_2} \delta C dV - b^-_{V_3} \int_\Omega C_{V_3} \delta C dV$$
$$+ b^-_{V_2} \int_\Omega C_{V_2} \delta C dV \tag{3.19}$$

for C_{V_3}: $\forall\ \delta C$ virtual field continuous enough, such that $\delta C = 0$ on $\partial\Omega_{C_{V_3}}$

$$\int_{\partial\Omega_{\varphi_{C_3}}} \overline{\varphi}_{C_{3N}} \delta C dS = \int_\Omega \frac{\partial C_{V_3}}{\partial t} \delta C dV + D_{V_3} \int_\Omega \boldsymbol{\nabla} C_{V_3} \boldsymbol{\nabla} \delta C dV + S_{V_3} D_{V_3} \int_\Omega C_{V_3} \delta C dV$$
$$- b^+_{V_1+V_2} \int_\Omega C_{V_1} C_{V_2} \delta C dV + b^-_{V_3} \int_\Omega C_{V_3} \delta C dV \tag{3.20}$$

Considering that

$$\frac{\partial C_{V_i}}{\partial t} \sim \frac{C_{V_i} - \tilde{C}_{V_i}}{\Delta t} \tag{3.21}$$

where Δt is the time increment and $\tilde{C}_{V_i}$ is the converged value of C_{V_i} at the previous increment, and assuming that $\delta C = [\boldsymbol{N}]\delta\boldsymbol{q}$, where $[\boldsymbol{N}]$ is the matrix composed of polynomial form function of the finite element, $\delta\boldsymbol{q}$ being the virtual degree of freedom (DOF) vector related to the virtual field δC, Equations 3.18 to 3.20 become

for C_{V_1}:

$$\begin{aligned}
&\frac{1}{\Delta t}\int_\Omega [\boldsymbol{N}]C_{V_1}dV + D_{V_1}\int_\Omega^t [\boldsymbol{\nabla N}]\cdot\boldsymbol{\nabla}C_{V_1}dV + S_{V_1}D_{V_1}\int_\Omega [\boldsymbol{N}]C_{V_1}dV + b^+_{V_1+V_1}\int_\Omega [\boldsymbol{N}]C^2_{V_1}dV \\
&+ b^+_{V_1+V_2}\int_\Omega [\boldsymbol{N}]C_{V_1}C_{V_2}dV - b^-_{V_2}\int_\Omega [\boldsymbol{N}]C_{V_2}dV - b^-_{V_3}\int_\Omega [\boldsymbol{N}]C_{V_3}dV \\
&= \int_{\partial\Omega_{\varphi C1}} [\boldsymbol{N}]\overline{\varphi}_{C_{1N}}dS + S_{V_1}D_{V_1}\int_\Omega [\boldsymbol{N}]C^{eq}_{V_1}dV + \frac{1}{\Delta t}\int_\Omega [\boldsymbol{N}]\tilde{C}_{V_1}dV
\end{aligned} \tag{3.22}$$

for C_{V_2}:

$$\begin{aligned}
&\frac{1}{\Delta t}\int_\Omega [\boldsymbol{N}]C_{V_2}dV + D_{V_2}\int_\Omega^t [\boldsymbol{\nabla N}]\cdot\boldsymbol{\nabla}C_{V_2}dV + S_{V_2}D_{V_2}\int_\Omega [\boldsymbol{N}]C_{V_2}dV - b^+_{V_1+V_1}\int_\Omega [\boldsymbol{N}]C^2_{V_1}dV \\
&+ b^+_{V_1+V_2}\int_\Omega [\boldsymbol{N}]C_{V_1}C_{V_2}dV + b^-_{V_2}\int_\Omega [\boldsymbol{N}]C_{V_2}dV - b^-_{V_3}\int_\Omega [\boldsymbol{N}]C_{V_3}dV \\
&= \int_{\partial\Omega_{\varphi C2}} [\boldsymbol{N}]\overline{\varphi}_{C_{2N}}dS + \frac{1}{\Delta t}\int_\Omega [\boldsymbol{N}]\tilde{C}_{V_2}dV
\end{aligned} \tag{3.23}$$

for C_{V_3}:

$$\begin{aligned}
&\frac{1}{\Delta t}\int_\Omega [\boldsymbol{N}]C_{V_3}dV + D_{V_3}\int_\Omega^t [\boldsymbol{\nabla N}]\cdot\boldsymbol{\nabla}C_{V_3}dV + S_{V_3}D_{V_3}\int_\Omega [\boldsymbol{N}]C_{V_2}dV - b^+_{V_1+V_2}\int_\Omega [\boldsymbol{N}]C_{V_1}C_{V_2}dV \\
&+ b^-_{V_3}\int_\Omega [\boldsymbol{N}]C_{V_3}dV \\
&= \int_{\partial\Omega_{\varphi C3}} [\boldsymbol{N}]\overline{\varphi}_{C_{3N}}dS + \frac{1}{\Delta t}\int_\Omega [\boldsymbol{N}]\tilde{C}_{V_3}dV
\end{aligned} \tag{3.24}$$

with $\boldsymbol{\nabla}C = [\boldsymbol{\nabla N}]\boldsymbol{q}$.

3.3 Implementation & Validation

3.3.1 Principle

The diffusion-reaction equations are implemented using a User ELement (UEL) user subroutine which will be defined in this part [296]. A UEL is a Fortran program allowing

the creation of new elements in Abaqus. They can be used in several ways: to define new behavior (as for cohesive elements [297]), and/or to activate new degrees of freedom, by specifying their behavior law [137,298,299]. The UEL elements are made of several degrees of freedom (DOFs): displacement (DOFs numbered from 1 to 3), temperature (DOF numbered 12 in the developed tools, this field is solved by UEL too), and $C_{V_i,i=1\rightarrow 9}$ (DOFs numbered from 13 to 20).

To activate a new degree of freedom, a UEL is superimposed on an Abaqus element (see figure 3.1). The Abaqus element and the UEL, therefore, share the same nodes, and consequently the same degrees of freedom: the stiffness matrices of these elements are summed (Figure 3.2).

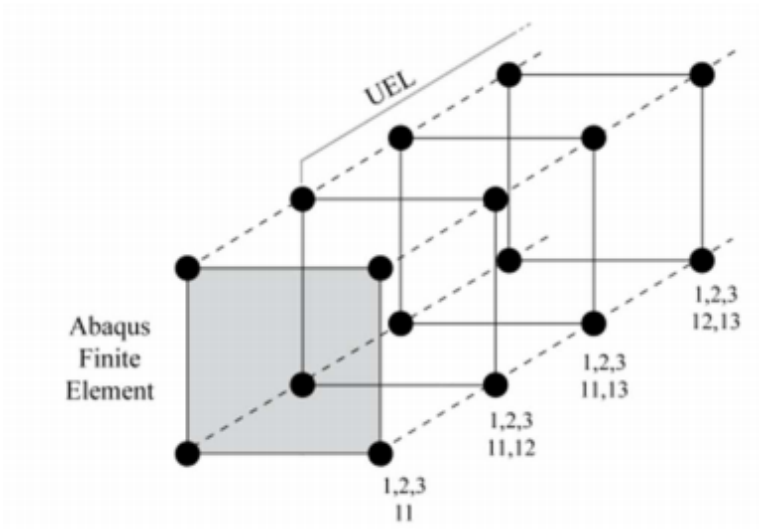

Figure 3.1: Principle of the superposition of Abaqus elements and UELs, in the case of a 'coupled temp-displacement procedure' containing both displacement and temperature as DOFs [298].

In addition to the standard degrees of freedom, the introduction of the UEL also makes possible the activation of additional degrees of freedom, starting from 12, not accessible by default. The physics associated with this DOF, as well as all the couplings, must be defined in the UEL procedure. The total number of DOFs per node is then defined by both the UEL and the Abaqus elements: Abaqus will increase automatically the dimension of its own stiffness matrices to account for the new DOFs.

To introduce the clustering procedure in Abaqus, with 9 species (C_{V_i}, $i = 1 \rightarrow 9$), and its coupling with other fields (displacements, temperature, hydrogen), the DOFs should go to:

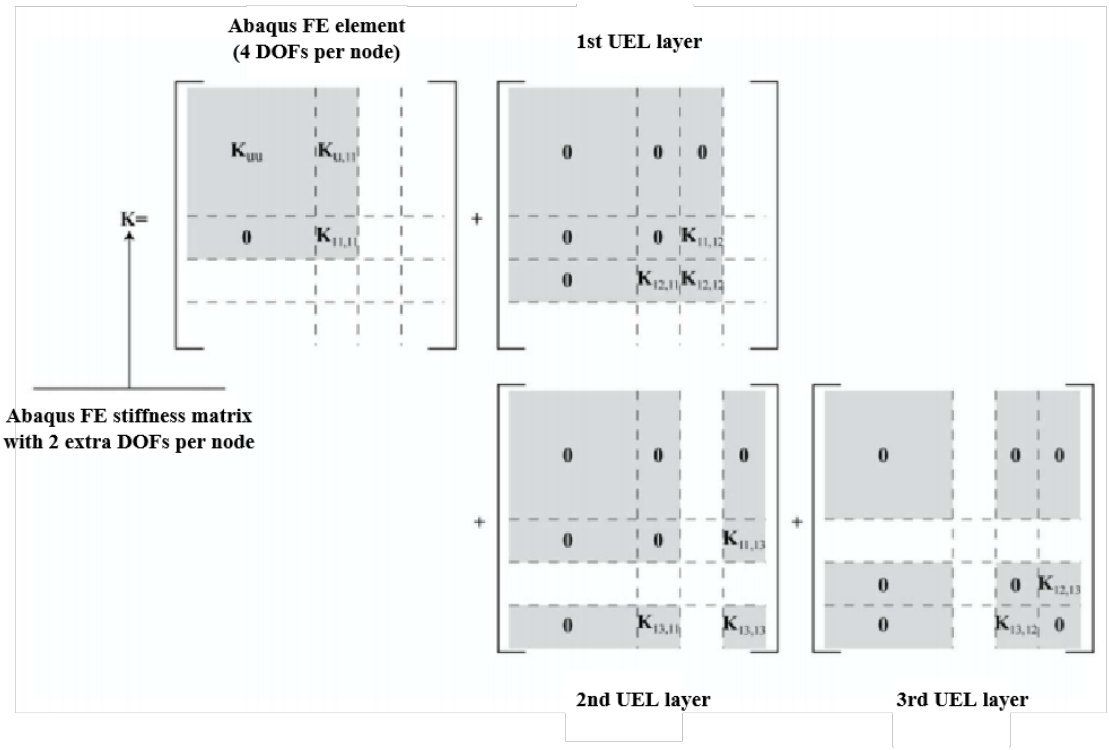

Figure 3.2: Final stiffness matrix resulting from the superposition of Abaqus element and UEL. [300]

- 1, 2, 3 for the displacements.
- 11 for the hydrogen if needed (e.g., in the case of the impact of H on V-cluster mobility).
- 12 for the temperature if needed (T fields computed by a specific UEL layer).
- 13 to 20 for the 9 species ($C_{V_1} \sim C_{V_9}$).

The total number of DOFs per node in the model is consequently at least 12.

3.3.2 UEL definition

To define a UEL element in Abaqus, it is mandatory to provide the software with the contribution of the UEL element to the global Newton-Raphson convergence scheme, through ***RHS*** vector and ***AMATRX*** matrix so that

$$\begin{cases} \boldsymbol{RHS} \cdot \delta\boldsymbol{q} = f(\boldsymbol{q}, \delta\boldsymbol{q}) \\ \\ \boldsymbol{AMATRX} = -\frac{\partial \boldsymbol{RHS}}{\partial \boldsymbol{q}} \end{cases} \tag{3.25}$$

where $f(\boldsymbol{q}, \delta\boldsymbol{q})$ is the problem of weak formulation ($\boldsymbol{q}$ and $\delta\boldsymbol{q}$ being respectively the DOF and the virtual DOF vectors) and its Jacobian.

As the implementation presentation is here limited to the three concentrations C_{V_1}, C_{V_2} and C_{V_3}, the UEL will be used to activate three complementary DOFs (13, 14 and 15, respectively), and to define their interactions. For each DOF, we can define the $\boldsymbol{RHS}$ vector, and the $\boldsymbol{AMATRX}$ matrix:

$$\begin{cases} \boldsymbol{RHS_{13}} \rightarrow \text{weak formulation for } C_{V_1} \\ \\ \boldsymbol{AMATRX_{13,13}} = -\frac{\partial \boldsymbol{RHS_{13}}}{\partial \boldsymbol{q_{13}}} \\ \\ \boldsymbol{AMATRX_{13,14}} = -\frac{\partial \boldsymbol{RHS_{13}}}{\partial \boldsymbol{q_{14}}} \\ \\ \boldsymbol{AMATRX_{13,15}} = -\frac{\partial \boldsymbol{RHS_{13}}}{\partial \boldsymbol{q_{15}}} \end{cases} \tag{3.26}$$

3.3.3 Application for C_{V_1}, C_{V_2} and C_{V_3}

The $\boldsymbol{RHS}$ vectors for the three species are:

$$\begin{aligned} \boldsymbol{RHS_{13}} =& (\frac{1}{\Delta t} + S_{V_1} D_{V_1}) \int_\Omega [\boldsymbol{N}] C_{V_1} dV + D_{V_1} \int_\Omega ({}^t[\boldsymbol{\nabla N}]) \cdot \boldsymbol{\nabla C_{V_1}} dV \\ & + b^+_{V_1+V_1} \int_\Omega [\boldsymbol{N}] C^2_{V_1} dV + b^+_{V_1+V_2} \int_\Omega [\boldsymbol{N}] C_{V_1} C_{V_2} dV - b^-_{V_3} \int_\Omega [\boldsymbol{N}] C_{V_3} dV \\ & - b^-_{V_2} \int_\Omega [\boldsymbol{N}] C_{V_2} dV - \int_{\partial\Omega_{\varphi C1}} [\boldsymbol{N}] \tilde{\varphi}_{C_{1N}} dS - S_{V_1} D_{V_1} \int_\Omega [\boldsymbol{N}] C^{eq}_{V_1} dV \\ & - \frac{1}{\Delta t} \int_\Omega [\boldsymbol{N}] \tilde{C}_{V_1} dV \end{aligned} \tag{3.27}$$

$$\begin{aligned}\boldsymbol{RHS_{14}} =&(\frac{1}{\Delta t}+S_{V_2}D_{V_2})\int_\Omega[\boldsymbol{N}]C_{V_2}dV+D_{V_2}\int_\Omega({}^t[\boldsymbol{\nabla N}])\cdot\boldsymbol{\nabla C_{V_2}}dV\\&-b^+_{V_1+V_1}\int_\Omega[\boldsymbol{N}]C^2_{V_1}dV+b^+_{V_1+V_2}\int_\Omega[\boldsymbol{N}]C_{V_1}C_{V_2}dV-b^-_{V_3}\int_\Omega[\boldsymbol{N}]C_{V_3}dV\\&+b^-_{V_2}\int_\Omega[\boldsymbol{N}]C_{V_2}dV-\int_{\partial\Omega_{\varphi C2}}[\boldsymbol{N}]\tilde{\varphi}_{C_{2N}}dS-\frac{1}{\Delta t}\int_\Omega[\boldsymbol{N}]\tilde{C}_{V_2}dV\end{aligned}\tag{3.28}$$

$$\begin{aligned}\boldsymbol{RHS_{15}} =&(\frac{1}{\Delta t}+S_{V_3}D_{V_3})\int_\Omega[\boldsymbol{N}]C_{V_3}dV+D_{V_3}\int_\Omega({}^t[\boldsymbol{\nabla N}])\cdot\boldsymbol{\nabla C_{V_3}}dV\\&-b^+_{V_1+V_2}\int_\Omega[\boldsymbol{N}]C_{V_1}C_{V_2}dV+b^-_{V_3}\int_\Omega[\boldsymbol{N}]C_{V_3}dV-\int_{\partial\Omega_{\varphi C3}}[\boldsymbol{N}]\tilde{\varphi}_{C_{3N}}dS\\&-\frac{1}{\Delta t}\int_\Omega[\boldsymbol{N}]\tilde{C}_{V_3}dV\end{aligned}\tag{3.29}$$

The Jacobian matrices are then, for C_{V_1}:

$$\begin{aligned}\boldsymbol{AMATRX_{13,13}}=-\frac{\partial\boldsymbol{RHS_{13}}}{\partial\boldsymbol{q_{13}}}=&-(\frac{1}{\Delta t}+S_{V_1}D_{V_1})\int_\Omega({}^t[\boldsymbol{N}][\boldsymbol{N}])dV-D_{V_1}\int_\Omega({}^t[\boldsymbol{\nabla N}][\boldsymbol{\nabla N}])dV\\&-2b^+_{V_1+V_1}\int_\Omega({}^t[\boldsymbol{N}][\boldsymbol{N}])C_{V_1}dV-b^+_{V_1+V_2}\int_\Omega({}^t[\boldsymbol{N}][\boldsymbol{N}])C_{V_2}dV\end{aligned}\tag{3.30}$$

$$\boldsymbol{AMATRX_{13,14}}=-\frac{\partial\boldsymbol{RHS_{13}}}{\partial\boldsymbol{q_{14}}}=-b^-_{V_2}\int_\Omega({}^t[\boldsymbol{N}][\boldsymbol{N}])dV-b^+_{V_1+V_2}\int_\Omega({}^t[\boldsymbol{N}][\boldsymbol{N}])C_{V_1}dV\tag{3.31}$$

$$\boldsymbol{AMATRX_{13,15}}=-\frac{\partial\boldsymbol{RHS_{13}}}{\partial\boldsymbol{q_{15}}}=-b^-_{V_3}\int_\Omega({}^t[\boldsymbol{N}][\boldsymbol{N}])dV\tag{3.32}$$

For C_{V_2}:

$$\begin{aligned}\boldsymbol{AMATRX_{14,14}}=-\frac{\partial\boldsymbol{RHS_{14}}}{\partial\boldsymbol{q_{14}}}=&-(\frac{1}{\Delta t}+S_{V_2}D_{V_2})\int_\Omega({}^t[\boldsymbol{N}][\boldsymbol{N}])dV-D_{V_2}\int_\Omega({}^t[\boldsymbol{\nabla N}][\boldsymbol{\nabla N}])dV\\&-b^-_{V_2}\int_\Omega({}^t[\boldsymbol{N}][\boldsymbol{N}])dV-b^+_{V_1+V_2}\int_\Omega({}^t[\boldsymbol{N}][\boldsymbol{N}])C_{V_1}dV\end{aligned}\tag{3.33}$$

$$\boldsymbol{AMATRX_{14,13}} = -\frac{\partial \boldsymbol{RHS_{14}}}{\partial \boldsymbol{q_{13}}} = 2b^{+}_{V_1+V_1}\int_{\Omega}({}^{t}[\boldsymbol{N}][\boldsymbol{N}])C_{V_1}dV - b^{+}_{V_1+V_2}\int_{\Omega}({}^{t}[\boldsymbol{N}][\boldsymbol{N}])C_{V_2}dV \tag{3.34}$$

$$\boldsymbol{AMATRX_{14,15}} = -\frac{\partial \boldsymbol{RHS_{14}}}{\partial \boldsymbol{q_{15}}} = b^{-}_{V_3}\int_{\Omega}({}^{t}[\boldsymbol{N}][\boldsymbol{N}])dV \tag{3.35}$$

For C_{V_3}:

$$\boldsymbol{AMATRX_{15,15}} = -\frac{\partial \boldsymbol{RHS_{15}}}{\partial \boldsymbol{q_{15}}} = -(\frac{1}{\Delta t} + S_{V_3}D_{V_3})\int_{\Omega}({}^{t}[\boldsymbol{N}][\boldsymbol{N}])dV - D_{V_3}\int_{\Omega}({}^{t}[\boldsymbol{\nabla N}][\boldsymbol{\nabla N}])dV - b^{-}_{V_3}\int_{\Omega}({}^{t}[\boldsymbol{N}][\boldsymbol{N}])dV \tag{3.36}$$

$$\boldsymbol{AMATRX_{15,13}} = -\frac{\partial \boldsymbol{RHS_{15}}}{\partial \boldsymbol{q_{13}}} = b^{+}_{V_1+V_2}\int_{\Omega}({}^{t}[\boldsymbol{N}][\boldsymbol{N}])C_{V_2}dV \tag{3.37}$$

$$\boldsymbol{AMATRX_{15,14}} = -\frac{\partial \boldsymbol{RHS_{15}}}{\partial \boldsymbol{q_{14}}} = b^{+}_{V_1+V_2}\int_{\Omega}({}^{t}[\boldsymbol{N}][\boldsymbol{N}])C_{V_1}dV \tag{3.38}$$

3.3.4 Benchmark to existing model (iron)

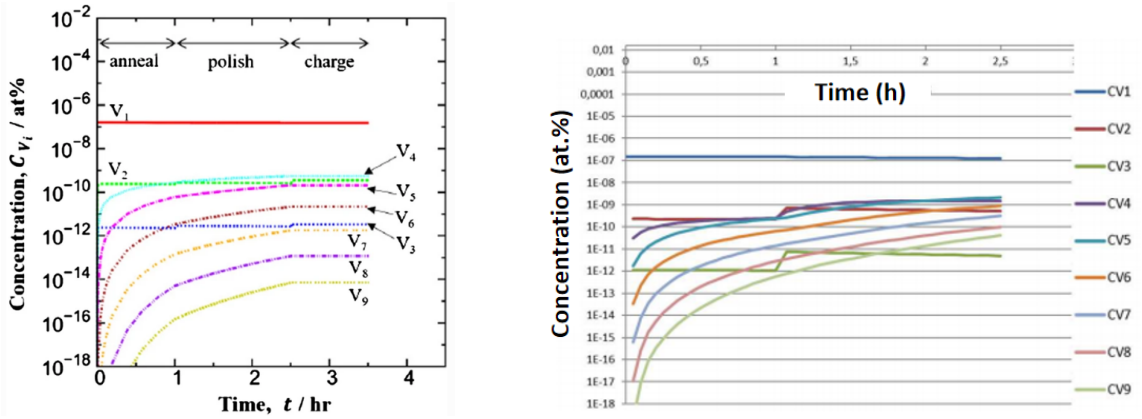

(a) (b)

Figure 3.3: Temporal evolution of C_{V_i}, 3.3a: Ebihara et al. [146], 3.3b: this present work.

Figure 3.3 (a) presents the results of the distribution of C_{V_i} of Ebihara et al. [146], during the annealing ($T_{annealing}$ = 303 K), polishing ($T_{polishing}$ = room temperature, as it is not given, we assume $T_{polishing}$ = 293 K), and charging ($T_{charging}$ = 303 K) processes, which are related to a cut-out $10 \times 10 \times 0.3$mm of the sample. In their case, the material used is pure iron, and the sample was subjected to a tensile test (303 K, $8.3 \times 10^{-6}\,\mathrm{s}^{-1}$, 25%) and then annealed for 1800 s at 1173 K to reduce defects. The initial C_{V_1} in their case has been set to 2.8×10^{-7} (at.%). Please refer to [146] for more details of the parameters utilized. In Figure 3.3 (b), our results calculated by Abaqus are presented.

We can see that the C_{V_1}, C_{V_2}, C_{V_3} and C_{V_4} are quite close to that of Ebihara et al. Furthermore, there's a jump for C_{V_2} and C_{V_3} when the temperature changes: $T_{annealing}$ = 303 K, $T_{polishing}$ = 293 K. This jump is related to the reaction coefficients $b^-_{V_2}$ and $b^-_{V_3}$. Due to the decrease in temperature, the dissociation rate for C_{V_2} and C_{V_3} also decreases, which leads to their accumulation during the polishing process. The $b^-_{V_i}$ (for i=4 $\rightarrow$ 9), in order of magnitude of 10^{-22} to 10^{-32} s^{-1}, is much smaller than $b^-_{V_2}$ and $b^-_{V_3}$, so the evolution for C_{V_4} to C_{V_9} is smoother.

Table 3.1: Dissociation rate for V_2 and V_3 (see Equation 3.1)

	$b^-_{V_2}$ (s^{-1})	$b^-_{V_3}$ (s^{-1})
T=303 K	2.93×10^{-4}	3.07×10^{-8}
T=293 K	1.25×10^{-4}	7.18×10^{-9}

However, the other vacancy clusters have an apparent discrepancy. Such a situation derives from several aspects, firstly, we found that the value of D_{0V_1} is not presented in the references, it was also found that for D_{0V_4}, D_{0V_5} and D_{0V_6}, there is a factor of 10 that was missing. Secondly, by checking the imposed initial condition (value of C_{V_1}), we found it is 1.5×10^{-7} instead of 2.8×10^{-7}, which was declared in [146].

3.3.5 Interaction with the thermal field

In the case of temperature interactions (gradient) are accounted for, which are not considered by Ebihara et al., $\boldsymbol{AMATRX_{i,12}} = -\partial \boldsymbol{RHS_{13}}/\partial \boldsymbol{q_{12}}$ must be defined too (it is worth noting that if hydrogen impact on C_{V_i} mobility is furthermore defined, $\boldsymbol{AMATRX_{i,11}}$ is needed too). In such a case, the expressions of $\boldsymbol{RHS}_i$ are not modified, although several parameters

become T-dependant, such as $D_{V_i}(T)$, $b^-_{V_{i+1}}(T)$ and $b^+_{V_1+V_i}(T)$:

$$\begin{cases} D_{V_i} = D_{0V_i} \exp\left(-\frac{Q_{V_i}}{RT}\right) \\ \\ b^+_{V_1+V_j} = 4\pi(r_{V_1} + r_{V_j})(D_{V_1} + D_{V_j}) \\ \\ b^-_{V_i} = 4\pi(r_{V_1} + r_{V_i})(D_{V_1} + D_{V_i}) N_S \exp\left(-\frac{E^b_{V_i}}{RT}\right) \end{cases} \tag{3.39}$$

The $\boldsymbol{AMATRX}$ components related to T can be written as:

$$\begin{aligned} \boldsymbol{AMATRX_{13,12}} = \frac{\partial \boldsymbol{RHS}_{12}}{\partial \boldsymbol{q}_{12}} = & \int_\Omega \frac{dT}{d\boldsymbol{q}_{12}} \frac{\partial D_{V_1}(T)}{\partial T}^t [\boldsymbol{\nabla N}] \boldsymbol{\nabla} C_{V_1} dV + \int_\Omega \frac{dT}{d\boldsymbol{q}_{12}} \frac{\partial (S_{V_1} D_{V_1})}{\partial T} C_{V_1} [\boldsymbol{N}] dV \\ & + \int_\Omega \frac{dT}{d\boldsymbol{q}_{12}} \frac{b^+_{V_1+V_1}}{\partial T} C^2_{V_1} [\boldsymbol{N}] dV - \int_\Omega \frac{dT}{d\boldsymbol{q}_{12}} \frac{b^-_{V_2}}{\partial T} C_{V_2} [\boldsymbol{N}] dV \\ & + \int_\Omega \frac{dT}{d\boldsymbol{q}_{12}} \frac{b^+_{V_1+V_2}}{\partial T} C_{V_1} C_{V_2} [\boldsymbol{N}] dV - \int_\Omega \frac{dT}{d\boldsymbol{q}_{12}} \frac{b^-_{V_3}}{\partial T} C_{V_3} [\boldsymbol{N}] dV \\ & - \int_\Omega \frac{dT}{d\boldsymbol{q}_{12}} \frac{\partial (S_{V_1} D_{V_1})}{\partial T} C^{eq}_{V_1} [\boldsymbol{N}] dV \end{aligned} \tag{3.40}$$

$$\begin{aligned} \boldsymbol{AMATRX_{14,12}} = \frac{\partial \boldsymbol{RHS}_{13}}{\partial \boldsymbol{q}_{12}} = & \int_\Omega \frac{dT}{d\boldsymbol{q}_{12}} \frac{\partial D_{V_2}(T)}{\partial T}^t [\boldsymbol{\nabla N}] \boldsymbol{\nabla} C_{V_2} dV + \int_\Omega \frac{dT}{d\boldsymbol{q}_{12}} \frac{\partial (S_{V_2} D_{V_2})}{\partial T} C_{V_2} [\boldsymbol{N}] dV \\ & - \int_\Omega \frac{dT}{d\boldsymbol{q}_{12}} \frac{b^+_{V_1+V_1}}{\partial T} C^2_{V_1} [\boldsymbol{N}] dV + \int_\Omega \frac{dT}{d\boldsymbol{q}_{12}} \frac{b^-_{V_2}}{\partial T} C_{V_2} [\boldsymbol{N}] dV \\ & + \int_\Omega \frac{dT}{d\boldsymbol{q}_{12}} \frac{b^+_{V_1+V_2}}{\partial T} C_{V_1} C_{V_2} [\boldsymbol{N}] dV - \int_\Omega \frac{dT}{d\boldsymbol{q}_{12}} \frac{b^-_{V_3}}{\partial T} C_{V_3} [\boldsymbol{N}] dV \end{aligned} \tag{3.41}$$

$$\begin{aligned} \boldsymbol{AMATRX_{15,12}} = \frac{\partial \boldsymbol{RHS}_{14}}{\partial \boldsymbol{q}_{12}} = & \int_\Omega \frac{dT}{d\boldsymbol{q}_{12}} \frac{\partial D_{V_3}(T)}{\partial T}^t [\boldsymbol{\nabla N}] \boldsymbol{\nabla} C_{V_3} dV + \int_\Omega \frac{dT}{d\boldsymbol{q}_{12}} \frac{\partial (S_{V_3} D_{V_3})}{\partial T} C_{V_3} [\boldsymbol{N}] dV \\ & - \int_\Omega \frac{dT}{d\boldsymbol{q}_{12}} \frac{b^+_{V_1+V_2}}{\partial T} C_{V_1} C_{V_2} [\boldsymbol{N}] dV + \int_\Omega \frac{dT}{d\boldsymbol{q}_{12}} \frac{b^-_{V_3}}{\partial T} C_{V_3} [\boldsymbol{N}] dV \end{aligned} \tag{3.42}$$

with

$$\begin{cases} \frac{dT}{d\boldsymbol{q}_{12}} =^{t} [\boldsymbol{N}] \\ \frac{\partial D_{V_i}(T)}{\partial T} = \frac{Q_{V_i}}{RT^2} D_{V_i}(T) \\ \frac{\partial S_{V_i} D_{V_i}}{\partial T} = D_{V_i}(\frac{\partial S_{V_i}}{\partial T} + \frac{Q_{V_i}}{RT^2} S_{V_i}) \\ \frac{\partial b^+_{V_1+V_1}}{\partial T} = \frac{2Q_{V_1}}{RT^2} b^+_{V_1+V_1} \\ \frac{\partial b^+_{V_1+V_i}}{\partial T} = (\frac{Q_{V_1}}{RT^2} D_{V_1} + \frac{Q_{V_i}}{RT^2} D_{V_i)} 4\pi(r_{V_1} + r_{V_i}) \\ \frac{\partial b^-_{V_i}}{\partial T} = \frac{\partial b^+_{V_1+V_i}}{\partial T} N_S \exp(-\frac{E^b_{V_i}}{RT}) + \frac{E^b_{V_i}}{RT^2} b^-_{V_i} \end{cases} \tag{3.43}$$

3.4 Application to Monoblock

In this part, the mobility and clustering of vacancies described before will be applied to ITER divertor monoblock.

3.4.1 Material properties

The geometry, mesh, thermal and mechanical properties of ITER divertor monoblock are the same as in the previous sections. We assume, for the reference case, that the value of the concentration of thermodynamic equilibrium $C^{eq}_{V_1}$ does not depend on the temperature and it is set to 10^{-4} at.% [301]. S_{V_i} (i=1 $\rightarrow$ 9) is set to 10^{14} m^{-2} [302,303] and D_{0V_i} (i=1 $\rightarrow$ 9) is set to 177×10^{-8} $m^2 s^{-1}$ [304]. Several values have been identified for the migration/diffusion and binding energies:

- Q_{V_1}=1.7 eV, Q_{V_2}=1.65 eV, Q_{V_3}=0.85 eV and Q_{V_i}= 0 for i > 3 [305].
- Q_{V_i}=1.66 eV for i=1 $\rightarrow$ 9 [56].

In view of the incompleteness of Q_{V_i} in [305] and the unicity of Q_{V_i} in [56], we decided to combine both of them for our computations: Q_{V_1}=1.7 eV, Q_{V_2}=1.65 eV, Q_{V_3}=0.85 eV and Q_{V_i}=1.66 eV for i=4 $\rightarrow$ 9.

Several propositions have been found in the literature regarding the vacancy cluster binding energy $E^b_{V_i}$ (see Table 3.2). On account of the integrity of data, firstly, only propositions 2 and 5 are appropriate to be considered. Secondly, besides the apparent differences between these

two propositions, we notice that the binding energy for divacancy ($E^b_{V_2}$) remains controversial: either positive or negative. However, in [306], $E^b_{V_2}$=0.6559 eV, which is very close to the only existing experimental value of 0.7 eV by JY Park et al. [307]. Moreover, CS Becquart et al. [304] indicated that more recent ab initio calculations using the software PLATO are in contradiction with their finding ($E^b_{V_2}$=-0.1 eV) as the authors of [308] obtained $E^b_{V_2}$=0.41 eV. In view of these two arguments, proposition 2 is used for our computations.

Table 3.2: Binding energy $E^b_{V_i}$ in eV

i	Prop. 1 [309]	Prop. 2 [306]	Prop. 3 [310]	Prop. 4 [311]	Prop. 5 [304]
1	-	-	-	-	-
2		0.6559	0.029	0.01	-0.1
3	0	1.1127	0.269	0.19	0.04
4	0.6	1.8942	1.065	0.78/0.64	0.64
5	1.3	1.7833	1.965/0.85		0.72
6	2.25	2.2953	2.11		0.89
7	2.9	1.7459			0.72
8		1.8353			0.88
9		2.2658			1.2

3.4.2 Simulation conditions

In [312], the vacancy clusters up to 8 vacancies (V_8) have been investigated in tungsten. On account of the variety of V_i and especially, for the lack of data of material parameters, we initially decide to limit up to 9 vacancies ($V_{i=1\rightarrow 9}$) in this present work.

The total simulation time is the same: 1.56×10^5 s, which represents a duration that has been estimated by assuming a scenario of 39 25s-pulses per day during 16 months (160 cycles, i.e. 3 days as a cycle). A thermal flux of 10 MW/m^2 due to plasma exposure is imposed on the surface S_{top}, and a constant temperature $T = 343$ K is maintained on the surface $S_{coolant}$ (see Figure 2.90).

We assume that only mono-vacancies (C_{V_1}) are initially present in the sample, so at $t = 0$, $C_{V_1} = 10^{-4}$ ($at.\%$) and $C_{V_{i=2\rightarrow 9}} = 0$. We chose this value because it is a classical value used by diffusion-reaction codes to reproduce TDS spectrum. A boundary condition, which is

described by a null flux of C_{V_i}, is also taken into account: ∇C_{V_i}=0 on the symmetry surfaces (see Figure 3.8a).

3.4.3 Results

In Figure 3.4 is presented the T field at the end of the computation.

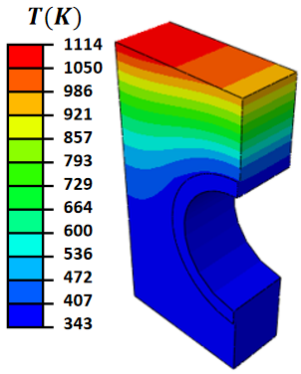

Figure 3.4: Temperature field at the end of the computation.

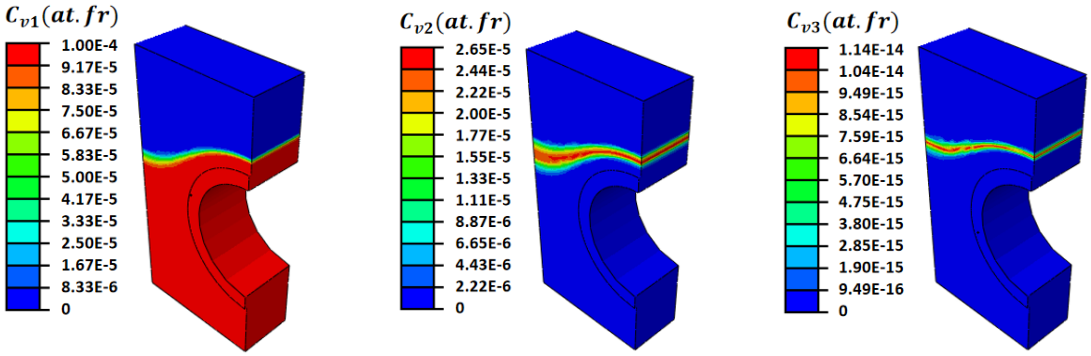

(a) (b) (c)

Figure 3.5: $C_{V_1} \sim C_{V_3}$ fields at the end of the computation.

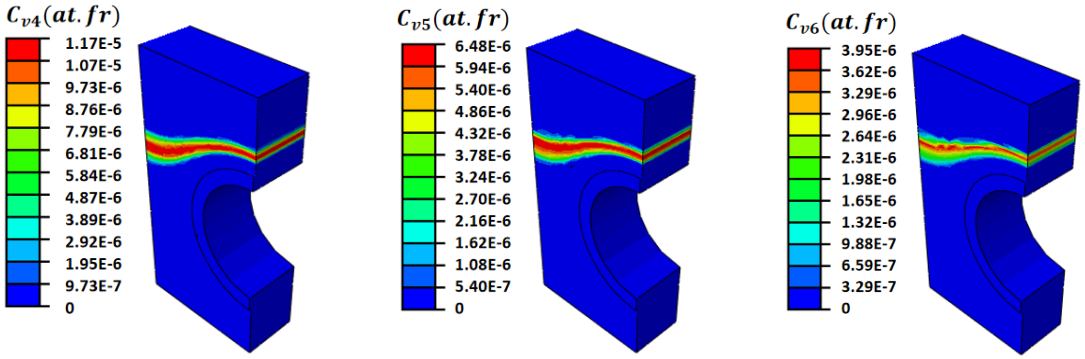

(a) (b) (c)

Figure 3.6: $C_{V_4} \sim C_{V_6}$ fields at the end of the computation.

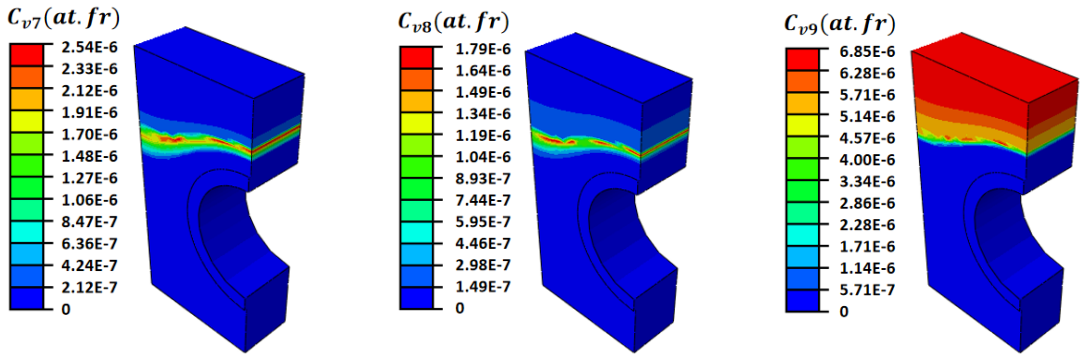

(a) (b) (c)

Figure 3.7: $C_{V_7} \sim C_{V_9}$ fields at the end of the computation.

It can be observed that all C_{V_i} field zones follow some certain isotherms, as is characteristic of a thermally activated process. Furthermore, the temperature increase leads to the occurrence of bigger-sized clusters: C_{V_i} fields are concentrated between two isotherms ($\sim 530K$ for $C_{V_{1\to 8}}$, $\sim 1100K$ for C_{V_9}). In Figure 3.8b is plotted the C_{V_i} evolution along the BA edge, at the end of the computation, confirming the analysis expressed on the whole model: all C_{V_1} would be consumed as soon as T is high enough. Then, clusters are created: a C_{V_i} species is consumed to form a $C_{V_{i+1}}$ one as soon as the temperature is high enough and if there is enough C_{V_1} left.

There is, last, almost no C_{V_3} left: all of it has transformed into C_{V_1}, C_{V_2} and C_{V_4}(see table 3.3). The higher the temperature, the more significant transformation of C_{V_3}.

Table 3.3: Reaction coefficients (see Equation 3.1)

	$b^+_{V_1+V_2}(mm^3/s)$	$b^-_{V_3}(s^{-1})$	$b^+_{V_1+V_3}(mm^3/s)$	$b^-_{V_4}(s^{-1})$
T=343K	2.90×10^{-10}	1.10×10^{-14}	197	5.83×10^{-38}
T=1114K	2.40×10^{7}	9.64×10^{5}	8.75×10^{10}	0.1

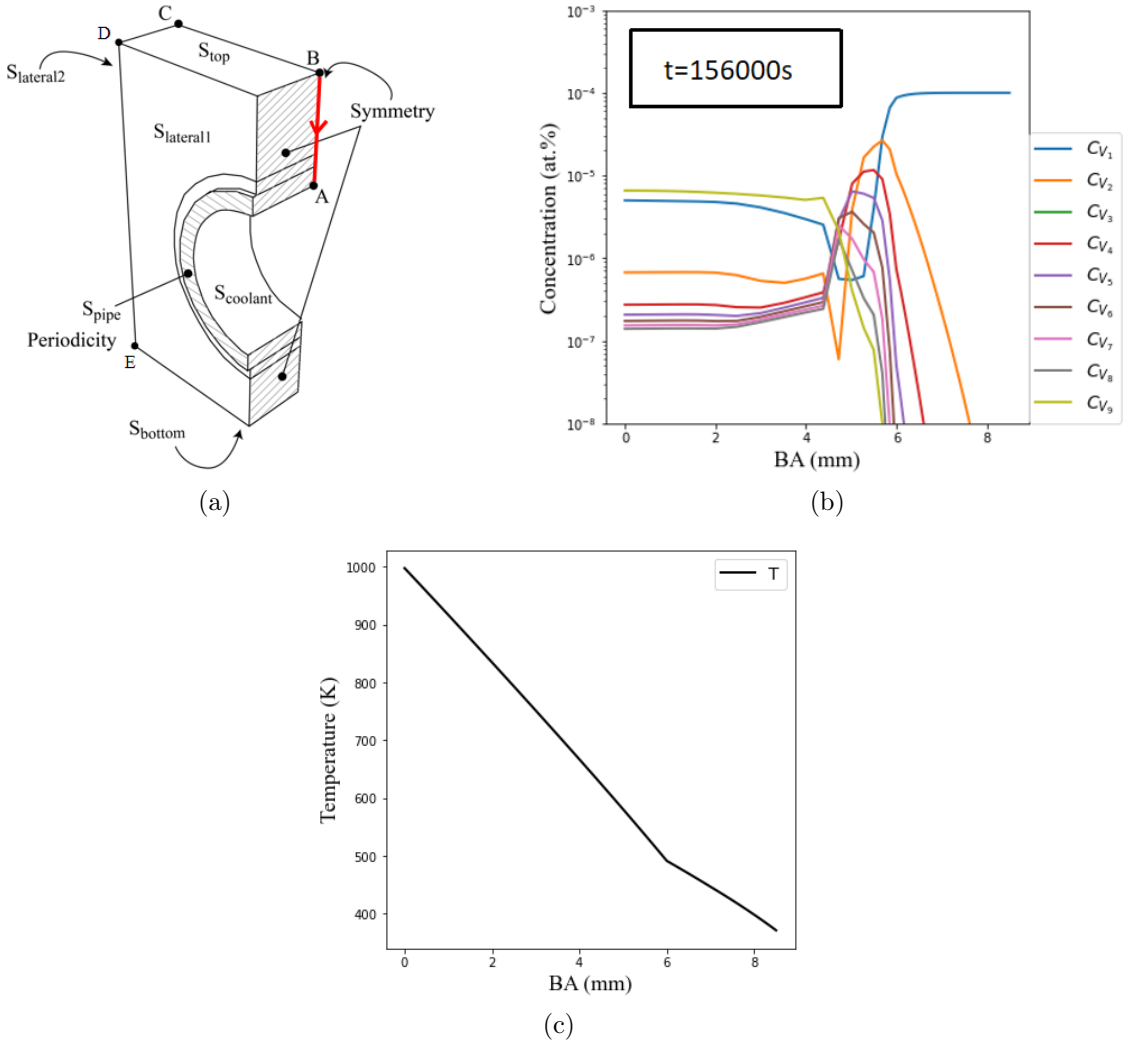

Figure 3.8: (a) BA edge on the monoblock, (b) Spatial evolution of C_{V_i} along BA edge, (c) Distribution of temperature along BA edge.

In Figure 3.9b is plotted the temporal evolution of the C_{V_i} around the middle of the DE

edge. At $t = 0$, all species are zero expect C_{V_1} which has been set to $10^{-4}\,at.\%$. Then, other species appear when C_{V_1} begins to decrease: as it is needed to have C_{V_i} to form $C_{V_{i+1}}$, the bigger the cluster, the lower its concentration. Interestingly, C_{V_3} is far lower than all other species concentrations, indicating that this kind of vacancy cluster, with the used material parameters, has been totally transformed into others. It is an unstable species.

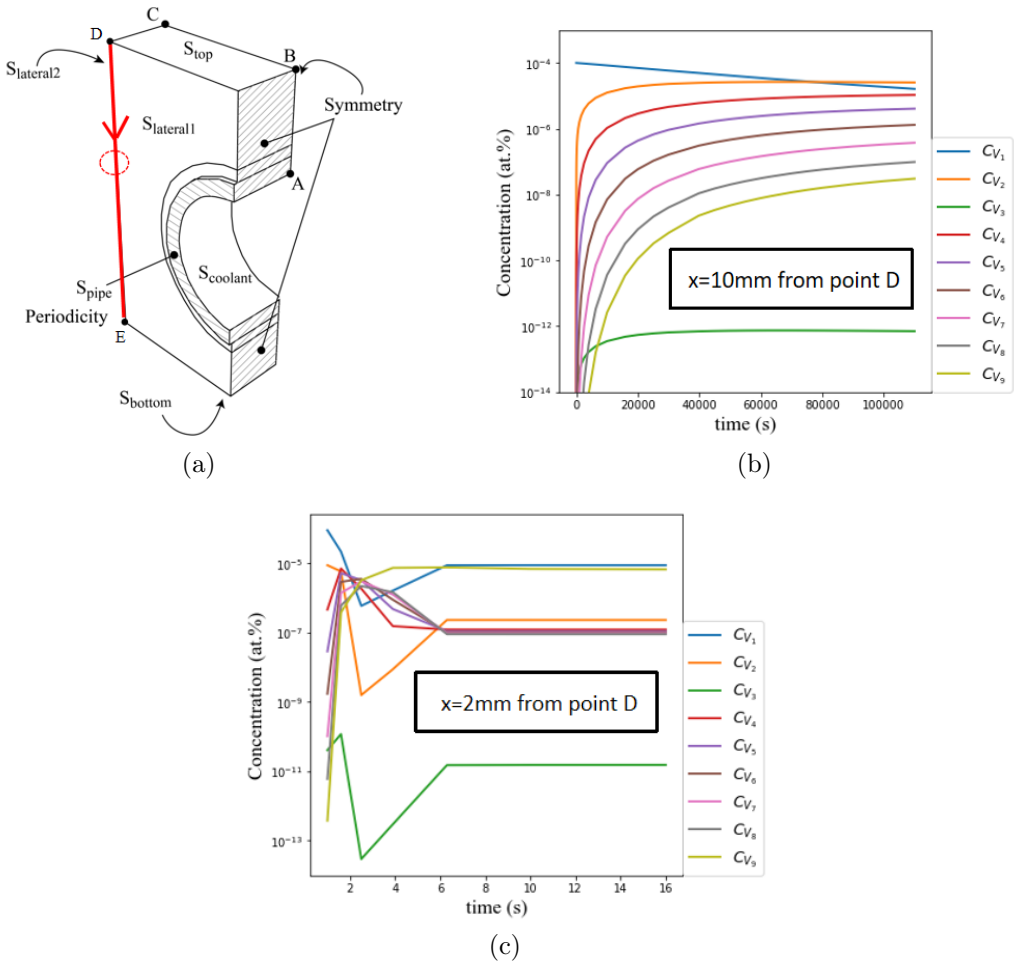

Figure 3.9: (a) Position x of DE edge, (b) & (c) Temporal evolution of C_{V_i} at x=10mm & 2mm of DE edge.

In Figure 3.9 (c), the temporal evolution is depicted similarly to that in Figure 3.9 (b) but near the hot surface S_{top}. It is evident that due to the elevated temperature, the steady state is achieved in approximately 6 seconds. At the end of the clustering process, the two dominant species are C_{V_1} and C_{V_9}. Although the other species are not as significant as C_{V_1}

and C_{V_9}, they cannot be overlooked since they play a crucial role in the formation of C_{V_9}.

3.4.4 Parametric Studies

3.4.4.1 Influence of diffusion term D_{V_i} (based on reference case)

When a vacancy traps H atoms, its barrier energy of diffusion increases so that the jump frequency of the vacancy is several orders of magnitude smaller than the case without trapping H atoms, which means the diffusion of vacancy will be suppressed by the presence of H atoms, and a similar situation may occur for vacancy clusters [146]. As for this suppression of the diffusion of vacancies or vacancy clusters, in [290], the authors have used a vacancy clustering process, in which the diffusion term was not taken into account. To investigate this suppression of the diffusion of vacancies or vacancy clusters, the same computation as previously (reference case) has been made, assuming $D_{V_i} = 0$ for all species in our model. The results are presented in Figures 3.10 to 3.12.

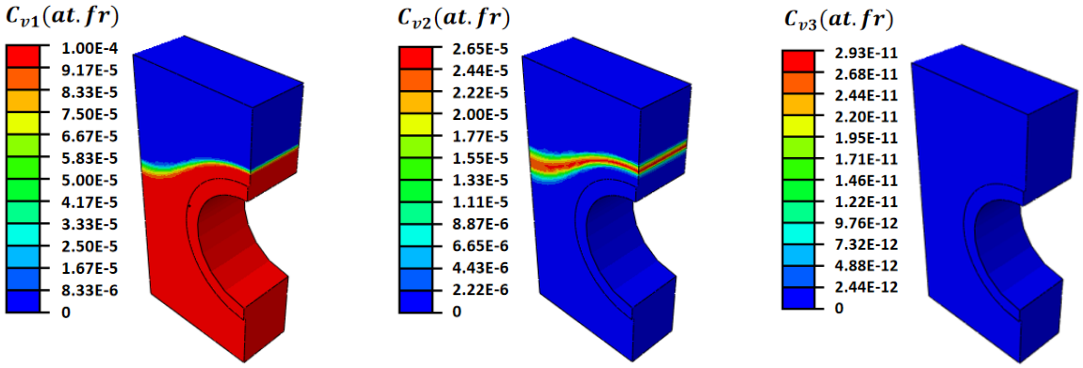

(a) (b) (c)

Figure 3.10: $C_{V_1} \sim C_{V_3}$.

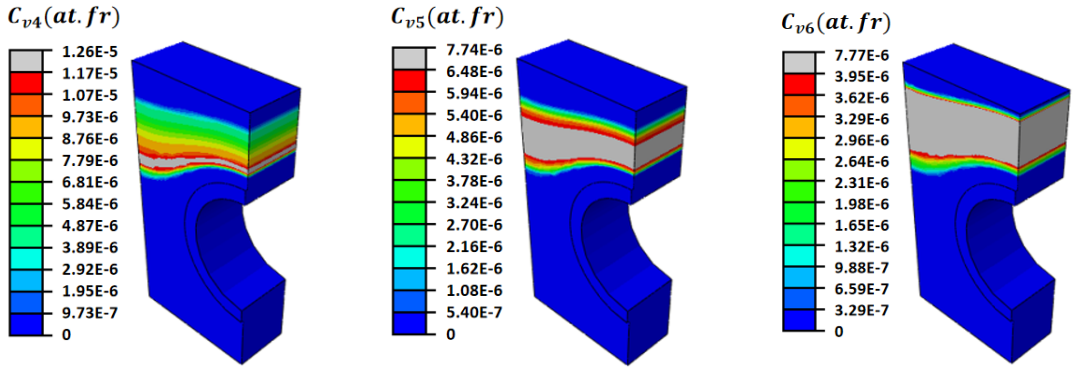

(a) (b) (c)

Figure 3.11: $C_{V_4} \sim C_{V_6}$.

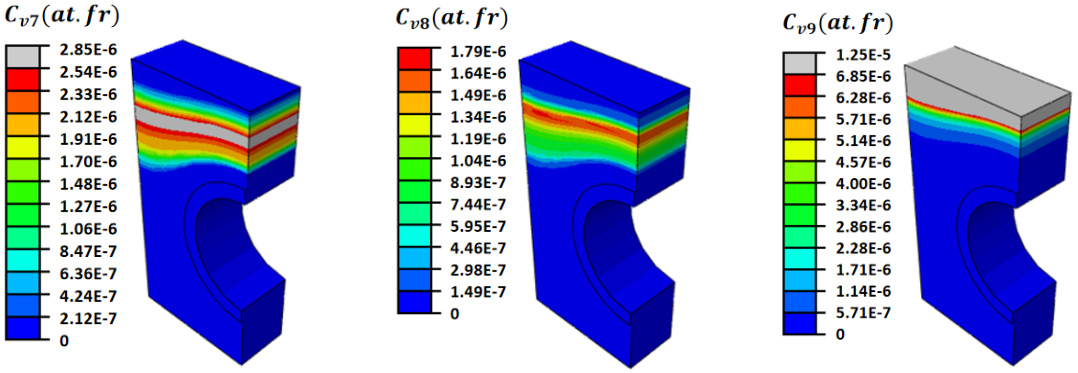

(a) (b) (c)

Figure 3.12: $C_{V_7} \sim C_{V_9}$.

While C_{V_1} to C_{V_3} fields seem not to be affected, the distribution of the other species is markedly modified in terms of localization and maximum value. Cluster diffusion, indeed, promotes the transport of vacancies from high-concentration zones to low ones, limiting the maximum value that can be reached. Furthermore, without diffusion, once all C_{V_1} is consumed by the reactions at one point, no more clustering reactions can occur.

3.4.4.2 Influence of boundary conditions (based on reference case)

In this part, C_{V_i} is set to 0 on all exterior surfaces except on the symmetry surfaces, to mimic the non-presence of vacancy clusters on the outer surfaces: vacancies/vacancy clusters should only exist inside the material. The results are presented in Figures 3.13 to 3.15. It can be observed that the change of this kind of boundary condition (C_{V_i}=0 on the exterior surfaces) has no impact on the C_{V_i} fields.

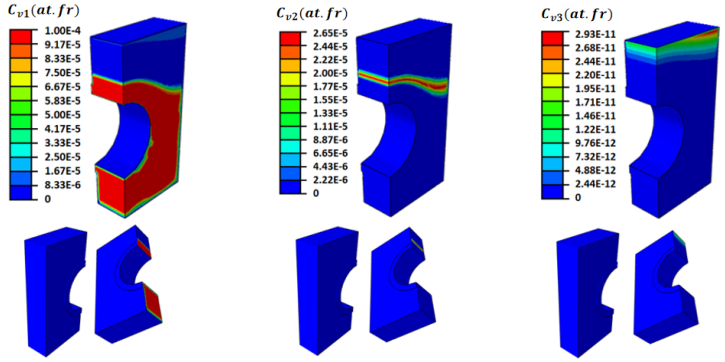

(a) (b) (c)

Figure 3.13: $C_{V_1} \sim C_{V_3}$.

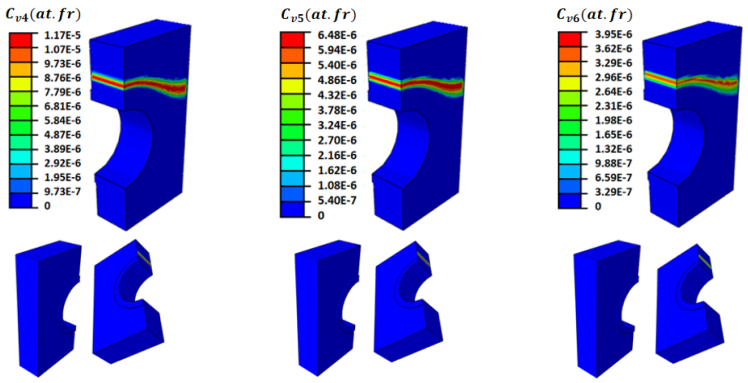

(a) (b) (c)

Figure 3.14: $C_{V_4} \sim C_{V_6}$.

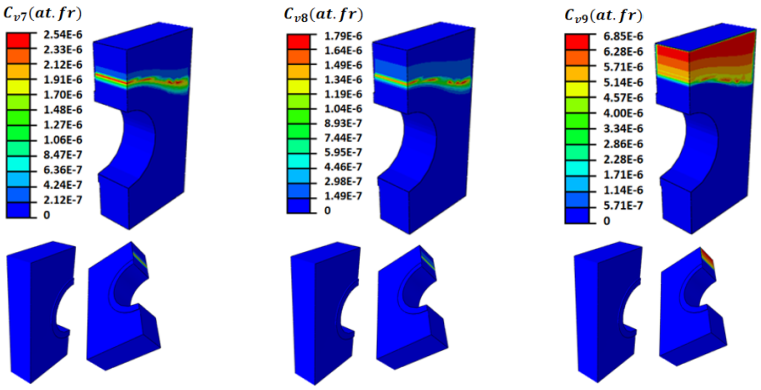

(a) (b) (c)

Figure 3.15: $C_{V_7} \sim C_{V_9}$.

3.4.4.3 Influence of $C_{V_1}^{eq}$ (based on 3.4.4.2)

In this part, $C_{V_1}^{eq}$ is set as a function of the temperature [313]:

$$C_{V_1}^{eq}(T) = \exp\left(-\frac{G_F}{k_B T}\right) = \exp\left(\frac{S_F}{k_B}\right)\exp\left(-\frac{H_F}{k_B T}\right) = A \cdot \exp\left(-\frac{H_F}{k_B T}\right) \tag{3.44}$$

where G_F denotes the Gibbs energy of the vacancy formation, H_F is the formation enthalpy (see Table 3.4 for the various values that can be found in the literature), S_F the formation entropy (not including the configurational entropy), k_B the Boltzmann constant, and T the absolute temperature.

Table 3.4: Vacancy formation enthalpy

Reference	[314]	[315]	[316]	[317]	[313]	[313]	[318]	[313]
H_F (eV)	3.27	3.43	3.62	3.80	4.00	4.10	4.57	4.60

An estimation of the formation entropy S_F was proposed by Varotsos [319]

$$S_F = S_F^* + V_F \beta B \tag{3.45}$$

$S_F = -(\partial G_F/\partial T)_P$ is the vacancy-formation entropy under constant pressure, $S_F^* = -(\partial G_F/\partial T)_V$ is the formation entropy under constant volume, $V_F = (\partial G_F/\partial p)_T$ is the formation volume, β is the volume thermal expansivity, and B is the isothermal bulk modulus, noting that

$$|S_F| > |S_F^*| \quad \text{and} \quad S_F^* \leq 0 \tag{3.46}$$

In most cases, S_F and V_F are positive, leading to

$$S_F \leq V_F \beta B \tag{3.47}$$

with $V_F = 0.4 \times V_{atomic}$, in which V_{atomic} is the atomic volume at room temperatures ($V_{atomic} = 1.58 \times 10^{-29}\, m^3$), $\beta = 3.2 \times 10^{-5}\, K^{-1}$ and $B = 3.1 \times 10^{11}\, N/m^2$. The upper limit of S_F is calculated as

$$S_F = V_F \beta B = (0.42\Omega)\beta B = 6.58 \times 10^{-23}\, J/K \tag{3.48}$$

and

$$A = \exp\left(\frac{S_F}{k_B}\right) = 117.95 \tag{3.49}$$

then

$$C_{V_1}^{eq}(T) = 117.95 \cdot \exp\left(-\frac{H_F}{k_B T}\right) \tag{3.50}$$

$C_{V_1}^{eq}$ at $T = T_{melting}$ =3695 K for the different H_F values listed in table 3.4 can be found in table 3.5, and in Figure 3.16a is plotted the $C_{V_1}^{eq}$ values as a function of T. We chose two extreme cases: $H_F = 3.27$eV and $H_F = 4.60$ eV for the comparison between $C_{V_1}^{eq}$=constant (10^{-4}) and $C_{V_1}^{eq}(T)$. In the range of the temperature field experienced by monoblock (343 $\sim$ 1114K), $C_{V_1}^{eq}$ is much lower than 10^{-4} (see Figure 3.16c).

Table 3.5: $C_{V_1}^{eq}$ at melting point of W

$T = T_{melting}$ =3695 K								
H_F (eV)	3.27	3.43	3.62	3.80	4.00	4.10	4.57	4.60
$C_{V_1}^{eq}$ (10^{-4} at.%)	40.9	24.7	13.6	7.74	4.13	3.02	0.69	0.63

It's interesting and important to introduce the characteristic time $\frac{1}{S_{V_1} D_{V_1}}$, which represents the necessary time for existing or implanted C_{V_1} to reach its thermodynamic equilibrium state($C_{V_1}^{eq}$). We can see that the higher the temperature, the shorter the time to reach the equilibrium state: t=0.3 s for T=1114 K; t=5.6×10^{16} s for T=343 K (see Figure 3.16d).

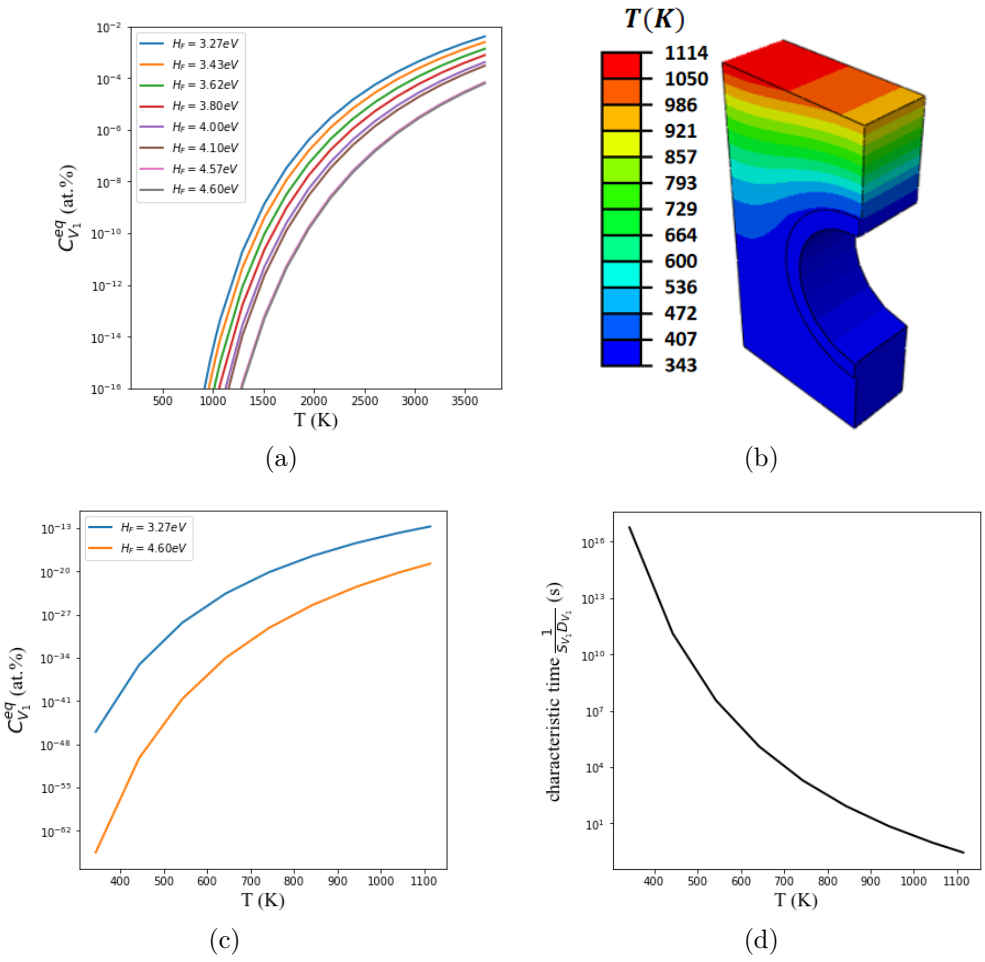

Figure 3.16: (a) $C_{V_1}^{eq}(T)$ for different formation enthalpies, (b) T-field, (c) $C_{V_1}^{eq}(T)$ with $H_F = 3.27\ eV$ and $4.60\ eV$, and (d) Characteristic time for C_{V_1} in terms of T.

In Figures 3.17 to 3.21 are plotted the results obtained when a $C_{V_1}^{eq}(T)$ function is used, with H_F=3.27 eV (corresponding to an extreme case). There's a negligible decrease of $C_{V_i, i=1...5}$, and a slight decrease of $C_{V_i, i=6...8}$. This can be explained by a decrease of the available C_{V_1} in the global reaction process. As a consequence, the chemical equilibrium is shifted to reduce the concentration of the other species.

Furthermore, the distribution of C_{V_1} in the actual case (Figure 3.17b) is almost the same, at the zone where T under 500K, as that of reference case (Figure 3.17a). For this, it can be explained by the characteristic time. Since the characteristic time for T $< 500\ K$ is around $\sim 10^9\ s$ to $10^{16}\ s$, which is much longer than our simulation time $10^5\ s$, so the C_{V_1} in this

low-temperature zone remains unchanged as the initial condition.

Finally, a significant reduction, due to the accumulated reduction of all smaller-sized clusters, of C_{V_9} is shown.

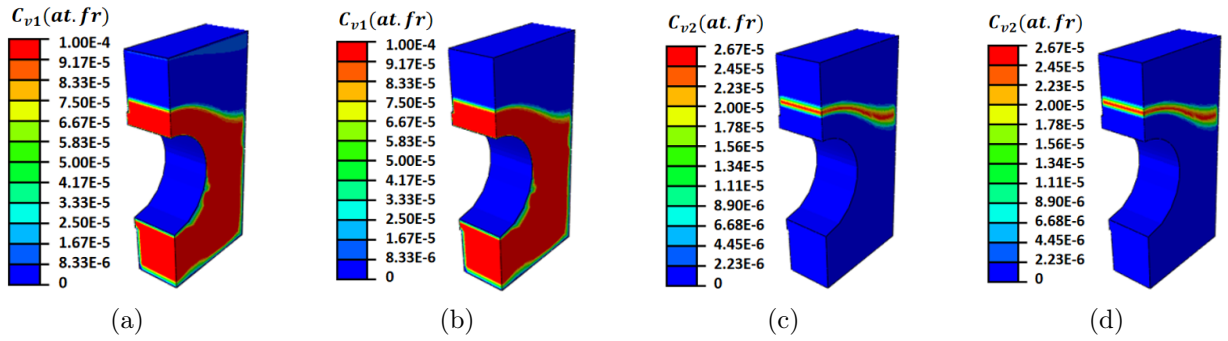

(a) (b) (c) (d)

Figure 3.17: $C_{V_1} \sim C_{V_2}$ (a & c: case in Section 3.4.4.2, b & d: present case).

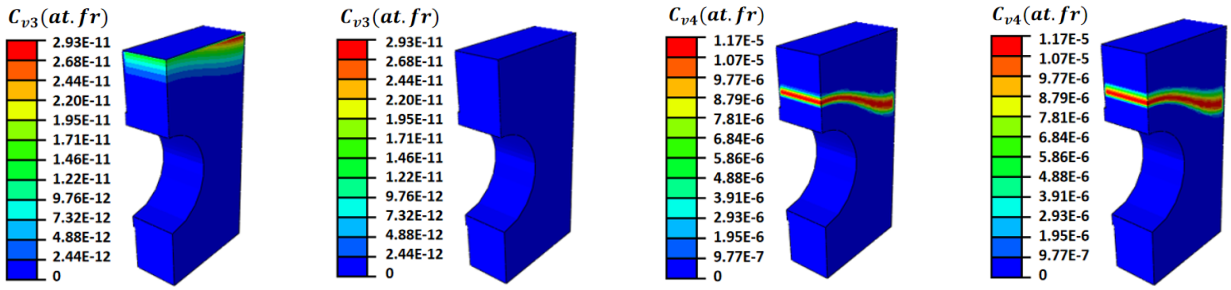

(a) (b) (c) (d)

Figure 3.18: $C_{V_3} \sim C_{V_4}$ (a & c: case in Section 3.4.4.2, b & d: present case).

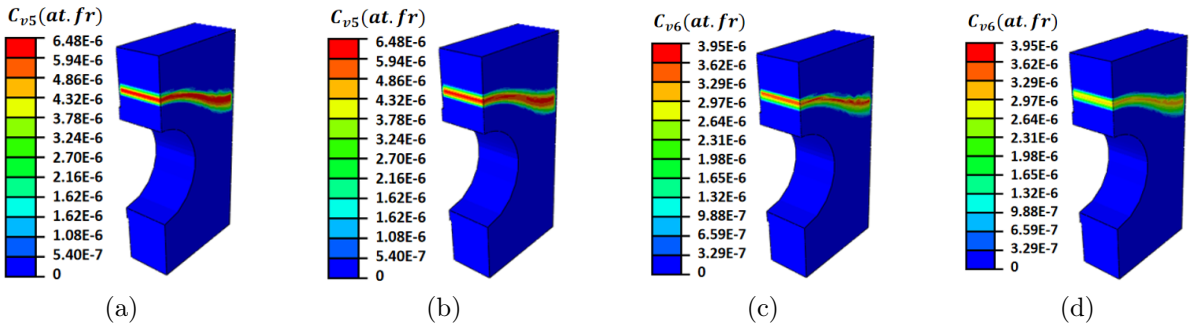

Figure 3.19: $C_{V_5} \sim C_{V_6}$ (a & c: case in Section 3.4.4.2, b & d: present case).

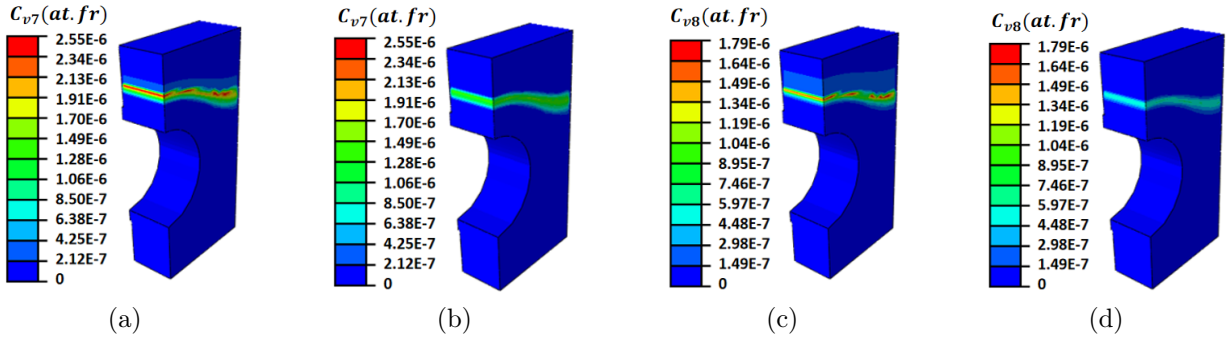

Figure 3.20: $C_{V_7} \sim C_{V_8}$ (a & c: case in Section 3.4.4.2, b & d: present case).

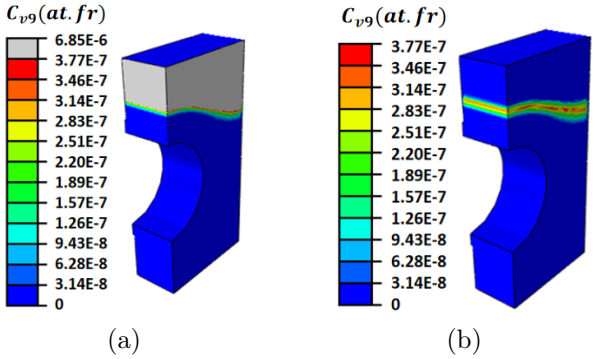

Figure 3.21: C_{V_9} (a: case in Section 3.4.4.2, b: present case).

3.4.5 Vacancy generation at the plasma exposed surface

In the previous section, only the thermodynamic vacancy source has been accounted for. However, other sources of vacancy can also be explored, as the ones due to the thermonuclear fusion environment. During plasma operations, tungsten is bombarded by intense fluxes of high-energy neutrons, hydrogen isotopes (HIs), and helium (He) particles [320]. The irradiation effects of these particles on tungsten are extremely important to be explored owing to the intensified structure modification and property degradation [291, 320–326].

A large number of mitigated edge localized modes (ELMs) are expected in ITER transient events [311, 327, 328], in which vacancy generation can take place [329]. M. Pečovnik et al. have conducted simulations to reproduce experimental results, in which tungsten was sequentially or simultaneously irradiated by 10.8 MeV W ions and 300 eV deuterium ones. A novel displacement damage creation and stabilization model was developed and introduced into the MHIMS-Reservoir code [284]. The effect of deuterium (D) presence, which was presented during ITER conditions (ELMs), was found to be largest in mono-vacancies as its concentration increased by about a factor of 3, as observed identified using positron annihilation lifetime spectroscopy (PALS) [330].

This section is dedicated to the modeling of surface vacancy generation. The first subsection presents the volumetric model of vacancy creation and its conversion to a surface boundary condition. The second one presents the value of the vacancy predicted by this model for ITER conditions. The third one presents some results of the impact of the boundary condition on vacancy concentration in the monoblock. Last a discussion is proposed for the competition between the surface condition and the annihilation term in the bulk.

3.4.5.1 Vacancy surface generation Model

A volume source term has been used to mimic the creation of mono-vacancy due to the plasma exposure, following a Gaussian distribution, such that

$$V(z) = \frac{\alpha \cdot \varphi_{imp}}{\sigma\sqrt{2\pi}} \exp\left(-\frac{(z-\mu)^2}{2\sigma^2}\right) \qquad (m^3 s^{-1}) \tag{3.51}$$

with

$$\begin{cases} \alpha : \text{ratio of vacancies/ions} \\ \varphi_{imp} = (1-r)\varphi_{inc} : \text{implantation ion flux} \\ r = 0.799 : \text{reflection ratio} \\ \varphi_{inc} = 10^{24}(m^{-2}s{-}1) : \text{incident ion flux} \\ \sigma : \text{implantation depth's standard deviation} \\ \mu : \text{mean implantation depth} \end{cases} \tag{3.52}$$

Ions / Energy	H (1 amu)	D (2 amu)	T (3 amu)
300 eV	0	0	0
1 keV	0.0	0.3	1.3
2 keV	0.2	1.8	4.6
3 keV	0.6	3.6	7.2

Figure 3.22: Ratio of vacancies to ions, denoted as α, for various incident energies.

For 3keV ions	H (1 amu)	D (2 amu)	T (3 amu)
μ	21.3 nm	24.9 nm	26.6 nm
σ	11.4 nm	13.5 nm	14.4 nm

Figure 3.23: Standard deviation and mean values of implantation depth for an incident energy of 3 keV.

In Figures 3.22 and 3.23 are presented the necessary parameters of equation 3.51. These parameter values were computed by "Monolayer Collision Steps", with an incidence angle of 0° for the ion flux, in SRIM 2008. As for hydrogen implantation, for the sake of simplicity, this C_{V_1} source term is transformed into a surface boundary condition $C_{V_1} = S_c$ on S_{top}

$$Sc = \frac{\alpha\mu}{D_{V_1}(T)\rho_W}\varphi_{ELM} \qquad (at.\%) \tag{3.53}$$

where ρ_W is the atom density of tungsten, φ_{ELM} the ELM-like ion flux, equal to $\varphi_{imp} \times (1\% \sim 10\%)$. This is made assuming that 1% to 10% of the implantation HIs flux will induce the mono-vacancy only.

3.4.5.2 Values of S_c for ITER conditions

The reference incident ion flux has been set to $\varphi_{inc1} = 10^{24}\, m^{-2}s^{-1}$. Other conditions have also been explored ($\varphi_{inc2} = 10^{23}\, m^{-2}s^{-1}$, $\varphi_{inc3} = 10^{22}\, m^{-2}s^{-1}$, $\varphi_{inc4} = 10^{20}\, m^{-2}s^{-1}$) as a parametric study in the previous chapter. As the heat flux is linked to the particle one, thus, the maximum temperature experienced by the monoblock is dependent on φ_{inc}, as is the temperature on S_{top} (see Figure 3.4). In figure 3.24 are reported, for each incident particle flux, the maximal and minimal temperatures on S_{top}, and the consequences on mono-vacancy's diffusion coefficient.

	T(K)	$D_{v1}(T)$
ϕ_{inc1}=10^{24} (m^{-2} s^{-1})	1114	3.57e-8
	966	2.36e-9
ϕ_{inc2}=10^{23} (m^{-2} s^{-1})	404	1.07e-21
	398	5.12e-22
ϕ_{inc3}=10^{22} (m^{-2} s^{-1})	391	2.11e-22
	388	1.43e-22
ϕ_{inc4}=10^{20} (m^{-2} s^{-1})	378	3.71e-23
	377	3.23e-23

Figure 3.24: Monovacancy's diffusion coefficient

As a consequence, the S_c values vary at each point on S_{top} and for each φ_{ELM} value. If 1%, 5% and 10%, respectively, are considered for the computation of φ_{ELM}, S_c variations on S_{top} can be evaluated for each φ_{inc} (see Figures 3.25 to 3.27).

	T(K)	Sc for 1k eV			Sc for 2k eV			Sc for 3k eV		
		H	D	T	H	D	T	H	D	T
ϕ_{ELM1}	Tmax: 1114	0	0.007	0.031	0.004	0.040	0.109	0.011	0.080	0.171
	Tmin: 966	0	0.100	0.465	0.057	0.603	1.646	0.172	1.206	2.576
ϕ_{ELM2}	Tmax: 404	0	2.2e10	1.0e11	1.3e10	1.3e11	3.6e11	3.8e10	2.7e11	5.7e11
	Tmin: 398	0	4.6e10	2.1e11	2.6e10	2.8e11	7.6e11	7.9e10	5.6e11	1.2e12
ϕ_{ELM3}	Tmax: 391	0	1.1e10	5.2e10	6.4e9	6.8e10	1.8e11	1.9e10	1.3e11	2.9e11
	Tmin: 388	0	1.7e10	7.7e10	9.5e9	1.0e11	2.7e11	2.9e10	2.0e11	4.3e11
ϕ_{ELM4}	Tmax: 378	0	6.4e8	3.0e9	3.7e8	3.8e9	1.0e10	1.0e9	7.7e9	1.6e10
	Tmin: 377	0	7.4e8	3.4e9	4.2e8	4.4e9	1.2e10	1.2e9	8.8e9	1.9e10

Figure 3.25: S_c for 1% ELM-like flux. (Equation 3.53)

	T(K)	Sc for 1k eV			Sc for 2k eV			Sc for 3k eV		
		H	D	T	H	D	T	H	D	T
ϕ_{ELM1}	Tmax:1114	0	0.033	0.154	0.019	0.200	0.545	0.057	0.400	0.853
	Tmin: 966	0	0.502	2.325	0.286	3.014	8.228	0.859	6.028	12.879
ϕ_{ELM2}	Tmax: 404	0	1.1e11	5.1e11	6.3e10	6.7e11	1.7e12	1.9e11	1.3e12	2.8e12
	Tmin: 398	0	2.3e11	1.1e12	1.3e11	1.4e12	3.6e12	4.0e11	2.8e12	6.0e12
ϕ_{ELM3}	Tmax: 391	0	5.6e10	2.6e11	3.2e10	3.4e11	9.2e11	9.6e10	6.8e11	1.4e12
	Tmin: 388	0	8.3e10	3.9e11	4.8e10	5.0e11	1.4e12	1.4e11	1.0e12	2.1e12
ϕ_{ELM4}	Tmax: 378	0	3.2e9	1.2e10	1.8e9	1.9e10	5.2e10	5.5e9	3.8e10	8.2e10
	Tmin: 377	0	3.7e9	1.4e10	2.1e9	2.2e10	6.0e10	6.3e9	4.4e10	9.4e10

Figure 3.26: S_c for 5% ELM-like flux. (Equation 3.53)

	T(K)	Sc for 1k eV			Sc for 2k eV			Sc for 3k eV		
		H	D	T	H	D	T	H	D	T
ϕ_{ELM1}	Tmax:1114	0	0.067	0.308	0.038	0.400	1.090	0.114	0.798	1.706
	Tmin: 966	0	1.005	4.651	0.573	6.028	16.457	1.719	12.056	25.759
ϕ_{ELM2}	Tmax: 404	0	2.2e11	1.0e12	1.3e11	1.3e12	3.6e12	3.8e11	2.7e12	5.7e12
	Tmin: 398	0	4.6e11	2.1e12	2.6e11	2.8e12	7.6e12	7.9e11	5.6e12	1.2e13
ϕ_{ELM3}	Tmax: 391	0	1.1e11	5.2e11	6.4e10	6.8e11	1.8e12	1.9e11	1.3e12	2.9e12
	Tmin: 388	0	1.7e11	7.7e11	9.5e10	1.0e12	2.7e12	2.9e11	2.0e12	4.3e12
ϕ_{ELM4}	Tmax: 378	0	6.4e9	3.0e10	3.7e9	3.8e10	1.0e11	1.0e10	7.7e10	1.6e11
	Tmin: 377	0	7.4e9	3.4e10	4.2e9	4.4e10	1.2e11	1.2e10	8.8e10	1.9e11

Figure 3.27: S_c for 10% ELM-like flux. (Equation 3.53)

As the unit of S_c is in atomic fraction (at.%), values greater than 1 (in red in Figures 3.25 to 3.27) are non-physical, which means that there are more vacancies/voids than atoms. In such a case, it has been considered that the material surface is not correctly defined and S_C is not realistic. Only the reference incident ion flux $\varphi_{inc1} = 10^{24}\, m^{-2}s^{-1}$ leads to realistic values for S_c (in green in Figures 3.25 to 3.27).

3.4.5.3 Results

As no relevant link between φ_{inc} and S_c can be proposed so far, an uniform boundary condition $C_{V_1} = S_c$ in at.% is imposed on S_{top}, with $S_c = 10^{-2}$, 10^{-3}, and 10^{-4} respectively. All the other boundary conditions and initial conditions are the same as in subsection 3.4.4.3.

The results of C_{V_1} to C_{V_9}, for $S_c = 10^{-4}$, are presented in Figures 3.28, 3.29 and 3.30. The distribution of C_{V_1} is the same as that in section 3.4.4.3, except the boundary condition we have imposed at S_{top}. For C_{V_2} to C_{V_9}, a concentration located at the top surface is indeed observed. Especially, C_{V_9} is highly accumulated (up to 10^{-2}).

In Figures 3.31 and 3.32 presented the C_{V_1} and C_{V_9} respectively for $S_c = 10^{-2}$ and $S_c = 10^{-3}$. We notice that the C_{V_9} for $S_c = 10^{-2}$ and $S_c = 10^{-3}$ is not realistic ($C_{V_9} > 1$).

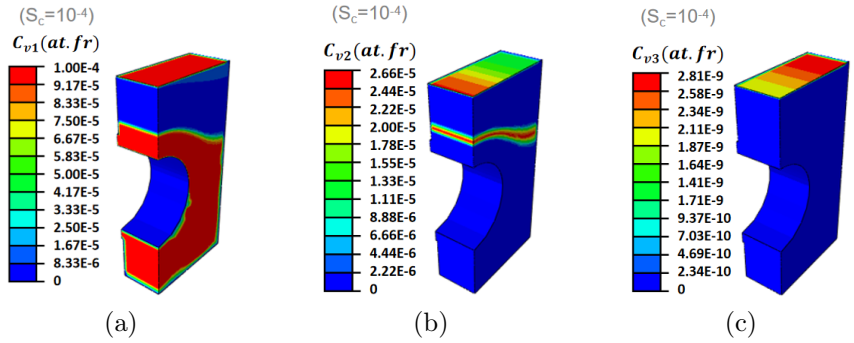

Figure 3.28: $S_c = 10^{-4}$ for (a) C_{V_1}, (b) C_{V_2} and (c) C_{V_3}.

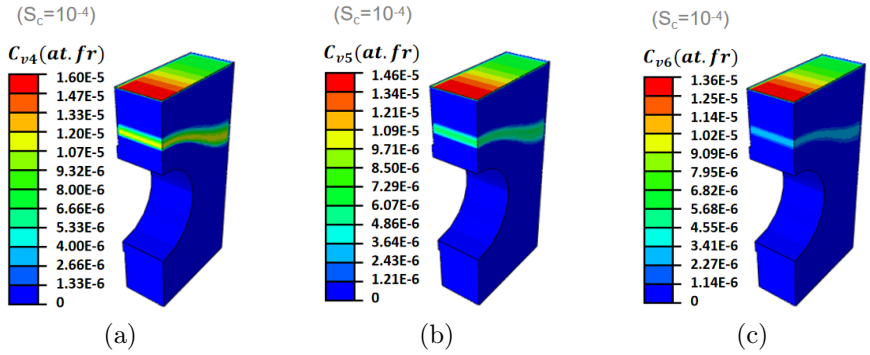

Figure 3.29: $S_c = 10^{-4}$ for (a) C_{V_4}, (b) C_{V_5} and (c) C_{V_6}.

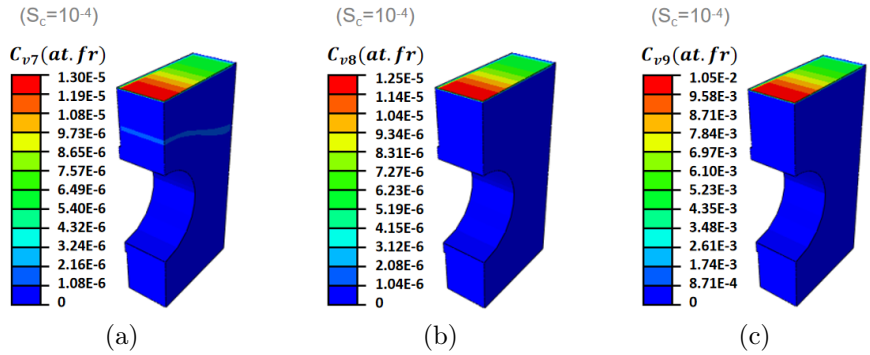

Figure 3.30: $S_c = 10^{-4}$ for (a) C_{V_7}, (b) C_{V_8} and (c) C_{V_9}.

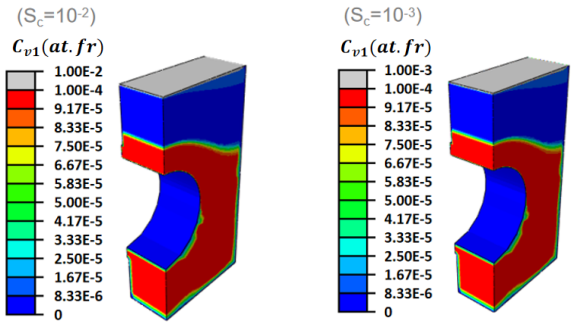

(a) (b)

Figure 3.31: C_{V_1} for (a) $S_c = 10^{-2}$, (b) $S_c = 10^{-3}$.

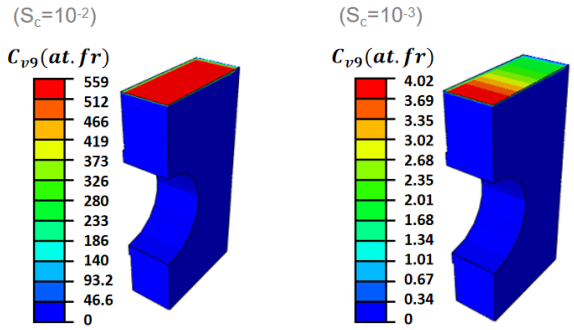

(a) (b)

Figure 3.32: C_{V_9} for (a) $S_c = 10^{-2}$, (b) $S_c = 10^{-3}$.

3.4.5.4 Competition between S_c and $C_{V_1}^{eq}$

In this final section, we fix $S_c = 10^{-4}$ at S_{top}, the initial condition imposed for C_{V_1} is always 10^{-4}, and then perform a comparison between $C_{V_1}^{eq}(T)$ (for $H_F = 4.60eV$) and $C_{V_1}^{eq} = 10^{-4}$, to study the impact of annihilation term $-S_{V_1} D_{V_1}(C_{V_1} - C_{V_1}^{eq})$.

In Figure 3.33 is presented the C_{V_1} distribution, where we can see that when there's no effect of annihilation, C_{V_1} exists also nearby the top surface (Figure 3.33a). From C_{V_2} to C_{V_9}, their concentration is located at the top surface and C_{V_9} is highly accumulated (Figure 3.34), just like the results in Section 3.4.5.3.

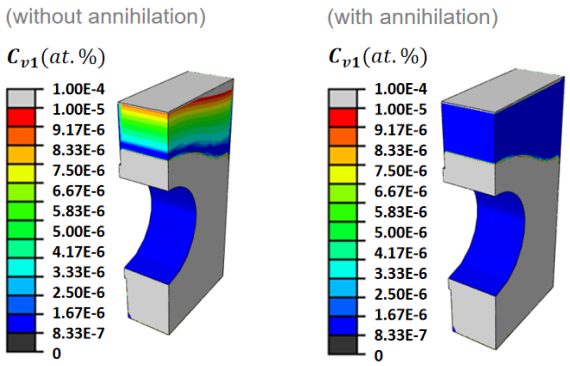

(a) (b)

Figure 3.33: C_{V_1} for (a) $C_V^{eq} = 10^{-4}$ (without annihilation), (b) $C_V^{eq}(T)$ (with annihilation).

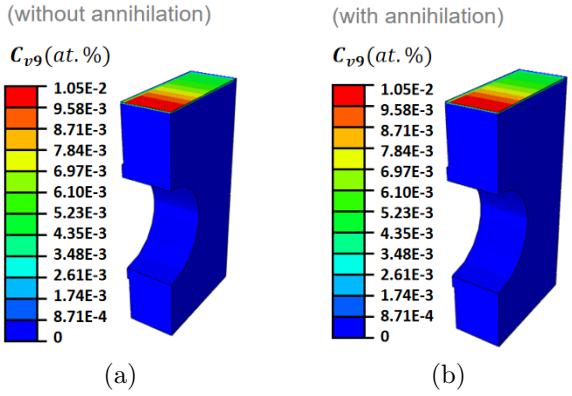

(a) (b)

Figure 3.34: C_{V_9} for (a) $C_V^{eq} = 10^{-4}$ (without annihilation), (b) $C_V^{eq}(T)$ (with annihilation).

3.5 Conclusion

A vacancy clustering model was introduced, with its weak formulation meticulously detailed. We implemented this model in Abaqus using the User Subroutine (UEL). To verify the model, we compared it with results obtained for iron by Ebihara et al. [146]. Subsequently, the model was applied to the ITER divertor monoblock. Notably, the dynamics of the vacancy clusters, up to V_9, were addressed without considering any interaction with hydrogen.

Regardless of the configuration, C_{V_3} is consistently negligible due to its magnitude being significantly smaller than 10^{-4}, this can be attributed to the active reaction coefficients (see Table 3.3), suggesting that V_3 is unstable and can rapidly transform to neighboring species (V_1, V_2, V_4). Furthermore, it has been demonstrated that the source term $C_{V_1}^{eq}$ exerts a more substantial influence on steady-state fields than boundary conditions.

Chemical equilibrium significantly influences the distribution and quantity of C_{V_i}. Any deviation of $C_{V_1}^{eq}$ from the implanted C_{V_1} value, either greater or smaller, will lead to a corresponding increase (creation) or decrease (annihilation) in C_{V_1} due to thermodynamic equilibrium adjustment. This deviation will subsequently induce similar variations in all other C_{V_i} species for i=2 to 9.

To simulate the damage caused by particle irradiation (specifically H in this work) on the plasma exposure surface, a boundary condition, denoted as S_c, was imposed on the exposure surface S_{top} of the ITER divertor monoblock. This irradiation effect manifests as a localized concentration of C_{V_i} at the exposure surface. Based on the S_c results showcased in figures 3.25, 3.26 and 3.27, there appears to be a need for a more refined model (relative to the existing model presented in Figure 3.53) for vacancy generation. For instance, calculations at the nanometric scale, incorporating a volumetric source term for vacancy creation, would be beneficial. This is because the concurrent creation of self-interstitial atoms, when vacancies form at the exposure surface, could also be factored in to constrain the S_c value. For the time being, an S_c value of 10^{-4} might be a viable choice for the GTN model, which will be detailed in the last chapter.

The upcoming work aims at, on the one hand, adding the effect of neutron damage, which implies the creation of vacancies (mono-vacancies) by neutron irradiation, on the other hand, adding the coupling between hydrogen and vacancy clusters: $V_i \rightarrow H_j V_i$. This will incorporate the generation of vacancies (mono-vacancies) due to the hydrogen and the stabilization of vacancy clusters as a result of the presence of trapped hydrogen.

Chapter 4

Porous plastic damage in metals: GTN model

Following our exploration of vacancy clustering, which pertains to the formation of voids within the material, we now shift our focus to the growth of these voids. In order to model void creation and growth, we have based our approach on existing models dedicated to ductile damage evolution in elastoplastic materials: the creation of pores in the material after vacancy clustering, though full of hydrogen gas, leads to a similar material state than the one after ductile damage initiation. The evolution of this porosity is then linked, on the one hand, to further vacancy sticking on voids, and on the other hand, to the development of plasticity in their vicinity. As a consequence, a ductile damage model, such as the GTN one, becomes very relevant to include in the simulation of H-related voids, the expansion of which is being controlled by plasticity.

The GTN model is first presented, and its implementation described. Several computations are then presented, before being applied to a monoblock configuration.

4.1 Introduction

Ductile damage is associated to the creation and the development of pores in the material, driven by the plastic strain. This lead to very characteristic crack surfaces, full of dimples, as it can be seen on figure 4.1a.

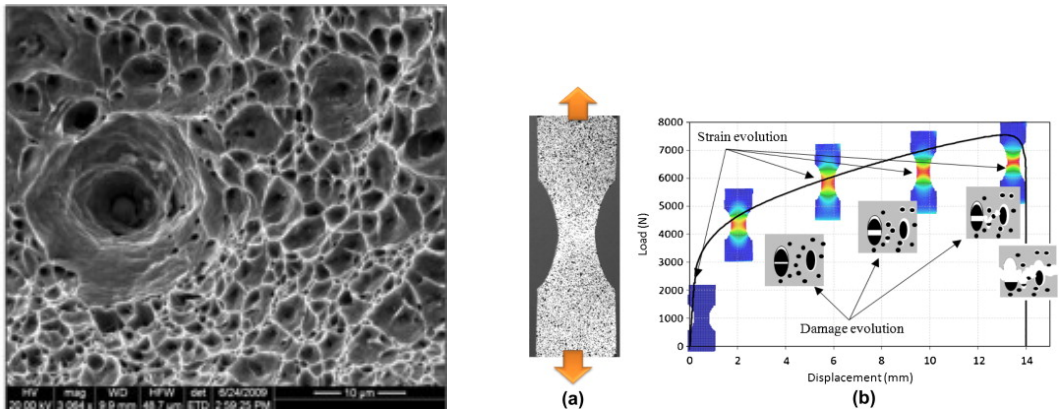

(a) (b)

Figure 4.1: (a) Ductile crack surface [331]. (b) Ductile damage mechanism [332].

The propagation of a ductile crack is the final stage of a progressive damage process (see Figure 4.1b): during, e.g., a tensile test, debounding or failure of inclusion appends, creating voids. Assisted by plastic strain, these voids increase in size while new voids are created. At a certain void density, a coalescence process is triggered, creating a macroscopic crack.

Such a process can be modeled in the frame of continuum mechanics by models such as the GTN one.

4.2 GTN model

The GTN (for Gurson-Tvergaard-Needleman) model allows to model plasticity development in porous metals, the porosity being the voids (being H or inclusion failure or debounding-induced). It thus states the following modified yield criterion [85, 89, 90]:

$$\Phi = \left(\frac{\sigma_{eq}}{\sigma_Y}\right)^2 + 2q_1 f^* \cosh\left(-\frac{3q_2\sigma_h}{2\sigma_y}\right) - \left(1 + q_3 f^{*2}\right) = 0 \tag{4.1}$$

where σ_{eq} denotes the von Mises equivalent stress, σ_Y the yield stress and $\sigma_h = -P_H$, the hydrostatic stress. q_1, q_2 and $q_3 = (q_1)^2$ are material parameters. q_1 especially describes the shape of the voids, with $q_1 > 3$ indicating flattened voids and $q_1 < 3$ indicating elongated voids; a value of 1.5 is classically used [89].

The void ratio in a volume V is defined by a parameter $f \in [0, 1]$ such that fV represents the void volume in V. f is linked to f^* (equation 4.1 by:

$$f^* = \begin{cases} f & \text{if } f \leq f_c \\ f_c + \frac{f_U - f_c}{f_F - f_c}(f - f_c) & \text{if } f_c < f < f_F \\ f_F & \text{if } f \geq f_F \end{cases} \tag{4.2}$$

f_c represents the critical value for f, at which the void formation is accelerated by their own interactions and thus begin to coalesce. For $f = f_F$, it is stated that coalescence has been completed and that macrocrack initiation and propagation have been triggered. The ultimate value f_U, at which the macroscopic stress-carrying capacity vanishes, is given by $f_U = 1/q_1$.

The total change in void volume fraction f is given as:

$$\dot{f} = \dot{f}_{nucleation} + \dot{f}_{growth} \tag{4.3}$$

where $\dot{f}_{nucleation}$ is due to nucleation of new voids and $\dot{f}_{growth}$ is due to existing voids' growth. $\dot{f}_{nucleation}$ is given by the following plastic strain-controlled relationship:

$$\begin{cases} \dot{f}_{nucleation} = A\dot{\epsilon}^m_{eq} \\ A = \frac{f_N}{S_N\sqrt{2\pi}} \times e^{-\frac{1}{2}\left(\frac{\epsilon^m_{eq} - \epsilon_N}{S_N}\right)^2} \end{cases} \tag{4.4}$$

where $\dot{\epsilon}^m_{eq}$ represents the equivalent plastic strain rate in the matrix (i.e., in the undamaged part of the material). This relationship describes a void nucleation probability density as a function of plastic deformation, in the form of a normal law, with a mean value ϵ_N and a standard deviation S_N (see Figure 4.2). f_N is a normalisation parameter.

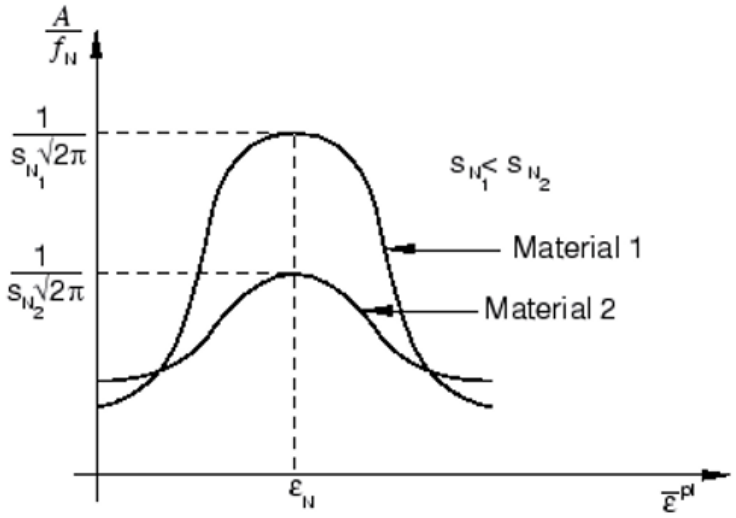

Figure 4.2: Nucleation function $\frac{A}{f_N}$

Growth of the existing voids is based on the law of conservation of mass and is expressed in terms of the void volume fraction f:

$$\dot{f}_{growth} = (1 - f)\dot{\boldsymbol{\epsilon}}_p : \underline{\underline{\mathbf{I}}} \tag{4.5}$$

where $\underline{\underline{\mathbf{I}}}$ is the second order identity tensor and $\boldsymbol{\epsilon}_p$ the plastic strain tensor in the volume V.

4.3 Implementation in Abaqus

The GTN model has been implemented in Abaqus thanks to Z. Zhang, from NTNU (Norway), which has provided the UMAT routine [333–340]. This section seeks to compare the results from this UMAT subroutine with those from both reference work and simulation using Abaqus' built-in module.

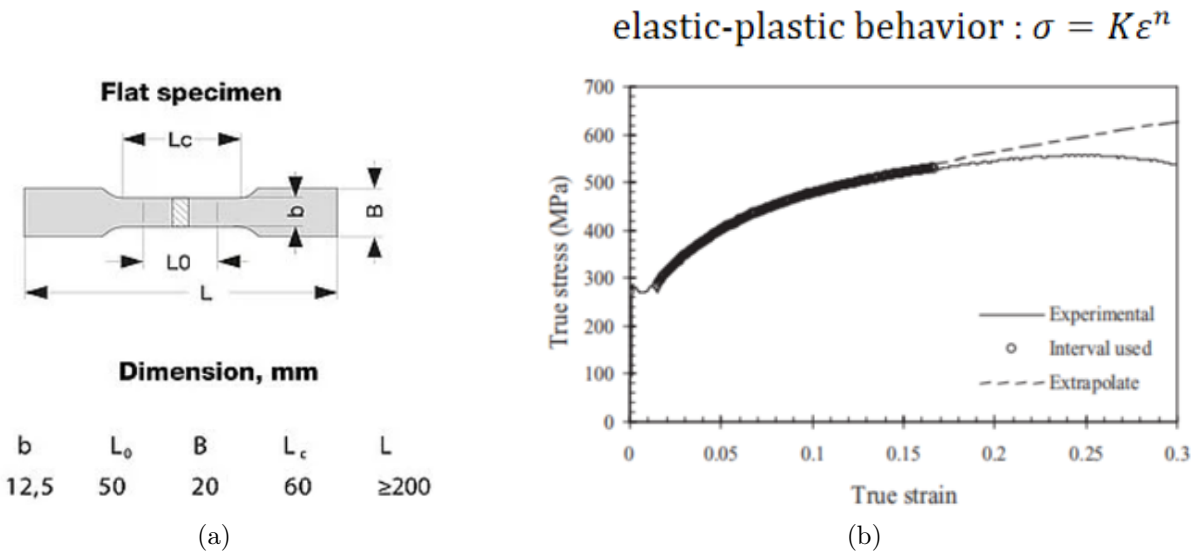

(a) (b)

Figure 4.3: (a) Sample characteristic [341] and (b) Mechanical behavior [342].

First, the results from [342] have sought to be reproduced. The same flat specimen has then been considered (Figure 4.3a), made of steel; the corresponding tensile curve is presented in figure 4.3b, and the identified parameters for the mechanical behavior are presented in table 4.1.

Table 4.1: Material parameters for steel [342]

f_0	f_c	f_N	f_F	ϵ_N	S_N
0	0.07	0.01285	0.1	0.1979	0.01
E (MPa)	ν	K (MPa)	n	q_1	q_2
2×10^5	0.3	854.5	0.256	1.5	1

In figure 4.4a are presented the results from [342] using the GTN model with the parameters presented in table 4.1, while in figure 4.4b are plotted the ones obtained when using Zhang's UMAT subroutine.

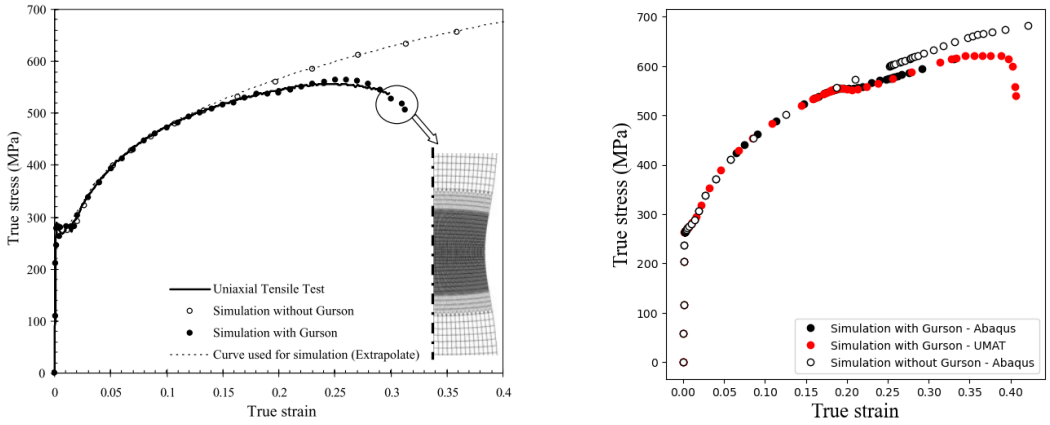

(a) (b)

Figure 4.4: Material behavior validation: (a) Reference work, (b) Present work.

It can be observed that, before necking and the decreased of the $\sigma - \epsilon$ curve, the UMAT and the reference curves are superimposed. However, while failure seems to appears at around 30% in the reference work, it increases to 40% when UMAT is used. As modelling fracture is not the aim of this section, these discrepancy are not investigated.

Table 4.2: Parameters of GTN model for tungsten [343]

f_0	f_N	ϵ_N	S_N	q_1	q_2	q_3
0	0.1036	0.1543	0.1431	1.4343	1.0225	2.0572

The second comparison is based on the work proposed in [343], in which GTN parameters have been identified for tungsten material, based on the experimental tensile curves presented in [344] (see table 4.2). The considered configuration is the same than previously (figure 4.3a).

In figure 4.5 can be seen the uniaxial tensile testing simulations results conducted with and without the UMAT subroutine, respectively. It can be seen that for both von Mises equivalent stress and equivalent plastic strain, the distribution is the same without and with the UMAT subroutine, localized where the sample is the thinnest (Figure 4.5a and 4.5b). Damage f is thus uniform in this region, with the same value for both cases (figure 4.5c).

In figures 4.5d and 4.5e are plotted the evolution of f with t and the equivalent plastic strain. It can be observed that both computations using Abaqus with and without UMAT provide the exact same curves, indicating the relevance of the UMAT subroutine, and especially when void creation is considered.

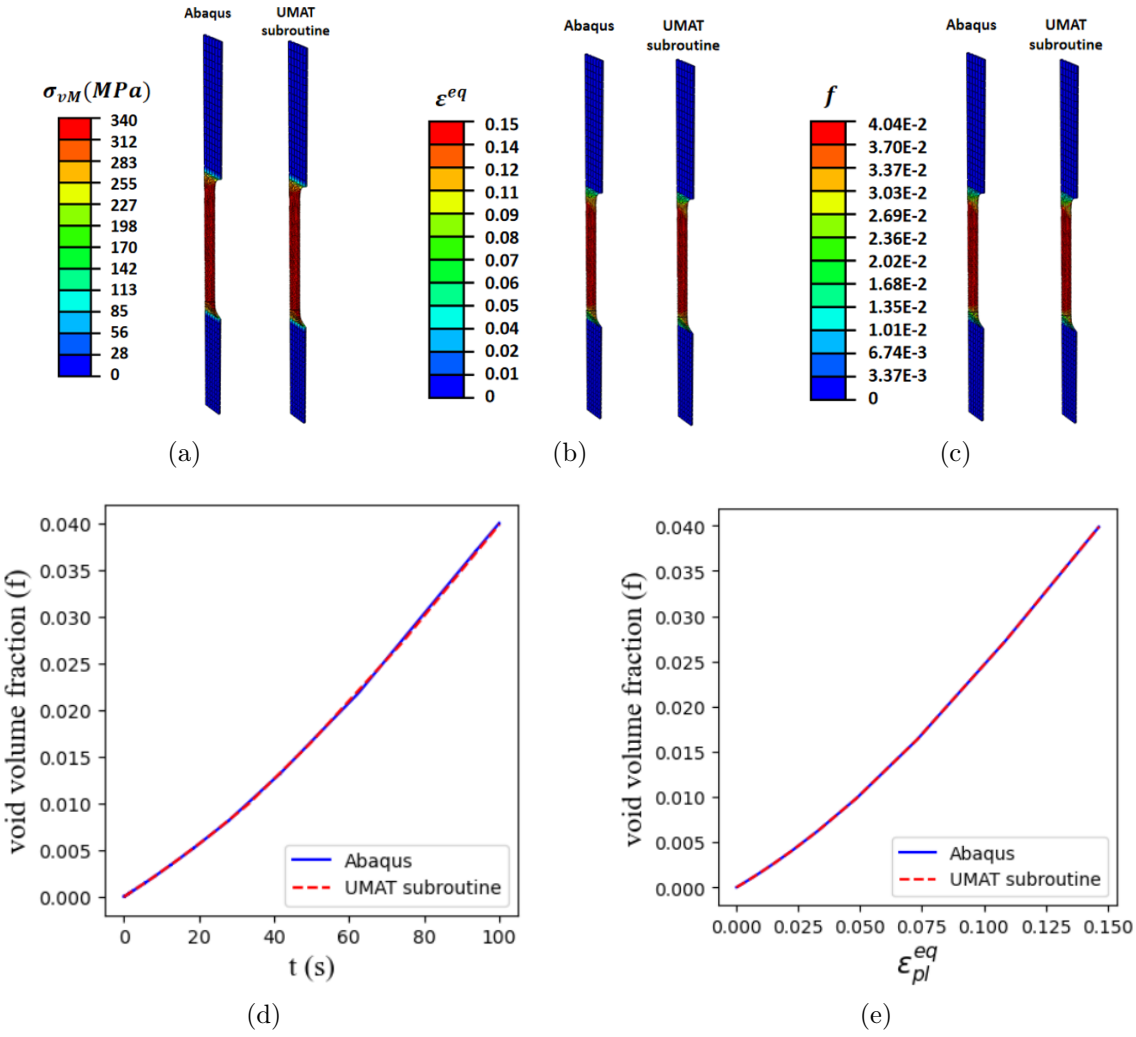

Figure 4.5: Comparison without (left) and with UMAT subroutine (right): (a) von Mises equivalent stress σ_{vM}, (b) equivalent plastic strain $\epsilon_{eq}(\neq \epsilon_{eq}^{m})$ (, (c) void volume fraction f, (d) evolution of void volume fraction with time, (e) evolution of void volume fraction with equivalent plastic strain.

4.4 Application to ITER Divertor Monoblock

The GTN model and the UMAT subroutine have been used with the monoblock configuration. The focus of this section is to investigate the extent to which the cyclic thermal loads, experienced during ITER plasma operations, influence the quantity and distribution of voids within the monoblock.

The geometry and boundary conditions for the monoblock are the same as in section 2.5.5.1 (see Figure 2.90); the scenario of plasma loading refers here to 13 pulses per day during 5 days (see Figure 4.6). The GTN parameters are the ones identified in [343]

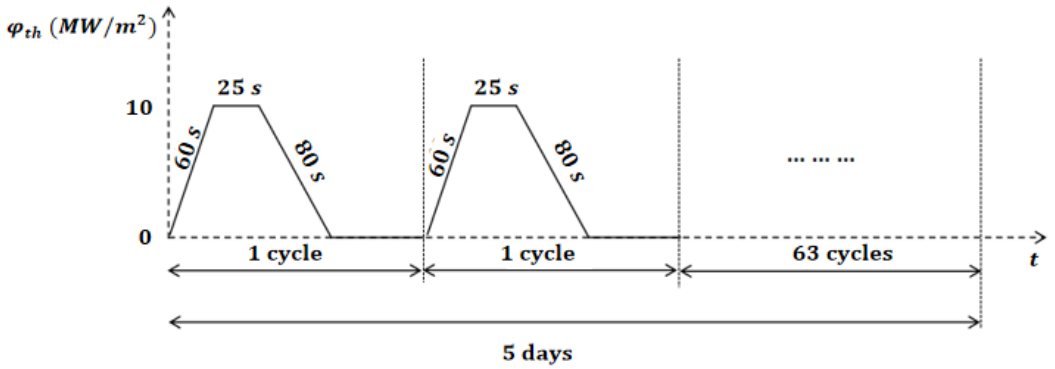

Figure 4.6: Plasma operations.

In an effort to establish a connection between f and vacancy clustering, we have used the result of vacancy clustering computations as the initial f values in the tungsten material (see Figure 3.15, Section 3.4.4.2): $f = C_{V_9}$). This can be done by exporting, thanks to a Python script, the C_{V_9} field to a text file (format: (x,y,z,C_{V_9})). Then, an Abaqus field $FV1$ is created in the GTN-based computation, initially set using an "*initial condition" based on that text file. Last, the initial value for f is considered in the UMAT subroutine by setting its value to the $FV1$ field. This transfer process is illustrated in Figure 4.7, in which the maps for both C_{V_9} and initial f values are compared.

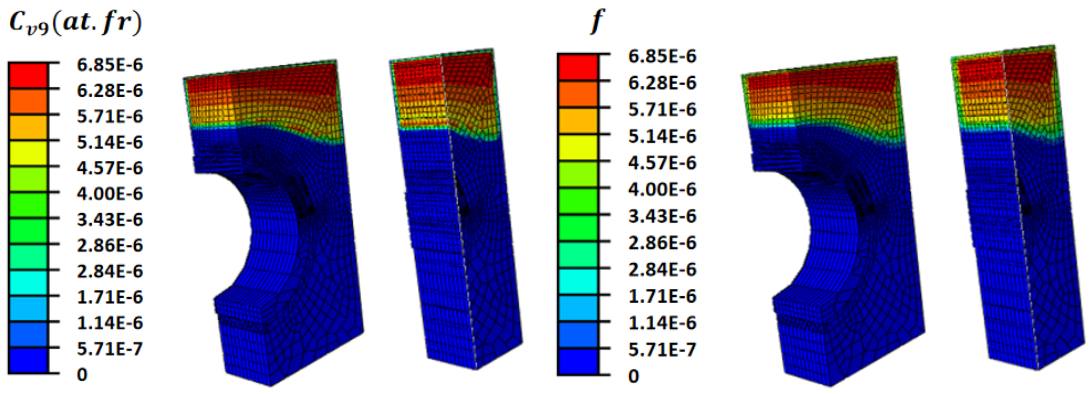

Figure 4.7: Comparison of (a) C_{V_9} and (b) initial f mapping.

The fields of f and ϵ_p after 65 cycles can be observed in Figure 4.8. Since plastic strain primarily accumulates near the multi-material interface and the outer surface, the global f field remains largely unchanged.

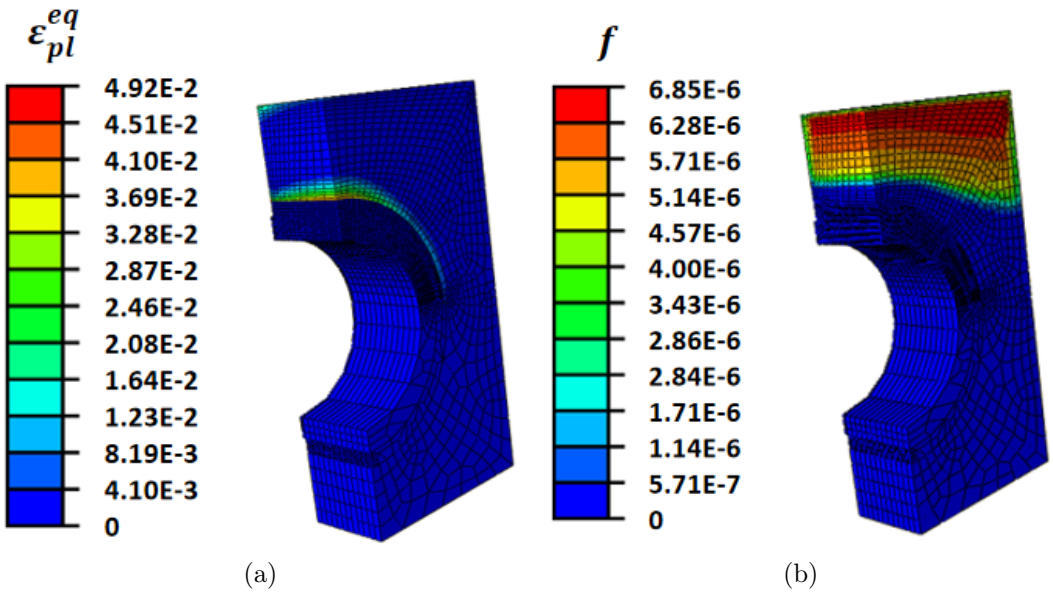

Figure 4.8: After 65 cycles: (a) ϵ_{pl}^{eq}, (b) f

Of course, the presence of voids will change the hydrogen transport process, as do the vacancies, while cycling should induce fatigue propagation of damage.

4.4.1 Conclusion

This section is dedicated to introducing a new mechanical behavior within the User Subroutine framework employed in this study, designed to replicate the presence of H-induced cavities. The initial void density value has been correlated with the results obtained from the vacancy clustering model, assuming a correspondence between C_{V_9} and f. It has also been demonstrated that plasticity, during plasma operations, is localized at a small area within the monoblock. However, it is important to note that the increase in void volume fraction is also influenced by internal hydrogen pressure and vacancy sticking, two phenomena that have not been addressed in this study.

Conclusions & Perspectives

The aim of this work was to path the way towards the numerical description of damage induced by plasma exposure. Initially, it has been necessary to investigate the hydrogen retention in several ITER components, these investigations then allowing us to consolidate the numerical tools used, for a better description of both thermomechanical and hydrogen fields evolution in space and time during plasma operation. The induced hydrogen retention profiles were investigated in depth to capture the impact of several parameters.

The heat transfer field descriptions have been improved, especially for expansion. Regarding hydrogen diffusion and trapping, specific attention has been paid on the impact of multi-material interfaces on the hydrogen transport equation, by accounting for both continuity of the C_L/S ratio (where C_L is the diffusive hydrogen concentration and S the Sievert solubility) and Fickian flux. This has also led to the modification of the boundary conditions, using C_L/S instead of a particle flux.

To obtain the first stage of plasma-induced damage, two different models have been introduced in Abaqus and in the User Subroutine used in this work. First, a vacancy clustering model, coupled with thermal fields, to describe the dynamics of creation of nano-void seeds. Several vacancy creations sources have been considered. This model was applied to the ITER monoblock configuration to capture the spatio-temporal evolution of all clusters. Second, a GTN model has been used and coupled with the results of the vacancy clustering one for its initial conditions. Neither approach is sufficient to model plasma-induced damage and blistering, but together they provide a more detailed, if yet still incomplete, understanding of the phenomena at play and their modeling.

There are a lot of remaining tasks to complete the description of H retention and plasma-induced damage. First of all, thermophoresis (or the Soret effect) can have an impact on the H fields in the monoblock, linked to the significant temperature gradient in the structure. Due to these gradients, recrystallization can take place, modifying the mechanical behavior, the density of the traps, and therefore the residual deformations. Finally, linked to cyclic loading, damage due to fatigue (and the initiation and/or propagation of cracks) could also be integrated into the modeling.

Regarding the formation of nano-voids, it is necessary to incorporate H trapping into both the vacancy clustering model and the GTN model. Additionally, a criterion for the transition from a vacancy cluster to a nano-cavity needs to be defined, and the influence of H on the mobility or stability of the clusters should also be considered. Lastly, it's worth noting that trapped H driven by mobile clusters can also have an impact on H fields.

References

[1] S Matsuda. Overview of iter project. objective, history, status of development, structure and its future. In GENES4/ANP2003, 2003.

[2] Y Shimomura, R Aymar, V Chuyanov, M Huguet, R Parker, et al. Iter overview. Nuclear Fusion, 39(9Y):1295, 1999.

[3] ITER Organization. ITER - The Way to New Energy. `https://www.iter.org`, 2023. : 2023-11-15.

[4] V Barabash, The ITER International Team, A Peacock, S Fabritsiev, G Kalinin, S Zinkle, A Rowcliffe, J-W Rensman, AA Tavassoli, P Marmy, et al. Materials challenges for iter–current status and future activities. Journal of Nuclear Materials, 367:21–32, 2007.

[5] AW Leonard, A Herrmann, K Itami, J Lingertat, A Loarte, TH Osborne, W Suttrop, ITER Divertor Physics Expert Group, et al. The impact of elms on the iter divertor. Journal of nuclear materials, 266:109–117, 1999.

[6] PT Lang, Alberto Loarte, G Saibene, LR Baylor, M Becoulet, M Cavinato, S Clement-Lorenzo, Edward Daly, TE Evans, ME Fenstermacher, et al. Elm control strategies and tools: status and potential for iter. Nuclear Fusion, 53(4):043004, 2013.

[7] Ahmed Hassanein. Prediction of material erosion and lifetime during major plasma instabilities in tokamak devices. Fusion engineering and design, 60(4):527–546, 2002.

[8] Alexander V Spitsyn, Nikolay P Bobyr, Timur V Kulevoy, Petr A Fedin, Alexander I Semennikov, and Valery S Stolbunov. Use of mev energy ion accelerators to simulate the neutron damage in fusion reactor materials. Fusion Engineering and Design, 146:1313–1316, 2019.

[9] V.Kh. Alimov, B. Tyburska-Püschel, S. Lindig, Y. Hatano, M. Balden, J. Roth, K. Isobe, M. Matsuyama, and T. Yamanishi. Temperature dependence of surface morphology and deuterium retention in polycrystalline iter-grade tungsten exposed to low-energy, high-flux d plasma. Journal of Nuclear Materials, 420(1):519–524, 2012.

[10] JB Condon and T Schober. Hydrogen bubbles in metals. Journal of Nuclear Materials, 207:1–24, 1993.

[11] T Venhaus, R Causey, R Doerner, and T Abeln. Behavior of tungsten exposed to high fluences of low energy hydrogen isotopes. Journal of Nuclear Materials, 290-293:505–508, 2001. 14th Int. Conf. on Plasma-Surface Interactions in Controlled Fusion D evices.

[12] Wenmin Wang, J Roth, S Lindig, and C.H Wu. Blister formation of tungsten due to ion bombardment. Journal of Nuclear Materials, 299(2):124–131, 2001.

[13] M.Y. Ye, H. Kanehara, S. Fukuta, N. Ohno, and S. Takamura. Blister formation on tungsten surface under low energy and high flux hydrogen plasma irradiation in nagdis-i. Journal of Nuclear Materials, 313-316:72–76, 2003. Plasma-Surface Interactions in Controlled Fusion Devices 15.

[14] Joachim Roth and Klaus Schmid. Hydrogen in tungsten as plasma-facing material. Physica Scripta, 2011(T145):014031, 2011.

[15] J C M Li, R A Oriani, and L S Darken. The Thermodynamics of Stressed Solids. Zeitschrift fur Physikalische Chemie, 49(3-5):271–290, May 1966.

[16] J O'M Bogkris, W Beck, M A Genshaw, P K Subramanyan, and F S Williams. The effect of stress on the chemical potential of hydrogen in iron and steel. 19(11):1209–1218, November 1971.

[17] Petros Sofronis and Robert M McMeeking. Numerical analysis of hydrogen transport near a blunting crack tip. Journal of the Mechanics and Physics of Solids, 37(3):317–350, 1989.

[18] A McNabb and P K Foster. A new analysis of the diffusion of hydrogen in iron and ferritic steels. Transactions of the Metallurgical Society of AIME, 227(3):618–627, 1963.

[19] Andreas Drexler, Tom Depover, Silvia Leitner, Kim Verbeken, and Werner Ecker. Microstructural based hydrogen diffusion and trapping models applied to Fe–CX alloys. Journal of Alloys and Compounds, 826:154057, June 2020.

[20] Richard A Oriani. The diffusion and trapping of hydrogen in steel. Acta metallurgica, 18(1):147–157, 1970.

[21] Alfons HM Krom, Ronald WJ Koers, and AD Bakker. Hydrogen transport near a blunting crack tip. Journal of the Mechanics and Physics of Solids, 47(4):971–992, 1999.

[22] I Moro. Fragilisation par l'hydrogène gazeux d'un acier ferrito-perlitique de grade API X80. PhD thesis, Institut Carnot CIRIMAT/ENSIACET, 2009.

[23] Alfonsus Hendricus Maria Krom, R W J Koers, and A D Bakker. Hydrogen transport near a blunting crack tip. Journal of the Mechanics and Physics of Solids, 47(4):971–992, 1999.

[24] Petros Sofronis, Yueming Liang, and Nikolaos Aravas. Hydrogen induced shear localization of the plastic flow in metals and alloys. European Journal of Mechanics-A/Solids, 20(6):857–872, 2001.

[25] Yann Charles, Jonathan Mougenot, and Monique Gaspérini. Effect of transient trapping on hydrogen transport near a blunting crack tip. International Journal of Hydrogen Energy, 46(18):10995–11003, January 2021.

[26] A Taha and Petros Sofronis. A micromechanics approach to the study of hydrogen transport and embrittlement. Engineering Fracture Mechanics, 68(6):803–837, 2001.

[27] Y Liang, Petros Sofronis, and R H Dodds Jr. Interaction of hydrogen with crack-tip plasticity: effects of constraint on void growth. Materials Science and Engineering: A, 366(2):397–411, February 2004.

[28] Hiroshi Kanayama, Stephane Ndong-Mefane, Masao Ogino, and Reza Miresmaeili. Reconsideration of the Hydrogen Diffusion Model Using the McNabb-Foster Formulation. Memoirs of the Faculty of Engineering, 69(4):146–161, 2009.

[29] Chang-Sik Oh, Y J Kim, and K B Yoon. Coupled analysis of hydrogen transport using ABAQUS. Journal of Solid Mechanics and Materials Engineering, 4(7):908–917, 2010.

[30] Mohsen Dadfarnia, Petros Sofronis, and Thirumalai Neeraj. Hydrogen interaction with multiple traps: Can it be used to mitigate embrittlement? International Journal of Hydrogen Energy, 36(16):10141–10148, August 2011.

[31] Mohsen Dadfarnia, May L Martin, Akihide Nagao, Petros Sofronis, and Ian M Robertson. Modeling hydrogen transport by dislocations. Journal of the Mechanics and Physics of Solids, 78:511–525, May 2015.

[32] Daisuke Sasaki, Motomichi Koyama, Kenji Higashida, Kaneaki Tsuzaki, and Hiroshi Noguchi. Effects of hydrogen-altered yielding and work hardening on plastic-zone evolution: A finite-element analysis. International Journal of Hydrogen Energy, 40(31):9825–9837, August 2015.

[33] Emilio Martínez-Pañeda, S del Busto, Christian F Niordson, and C Betegón. Strain gradient plasticity modeling of hydrogen diffusion to the crack tip. International Journal of Hydrogen Energy, 41(24):10265–10274, June 2016.

[34] Emilio Martínez-Pañeda, Andres Díaz, Louise Wright, and Alan Turnbull. Generalised boundary conditions for hydrogen transport at crack tips. Corrosion Science, page 108698, May 2020.

[35] GJ Thomas. Experimental studies of helium in metals. Radiation effects, 78(1-4):37–51, 1983.

[36] WD Wilson, CL Bisson, and MI Baskes. Self-trapping of helium in metals. Physical Review B, 24(10):5616, 1981.

[37] OV Ogorodnikova, T Schwarz-Selinger, K Sugiyama, and V Kh Alimov. Deuterium retention in tungsten exposed to low-energy pure and helium-seeded deuterium plasmas. Journal of Applied Physics, 109(1):013309, 2011.

[38] Y Ueda, H Kashiwagi, M Fukumoto, Y Ohtsuka, and N Yoshida. Effects of helium ions on hydrogen isotope behavior in tungsten. Fusion science and technology, 56(1):85–90, 2009.

[39] Y Ueda, M Fukumoto, J Yoshida, Y Ohtsuka, R Akiyoshi, H Iwakiri, and N Yoshida. Simultaneous irradiation effects of hydrogen and helium ions on tungsten. Journal of Nuclear Materials, 386:725–728, 2009.

[40] Mykola Ialovega, Elodie Bernard, Régis Bisson, Celine Martin, Ryuichi Sakamoto, Arkadi Kreter, Etienne Hodille, Thierry Angot, and Christian Grisolia. Hydrogen trapping in tungsten: impact of helium irradiation and thermal cycling. Physica Scripta, T171:014066, jan 2020.

[41] OV Ogorodnikova, K Sugiyama, A Markin, Yu Gasparyan, V Efimov, A Manhard, and M Balden. Effect of nitrogen seeding into deuterium plasma on deuterium retention in tungsten. Physica Scripta, 2011(T145):014034, 2011.

[42] L Gao, W Jacob, P Wang, U Von Toussaint, and A Manhard. Influence of nitrogen pre-implantation on deuterium retention in tungsten. Physica Scripta, 2014(T159):014023, 2014.

[43] Sheng Wang, Xiang-Shan Kong, Xuebang Wu, QF Fang, Jun-Ling Chen, G-N Luo, and CS Liu. Effects of nitrogen on hydrogen retention in tungsten: First-principles calculations. Journal of Nuclear Materials, 459:143–149, 2015.

[44] Xiang-Shan Kong, Jie Hou, Xiang-Yan Li, Xuebang Wu, CS Liu, Jun-Ling Chen, and G-N Luo. First principles study of inert-gas (helium, neon, and argon) interactions with hydrogen in tungsten. Journal of Nuclear Materials, 487:128–134, 2017.

[45] A Kreter, D Nishijima, RP Doerner, M Freisinger, Ch Linsmeier, Y Martynova, S Möller, M Rasinski, M Reinhart, A Terra, et al. Influence of plasma impurities on the fuel retention in tungsten. Nuclear fusion, 59(8):086029, 2019.

[46] Jong-Lam Lee and Jai-Young Lee. Identification of defects generated during cathodic charging in pure iron by thermal analysis technique. Metallurgical Transactions A, 16(3):468–471, 1985.

[47] C Quirós, J Mougenot, G Lombardi, M Redolfi, O Brinza, Yann Charles, A Michau, and K Hassouni. Blister formation and hydrogen retention in aluminium and beryllium: A modeling and experimental approach. Nuclear Materials and Energy, 12:1178–1183, March 2017.

[48] Y S Chung, J H Moon, H J Cho, and H R Kim. Determination of the hydrogen concentration in coal and titanium alloy by prompt gamma neutron activation analysis. Journal of Radioanalytical and Nuclear Chemistry, 272(2):391–395, May 2007.

[49] T Hoshihira, T Otsuka, and T Tanabe. Visualization of hydrogen distribution around blisters by tritium radio-luminography. Journal of Nuclear Materials, 386-388:776–779, April 2009.

[50] K Ouaras, M Redolfi, D Vrel, C Quirós, G Lombardi, Xavier Bonnin, and K Hassouni. Tungsten Blister Formation Kinetic as a Function of Fluence, Ion Energy and Grain Orientation Dependence Under Hydrogen Plasma Environment. Journal of Fusion Energy, 37(2):144–153, June 2018.

[51] Sabrine Ayadi, Yann Charles, Monique Gaspérini, I Caron Lemaire, and T Da Silva Botelho. Effect of loading mode on blistering in iron submitted to plastic prestrain before hydrogen cathodic charging. International Journal of Hydrogen Energy, 42(15):10555–10567, March 2017.

[52] X C Ren, Q J Zhou, G B Shan, Wuyang Chu, J X Li, Y J Su, and L J Qiao. A Nucleation Mechanism of Hydrogen Blister in Metals and Alloys. Metallurgical and Materials Transactions A, 39(1):87–97, November 2007.

[53] J B Condon and T Schober. Hydrogen bubbles in metals. Journal of Nuclear Materials, 207:1–24, December 1993.

[54] Marie C Tiegel, May L Martin, Annegret K Lehmberg, Martin Deutges, Christine Borchers, and Reiner Kirchheim. Crack and blister initiation and growth in purified iron due to hydrogen loading. Acta Materialia, 115:24–34, 2016.

[55] Axel Griesche, Eitan Dabah, Thomas Kannengiesser, Nikolay Kardjilov, André Hilger, and Ingo Manke. Three-dimensional imaging of hydrogen blister in iron with neutron tomography. Acta Materialia, 78:14–22, 2014.

[56] Chao Meng, Lifang Wang, Ke Xu, Jiannan Hao, Hong-bo Zhou, Xiaolin Shu, Shuo Jin, Linyun Liang, Guang-Hong Lu, and CS Becquart. Object kinetic monte carlo simulation of hydrogen clustering behaviour with vacancies in tungsten. Journal of Nuclear Materials, 526:151768, 2019.

[57] Michael P Surh, Jess B Sturgeon, and Wilhelm G Wolfer. Void nucleation, growth, and coalescence in irradiated metals. Journal of nuclear materials, 378(1):86–97, 2008.

[58] RH Ning, YG Li, WH Zhou, Z Zeng, and X Ju. An improved cluster dynamics model for hydrogen retention in tungsten. International Journal of Modern Physics C, 23(06):1250042, 2012.

[59] Richard Skorek, Serge Maillard, Amélie Michel, Gaelle Carlot, Eric Gilabert, and Thomas Jourdan. Modelling fission gas bubble distribution in uo2. In Defect and Diffusion Forum, volume 323, pages 209–214. Trans Tech Publ, 2012.

[60] WR Wampler, T Schober, and B Lengeler. Precipitation and trapping of hydrogen in copper. Philosophical Magazine, 34(1):129–141, 1976.

[61] Valery I Levitas and Hamed Attariani. Mechanochemical continuum modeling of nanovoid nucleation and growth in reacting nanoparticles. The Journal of Physical Chemistry C, 116(1):54–62, 2012.

[62] Daniel R Mason, Duc Nguyen-Manh, and Charlotte S Becquart. An empirical potential for simulating vacancy clusters in tungsten. Journal of Physics: Condensed Matter, 29(50):505501, 2017.

[63] Jie Hou, Xiang-Shan Kong, CS Liu, and Jun Song. Hydrogen clustering in bcc metals: Atomic origin and strong stress anisotropy. Acta Materialia, 201:23–35, 2020.

[64] Lu Sun, Shuo Jin, Hong-Bo Zhou, Ying Zhang, Wenqing Zhang, Y Ueda, HT Lee, and Guang-Hong Lu. Critical concentration for hydrogen bubble formation in metals. Journal of Physics: Condensed Matter, 26(39):395402, 2014.

[65] GW Greenwood, AJE Foreman, and DE Rimmer. The role of vacancies and dislocations in the nucleation and growth of gas bubbles in irradiated fissile material. Journal of Nuclear Materials, 1(4):305–324, 1959.

[66] Xue Yang and Ahmed Hassanein. Molecular dynamics simulation of deuterium trapping and bubble formation in tungsten. Journal of nuclear materials, 434(1-3):1–6, 2013.

[67] WG Wolfer. The pressure for dislocation loop punching by a single bubble. Philosophical Magazine A, 58(2):285–297, 1988.

[68] WG Wolfer. Dislocation loop punching in bubble arrays. Philosophical Magazine A, 59(1):87–103, 1989.

[69] JH Evans. An interbubble fracture mechanism of blister formation on helium-irradiated metals. Journal of Nuclear Materials, 68(2):129–140, 1977.

[70] TE Volin and RW Balluffi. Annealing kinetics of voids and the self-diffusion coefficient in aluminum. physica status solidi (b), 25(1):163–173, 1968.

[71] ID Skrypnyk. Analytic evaluation of hydrogen-assisted void growth at high temperatures. Materials Science, 33(4):478–490, 1997.

[72] Franz Dieter Fischer and Jiri Svoboda. Void growth due to vacancy supersaturation–a non-equilibrium thermodynamics study. Scripta materialia, 58(2):93–95, 2008.

[73] Chaofeng Sang, Xavier Bonnin, Manoj Warrier, Abha Rai, Ralf Schneider, Jizhong Sun, and Dezhen Wang. Modelling of hydrogen isotope inventory in mixed materials including porous deposited layers in fusion devices. Nuclear Fusion, 52(4):043003, 2012.

[74] C Quirós, J Mougenot, G Lombardi, M Redolfi, O Brinza, Y Charles, A Michau, and K Hassouni. Blister formation and hydrogen retention in aluminium and beryllium: A modeling and experimental approach. Nuclear Materials and Energy, 12:1178–1183, 2017.

[75] Åsa Martinsson and Rolf Sandström. Hydrogen depth profile in phosphorus-doped, oxygen-free copper after cathodic charging. Journal of Materials Science, 47(19):6768–6776, 2012.

[76] Franz Dieter Fischer and J Svoboda. Formation of bubbles by hydrogen attack and elastic–plastic deformation of the matrix. International Journal of Plasticity, 63:110–123, 2014.

[77] Mei Qiang Chandler, Douglas J Bammann, and M F Horstemeyer. A continuum model for hydrogen-assisted void nucleation in ductile materials. Modelling and Simulation in Materials Science and Engineering, 21(5):055028, 2013.

[78] Paul C Millett, Anter El-Azab, Srujan Rokkam, Michael Tonks, and Dieter Wolf. Phase-field simulation of irradiated metals: Part i: Void kinetics. Computational materials science, 50(3):949–959, 2011.

[79] Paul C Millett, Anter El-Azab, and Dieter Wolf. Phase-field simulation of irradiated metals: Part ii: Gas bubble kinetics. Computational Materials Science, 50(3):960–970, 2011.

[80] O Barrera and ACF Cocks. Computational modelling of hydrogen embrittlement in welded structures. Philosophical Magazine, 93(20):2680–2700, 2013.

[81] Eugene Ogosi, Amir Siddiq, Umair Bin Asim, and Mehmet E Kartal. Crystal plasticity based study to understand the interaction of hydrogen, defects and loading in austenitic stainless-steel single crystals. International Journal of Hydrogen Energy, 45(56):32632–32647, November 2020.

[82] Y Liang, DC Ahn, Petros Sofronis, RH Dodds Jr, and D Bammann. Effect of hydrogen trapping on void growth and coalescence in metals and alloys. Mechanics of Materials, 40(3):115–132, 2008.

[83] Andrés Díaz, Jesus Manuel Alegre, II Cuesta, and Zhiliang Zhang. Numerical study of hydrogen influence on void growth at low triaxialities considering transient effects. International Journal of Mechanical Sciences, 164:105176, 2019.

[84] Paweł Grzegorz Kossakowski. Influence of initial porosity on strength properties of s235jr steel at low stress triaxiality. Archives of Civil Engineering, 58(3):293–308, 2012.

[85] Arthur L Gurson. Continuum theory of ductile rupture by void nucleation and growth: Part i—yield criteria and flow rules for porous ductile media. Journal of Engineering Materials and Technology, 99:2–15, 1977.

[86] Arthur L Gurson. Plastic flow and fracture behavior of ductile materials incorporating void nucleation, growth, and interaction. 1977.

[87] Alberto Corigliano, Stefano Mariani, and Barbara Orsatti. Identification of gurson–tvergaard material model parameters via kalman filtering technique. i. theory. International journal of fracture, 104(4):349–373, 2000.

[88] Viggo Tvergaard. Influence of void nucleation on ductile shear fracture at a free surface. Journal of the Mechanics and Physics of Solids, 30(6):399–425, 1982.

[89] Viggo Tvergaard and Alan Needleman. Analysis of the cup-cone fracture in a round tensile bar. Acta metallurgica, 32(1):157–169, 1984.

[90] CC Chu and A Needleman. Void nucleation effects in biaxially stretched sheets. Journal of Engineering Materials and Technology, 102:249–256, 1993.

[91] Abdelkader Slimane, Benattou Bouchouicha, Mohamed Benguediab, and Sid-Ahmed Slimane. Parametric study of the ductile damage by the gurson–tvergaard–needleman model of structures in carbon steel a48-ap. Journal of Materials Research and Technology, 4(2):217–223, 2015.

[92] Thomas Pardoen, Issam Doghri, and Francis Delannay. Experimental and numerical comparison of void growth models and void coalescence criteria for the prediction of ductile fracture in copper bars. Acta Materialia, 46(2):541–552, 1998.

[93] Pierre-Guy Vincent, Pierre Suquet, Yann Monerie, and Hervé Moulinec. Effective flow surface of porous materials with two populations of voids under internal pressure: I. a gtn model. International Journal of Plasticity, 56:45–73, 2014.

[94] Pierre-Guy Vincent, Pierre Suquet, Yann Monerie, and Hervé Moulinec. Effective flow surface of porous materials with two populations of voids under internal pressure: Ii. full-field simulations. International Journal of Plasticity, 56:74–98, 2014.

[95] Youbin Chen, Chunyu Zhang, and Christophe Varé. An extended gtn model for indentation-induced damage. Computational Materials Science, 128:229–235, 2017.

[96] J Hure, PO Barrioz, and B Tanguy. Assessing size effects on the deformation of nanovoids in metallic materials. Scripta Materialia, 177:54–57, 2020.

[97] Luc Dormieux and Djimedo Kondo. An extension of gurson model incorporating interface stresses effects. International Journal of Engineering Science, 48(6):575–581, 2010.

[98] G De Temmerman, T Hirai, and R A Pitts. The influence of plasma-surface interaction on the performance of tungsten at the ITER divertor vertical targets. Plasma Physics and Controlled Fusion, 60(4):044018, mar 2018.

[99] Michael Rieth, Russell Doerner, Akira Hasegawa, Yoshio Ueda, and Marius Wirtz. Behavior of tungsten under irradiation and plasma interaction. Journal of Nuclear Materials, 519:334–368, 2019.

[100] L. Buzi, G. De Temmerman, B. Unterberg, M. Reinhart, T. Dittmar, D. Matveev, Ch. Linsmeier, U. Breuer, A. Kreter, and G. Van Oost. Influence of tungsten microstructure and ion flux on deuterium plasma-induced surface modifications and deuterium retention. Journal of Nuclear Materials, 463:320–324, 2015. PLASMA-SURFACE INTERACTIONS 21.

[101] Ting Wang, Yue Yuan, Wangguo Guo, Xiaolei Ma, Mi Liu, Jun Wang, Long Cheng, Xiu-Li Zhu, and Guang-Hong Lu. Deuterium behavior in tungsten exposed to

deuterium plasma with rising or declining temperature. Journal of Nuclear Materials, 537:152243, 2020.

[102] K. Tokunaga, M.J. Baldwin, R.P. Doerner, N. Noda, Y. Kubota, N. Yoshida, T. Sogabe, T. Kato, and B. Schedler. Blister formation and deuterium retention on tungsten exposed to low energy and high flux deuterium plasma. Journal of Nuclear Materials, 337-339:887–891, 2005. PSI-16.

[103] W.M. Shu, G.-N. Luo, and T. Yamanishi. Mechanisms of retention and blistering in near-surface region of tungsten exposed to high flux deuterium plasmas of tens of ev. Journal of Nuclear Materials, 367-370:1463–1467, 2007. Proceedings of the Twelfth International Conference on Fusion Reactor Materials (ICFRM-12).

[104] J.P. Sharpe, R.D. Kolasinski, M. Shimada, P. Calderoni, and R.A. Causey. Retention behavior in tungsten and molybdenum exposed to high fluences of deuterium ions in tpe. Journal of Nuclear Materials, 390-391:709–712, 2009. Proceedings of the 18th International Conference on Plasma-Surface Interactions in Controlled Fusion Device.

[105] H.Y. Xu, G.N. Luo, H. Schut, Y. Yuan, B.Q. Fu, A. Godfrey, W. Liu, and G.De. Temmerman. Enhanced modification of tungsten surface by nanostructure formation during high flux deuterium plasma exposure. Journal of Nuclear Materials, 447(1):22–27, 2014.

[106] Y.Z. Jia, G. De Temmerman, G.-N. Luo, H.Y. Xu, C. Li, B.Q. Fu, and W. Liu. Surface morphology and deuterium retention in tungsten exposed to high flux d plasma at high temperatures. Journal of Nuclear Materials, 457:213–219, 2015.

[107] M. Zibrov, M. Balden, T.W. Morgan, and M. Mayer. Deuterium trapping and surface modification of polycrystalline tungsten exposed to a high-flux plasma at high fluences. Nuclear Fusion, 57(4):046004, feb 2017.

[108] L. Buzi, G. De Temmerman, D. Matveev, M. Reinhart, T. Schwarz-Selinger, M. Rasinski, B. Unterberg, Ch. Linsmeier, and G. Van Oost. Surface modifications and deuterium retention in polycrystalline and single crystal tungsten as a function of particle flux and temperature. Journal of Nuclear Materials, 495:211–219, 2017.

[109] K Touhouche and B Terreault. Surface microstructure of high temperature beryllium implanted with deuterium. MRS Online Proceedings Library Archive, 316, 1993.

[110] O.V Ogorodnikova, J Roth, and M Mayer. Deuterium retention in tungsten in dependence of the surface conditions. Journal of Nuclear Materials, 313-316:469–477, 2003. Plasma-Surface Interactions in Controlled Fusion Devices 15.

[111] D. Pérez Escobar, C. Miñambres, L. Duprez, K. Verbeken, and M. Verhaege. Internal and surface damage of multiphase steels and pure iron after electrochemical hydrogen charging. Corrosion Science, 53(10):3166–3176, 2011.

[112] D Nishijima, H Iwakiri, K Amano, MY Ye, N Ohno, K Tokunaga, N Yoshida, and S Takamura. Suppression of blister formation and deuterium retention on tungsten surface due to mechanical polishing and helium pre-exposure. Nuclear fusion, 45(7):669, 2005.

[113] YZ Jia, W Liu, B Xu, G-N Luo, SL Qu, TW Morgan, and G De Temmerman. Mechanism for orientation dependence of blisters on w surface exposed to d plasma at low temperature. Journal of Nuclear Materials, 477:165–171, 2016.

[114] M. Zibrov, W. Egger, J. Heikinheimo, M. Mayer, and F. Tuomisto. Vacancy cluster growth and thermal recovery in hydrogen-irradiated tungsten. Journal of Nuclear Materials, 531:152017, 2020.

[115] D. Terentyev, C. Yin, A. Dubinko, C.C. Chang, and J.H. You. Neutron irradiation hardening across iter diverter tungsten armor. International Journal of Refractory Metals and Hard Materials, 95:105437, 2021.

[116] International Organization for Standardization. Transportable gas cylinders – compatibility of cylinder and valve materials with gas contents – part 4: test methods for selecting metallic materials resistant to hydrogen embrittlement. International Organization for Standardization, Vernier, Geneva, Switzerland, ISO 11114-4:2005 edition, 2005.

[117] J P Fidelle and R Arnould-Laurent. The Embedded Disk Pressure Test (DPT): A Sensitive Technique to Investigate Materials Embrittlement. In Atomistics of Fracture. Springer Science & Business Media, December 2012.

[118] J P Fidelle. On disk pressure selection of materials and hydrogen environments. In International symposium on the recent solutions to hydrogen probles in steel, pages 1–15, Washigton DC, USA, November 1982.

[119] Xiyue Cheng ShuiquanDeng Xiaoyan Kang. The bubble problem of the plasma facing material: A finite element study. Nuclear Engineering and Technology, 52(10):2290–2298, October 2020.

[120] H Toda, P C Qu, S Ito, K Shimizu, K Uesugi, A Takeuchi, Y Suzuki, and M Kobayashi. Formation behaviour of blister in cast aluminium alloy. International Journal of Cast Metals Research, October 2014.

[121] Jeong-Ha You. Mechanics of tungsten blistering: A finite element study. Journal of nuclear materials, 437(1-3):24–28, 2013.

[122] Naruaki Enomoto, Shunsuke Muto, Tetsuo Tanabe, JW Davis, and AA Haasz. Grazing-incidence electron microscopy of surface blisters in single-and polycrystalline tungsten formed by h+, d+ and he+ irradiation. Journal of Nuclear Materials, 385(3):606–614, 2009.

[123] Muyuan Li and Jeong-Ha You. Mechanics of tungsten blistering ii: Analytical treatment and fracture mechanical assessment. Journal of Nuclear Materials, 465:702–709, 2015.

[124] W. Schmitt and R. Kienzler. The j-integral concept for elastic-plastic material behavior. Engineering Fracture Mechanics, 32(3):409–418, 1989.

[125] Jun Hu, Fei Liu, Quan Duan, Guangxu Cheng, and Zaoxiao Zhang. Failure analysis based on J-integral values: A case study of hydrogen blistering defect. Engineering Failure Analysis, 18(3):924–932, April 2011.

[126] Congwei Ji, Shaojie Zhang, and Hehui Wang. Simulation Analysis of the Mutual Influence of the Stress Intensity Factor on the Multiple Blisters Caused by Hydrogen Induced Damage. IOP Conference Series: Materials Science and Engineering, 322(4):042014, March 2018.

[127] Jorge Luis González and Alfredo Morales. Analysis of laminations in x52 steel pipes by nonlinear by finite element. Journal of pressure vessel technology, 130(2), 2008.

[128] N Razak, A Sulaiman, and N Alang. Interaction effect of pressurized lamination pipe by using 2d finite element analysis. In IOP Conference Series: Materials Science and Engineering, volume 36, page 012027. IOP Publishing, 2012.

[129] Abderrazak Traidia, Marco Alfano, Gilles Lubineau, Sebastien Duval, and Abdelmounam Sherik. An effective finite element model for the prediction of hydrogen induced cracking in steel pipelines. International Journal of Hydrogen Energy, 37(21):16214–16230, 2012.

[130] Nicholas T Kattamis, Matthew S Brown, and Craig B Arnold. Finite element analysis of blister formation in laser-induced forward transfer. Journal of Materials Research, 26(18):2438, 2011.

[131] Jinhua Hong. Thermo-mechanical analysis of blister formation on a rigid substrate in blister-actuated laser-induced forward transfer. IEEE Transactions on Components, Packaging and Manufacturing Technology, 10(4):637–643, 2019.

[132] Shu Guo, Kai-Tak Wan, and David A Dillard. A bending-to-stretching analysis of the blister test in the presence of tensile residual stress. International Journal of Solids and Structures, 42(9-10):2771–2784, 2005.

[133] Jian-ming Gong, Wen-chun Jiang, Jian-qun Tang, and Shan-tung Tu. Experiment study and numerical simulation on the hydrogen blister in 16mnr steel at wet h2s environment. Pressure Vessel Technology, 2, 2007.

[134] LM Jiang, YC Zhou, YG Liao, and CQ Sun. A pressurized blister test model for the interface adhesion of dissimilar elastic–plastic materials. Materials Science and Engineering: A, 487(1-2):228–234, 2008.

[135] Petros Sofronis and Howard K Birnbaum. Mechanics of the hydrogendashdislocation-dashimpurity interactions—i. increasing shear modulus. Journal of the Mechanics and Physics of Solids, 43(1):49–90, 1995.

[136] Sofiane Benannoune, Yann Charles, Jonathan Mougenot, and Monique Gaspérini. Numerical simulation of the transient hydrogen trapping process using an analytical approximation of the mcnabb and foster equation. International Journal of Hydrogen Energy, 43(18):9083–9093, 2018.

[137] Sofiane Benannoune, Yann Charles, Jonathan Mougenot, Monique Gaspérini, and Greg De Temmerman. Multidimensional finite-element simulations of the diffusion and trapping of hydrogen in plasma-facing components including thermal expansion. Physica Scripta, 2020(T171):014011, 2020.

[138] Chaofeng Sang, Jizhong Sun, Xavier Bonnin, Shengguang Liu, and Dezhen Wang. Numerical simulation of the bubble growth due to hydrogen isotopes inventory processes in plasma-irradiated tungsten. Journal of Nuclear Materials, 443(1):403–408, 2013.

[139] X. Bonnin, E. Hodille, N. Ning, C. Sang, and Ch. Grisolia. Rate equations modeling for hydrogen inventory studies during a real tokamak material thermal cycle. Journal of Nuclear Materials, 463:970–973, 2015. PLASMA-SURFACE INTERACTIONS 21.

[140] G Longhurst. Tmap7 user manual ineel. Technical report, EXT-04–02352, Rev. 2, 2008.

[141] Rémi Delaporte-Mathurin, Etienne A Hodille, Jonathan Mougenot, Yann Charles, and Christian Grisolia. Finite element analysis of hydrogen retention in iter plasma facing components using festim. Nuclear Materials and Energy, 21:100709, 2019.

[142] Rémi Delaporte-Mathurin, Etienne A Hodille, Jonathan Mougenot, Yann Charles, Gregory De Temmerman, Floriane Leblond, and Christian Grisolia. Influence of interface conditions on hydrogen transport studies. Nuclear Fusion, 61(3):036038, 2021.

[143] Rémi Delaporte-Mathurin, Etienne Hodille, Jonathan Mougenot, Gregory De Temmerman, Yann Charles, and Christian Grisolia. Parametric study of hydrogenic inventory in the ITER divertor based on machine learning. 10(1).

[144] EA Hodille, X Bonnin, Régis Bisson, T Angot, CS Becquart, JM Layet, and C Grisolia. Macroscopic rate equation modeling of trapping/detrapping of hydrogen isotopes in tungsten materials. Journal of Nuclear Materials, 467:424–431, 2015.

[145] E A Hodille, E Bernard, S Markelj, J Mougenot, C S Becquart, R Bisson, and C Grisolia. Estimation of the tritium retention in ITER tungsten divertor target using macroscopic rate equations simulations. Physica Scripta, T170:014033, oct 2017.

[146] Ken-ichi Ebihara, Yuri Sugiyama, Ryosuke Matsumoto, Kenichi Takai, and Tomoaki Suzudo. Numerical interpretation of hydrogen thermal desorption spectra for iron with hydrogen-enhanced strain-induced vacancies. Metallurgical and Materials Transactions A, 52(1):257–269, 2021.

[147] Abderrazak Traidia, Marco Alfano, Gilles Lubineau, Sebastien Duval, and Abdelmounam Sherik. An effective finite element model for the prediction of hydrogen induced cracking in steel pipelines. 37(21):16214–16230.

[148] D Matveev, M Wensing, L Ferry, F Virot, M Barrachin, Y Ferro, and Ch Linsmeier. Reaction-diffusion modeling of hydrogen transport and surface effects in application to single-crystalline be. Nuclear Instruments and Methods in Physics Research Section B: Beam Interactions with Materials and Atoms, 430:23–30, 2018.

[149] Glen R Longhurst. The soret effect and its implications for fusion reactors. Journal of nuclear materials, 131(1):61–69, 1985.

[150] Yann Charles, Jonathan Mougenot, and Monique Gaspérini. Effect of transient trapping on hydrogen transport near a blunting crack tip. International Journal of Hydrogen Energy, 46(18):10995–11003, 2021.

[151] K Schmid, J Bauer, T Schwarz-Selinger, S Markelj, U v Toussaint, A Manhard, and W Jacob. Recent progress in the understanding of h transport and trapping in w. Physica Scripta, T170:014037, oct 2017.

[152] E A Hodille, Y Ferro, N Fernandez, C S Becquart, T Angot, J M Layet, R Bisson, and C Grisolia. Study of hydrogen isotopes behavior in tungsten by a multi trapping macroscopic rate equation model. Physica Scripta, T167:014011, jan 2016.

[153] Paul Bastien and P Azou. Influence of the amplitude and of the speed of plastic deformation of the segregation of hydrogen in iron and steels. Comptes Rendus Hebdomadaires des séances de l'Académie des Sciences, 232:69–71, 1951.

[154] T Boniszewski and G C Smith. The influence of hydrogen on the plastic deformation ductility, and fracture of nickel in tension. Acta Metallurgica, 11(3):165–178, March 1963.

[155] B A Wilcox and G C Smith. Intercrystalline fracture in hydrogen-charged nickel. Acta Metallurgica, 13(3):331–343, March 1965.

[156] James A Donovan. Accelerated evolution of hydrogen from metals during plastic deformation. Metallurgical Transactions A, 7(11):1677–1683, November 1976.

[157] A H Windle and G C Smith. The Effect of Hydrogen on the Plastic Deformation of Nickel Single Crystals. Metal Science Journal, 2(1):187–191, 1968.

[158] L M Foster, T H Jack, and W W Hill. Structures revealed in zone refined aluminum by tritium decoration. Metallurgical and Materials Transactions B, 1(11):3117–3124, November 1970.

[159] MacIntyre R Louthan, G R Caskey Jr., James A Donovan, and D E Rawl Jr. Hydrogen embrittlement of metals. Materials Science and Engineering: A, 10:357–368, January 1972.

[160] R Broudeur, J P Fidelle, and H Auchers. Experience montrant le role des dislocations dans le transport de l'hydrogene. In L'hydrogène Dans Les Métaux: Congrès International, pages 106–107, Paris, France, 1972.

[161] Anthony W Thompson. Hydrogen embrittlement of stainless steels by lithium hydride. Metallurgical and Materials Transactions B, 4(12):2819–2825, December 1973.

[162] Anthony W Thompson. The behavior of sensitized 309S stainless steel in hydrogen. Materials Science and Engineering: A, 14(3):253–264, June 1974.

[163] J D Frandsen and H L Marcus. The correlation between grain size and plastic zone size for environmental hydrogen assisted fatigue crack propagation. Scripta Metallurgica, 9(10):1089–1094, October 1975.

[164] Cherngye Hwang and I M Bernstein. A demonstration of dislocation transport of hydrogen in iron. Scripta Metallurgica, 17(11):1299–1304, November 1983.

[165] E Fricke, H P Stüwe, and G Vibrans. Dissolution of hydrogen from the gas in steel at room temperature. Metallurgical Transactions A, 2(9):2697–2700, September 1971.

[166] R Otsuka and M Isaji. On the electrochemical permeation measurements of hydrogen in nickel undergoing plastic deformation. Scripta Metallurgica, 15(10):1153–1156, October 1981.

[167] John K Tien, Rebecca J Richards, Otto Buck, and Harris L Marcus. Model of dislocation sweep-in of hydrogen during fatigue crack growth. Scripta Metallurgica, 9(10):1097–1101, October 1975.

[168] Yann Charles, Tuan Hung Nguyen, Kevin Ardon, and Monique Gaspérini. Scale Transition in Finite Element Simulations of Hydrogen–Plasticity Interactions. In I Ionescu, Sylvain Queyreau, Catalin Picu, and Oguz Umut Salman, editors, Mechanics and Physics of Solids at Micro- and Nano-Scales, pages 87–129. Wiley, December 2019.

[169] AJ Kumnick and HH Johnson. Deep trapping states for hydrogen in deformed iron. Acta Metallurgica, 28(1):33–39, 1980.

[170] Dmitry Terentyev, Gregory De Temmerman, Boris Minov, Yevhen Zayachuk, Konstantza Lambrinou, TW Morgan, Andrii Dubinko, Kirill Bystrov, and Guido Van Oost. Synergy of plastic deformation and gas retention in tungsten. Nuclear Fusion, 55(1):013007, 2014.

[171] E. A. Hodille, N. Fernandez, Z. A. Piazza, M. Ajmalghan, and Y. Ferro. Hydrogen supersaturated layers in h/d plasma-loaded tungsten: A global model based on thermodynamics, kinetics and density functional theory data. Phys. Rev. Materials, 2:093802, Sep 2018.

[172] Y. Li, T.W. Morgan, D. Terentyev, S. Ryelandt, A. Favache, S. Wang, M. Wirtz, J.P.M. Hoefnagels, J.A.W. van Dommelen, G. De Temmerman, K. Verbeken, and M.G.D. Geers. Three mechanisms of hydrogen-induced dislocation pinning in tungsten. Nuclear Fusion, 60(8):086015, jul 2020.

[173] T Faney and B D Wirth. Spatially dependent cluster dynamics modeling of microstructure evolution in low energy helium irradiated tungsten. Modelling and Simulation in Materials Science and Engineering, 22(6):065010, aug 2014.

[174] N. Fernandez, Y. Ferro, and D. Kato. Hydrogen diffusion and vacancies formation in tungsten: Density functional theory calculations and statistical models. Acta Materialia, 94:307–318, 2015.

[175] Donald F. Johnson and Emily A. Carter. Hydrogen in tungsten: Absorption, diffusion, vacancy trapping, and decohesion. Journal of Materials Research, 25(2):315–327, 2010.

[176] K. Heinola, F. Djurabekova, and T. Ahlgren. On the stability and mobility of di-vacancies in tungsten. Nuclear Fusion, 58(2):026004, dec 2017.

[177] T. Faney, S.I. Krasheninnikov, and B.D. Wirth. Spatially dependent cluster dynamics model of he plasma surface interaction in tungsten for fusion relevant conditions. Nuclear Fusion, 55(1):013014, dec 2014.

[178] Sophie Blondel, David E. Bernholdt, Karl D. Hammond, and Brian D. Wirth. Continuum-scale modeling of helium bubble bursting under plasma-exposed tungsten surfaces. Nuclear Fusion, 58(12):126034, nov 2018.

[179] Adrián Del-Pozo, Julio C Villalobos, and Sergio Serna. A general overview of hydrogen embrittlement. In Current Trends and Future Developments on (Bio-) Membranes, pages 139–168. Elsevier, January 2020.

[180] Xinfeng Li, Xianfeng Ma, Jin Zhang, Eiji Akiyama, Yanfei Wang, and Xiaolong Song. Review of Hydrogen Embrittlement in Metals: Hydrogen Diffusion, Hydrogen Characterization, Hydrogen Embrittlement Mechanism and Prevention. Acta Metallurgica Sinica (English Letters), 15:1–15, April 2020.

[181] N N Sergeev, A N Sergeev, S N Kutepov, A G Kolmakov, and A E Gvozdev. Mechanism of the Hydrogen Cracking of Metals and Alloys, Part I (Review). Inorganic Materials: Applied Research, 10(1):24–31, May 2019.

[182] N N Sergeev, A N Sergeev, S N Kutepov, A G Kolmakov, and A E Gvozdev. Mechanism of the Hydrogen Cracking of Metals and Alloys, Part II (Review). Inorganic Materials: Applied Research, 10(1):32–41, May 2019.

[183] Sandeep Kumar Dwivedi and Manish Vishwakarma. Hydrogen embrittlement in different materials: A review. International Journal of Hydrogen Energy, 43(46):21603–21616, November 2018.

[184] Zeynab Shirband, Mohammad Reza Shishesaz, and Ali Ashrafi. Hydrogen degradation of steels and its related parameters, a review. Phase Transitions, 84(11-12):924–943, November 2011.

[185] John P Hirth. Effects of hydrogen on the properties of iron and steel. Metallurgical Transactions A, 11(6):861–890, 1980.

[186] M R Louthan. Hydrogen Embrittlement of Metals: A Primer for the Failure Analyst. Journal of Failure Analysis and Prevention, 8(3):289–307, June 2008.

[187] Akihide Nagao, Cynthia D Smith, Mohsen Dadfarnia, Petros Sofronis, and Ian M Robertson. The role of hydrogen in hydrogen embrittlement fracture of lath martensitic steel. Acta Materialia, 60(13-14):5182–5189, August 2012.

[188] Maoqiu Wang, Eiji Akiyama, and Kaneaki Tsuzaki. Effect of hydrogen and stress concentration on the notch tensile strength of AISI 4135 steel. Materials Science and Engineering: A, 398(1-2):37–46, May 2005.

[189] Ian M Robertson, Petros Sofronis, Akihide Nagao, May L Martin, S Wang, D W Gross, and K E Nygren. Hydrogen Embrittlement Understood. Metallurgical and Materials Transactions B, 46(3):1085–1103, March 2015.

[190] Stan Lynch. Hydrogen embrittlement phenomena and mechanisms. Corrosion Reviews, 30(3-4):105–123, June 2012.

[191] May L Martin, Mohsen Dadfarnia, Akihide Nagao, Shuai Wang, and Petros Sofronis. Enumeration of the hydrogen-enhanced localized plasticity mechanism for hydrogen embrittlement in structural materials. Acta Materialia, 165:734–750, February 2019.

[192] Abderrazak Traidia, E Chatzidouros, and M Jouiad. Review of hydrogen-assisted cracking models for application to service lifetime prediction and challenges in the oil and gas industry. Corrosion Reviews, 36(4):323–347, 2018.

[193] Milos B Djukic, Gordana M Bakic, Vera Sijacki Zeravcic, Aleksandar Sedmak, and Bratislav Rajicic. Hydrogen Embrittlement of Industrial Components: Prediction, Prevention, and Models. Corrosion, 72(7):943–961, July 2016.

[194] I M Bernstein. Hydrogen-induced cracking in iron: Morphology and crack path dependence. Metallurgical and Materials Transactions B, 1(11):3143–3150, November 1970.

[195] Goutam Ghosh, Paul Rostron, Rajnish Garg, and Ashoutosh Panday. Hydrogen induced cracking of pipeline and pressure vessel steels: A review. Engineering Fracture Mechanics, 199:609–618, June 2018.

[196] Stan Lynch. Discussion of some recent literature on hydrogen-embrittlement mechanisms: addressing common misunderstandings. Corrosion Reviews, 37(5):377–395, 2019.

[197] Milos B Djukic, Gordana M Bakic, Vera Sijacki Zeravcic, Aleksandar Sedmak, and Bratislav Rajicic. The synergistic action and interplay of hydrogen embrittlement mechanisms in steels and iron: Localized plasticity and decohesion. Engineering Fracture Mechanics, 216:106528, June 2019.

[198] Shuang Liang, Minsheng Huang, Lv Zhao, Yaxin Zhu, and Zhenhuan Li. Effect of multiple hydrogen embrittlement mechanisms on crack propagation behavior of FCC metals: Competition vs. synergy. International Journal of Plasticity, 143:103023, August 2021.

[199] D Guedes, L Cupertino Malheiros, Abdelali Oudriss, S Cohendoz, J Bouhattate, J Creus, F Thébault, M Piette, and Xavier Feaugas. The role of plasticity and hydrogen flux in the fracture of a tempered martensitic steel: A new design of mechanical test

until fracture to separate the influence of mobile from deeply trapped hydrogen. Acta Materialia, 186:133–148, March 2020.

[200] L Jemblie, Vigdis Olden, and Odd Magne Akselsen. A review of cohesive zone modelling as an approach for numerically assessing hydrogen embrittlement of steel structures. Philosophical Transactions of the Royal Society A: Mathematical, Physical and Engineering Sciences, 375(2098):20160411–15, June 2017.

[201] A A Griffith. The phenomena of rupture and flow in solids. Philosophical Transactions of the Royal Society of London. Series A, Containing Papers of a Mathematical or Physical Character, 221(582-593):163–198, 1921.

[202] S Serebrinsky, Emily A Carter, and M Ortiz. A quantum-mechanically informed continuum model of hydrogen embrittlement. Journal of the Mechanics and Physics of Solids, 52:2403–2430, 2004.

[203] A G Varias and A R Massih. Simulation of hydrogen embrittlement in zirconium alloys under stress and temperature gradients. Journal of Nuclear Materials, 279:273–285, 2000.

[204] Y Liang and Petros Sofronis. Toward a phenomenological description of hydrogen-induced decohesion at particle/matrix interfaces. Journal of the Mechanics and Physics of Solids, 51:1509–1531, 2003.

[205] D E Jiang and Emily A Carter. First principles assessment of ideal fracture energies of materials with mobile impurities: implications for hydrogen embrittlement of metals. Acta Materialia, 52(16):4801–4807, 2004.

[206] Antonio Alvaro, I Thue Jensen, N Kheradmand, O M Løvvik, and Vigdis Olden. Hydrogen embrittlement in nickel, visited by first principles modeling, cohesive zone simulation and nanomechanical testing. International Journal of Hydrogen Energy, July 2015.

[207] Yann Charles, Monique Gaspérini, J Disashi, and Patrice Jouinot. Numerical modeling of the Disk Pressure Test up to failure under gaseous hydrogen. Journal of Materials Processing Technology, 212(8):1761–1770, 2012.

[208] Takeshi Takaishi. Phase Field Crack Growth Model with Hydrogen Embrittlement. In Mathematical Analysis of Continuum Mechanics and Industrial Applications, pages 27–34. Springer, Singapore, November 2016.

[209] Fernando P Duda, A Ciarbonetti, S Toro, and A E Huespe. A phase-field model for solute-assisted brittle fracture in elastic-plastic solids. International Journal of Plasticity, 102:16–40, December 2017.

[210] Lallit Anand, Yunwei Mao, and Brandon Talamini. On modeling fracture of ferritic steels due to hydrogen embrittlement. Journal of the Mechanics and Physics of Solids, 122:280–314, January 2019.

[211] Dhiraj Kumar Singh, S K Maiti, Tanmay K Bhandakkar, and R K Singh Raman. Cohesive zone based axisymmetric modelling of hydrogen-assisted cracking in a circumferentially notched tensile specimen. International Journal of Hydrogen Energy, 43(27):12530–12542, July 2018.

[212] Vigdis Olden, Christian Thaulow, Roy Johnsen, Erling Østby, and Torodd Berstad. Influence of hydrogen from cathodic protection on the fracture susceptibility of 25SENT testing and FE-modelling using hydrogen influenced cohesive zone elements. Engineering Fracture Mechanics, 76(7):827–844, May 2009.

[213] Chiara Colombo, Alfredo Zafra García, Javier Belzunce, and Inés Fernandez Pariente. Sensitivity to hydrogen embrittlement of AISI 4140 steel: A numerical study on fracture toughness. Theoretical and Applied Fracture Mechanics, 110:102810, December 2020.

[214] W J D Shaw H Huang. Hydrogen-Embrittlement-Interactions-in-Cold-Worked. Corrosion, 51(1):30–36, 1995.

[215] R Falkenberg, Wolfgang Brocks, W Dietzel, and Ingo Scheider. Modelling the effect of hydrogen on ductile tearing resistance of steels. International Journal of Materials Research, 101(8):989–996, August 2010.

[216] Yanfei Wang, Xuanpei Wu, Zhiling Zhou, and Xinfeng Li. Numerical analysis of hydrogen transport into a steel after shot peening. Results in Physics, 11:5–16, December 2018.

[217] Yu Estrin and H Mecking. A unified phenomenological description of work hardening and creep based on one-parameter models. Acta metallurgica, 32(1):57–70, 1984.

[218] Ian M Robertson, Howard K Birnbaum, and Petros Sofronis. Hydrogen Effects on Plasticity. In John P Hirth and L P Kubin, editors, Dislocations in Solids, pages 249–293. Elsevier, 2009.

[219] G Hachet, Abdelali Oudriss, Afrooz Barnoush, T Hajilou, D Wang, Arnaud Metsue, and Xavier Feaugas. Antagonist softening and hardening effects of hydrogen investigated using nanoindentation on cyclically pre-strained nickel single crystal. Materials Science and Engineering: A, page 140480, November 2020.

[220] Daniel P Abraham and Carl J Altstetter. The effect of hydrogen on the yield and flow stress of an austenitic stainless steel. Metallurgical and Materials Transactions A, 26(11):2849–2858, November 1995.

[221] A H Cottrell and M A Jaswon. Distribution of solute atoms round a slow dislocation. Proceedings of the Royal Society of London. Series A. Mathematical and Physical Sciences, October 1949.

[222] T Matsumoto, J Eastman, and Howard K Birnbaum. Direct observations of enhanced dislocation mobility due to hydrogen. Scripta Metallurgica, 15(9):1033–1037, September 1981.

[223] A M Brass and Jacques Chêne. Influence of deformation on the hydrogen behavior in iron and nickel base alloys: a review of experimental data. Materials Science and Engineering: A, 242(1-2):210–221, 1998.

[224] Daniel P Abraham and Carl J Altstetter. Hydrogen-enhanced localization of plasticity in an austenitic stainless steel. Metallurgical and Materials Transactions A, 26(11):2859–2871, November 1995.

[225] P J Ferreira, Ian M Robertson, and Howard K Birnbaum. Hydrogen effects on the interaction between dislocations. Acta Materialia, 46(5):1749–1757, 1998.

[226] H Kimura and H Matsui. Mechanism of hydrogen-induced softening and hardening in iron. Scripta Metallurgica, 21(3):319–324, March 1987.

[227] H Matsui, H Kimura, and S Moriya. The effect of hydrogen on the mechanical properties of high purity iron I. Softening and hardening of high purity iron by hydrogen charging during tensile deformation. Materials Science and Engineering: A, 40(2):207–216, 1979.

[228] Reza Miresmaeili, Masao Ogino, T Nakagawa, and Hiroshi Kanayama. A coupled elastoplastic-transient hydrogen diffusion analysis to simulate the onset of necking in tension by using the finite element method. International Journal of Hydrogen Energy, 35(3):1506–1514, 2010.

[229] Eugene Ogosi, U B Asim, M A Siddiq, and M E Kartal. Modelling Hydrogen Induced Stress Corrosion Cracking in Austenitic Stainless Steel. Journal of Mechanics, 36(2):213–222, April 2020.

[230] N Vasios. Crystal Plasticity. A rate–independent constitutive model. The effect of Hydrogen concentration. Master's thesis, University of Thessaly, Greece, 2015.

[231] Shulin Yuan, Yaxin Zhu, Minsheng Huang, Shuang Liang, and Zhenhuan Li. Dislocation-density based crystal plasticity model with hydrogen-enhanced. Mechanics of Materials, 148:103472, 2020.

[232] H Peisl. Lattice strains due to hydrogen in metals. In Hydrogen in Metals I, pages 53–74. Springer, Berlin, Heidelberg, 1978.

[233] Ksenia P Frolova, Elena N Vilchevskaya, Vladimir A Polyanskiy, and Yuriy A Yakovlev. Modeling the skin effect associated with hydrogen accumulation by means of the micropolar continuum. Continuum Mechanics and Thermodynamics, 33(3):697–711, May 2021.

[234] Song Huang, Yalin Zhang, Chao Yang, and Hui Hu. Fracture strain model for hydrogen embrittlement based on hydrogen enhanced localized plasticity mechanism. International Journal of Hydrogen Energy, 45(46):25541–25554, September 2020.

[235] Jiaqing Li, Abdelali Oudriss, Arnaud Metsue, J Bouhattate, and Xavier Feaugas. Anisotropy of hydrogen diffusion in nickel single crystals: the effects of self-stress and hydrogen concentration on diffusion. Scientific Reports, 7:45041, March 2017.

[236] R.A. Pitts, B. Bazylev, J. Linke, I. Landman, M. Lehnen, D. Loesser, Th. Loewenhoff, M. Merola, R. Roccella, G. Saibene, M. Smith, and V.S. Udintsev. Final case for a stainless steel diagnostic first wall on ITER. Journal of Nuclear Materials, 463:748–752, 2015.

[237] D. Loesser. DFW Design Description Document (4D7MK6). Technical Report 4D7MK6, ITER, 2011.

[238] Sofiane Benannoune, Yann Charles, Jonathan Mougenot, Monique Gaspérini, and Greg De Temmerman. Multidimensional finite-element simulations of the diffusion and trapping of hydrogen in plasma-facing components including thermal expansion. Physica Scripta, T171:014011, 2020.

[239] A. McNabb and P. K. Foster. A new analysis of the diffusion of hydrogen in iron and ferritic steels. Transactions of the Metallurgical Society of AIME, 227:618–627, 1963.

[240] Andreas Drexler, Tom Depover, Silvia Leitner, Kim Verbeken, and Werner Ecker. Microstructural based hydrogen diffusion and trapping models applied to fe–cx alloys. Journal of Alloys and Compounds, 826:154057, 2020.

[241] D Umbrello, R M'saoubi, and JC Outeiro. The influence of johnson–cook material constants on finite element simulation of machining of aisi 316l steel. International Journal of Machine Tools and Manufacture, 47(3-4):462–470, 2007.

[242] Gordon R Johnson. A constitutive model and data for materials subjected to large strains, high strain rates, and high temperatures. Proc. 7th Inf. Sympo. Ballistics, pages 541–547, 1983.

[243] Onur Sayman, Faruk Sen, Erdal Celik, and Yusuf Arman. Thermal stress analysis of wc–co/cr–ni multilayer coatings on 316l steel substrate during cooling process. Materials & Design, 30(3):770–774, 2009.

[244] H Chandrasekaran, R M'saoubi, and H Chazal. Modelling of material flow stress in chip formation process from orthogonal milling and split hopkinson bar tests. Machine Science and Technology, 9(1):131–145, 2005.

[245] R.-D. Penzhorn, Y. Torikai, K. Watanabe, M. Matsuyama, and A. Perevezentsev. On the fate of tritium in thermally treated stainless steel type 316L. Journal of Nuclear Materials, 429(1-3):346–352, 2012.

[246] A.J. Kumnick and H.H. Johnson. Deep trapping states for hydrogen in deformed iron. Acta Metallurgica, 28(1):33–39, 1980.

[247] P. Sofronis and R.M. McMeeking. Numerical analysis of hydrogen transport near a blunting crack tip. Journal of the Mechanics and Physics of Solids, 37(3):317–350, 1989.

[248] Y. Charles, H.T. Nguyen, and M. Gaspérini. FE simulation of the influence of plastic strain on hydrogen distribution during an U-bend test. International Journal of Mechanical Sciences, 120:214–224, 2017.

[249] S. Benannoune, Y. Charles, J. Mougenot, and M. Gaspérini. Piégeage transitoire de l'hydrogène dans les matériaux métalliques. In Journée Jeune Chercheur CEFRACOR, Sciences de la matière, pages 129–136. C. Blanc, C. Bosch, S. Dejardin, Paris, presses des mines edition, 2017.

[250] Yann Charles, Sofiane Benannoune, Jonathan Mougenot, and Monique Gaspérini. Numerical simulation of the transient hydrogen trapping process using an analytical approximation of the mcnabb and foster equation. part 2: Domain of validity. International Journal of Hydrogen Energy, 46(58):30173–30189, 2021.

[251] G. De Temmerman. Tritium permeation to cooling water through a steel surface (VP88QL). Technical Report VP88QL, ITER, 2018.

[252] E. A. Hodille, N. Fernandez, Z. A. Piazza, M. Ajmalghan, and Y. Ferro. Hydrogen supersaturated layers in H/D plasma-loaded tungsten: A global model based on thermodynamics, kinetics and density functional theory data. Physical Review Materials, 2(9), 2018.

[253] Rémi Delaporte-Mathurin, Etienne Hodille, Jonathan Mougenot, Gregory De Temmerman, Yann Charles, and Christian Grisolia. Parametric study of hydrogenic inventory in the ITER divertor based on machine learning. Scientific Reports, 10(1), 2020.

[254] Yann Charles, Hung Tuan Nguyen, and Monique Gaspérini. Comparison of hydrogen transport through pre-deformed synthetic polycrystals and homogeneous samples by

finite element analysis. international journal of hydrogen energy, 42(31):20336–20350, 2017.

[255] Steven PK Sternberg. Dispersion measurements in highly heterogeneous laboratory scale porous media. Transport in Porous Media, 54(1):107–124, 2004.

[256] Xiaoxian Zhang, Xuebin Qi, and Dongmei Qiao. Change in macroscopic concentration at the interface between different materials: Continuous or discontinuous. Water Resources Research, 46(10), 2010.

[257] Brian Berkowitz, Andrea Cortis, Ishai Dror, and Harvey Scher. Laboratory experiments on dispersive transport across interfaces: The role of flow direction. Water resources research, 45(2), 2009.

[258] Xue-Jun Fan and Ephraim Suhir. Moisture sensitivity of plastic packages of IC devices. Springer, 2010.

[259] Liangbiao Chen, Jenny Zhou, Hsing-Wei Chu, and Xuejun Fan. A unified and versatile model study for moisture diffusion. In 2017 IEEE 67th Electronic Components and Technology Conference (ECTC), pages 1660–1667. IEEE, 2017.

[260] DT Wadiak. Application of the finite-element method to the diffusion and reaction of chemical species in multilayered polymeric bodies. Mathematical Modelling, 7(2-3):385–395, 1986.

[261] M A Rahman and M Z Saghir. Thermodiffusion or Soret effect: Historical review. International Journal of Heat and Mass Transfer, 73:693–705, 2014.

[262] Alfons HM Krom and AD Bakker. Hydrogen trapping models in steel. Metallurgical and materials transactions B, 31(6):1475–1482, 2000.

[263] Petros Sofronis. The influence of mobility of dissolved hydrogen on the elastic response of a metal. Journal of the Mechanics and Physics of Solids, 43(9):1385–1407, 1995.

[264] Frantz Martin, Xavier Feaugas, Abdelali Oudriss, Döme Tanguy, Laurent Briottet, and Jean Kittel. State of hydrogen in matter: Fundamental ad/absorption, trapping and transport mechanisms. In Mechanics-Microstructure-Corrosion Coupling, pages 171–197. Elsevier, 2019.

[265] ABAQUS Documentation. Simulia. Providence, Rhode Island, 2012.

[266] A McNabb and PK Foster. A new analysis of diffusion of hydrogen in iron and ferritic steels. Transactions of the Metallurgical Society of AIME, 227(3):618, 1963.

[267] Chang-Sik Oh, Yun-Jae Kim, and Kee-Bong Yoon. Coupled analysis of hydrogen transport using abaqus. Journal of Solid Mechanics and Materials Engineering, 4(7):908–917, 2010.

[268] Sofiane Benannoune, Yann Charles, Jonathan Mougenot, and Monique Gaspérini. Numerical simulation of the transient hydrogen trapping process using an analytical approximation of the mcnabb and foster equation. International Journal of Hydrogen Energy, 43(18):9083–9093, 2018.

[269] JW Davis and PD Smith. Iter material properties handbook. Journal of Nuclear Materials, 233:1593–1596, 1996.

[270] Jörg Hohe, Sascha Fliegener, Claudio Findeisen, Jens Reiser, Verena Widak, and Michael Rieth. Numerical exploration into the potential of tungsten reinforced cucrzr matrix composites. Journal of Nuclear Materials, 470:13–29, 2016.

[271] R Frauenfelder. Solution and diffusion of hydrogen in tungsten. Journal of Vacuum Science and Technology, 6(3):388–397, 1969.

[272] N Fernandez, Y Ferro, and D Kato. Hydrogen diffusion and vacancies formation in tungsten: density functional theory calculations and statistical models. Acta Materialia, 94:307–318, 2015.

[273] Donald F Johnson and Emily A Carter. Hydrogen in tungsten: Absorption, diffusion, vacancy trapping, and decohesion. Journal of Materials Research, 25(2):315–327, 2010.

[274] A Driessen, P Sanger, H Hemmes, and R Griessen. Metal hydride formation at pressures up to 1 mbar. Journal of physics: Condensed matter, 2(49):9797, 1990.

[275] F Reiter, G Gervasini, and KS Forcey. A compilation of tritium-material interaction parameters in fusion reactor materials. Office for Official Publications of the European Communities, 1993.

[276] I Peñalva, G Alberro, F Legarda, GA Esteban, and B Riccardi. Interaction of copper alloys with hydrogen. Copper Alloys-Early Applications and Current Performance-Enhancing Processes, pages 31–48, 2012.

[277] Roman Nazarov, Tilmann Hickel, and Jörg Neugebauer. Ab initio study of h-vacancy interactions in fcc metals: Implications for the formation of superabundant vacancies. Physical Review B, 89(14):144108, 2014.

[278] D. Guillermain. Internship's report D. Guillermain (T2YEND). Technical Report T2YEND, ITER, 2016.

[279] E Serra and A Perujo. Hydrogen and deuterium transport and inventory parameters in a cu–0.65 cr–0.08 zr alloy for fusion reactor applications. Journal of nuclear materials, 258:1028–1032, 1998.

[280] Rémi Delaporte-Mathurin, Etienne Hodille, Jonathan Mougenot, Gregory De Temmerman, Yann Charles, and Christian Grisolia. Parametric study of hydrogenic inventory in the iter divertor based on machine learning. Scientific reports, 10(1):1–12, 2020.

[281] D Terentyev, G De Temmerman, TW Morgan, Y Zayachuk, K Lambrinou, B Minov, A Dubinko, K Bystrov, and G Van Oost. Effect of plastic deformation on deuterium retention and release in tungsten. Journal of Applied Physics, 117(8):083302, 2015.

[282] Sellami Leila. Internship report. Technical report, LSPM, 2019.

[283] EA Hodille, N Fernandez, ZA Piazza, M Ajmalghan, and Y Ferro. Hydrogen supersaturated layers in h/d plasma-loaded tungsten: a global model based on thermodynamics, kinetics and density functional theory data. Physical Review Materials, 2(9):093802, 2018.

[284] EA Hodille, Yves Ferro, Nicolas Fernandez, CS Becquart, Thierry Angot, Jean-Marc Layet, Régis Bisson, and Christian Grisolia. Study of hydrogen isotopes behavior in tungsten by a multi trapping macroscopic rate equation model. Physica Scripta, 2016(T167):014011, 2016.

[285] Rémi Delaporte-Mathurin, Hao Yang, Julien Denis, James Dark, Etienne A Hodille, Gregory De Temmerman, Xavier Bonnin, Jonathan Mougenot, Yann Charles, Hugo Bufferand, et al. Fuel retention in west and iter divertors based on festim monoblock simulations. Nuclear Fusion, 61(12):126001, 2021.

[286] RA Pitts, X Bonnin, F Escourbiac, H Frerichs, JP Gunn, T Hirai, AS Kukushkin, E Kaveeva, MA Miller, D Moulton, et al. Physics basis for the first iter tungsten divertor. Nuclear Materials and Energy, 20:100696, 2019.

[287] Huy Duong Bui and S Taheri. La singularité «epine» dans les bi-matériaux en thermoélastoplasticité. Comptes rendus de l'Académie des sciences. Série 2, Mécanique, Physique, Chimie, Sciences de l'univers, Sciences de la Terre, 309(16):1527–1533, 1989.

[288] EA Hodille, Rémi Delaporte-Mathurin, J Denis, M Pecovnik, E Bernard, Y Ferro, R Sakamoto, Y Charles, J Mougenot, A De Backer, et al. Modelling of hydrogen isotopes trapping, diffusion and permeation in divertor monoblocks under iter-like conditions. Nuclear Fusion, 61(12):126003, 2021.

[289] S. Ben Ayed. Simulation par Éléments finis de la diffusion et de l'agrégation des lacunes dans les structures métalliques, 2022.

[290] MA Oude Vrielink, JAW van Dommelen, and MGD Geers. Multi-scale fracture probability analysis of tungsten monoblocks under fusion conditions. Nuclear Materials and Energy, 28:101032, 2021.

[291] T Toyama, K Ami, K Inoue, Y Nagai, K Sato, Q Xu, and Y Hatano. Deuterium trapping at vacancy clusters in electron/neutron-irradiated tungsten studied by positron annihilation spectroscopy. Journal of Nuclear Materials, 499:464–470, 2018.

[292] XC Ren, QJ Zhou, GB Shan, WY Chu, JX Li, YJ Su, and LJ Qiao. A nucleation mechanism of hydrogen blister in metals and alloys. Metallurgical and materials transactions A, 39(1):87–97, 2008.

[293] M Zibrov, W Egger, J Heikinheimo, M Mayer, and F Tuomisto. Vacancy cluster growth and thermal recovery in hydrogen-irradiated tungsten. Journal of Nuclear Materials, 531:152017, 2020.

[294] LS Dubrovinsky and SK Saxena. Thermal expansion of periclase (mgo) and tungsten (w) to melting temperatures. Physics and Chemistry of Minerals, 24(8):547–550, 1997.

[295] Dora Nagy and Samuel A Humphry-Baker. An oxidation mechanism map for tungsten. Scripta Materialia, 209:114373, 2022.

[296] Simulia. abaqus user subroutines reference guide. dassault systèmes, 2011.

[297] Y Charles, M Gaspérini, J Disashi, and P Jouinot. Numerical modeling of the disk pressure test up to failure under gaseous hydrogen. Journal of Materials Processing Technology, 212(8):1761–1770, 2012.

[298] Elisabeth Vasikaran, Yann Charles, and Pierre Gilormini. Implementation of a reaction-diffusion process in the abaqus finite element software. Mechanics & Industry, 21(5):508, 2020.

[299] Yann Charles, Jonathan Mougenot, and Monique Gasperini. Modeling hydrogen dragging by mobile dislocations in finite element simulations. International Journal of Hydrogen Energy, 47(28):13746–13761, 2022.

[300] Aimad Oukhlef, Abdelhak Ambari, and Stéphane Champmartin. Identification of the pore size distribution of a porous medium by yield stress fluids using herschel-bulkley model. Mechanics & Industry, 21(5):509, 2020.

[301] KD Rasch, RW Siegel, and H Schultz. Quenching and recovery investigations of vacancies in tungsten. Philosophical Magazine A, 41(1):91–117, 1980.

[302] T Ahlgren, K Heinola, K Vörtler, and J Keinonen. Simulation of irradiation induced deuterium trapping in tungsten. Journal of nuclear materials, 427(1-3):152–161, 2012.

[303] Osman El-Atwani, W Streit Cunningham, Jason R Trelewicz, Meimei Li, Brian David Wirth, and Stuart Andrew Maloy. Revealing the synergistic effects of sequential and simultaneous dual beam irradiations in tungsten via in-situ tem. Journal of Nuclear Materials, 538:152150, 2020.

[304] Charlotte S Becquart, Christophe Domain, Utpal Sarkar, Andrée Debacker, and Marc Hou. Microstructural evolution of irradiated tungsten: Ab initio parameterisation of an okmc model. Journal of nuclear materials, 403(1-3):75–88, 2010.

[305] Hao-Xuan Huang, Yu-Hao Li, Zhong-Zhu Li, Peng-Wei Hou, Fang-Fei Ma, Qing-Yuan Ren, Hong-Bo Zhou, and Guang-Hong Lu. Role of hydrogen in stability and mobility of vacancy clusters in tungsten. Tungsten, pages 1–12, 2022.

[306] T Ahlgren, K Heinola, Niklas Juslin, and Antti Kuronen. Bond-order potential for point and extended defect simulations in tungsten. Journal of Applied Physics, 107(3):033516, 2010.

[307] JY Park, HCW Huang, RW Siegel, and RW Balluffi. A quantitative study of vacancy defects in quenched tungsten by combined field-ion microscopy and electrical resistometry. Philosophical Magazine A, 48(3):397–419, 1983.

[308] Peter M Derlet, D Nguyen-Manh, and SL Dudarev. Multiscale modeling of crowdion and vacancy defects in body-centered-cubic transition metals. Physical Review B, 76(5):054107, 2007.

[309] CS Becquart and C Domain. Ab initio calculations about intrinsic point defects and he in w. Nuclear Instruments and Methods in Physics Research Section B: Beam Interactions with Materials and Atoms, 255(1):23–26, 2007.

[310] M Muzyk, D Nguyen-Manh, KJ Kurzydłowski, NL Baluc, and SL Dudarev. Phase stability, point defects, and elastic properties of wv and w-ta alloys. Physical Review B, 84(10):104115, 2011.

[311] K Heinola, F Djurabekova, and T Ahlgren. On the stability and mobility of di-vacancies in tungsten. Nuclear Fusion, 58(2):026004, 2017.

[312] Jie Hou, Xiang-Shan Kong, Xuebang Wu, Jun Song, and CS Liu. Predictive model of hydrogen trapping and bubbling in nanovoids in bcc metals. Nature Materials, 18(8):833–839, 2019.

[313] Yaakov Kraftmakher. Equilibrium vacancies and thermophysical properties of metals. Physics Reports, 299(2-3):79–188, 1998.

[314] T Korhonen, Martti J Puska, and Risto M Nieminen. Vacancy-formation energies for fcc and bcc transition metals. Physical Review B, 51(15):9526, 1995.

[315] BF Kostromin, Yu M Plishkin, IE Podchinenov, and I Sh Trakhtenberg. Determination of diffusion parameter connection with microscopic characteristics of point defects by computerized simulation. Fizika Metallov i Metallovedenie, 55(3):450–454, 1983.

[316] JM Harder and DJ Bacon. Point-defect and stacking-fault properties in body-centred-cubic metals with n-body interatomic potentials. Philosophical Magazine A, 54(5):651–661, 1986.

[317] L Kornblit. Single vacancy formation energies in bcc metals. Physica B+ C, 106(3):351–355, 1981.

[318] U Krause, JP Kuska, and R Wedell. Monovacancy formation energies in cubic crystals. physica status solidi (b), 151(2):479–494, 1989.

[319] P Varotsos. Thermodynamic criterion for the analysis of point-defect data in solids. Physical Review B, 37(11):6511, 1988.

[320] Y Ueda, K Schmid, M Balden, JW Coenen, Th Loewenhoff, A Ito, A Hasegawa, C Hardie, M Porton, and M Gilbert. Baseline high heat flux and plasma facing materials for fusion. Nuclear Fusion, 57(9):092006, 2017.

[321] JN Brooks, Jean Paul Allain, RP Doerner, A Hassanein, R Nygren, TD Rognlien, and DG Whyte. Plasma–surface interaction issues of an all-metal iter. Nuclear Fusion, 49(3):035007, 2009.

[322] V Philipps. Tungsten as material for plasma-facing components in fusion devices. Journal of nuclear materials, 415(1):S2–S9, 2011.

[323] Giovanni Bonny, MJ Konstantinovic, Anastasiia Bakaeva, Chao Yin, Nicolas Castin, K Mergia, V Chatzikos, S Dellis, T Khvan, A Bakaev, et al. Trends in vacancy distribution and hardness of high temperature neutron irradiated single crystal tungsten. Acta Materialia, 198:1–9, 2020.

[324] Xunxiang Hu, Takaaki Koyanagi, Makoto Fukuda, Yutai Katoh, Lance L Snead, and Brian D Wirth. Defect evolution in single crystalline tungsten following low temperature and low dose neutron irradiation. Journal of Nuclear Materials, 470:278–289, 2016.

[325] Yuji Hatano, Masashi Shimada, Yasuhisa Oya, Guoping Cao, Makoto Kobayashi, Masanori Hara, Brad J Merrill, Kenji Okuno, Mikhail A Sokolov, and Yutai Katoh. Retention of hydrogen isotopes in neutron irradiated tungsten. Materials Transactions, page MG201204, 2013.

[326] Hiroe Fujita, Kenta Yuyama, Xiaochun Li, Yuji Hatano, Takeshi Toyama, Masayuki Ohta, Kentaro Ochiai, Naoaki Yoshida, Takumi Chikada, and Yasuhisa Oya. Effect of neutron energy and fluence on deuterium retention behaviour in neutron irradiated tungsten. Physica Scripta, 2016(T167):014068, 2016.

[327] G De Temmerman, T Hirai, and RA Pitts. The influence of plasma-surface interaction on the performance of tungsten at the iter divertor vertical targets. Plasma Physics and Controlled Fusion, 60(4):044018, 2018.

[328] SV Malykhin, IE Garkusha, VA Makhlai, SV Surovitskiy, SS Herashchenko, and OI Girka. Mechanisms of crack generation in high-pure tungsten exposed to high power density plasma. Nuclear Instruments and Methods in Physics Research Section B: Beam Interactions with Materials and Atoms, 481:6–11, 2020.

[329] K Heinola, T Ahlgren, S Brezinsek, T Vuoriheimo, S Wiesen, and JET Contributors. Modelling of the effect of elms on fuel retention at the bulk w divertor of jet. Nuclear materials and energy, 19:397–402, 2019.

[330] M Pečovnik, EA Hodille, T Schwarz-Selinger, C Grisolia, and Sabina Markelj. New rate equation model to describe the stabilization of displacement damage by hydrogen atoms during ion irradiation in tungsten. Nuclear Fusion, 60(3):036024, 2020.

[331] André Pineau, Amine A Benzerga, and Thomas Pardoen. Failure of metals i: Brittle and ductile fracture. Acta Materialia, 107:424–483, 2016.

[332] Fethi Abbassi, Touhami Belhadj, Sébastien Mistou, and Ali Zghal. Parameter identification of a mechanical ductile damage using artificial neural networks in sheet metal forming. Materials & Design, 45:605–615, 2013.

[333] ZL Zhang and H Hauge. On the gurson micro-mechanical parameters. Fatigue and Fracture Mechanics: Twenty-Ninth Volume. ASTM STP, 1332:364–383, 1999.

[334] ZL Zhang and E Niemi. Analyzing ductile fracture using dual dilational constitutive equations. Fatigue & Fracture of Engineering Materials & Structures, 17(6):695–707, 1994.

[335] ZL Zhang and E Niemi. Studies on the ductility predictions by different local failure criteria. Engineering Fracture Mechanics, 48(4):529–540, 1994.

[336] ZL Zhang and E Niemi. A new failure criterion for the gurson-tvergaard dilational constitutive model. International Journal of Fracture, 70:321–334, 1994.

[337] ZL Zhang and E Niemi. A class of generalized mid-point algorithms for the gurson–tvergaard material model. International Journal for Numerical Methods in Engineering, 38(12):2033–2053, 1995.

[338] ZL Zhang. Explicit consistent tangent moduli with a return mapping algorithm for pressure-dependent elastoplasticity models. Computer methods in applied mechanics and engineering, 121(1-4):29–44, 1995.

[339] ZL Zhang. On the accuracies of numerical integration algorithms for gurson-based pressure-dependent elastoplastic constitutive models. Computer methods in applied mechanics and engineering, 121(1-4):15–28, 1995.

[340] ZL Zhang. A complete gurson model. Nonlinear fracture and damage mechanics, pages 223–248, 2001.

[341] Astm | e8m méthode d'essai normalisée pour l'essai de traction sur matériaux métalliques. https://www.zwickroell.com/fr/secteurs-dactivite/metal/normes-metal/essai-de-traction-materiaux-metalliques-astm-e8/. Accessed: 2023-12-06.

[342] II Cuesta, JM Alegre, and R Lacalle. Determination of the gurson–tvergaard damage model parameters for simulating small punch tests. Fatigue & fracture of engineering materials & structures, 33(11):703–713, 2010.

[343] S. Chroeun and M.D. Nguyen. Contraintes à rupture d'une bulle d'hélium en surface du tungstène, February 2023.

[344] Alexander Bakaev, Dmitry Terentyev, Aleksandr Zinovev, Chih-Cheng Chang, Chao Yin, Viktor A Bakaev, and Evgeny E Zhurkin. Application of sub-miniaturized bending tests to extract tensile properties from neutron-irradiated metallic alloys. Journal of Nuclear Materials, 558:153320, 2022.

Résumé

L'objectif de ce travail est d'étudier numériquement la rétention et la perméation de l'hydrogène dans certains composants du tokamak ITER exposés à des plasmas. Pour cela, le logiciel par éléments finis Abaqus est utilisé, et couplé avec des procédures utilisateurs pré-existantes ou créées spécifiquement pour ce travail, permettant ainsi les couplages entre champ de température, champ mécaniques, interfaces multi-matériaux, diffusion et piégeage de l'hydrogène. Des études paramétriques ont été effectuées sur des composants du réacteur à fusion ITER, en particulier le diagnostic first wall (DFW) et les monoblocs du divertor, afin d'estimer la rétention de l'hydrogène dans ces composants ainsi que sa perméation vers le circuit de refroidissement sous des conditions extrêmes. Afin de prendre en compte l'endommagement induit par les conditions d'exposition, et en particulier la création de bulles dans le matériau, un modèle de dynamique d'amas de la littérature, dédié à la simulation de la diffusion et la création/dissociation de clusters de lacune, a été implémenté dans Abaqus et couplé au champ thermique. Un modèle d'endommagement ductile (Gurson–Tvergaard–Needleman) a enfin été considéré pour permettre la prise en compte des bulles d'hydrogène, créées à partir de clusters de lacune ; dans ce cadre, des résultats préliminaires sont présentés.

Abstract

The aim of this work is to numerically study the retention and permeation of hydrogen in specific components of the ITER tokamak exposed to plasmas. For this objective, the Abaqus finite element software is used, coupled with pre-existing or created specifically for this work user subroutines, thus allowing couplings between thermal and mechanical fields, multi-material interfaces, diffusion and trapping of hydrogen. Parametric studies were carried out on the components of the ITER fusion reactor, especially the diagnosis first wall (DFW) and the diverter monoblocks, in order to estimate the retention of hydrogen in these components as well as its permeation towards the cooling circuit, under extreme conditions. In order to account for the damage induced by exposure conditions, and especially the creation of bubbles in the material, a cluster dynamics model from the literature, dedicated to the simulation of diffusion and creation/dissociation of clusters gap, was implemented in Abaqus and coupled to the thermal field. A ductile damage model (Gurson-Tvergaard-Needleman) was last considered to allow the introduction of hydrogen bubbles, created from clusters of vacancies; in this context, preliminary results are presented.